Atom Probe Tomography Characterization of Engineering Ceramics



Jaspreet Singh

Keble College

University of Oxford

A thesis submitted for the degree of

Doctor of Philosophy

Michaelmas Term 2021

To my parents and brother.

Sometimes science is more art than science.

- Rick Sanchez

Abstract

This doctoral thesis aims to characterize the effects of carbon doping on alumina grain boundaries and the effects of flash sintering on YSZ and SiC microstructure using a variety of techniques with a particular emphasis on atom probe tomography (APT).

Laser assisted APT, as applied to the analysis of ceramics, is a relatively nascent technique, so optimal operating conditions for the subject materials were rigorously investigated. A systematic and reproducible workflow with minimal subjective input for measuring the composition of features found in APT datasets was developed including a novel peak fitting ranging technique. Additionally, the effects of several APT reconstruction artefacts on compositional measurements were quantified, and the use of charge-state-ratios (CSR) was explored as a tool for minimizing these effects.

Scanning electron microscopy (SEM) analysis of carbon-doped and undoped fracture surfaces demonstrated a quantitative increase in transgranular fracture with carbon doping. Grain boundary relative energy measurements made using atomic force microscopy (AFM) highlight the need for careful experimental parameter consideration alongside the limitation of the technique when applied to highly reconstructed surfaces. APT analysis demonstrates little evidence of carbon segregation to doped alumina grain boundaries contrary to previously published work, probably the result of an unconsidered peak overlap between carbon and magnesium [1].

APT analysis of conventionally sintered 3 mole percent yttria stabilized zirconia (3YSZ) alongside samples flash sintered in a variety of electrochemically reducing environments yields key microstructural insights and differences. Flash sintered samples demonstrate improved yttrium homogeneity which may indicate less susceptibility to often detrimental phase transformation. APT analysis of grain boundary chemistry demonstrates flash sintering in strong reducing environments reduces grain boundary segregation opening the door for grain boundary engineering. Bulk analysis demonstrates evidence of the first successful flash sintering of zirconium oxycarbide. Lastly, triple point analysis yields evidence of sub-structuring occurring along the length of the junctions, however electric field induced artefacts must be considered.

The multi-scale analysis of conventionally and flash sintered SiC sintered with boron and carbon additives demonstrates fine-scale differences which may impact mechanical properties. Conventionally sintered samples subjected to long sintering times contain a bimodal grain structure with abnormal elongated grains, likely detrimental to mechanical properties. Electron backscatter diffraction (EBSD) analysis demonstrates no significant difference in polytype composition resulting from flash sintering, while energy dispersive x-ray spectroscopy (EDS) analysis shows microstructures with dispersed microscale boron/carbon rich inclusions. APT observation of nanoscale boron rich clusters prevalent in samples flash sintered using high power may help explain the anomalously high hardness values these samples demonstrate. Grain boundary analysis demonstrates the power used to flash sinter affects grain boundary segregation of boron and aluminum potentially due to differences in degree of sintering achieved and/or resulting grain size.

Preface

The work presented in this DPhil thesis has been conducted at the Department of Materials at the University of Oxford between October 2018 and October 2021 under the supervision of Prof. Richard Todd, Prof. Michael Moody, and Prof Peter Nellist. The work in this thesis is original, and the work of others included within is acknowledged and referenced. No parts of this thesis have been included in a degree at this or any other university. Some of the work undertaken in this thesis has been presented at conferences as listed below:

J. Singh, R. Todd, M. Moody. *Grain Boundary Analysis of Carbon-Doped Alumina.* European Atom Probe Tomography Workshop, Rouen, France. November 2019.

J. Singh, Y. Kubota, Y. Li, R. Todd, M. Moody. *Atom Probe Tomography of Conventionally and Flash Sintered YSZ.* Atom Probe Tomography and Microscopy, Virtual. November 2020.

J. Singh, Y. Kubota, Y. Li, M. Moody, R. Todd. *Atom Probe Tomography of YSZ.* 2 Day Research Meeting on Advanced Ceramics, Virtual, August 2020.

P. Gopon, J.O. Douglas, F. Meisenkothen, **J. Singh**, A.J. London, M.P. Moody. *Atom Probe Tomography for Isotopic Analysis: Development of the $^{34}S/^{32}S$ System in Sulfides*. Atom Probe Tomography and Microscopy, Virtual, September 2021.

Disclaimer:

The views expressed in this thesis are those of the author and do not reflect the official policy or position of the United States Air Force, Department of Defense, or the U.S. Government.

Acknowledgments

I would like to begin by thanking my supervisors Prof. Richard Todd and Prof Michael Moody for affording me the opportunity to pursue a DPhil. I am extremely grateful for the enormous amount of time and effort they have poured into me and my project. This thesis would not have been possible without their extraordinary support.

I would like to thank the Rhodes Trust for their financial support and for providing me the opportunity to pursue studies at Oxford. I am particularly grateful for the support Ms. Mary Eaton has provided over the years along with the support, friendship, and mentorship of Mr. Ricky Veloso.

Thank you to the countless members of the Materials Department who helped me during my studies. Mr. Anthony Wheeler, Dr. Gareth Hughes, Dr. Ian Griffiths, Mr. Graham Wyatt, Ms. Nicola Flanagan, and Ms. Jennifer Holter deserve special thanks for their support and guidance.

I would like to thank the members of the Ceramics group for their contribution and friendship. Thank you to Yasuhiro for your kindness and optimism. Thank you to Dr. Tom Scott and Dr. Jiawei, “Jiang Jiang,” Jiang for your warm welcome to the group and early guidance. And thank you to Gibby, our time together has truly been “somewhere between the best and the best.”

It has also been a true delight to be a member of the Atom Probe group during my DPhil. Thank you to Dr. James Douglas for the enormous amount of time you spent training and guiding me through the FIB specimen preparation process. Thank you to Dr. Benjamin Jenkins for your expert help in analyzing grain boundaries and for all the beers. Thanks to Dr. Paul Bagot for your support with APT experiments, and for making sure I don’t break the LEAPs. Thanks to Dr. Phil Gopon for the great banter and for allowing me to collaborate on geoscience projects. And a big thanks to Dr. Andrew London for your help using Atom Probe Lab, without which much of my data analysis would not have been possible.

I wish to thank the extraordinary friends I have made in Oxford. I will always cherish the laughs, memories, and support I was flooded with by the community I was lucky enough to become a part of here in Oxford. Thanks to Lewis, Jean, Clauds, Em, Shaan, Rob, Michelle, Taylor, and the countless others who made this such an unforgettable place to call home. I’d also like to thank “the bois” back home for their “support.”

Finally, and most importantly, I would like to thank my family for their love and support. Thank you to my dad for teaching me what it means to be a good man. Thank you to my mom for your unconditional love, relentless support, and extraordinary patience. And thank you to my brother. You’re my best friend and my role model; none of this would have been possible without you.

Acronyms

ACAFM: Alternating current atomic force microscopy

ADF: Annular dark field

AFM: Atomic force microscopy

APT: Atom probe tomography

CSL: Coincident site lattice

CSR: Charge state ratio

DFT: Density functional theory

EBPVD: Electron-beam physical vapor deposition

EBSD: Electron backscatter diffraction

EDS: Energy dispersive x-ray spectroscopy

EELS: Electron energy loss spectroscopy

EUVAPT: Extreme ultraviolet atom probe tomography

FAST: Field assisted sintering technology

FIB: Focused ion beam

FSPS: Flash spark plasma sintering

FWHM: Full width at half maximum

FWTM: Full width at tenth of maximum

GBSIPTM: Grain boundary segregation-induced phase transformation model

HAADF: High angle annular dark field

HRSTEM: High resolution scanning transmission electron microscopy

HRTEM: High resolution transmission electron microscopy

HV: High vacuum

IVAS: Integrated Visualization and Analysis Software

LEAP: Local Electrode Atom Probe

m/q: Mass to charge ratio

PECS: Pulsed electric current sintering

PSM: Pre-sharpened silicon microtip

ROI: Region of interest

SADP: Selected area diffraction pattern

SEM: Scanning electron microscopy

SPS: Spark plasma sintering

STEM: Scanning transmission electron microscopy

TEM: Transmission electron microscopy

TKD: Transmission Kikuchi diffraction

XRD: X-ray diffraction

YAG: Yttrium aluminum garnet

Contents

Chapter I Introduction 14

Chapter II Literature Review 17

1 Engineering Relevance 17

2 Carbon-doped Alumina 17

2.1 Engineering Relevance 17

2.2 Crystal Structure 18

2.3 Complexion Science 19

2.4 Role of MgO 20

2.5 Carbon-doped Alumina Analysis Motivation 22

2.6 Carbon-doped Alumina 23

2.7 Alumina Grain Boundary TEM/STEM Characterization 28

2.8 Alumina APT Analysis 30

2.9 Grain Boundary Relative Energy Measurement 31

2.10 Conclusions 34

3 Flash Sintered 3YSZ 35

3.1 Engineering Relevance 35

3.2 Phase Stability 35

3.3 Flash Sintering 37

3.3.1 Flash Sintering Setups 37

3.3.2 Flash Sintering Mechanism 38

3.4 High Resolution YSZ Microstructural Characterization 40

3.4.1 TEM/STEM Grain Boundary Analysis 40

3.4.2 TEM/STEM Analysis of Bulk YSZ Chemistry and Structure 43

3.4.3 APT Analysis of YSZ 45

3.4.4 Flash Sintered YSZ TEM/STEM Characterization 47

3.5 Conclusions 50

4 Flash Sintered SiC 50

4.1 Engineering Relevance 50

4.2 Crystal Structure 50

4.3 Role of Carbon and Boron in SiC Sintering 52

4.4 SiC Bimodal Microstructure 53
4.5 Flash Sintering and Flash Spark Plasma Sintering of SiC 54
4.6 High Resolution SiC Bulk Analysis 56
4.7 High Resolution SiC Grain Boundary Analysis 58
4.8 APT Analysis of SiC 59
4.9 Conclusions 61
5 APT Analysis of Ceramics 62
6 Conclusions 66
Chapter III Materials and Methods 68
1 Powder Processing and Sintering 68
1.1 Alumina 68
1.2 3YSZ 69
1.2.1 Powder Processing 70
1.2.2 Sintering 71
1.2.2.1 Conventional Sintering 71
1.2.2.2 Flash Sintering (FS C and FS A) 72
1.2.2.3 Flash Sintering Reduced (FS C R) 72
1.2.2.4 Flash Sintering He (FS C He/FS A He) 73
1.2.2.5 Flash Sintering He 1 Hr (FS C He 1 Hr) 73
1.2.3 Density Measurement 73
1.3 SiC 74
1.3.1 Powder Processing 74
1.3.2 Sintering 75
1.3.1.1 Fire 1 75
1.3.1.2 Fire 2 75
1.3.3.3 FS 75
1.3.3.4 FS Hard 75
1.3.3 Density and Hardness Measurements 76
2 Atom Probe Tomography 76
2.1 Experimental Principles 76
2.2 Specimen Preparation 79
2.3 APT Data Analysis Tools and Techniques 81

2.3.1 Peak Identification and Ranging 81
2.3.2 Compositional Measurements 81
2.3.3 Concentration Profiles 82
2.3.4 Isoconcentration/Isodensity Surfaces and Proxigrams 82
2.3.5 Volume Renderings 83
2.3.6 Binomial Analysis 83
2.3.7 Clustering Analysis 84
2.3.8 Gibbsian Interfacial Excess 85
3 Electron Microscopy 87
3.1 Scanning Electron Microscopy Imaging 87
3.1.1 Linear Intercept Grain Size Measurement 87
3.1.2 Percentage of Transgranular Fracture Characterization 88
3.2 Energy Dispersive X-ray Spectroscopy 88
3.3 Electron Backscatter Diffraction 89
3.4 Transmission Kikuchi Diffraction 90
3.5 Scanning Transmission Electron Microscopy 92
4 Grain Boundary Relative Energy Measurement 92
Chapter IV APT Operating Conditions and Compositional Comparison Considerations 95
1 APT Experimental Conditions Sweep 95
2 APT Composition Comparison Considerations 97
2.1 Ranging of the Mass Spectra 97
2.2 Peak Overlaps 102
2.2 Tip Blunting 103
2.3 Laser Illumination Proximity 103
2.4 Correlative Evaporation Histograms 104
2.6 Sample Size 107
3 3YSZ Results 107
3.1 Laser Energy Sweep 108
3.2 Reflectron (LEAP 5000XR) vs. Straight Flightpath (LEAP 5000XS) 109
3.3 Ranging 109
3.4 Peak Overlaps 110

3.5 Tip Blunting 111
3.6 Laser Illumination Proximity 113
3.7 Correlative Evaporation Histogram 114
3.8 Sample Size 116
4 Alumina Results 117
4.1 Laser Energy Sweep 118
4.2 Reflectron (LEAP 5000XR) vs. Straight Flightpath (LEAP 5000XS) 119
4.3 Ranging 120
4.4 Peak Overlaps 120
4.5 Tip Blunting 121
4.6 Laser Illumination Proximity 122
4.7 Correlative Evaporation Histogram 124
4.8 Sample Size 125
5 SiC Results 126
5.1 Laser Energy Sweep 127
5.2 Laser Pulsing Mode vs. Voltage Pulsing Mode 128
5.3 Reflectron (LEAP 5000XR) vs. Straight Flightpath (LEAP 5000XS) 128
5.4 Ranging 128
5.5 Peak Overlaps 129
5.6 Tip Blunting 130
5.7 Laser Illumination Proximity 132
5.8 Correlative Evaporation Histogram 132
5.9 Sample Size 135
6 Discussion 135
6.1 Laser Energy Sweep 135
6.2 Laser Pulsing vs. Voltage Pulsing 136
6.3 Reflectron (LEAP 5000XR) vs. Straight Flightpath (LEAP 5000XS) 137
6.4 Ranging 138
6.5 Peak Overlaps 139
6.6 Tip Blunting 139
6.7 Laser Illumination Proximity 142
6.8 Correlative Evaporation Histogram 143

6.9 Sample Size....144
7 Conclusions....145
Chapter V Alumina Analysis....148
1 Results....148
1.1 SEM Characterization....148
1.2 Grain Boundary Relative Energy Analysis....151
1.3 STEM Analysis....154
1.4 Atom Probe Analysis....155
1.4.1 Bulk Analysis....155
1.4.2 Grain Boundary Analysis....156
1.4.3 Triple Point Analysis....160
2 Discussion....161
2.1 SEM Characterization....161
2.2 Grain Boundary Relative Energy Analysis....162
2.3 STEM Analysis....165
2.4 APT Analysis....166
3 Conclusions....168
Chapter VI 3YSZ APT Analysis....170
1 Results....170
1.1 Bulk Analysis....170
1.1.1 Bulk Composition....170
1.1.2 Binomial Grid-Based Frequency Analysis....175
1.1.3 Round Intragranular Yttrium-Rich Features....176
1.1.4 Lath-like Yttrium Rich Features....179
1.1.5 Grain Boundary Adjacent Yttrium Enrichment....180
1.1.6 Grain Boundary Adjacent Yttrium Depletion....183
1.1.7 FS C He 1Hr Carbon Rich Phase....185
1.2 Grain Boundary Analysis....189
1.2.1 Gibbsian Interfacial Excess....189
1.2.2 Grain Boundary Composition....190
1.2.3 Grain Boundary Structure....191
1.3 Triple Point Characterization....196

2 Discussion 201
2.1 Bulk Analysis 201
2.2 Zirconium Oxycarbide Phase 209
2.3 Grain Boundary Analysis 210
2.4 Triple Point Analysis 213
3 Conclusions 213
Chapter VII SiC Analysis 215
1 Results 215
1.1 Bulk SEM Analysis 215
1.1.1 EBSD Analysis 215
1.1.2 EDS Analysis 217
1.2 APT Bulk Analysis 218
1.2.1 SiC Bulk Composition 218
1.2.2 Binomial Grid-Based Frequency Analysis 220
1.2.3 Cluster Analysis 221
1.2.4 B_4C Bulk Composition 223
1.3 APT Grain Boundary Analysis 223
1.3.1 Gibbsian Interfacial Excess 223
1.3.2 Polytype Boundary 225
1.4 APT B_4C-SiC Phase Boundary Analysis 226
1.5 APT Triple Point Analysis 227
2 Discussion 228
2.1 Bulk SEM Analysis 228
2.2 APT Bulk Analysis 230
2.3 APT Grain Boundary Analysis 234
2.4 APT B_4C-SiC Phase Boundary Analysis 236
2.5 APT Triple Point Analysis 237
3 Conclusions 237
Chapter VIII Conclusions 238
Chapter IX Future Work 242
Chapter X Works Cited 245

Chapter I

Introduction

Evidence for the use of ceramics in engineering applications has been found alongside remnants of the earliest signs of civilization [2]. Engineering ceramics have evolved far beyond the traditional clay-based materials employed thousands of years ago. Today, ceramics are used in a broad array of industries including nuclear energy, mining, aerospace, energy storage, solar energy, and much more. With such diverse and widespread usages, interest in improving the properties, reliability, and economy of ceramics is of high interest.

As with all other types of materials, atomic level structure determines the properties of ceramics. Therefore, any attempt to push the boundaries of ceramic processing and resulting macroscale properties necessitates a thorough understanding of atomic chemistry and structure provided by high resolution microscopy. Traditionally, high resolution atomic scale characterization of ceramics has been conducted using transmission electron microscopy (TEM). However, with the recent advent of laser assisted APT, the possibility for three-dimensional chemical characterization of ceramics at the sub nanometer scale has been realized. In this thesis, APT and several other characterization techniques have been used to investigate the effect of processing and powder chemistry on three engineering ceramic systems: carbon-doped alumina, flash sintered 3YSZ, and flash sintered silicon carbide. Furthermore, analysis of these three ceramics has yielded important experimental factors to consider when applying APT to other ceramic materials as the technique becomes more widely available.

This thesis is divided into 9 chapters. Chapter II provides a critical overview of the state of the literature regarding microscopic characterization of the three ceramic systems of interest to this thesis with a particular emphasis placed on atomic scale resolution characterization. Chapter III describes the synthesis of the materials analyzed in further chapters along with a description of the analysis methods and data analysis tools used throughout the course of the study.

Chapter IV provides a description of a novel data treatment method developed to improve reproducibility and minimize user subjectivity when determining composition using APT. Chapter IV also analyzes the effects of measurement artefacts on APT analysis of the three materials studied which can be generalized to other similar ceramic systems. Finally, Chapter IV discusses attempts to optimize APT experimental conditions to achieve accurate compositional measurements.

Chapter V presents the results of multi-scale analyses conducted on carbon-doped and undoped alumina grain boundaries. APT was used to characterize the chemistry of grain boundaries while AFM was employed to study any energy differences present between samples sintered using different powder chemistries or in different sintering environments. TEM and scanning electron microscopy characterization of carbon-doped and undoped alumina can also be found in Chapter V.

Chapter VI describes the results of APT analysis of conventionally sintered 3YSZ alongside 3YSZ flash sintered in a variety of different chemical environments.

The multiscale analysis of conventionally and flash sintered SiC using techniques such as EDS, EBSD, and APT is discussed in Chapter VII.

Chapter VIII provides a summary of the key findings presented throughout the thesis before Chapter IX closes with a discussion of potential future work to build on the findings in this thesis.

Chapter II

Literature Review

1 Engineering Relevance

Ceramics are an incredibly versatile class of materials with applications spanning many diverse industries. Like any material, the chemistry and structure of ceramics dictates properties and applications [2], [3]. Therefore, microstructural characterization of engineering ceramics down to the atomic scale is necessary for field advancement. The next several sections of this thesis will highlight work from literature examining chemistry and microstructure of the three materials examined in this thesis: carbon-doped Al_2O_3, flash sintered 3YSZ, and flash sintered SiC. A final section will discuss literature relevant to the examination of ceramics and bulk nonmetals using APT, a method which will constitute most of the results in this thesis.

2 Carbon-doped Alumina

2.1 Engineering Relevance

Alumina, or aluminum oxide (Al_2O_3), is a common engineering ceramic with a wide array of applications. Alumina applications are derived from its unique characteristics: high melting temperature, high chemical/oxidation resistance, high hardness, and good wear resistance [1]. These characteristics lead to applications including abrasives, refractories, glass production, and use as engineering ceramics in a wide range of fields from medicine to electrical engineering [2]. Like many engineering ceramics, alumina suffers from brittle

fracture [2].

Improvement of mechanical properties of alumina is an important research interest in ceramic science. Recent research into alumina nanocomposites and impurity doped alumina have highlighted the importance grain boundary science plays in the mechanical properties of alumina [4]–[6]. Of interest to this review is the influence of carbon doping on alumina grain boundaries and therefore alumina macroscopic properties. To develop a better understanding of this phenomenon, an introduction to carbon-doped alumina, grain boundary science, and specific work into alumina grain boundaries will be detailed in the following sections.

2.2 Crystal Structure

The crystal structure of α-Al_2O_3, the most used polymorph in engineering ceramics, is the corundum structure. This structure closely resembles that of the oxygen anions occupying hexagonally close-packed sites with aluminum cations occupying two thirds of octahedral interstitial sites [7]. The crystal structure is represented in Figure 1.

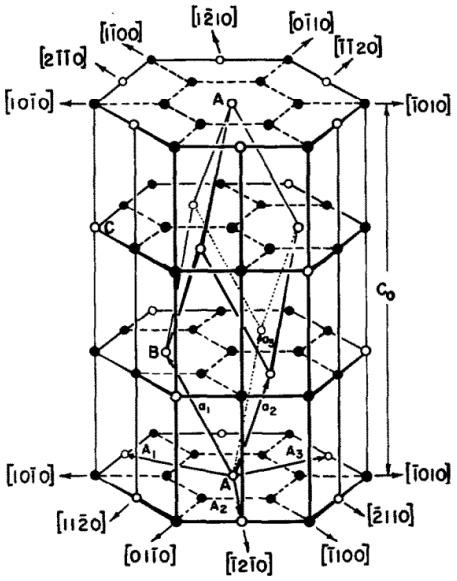


Figure 1: Crystal structure of alpha alumina. Reprinted with permission from [8]

2.3 Complexion Science

As the justification for this study is to analyze the impact of carbon doping on grain boundary properties dictated by chemistry and structure, it is helpful to briefly introduce the grain boundary complexion framework [9]. Grain boundaries do not meet the Gibbs definition of a phase because they are inhomogeneous and can have spatial gradients of structure and chemistry [6]. Thus, a complexion is defined as "interfacial strata that is in thermodynamic equilibrium with its abutting phases" by a seminal review authored by Cantwell *et al.* [6]. Just as bulk phase changes can result in significant changes in macroscopic properties, complexion transitions can result in similarly significant changes. Thus the goal of many complexion studies is to create grain boundary complexion diagrams (like phase diagrams) and time-temperature-transformation complexion diagrams to help predict complexion transitions and ultimately engineer desirable complexions. This thesis will explore the possibility that carbon doping causes a complexion transition when compared to undoped alumina causing a change in grain boundary mechanical properties. A somewhat competing

grain boundary classification system primarily used by Kang *et al*. to describe grain growth during liquid phase sintering broadly categorizes grain boundaries as either atomically smooth/macroscopically faceted or atomically rough/macroscopically rounded [10]. Atomically rough boundaries and atomically smooth boundaries demonstrate different grain growth rates and mechanisms during liquid phase sintering. Atomically rough grain boundaries possess many atomic sites for atom attachment, and therefore growth is diffusion limited resulting in normal grain growth. Atomically smooth boundaries do not possess as many energetically favorable sites for attachment (due to a higher likelihood of dangling bonds), and therefore growth is limited by interfacial reaction which can result in either abnormal or normal grain growth. A review by Kang *et al*. on rough and smooth boundaries makes no explicit statement regarding complexions, however a seminal review of complexions by Harmer *et al*. does discuss grain boundary roughening transformations [6], [10]. There exists significant room for further synthesis of the two schools of thought and classification systems.

2.4 Role of MgO

The alumina samples analyzed in this thesis are made from commercially available powder containing magnesia as an impurity. Furthermore, many of the alumina specimens analyzed in this thesis are doped with additional magnesia. Therefore, the role of magnesia in the sintering of alumina is an important topic to consider. During the sintering of alumina, grain boundary diffusion appears to be the rate limiting pathway leading to densification [11]. Thus, grain boundary structure and chemistry play a very important role in not only mechanical properties, but also sintering and fabrication of alumina. At the temperatures required for sintering, grain growth caused by the movement of grain boundaries and

consumption of smaller grains by larger grains can become prevalent. In alumina, grain growth during sintering can lead to pore entrapment within the lattice preventing vacancy diffusion along grain boundaries during final stage sintering and decreased densities [3]. In the late 1950s, Robert Coble discovered that MgO added before sintering prevented excessive grain growth [12]. The mechanisms causing this phenomenon are outlined in Table 1.

Table 1: Influence of Magnesia on Alumina Sintering

1. Magnesia segregation to grain boundaries lowers grain boundary mobility by solid solution drag. Pores remain attached to immobile grain boundaries [3], [13], [14].
2. Magnesia changes the equilibrium geometry of the pores, causing increased pore induced grain boundary drag. Pores remain attached to immobile grain boundaries [3], [13].
3. Magnesia increases rate of densification versus grain growth by increasing the mobility of atoms across and along grain boundaries leading to sintering instead of coarsening [3], [13].
4. Magnesia increases surface diffusion rate in alumina and pore mobility allowing pores to migrate with grain boundaries [3], [15].

All of the aforementioned phenomena are believed to positively influence alumina sintering, however the relative effects of each is still disputed [3] [14]. The interplay of magnesia with alumina grain boundaries highlights the effects a dopant or impurity may have on grain boundary chemistry/structure resulting in dramatic changes in mechanical properties.

2.5 Carbon-doped Alumina Analysis Motivation

Interest in the study of carbon-doped alumina grain boundaries stems from research conducted on alumina nanocomposites, specifically alumina/silicon carbide nanocomposites. Several studies have demonstrated the notable effects on mechanical properties SiC nanoparticles have on Al_2O_3 including an increase in wear resistance and toughness [4], [16]–[22]. The increased toughness and wear resistance were attributed to crack deflection from grain boundaries into alumina grains causing a more tortuous crack path [4]. A more circuitous crack path leads to higher fracture surface energy requiring more energy to form [3]. Intergranular SiC particles were believed to sufficiently explain this strengthening phenomenon. TEM studies by Jiao *et al*. demonstrate mode I crack propagation deflected into bulk grains, shown in Figure 2 [23].

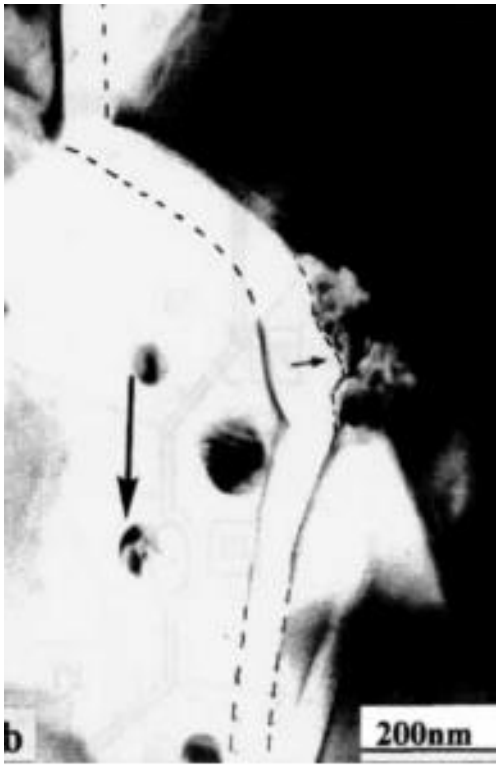


Figure 2: Mode I crack propagation deflected by intergranular SiC particle (indicated by small arrow). Reprinted with permission from [23].

In the figure above, the intergranular SiC particle, indicated by the small arrow, deflects the crack along the grain boundary into the bulk grain, while the intragranular SiC particle indicated by the large arrow has no effect on the crack propagation. This phenomenon partially explains the grain boundary strengthening of the SiC/Al_2O_3 nanocomposites; however, it is not a sufficient explanation. Experiments conducted by Todd and Ortiz-Merino indicate intragranular SiC particles also have a strengthening effect on SiC/Al_2O_3 nanocomposites [4]. Results from this study demonstrate SiC/Al_2O_3 nanocomposites comprised of SiC particles with a low fraction of particles on grain boundaries also demonstrate low area fraction of pullout during wear [4]. Thus crack deflection by intergranular SiC particles is not a sufficient explanation for the strengthening of SiC/Al_2O_3 nanocomposites. Another possible grain boundary strengthening mechanism induced by the addition of SiC particles to alumina is impurity segregation to grain boundaries causing strengthening and crack deflection. A major impurity found in SiC is free carbon.

2.6 Carbon-doped Alumina

The effects of free carbon on alumina structure/mechanical properties are not as well studied as the effects of SiC on alumina. Studies conducted by Sedlacek *et al*. found carbon addition to alumina improved wear resistance compared to monolithic alumina [24]. However, this study used 3 wt% C and attributed the improved wear resistance to graphite lubrication, a previously characterized mechanism stemming from formation of a low-friction graphite layer between the wear agent and wear surface [25], [26]. This lubrication effect does not likely occur at the concentration of free carbon resulting from SiC impurity.

Studies conducted by Yahya and Todd examine the wear/mechanical effects of carbon

content matching SiC impurity levels [27]. Free carbon resulting from SiC impurity was estimated at 0.012 wt%, and the wear/fracture effects of this doping level were investigated. The addition of trace carbon pre-sintering had no effect on final sintered grain size yet doping had a measurable effect on wear and fracture. The carbon effect on wear crater diameter and wear volume caused by a rotating chrome steel ball are summarized in Figure 3.

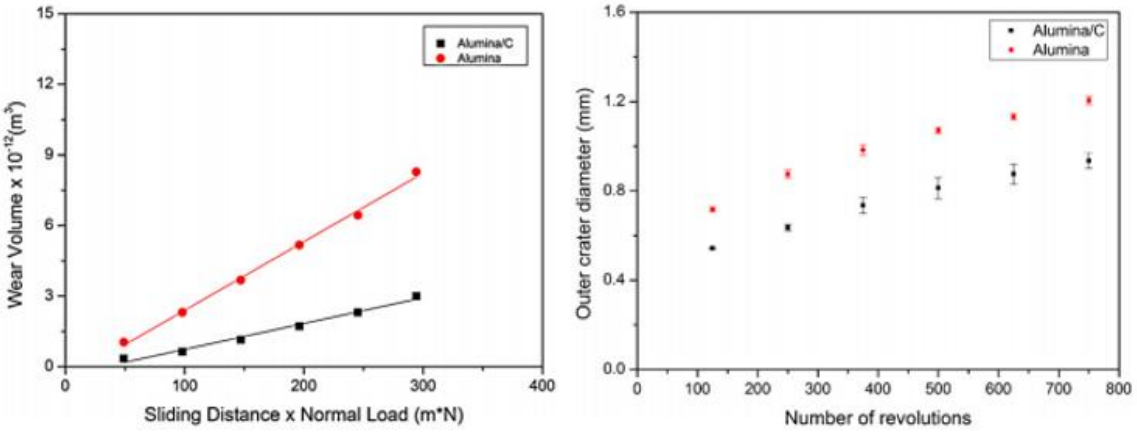


Figure 3: Left plot demonstrates wear volume versus sliding distance x normal load for carbon-doped and pure alumina specimens. Right plot shows wear crater diameter versus number of revolutions for doped and undoped specimens. Reprinted with permission from [27].

The results demonstrate the improved wear resistance of impurity level carbon doping in alumina. The same study also compared the fracture surfaces of doped and undoped specimens, shown in Figure 4.

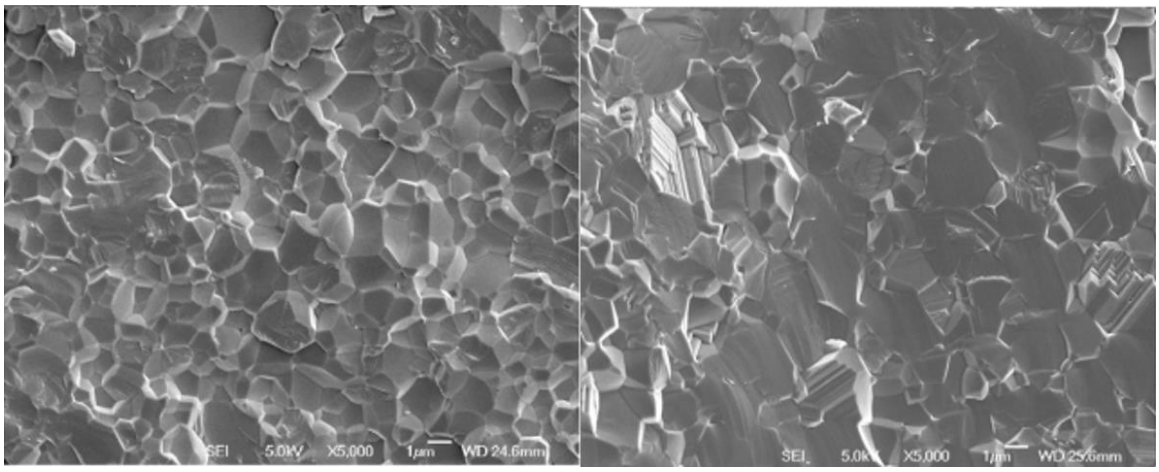


Figure 4: Fracture surface of pure (left) alumina versus carbon-doped (right) alumina. Reprinted with permission from [27].

The micrographs indicate largely transgranular fracture for the carbon-doped specimen versus largely intergranular fracture for the undoped specimen. The fracture surfaces demonstrate a qualitative difference in fracture for carbon-doped specimens. However, the study did not complete a rigorous quantitative analysis of fracture nature. Yahya's doctoral thesis also characterizes the effects on mechanical properties and microstructure of impurity level carbon-doped alumina [28]. Yahya demonstrated that carbon had little effect on the grain size of sintered alumina but led to an increase in hardness [28]. Yahya also reported the effect of 0.012 wt% C on the flexural strength and fracture toughness of alumina using four point bending tests with and without notches. Values were determined both for pure and doped specimens at two different grain sizes. For both the smaller and larger grain sizes, flexural strength and fracture toughness increased with carbon addition [28]. Carbon doping caused an increase in hardness and an insignificant change in elasticity [28].

The influence of carbon doping on the mechanical properties of alumina is becoming better understood. However, a mechanistic understanding of the influence carbon has on alumina microstructure remains largely unstudied. Seminal APT analysis conducted by Marquis *et*

al. is one of a few such mechanistic studies [1]. APT allows investigation of the three-dimensional chemical structure of materials. Due to carbon surface contamination inherent to high vacuum systems, high resolution z-contrast scanning transmission electron microscopy used to characterize impurity distribution of other elements in alumina is not suitable to the study of carbon segregation. This makes atom probe an attractive option for carbon characterization in alumina. Using laser assisted APT, Marquis studied the microstructural effects of carbon doping on alumina. Specimen preparation workflow and important results are found in Figure 5.

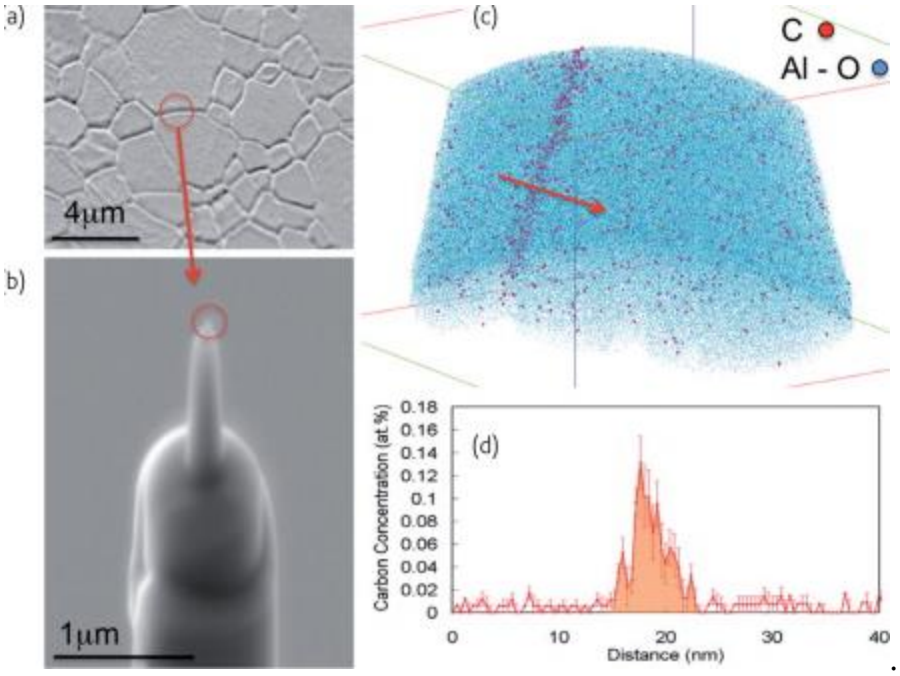


Figure 5: Atom probe specimen preparation and results. Reprinted with permission from [1].

Marquis prepared an atom probe specimen from a thermally etched and platinum coated specimen shown in Figure 5(a). Specimen preparation was performed using a dual beam focused ion beam (FIB) using established in situ lift-out/deposition techniques [29]. A grain boundary identified via thermal etching was placed within 50 nm of the tip of the specimen. Three-dimensional atom-by-atom reconstruction of the data is shown in (c) with a carbon

decorated grain boundary. Finally, a one-dimensional concentration profile is shown in (d) demonstrating carbon segregation to a grain boundary. The grain boundary width is shown by the shaded region of (d) and corresponds to a carbon distribution of 1.5±0.5 atom/nm^2 [1]. A pure undoped specimen was not analyzed in the study, therefore a direct comparison is not possible. Furthermore, an accompanying APT mass spectrum highlighting the peaks identified as carbon was not presented. The grain boundary analyzed was located via thermal etching and analyzed via targeted lift out. It is possible that during the thermal etching process local chemistry changes and mass transport could have taken place at the grain boundary resulting in a different chemical structure than in the sintered specimen. Thus, a targeted lift out method omitting a thermal grooving treatment would be preferred.

Carbon doping of alumina has been demonstrated to increase strength, toughness, and wear resistance. Additionally, early chemical characterization seems to indicate carbon segregates to grain boundaries. However, the mechanism by which the mechanical property changes are achieved is not sufficiently explained in literature. A couple proposed mechanisms follow. The fracture surfaces of carbon doped samples have an increased proportion of transgranular fracture, however the fracture surfaces are still mixed intergranular and transgranular. Perhaps carbon doping sufficiently strengthens some boundaries to a strength capable of causing crack deflection while not sufficiently strengthening others. This would cause intragranular crack deflection at some grain boundaries while allowing cracks to travel along other boundaries, achieving a similar result as SiC particles being found only at certain grain boundaries. The net result would be a more circuitous crack path leading to increased wear resistance, strength, and toughness. Section 2.4 also demonstrates the effect

impurities/dopants (MgO in this case) can have on grain boundary chemistry and sintering. Perhaps carbon affects the mass transport pathways present during sintering by segregating to grain boundaries or by causing local chemistry changes. These effects could cause changes in porosity which lead to less defect sites for crack initiation/propagation leading to improved mechanical properties. Both of these mechanisms imply strengthening due to carbon doping may be related to grain boundary structure and chemistry. Thus, a detailed analysis of existing literature analyzing alumina grain boundaries will be presented in the following sections.

2.7 Alumina Grain Boundary TEM/STEM Characterization

Much of the structural characterization of alumina grain boundaries focuses on characterization of artificially bonded bicrystals. This allows careful control of grain boundary characteristics and isolation of parameters for testing. Many of these artificially bonded grain boundaries are special grain boundaries called coincident site lattice (CSL) grain boundaries which form from grains meeting with overlapping lattice sites that possess unique properties [30], [31]. These boundaries are characterized by the reciprocal density of coincidence sites versus crystal lattice sites known as the Σ value [30]. CSL grain boundaries in polycrystalline pure alumina have been observed via high resolution transmission electron microscopy (HRTEM) in various studies [32]–[36]. Alongside pure alumina grain boundary imaging, it is also of interest to study the effect on bicrystals of segregating impurities. Often high atomic number impurities are studied due to the resulting contrast differences seen in high resolution scanning transmission electron microscopy (HRSTEM). Several studies focus on the structural effects of rare earth metal doping on alumina grain boundaries, as rare earth metals tend to improve resistance to high temperature creep via solute drag at grain

boundaries [37], [38]. These studies identify the segregating impurities by Z-contrast (atomic number contrast) using high angle annular dark field (HAADF) scanning transmission electron microscopy (STEM) which measures very high angle incoherently scattered (Rutherford scattered) electrons providing strong atomic number contrast [39]. This type of contrast is not possible for light elements such as carbon.

Structural grain boundary studies have however been carried out on segregating impurities with similar atomic numbers to lattice aluminum and oxygen. One such study investigated the segregation of titanium and silicon, two common impurities in alumina powders, to alumina grain boundaries [5]. This study used polycrystalline sintered alumina to characterize several grain boundaries as opposed to one well controlled bicrystal boundary. The study concluded Si and Ti have a strong tendency to segregate to grain boundaries, but are more likely to do so at specific misorientations and special boundary types [5]. Silicon segregates preferentially to boundaries with boundary planes parallel to the basal plane of one of the abutting boundaries possibly due to an epitaxial reaction of SiO_2 with alumina which can lead to amorphous thin film formation [5]. Titanium segregates preferentially to boundaries with boundary planes parallel to the rhombohedral plane of one grain as well as parallel to planes with low atomic densities [5]. This may be explained by the larger size of titanium atoms as compared to aluminum and oxygen atoms. Another similar study investigated the preferential segregation of calcium to twin boundaries in alumina using HRSTEM and EDS analysis [40]. These studies are powerful in their paired chemical/structural characterization of grain boundaries without relying upon heavy atom induced atomic number contrast or artificially bonded bicrystals, which may not be

representative of the structural distribution of random grain boundaries in polycrystalline systems. However, due to the issue of HV carbon contamination, such correlative EDS/HRTEM determination is more difficult when investigating potential carbon segregation to grain boundaries.

Along with well-structured clean grain boundaries, HRTEM studies often find thin intergranular film complexions at higher angle boundaries and at triple points [6]. These intergranular films are amorphous and for alumina tend to be on the order of ~1nm thick [41]. EDS analysis shows that these intergranular films tend to be enriched with certain common alumina impurities such as silica and calcia [42]. Although these thin films are more common in liquid sintered samples, the films have been observed in high purity aluminas such as Lucalox [43]. Even in high purity alumina, silica remains a common impurity and segregates to boundaries to form thin intergranular films and its removal could result in a decrease in intergranular film formation [6], [42]. As a strong reducing agent, it is possible carbon is not directly strengthening grain boundaries but removing other impurities like silica. Molecular dynamics simulations by Garofalini *et al*. demonstrate calcium cations can segregate to specific cage-like structures formed at the interface of silica thin films and alumina grains promoting structuring and strengthening of the amorphous films [44]–[46]. Perhaps carbon plays a similar role in facilitating structuring of otherwise amorphous siliceous phases.

2.8 Alumina APT Analysis

Along with the work conducted by Marquis *et al.*, a few other studies have analyzed alumina using APT. However, these studies have focused on thermally grown alumina scale on

aluminum alloys as opposed to bulk sintered alumina. Work conducted by Povstugar *et al.* demonstrated titanium, yttrium, and silicon segregation to grain boundaries in alumina scale [47]. Another study by Stiller *et al.* studied the chemical distribution of dopants within alumina oxide scales formed atop several different alloys [48]. These further demonstrate the feasibility of APT analysis of alumina while also providing guidance on specimen preparation and APT experimental conditions.

Direct observation of grain boundary structure and chemistry is not the only way to identify changes in grain boundary nature caused by chemical doping. Using AFM, changes in grain boundary energy can be measured as discussed in the following section.

2.9 Grain Boundary Relative Energy Measurement

The fundamental thermodynamic parameter describing a grain boundary is the energy per unit area, γ. Complexion transformations are often associated with a reduction in γ [6]. The absolute value of the boundary energy is difficult to measure, yet it is easier to calculate the relative energy of a grain boundary compared to a free surface [6]. The relative energy of a grain boundary can be calculated from the dihedral angle formed via thermal grooving of a grain boundary at a free surface using the following equation [49].

$$\frac{\gamma_{GB}}{\gamma_s} = 2\ \cos\frac{\psi_s}{2}$$

γ_{GB} and γ_s represent the energy per unit area of the grain boundary and surface free surface respectively [49]. A schematic demonstrating the dihedral angle formed via grain boundary grooving can be found in Figure 6.

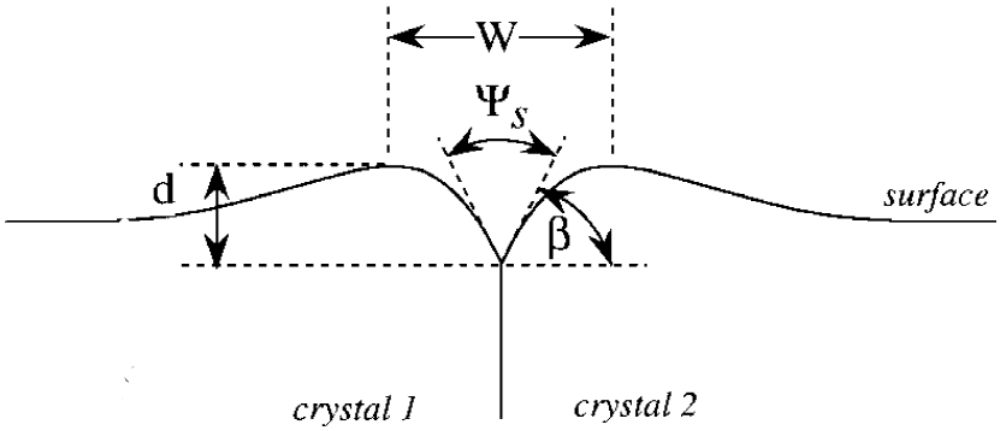


Figure 6: Grain boundary groove formed via thermal etching with labeled depth (d), width (W) and dihedral angle (ψ). Reprinted with permission from [49].

Direct measurement of the dihedral angle at the root of a boundary groove is difficult, however using analysis conducted by Mullins and Robertson it is possible to find the dihedral angle at the groove root using measurement of d and W [50],[51]. These geometric values are measured with AFM using a nanoscale tip drawn across the surface of a groove measuring its depth profile. This method was first introduced by Rohrer and Mullins to compare the relative energy values of low angle alumina grain boundaries with varying Σ values [49]. This method has subsequently been applied to alumina to measure grain boundary relative energies of different complexions due to dopant segregation, temperature changes, abnormal grain growth, and grain boundary misorientation [52], [53], [54]. Grain boundary relative energy measurements are a powerful tool to identify complexion transitions, however the method makes some important assumptions and suffers from significant limitations. Tip convolution is an issue inherent to any AFM measurement, and thus only sufficiently shallow grooves must be measured. Saylor and Rohrer addressed this issue in their seminal study and provided measurement guidelines [49]. The equation relating the dihedral angle of a groove and the relative energy of a grain boundary makes the

following assumptions [49]:

1. The surface energy is isotropic.
2. The grain boundary is normal to the surface plane.
3. Grain boundary energy is a function of misorientation but not boundary tangent plane.

These assumptions may not always valid for a given boundary. Thus in grain boundary relative energy studies hundreds of boundaries are sampled, and cumulative distribution plots are presented [55]. A plot demonstrating the difference in relative grain boundary energies between alumina grain boundaries separating normal and abnormal grain can be found in Figure 7.

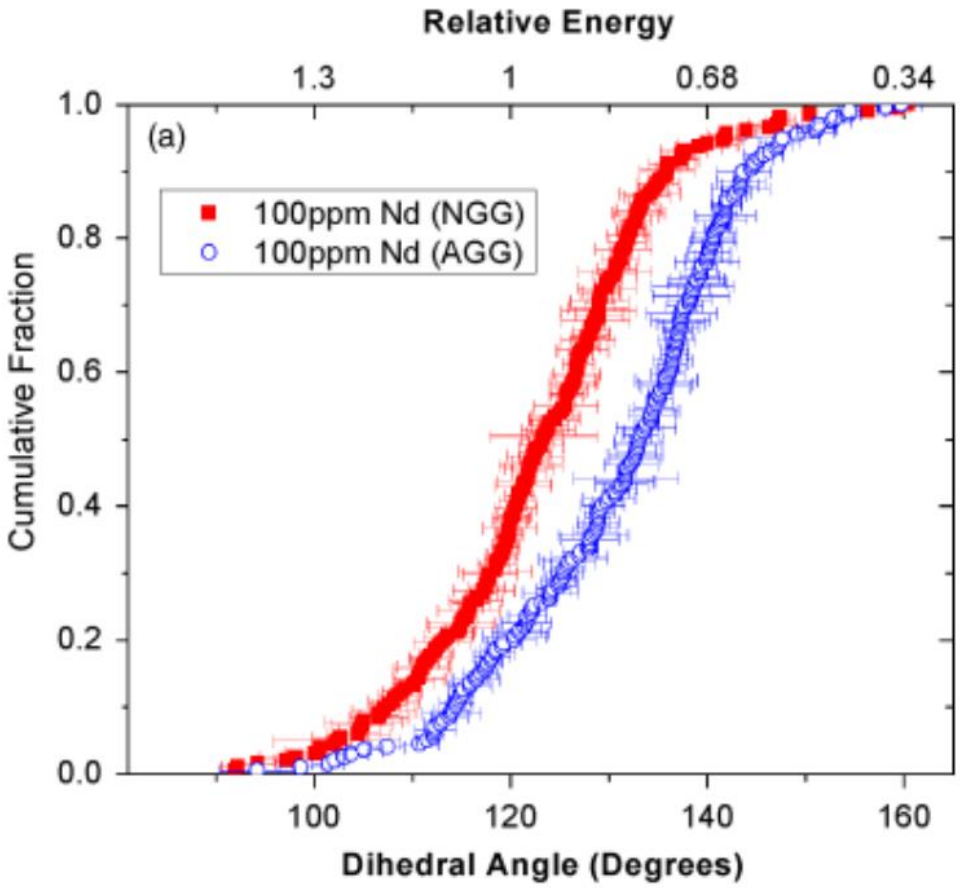


Figure 7: Dihedral angle and relative energy distributions for neodymia-doped alumina grain boundaries demonstrating normal and abnormal grain growth. Reprinted with permission from [52].

2.10 Conclusions

Interest in carbon-doped alumina stems from grain boundary strengthening observed in SiC-alumina composites that cannot be explained by intergranular SiC particles alone. The strengthening effects of carbon-doped alumina at grain boundaries have been observed in several studies, however the mechanism causing these mechanical property changes is not well understood. Finally, grain boundary studies of alumina from literature provide inspiration for techniques to employ when studying the effect of carbon doping on alumina grain boundaries while highlighting strengths and weaknesses of these techniques when applied to carbon analysis.

3 Flash Sintered 3YSZ

3.1 Engineering Relevance

Zirconia is an engineering ceramic with a wide array of applications stemming from its unique properties. Its chemical inertness, high temperature resistance, and mechanical strength lend it to use in cases such as dental implants, thermal barrier coatings, and as a refractory [3], [56], [57]. Due to its high ionic conductivity, zirconia has become an important material used in solid oxide fuel cell applications [58]. With such a diverse list of applications in critical industries, interest in economic sintering of zirconia is high [59]. In this section, literature relevant to the microstructural characterization of zirconia sintered using a relatively new and novel technique, flash sintering, will be explored.

3.2 Phase Stability

At atmospheric pressure, zirconia exists as three polymorphs: cubic, tetragonal, and monoclinic [3]. Under equilibrium conditions at room temperature, zirconia exists in the monoclinic form [56]. However, with the addition of stabilizers such as yttria, the cubic and tetragonal forms can become stable or metastable at room temperature [3]. The zirconia-yttria phase diagram can be found in Figure 8.

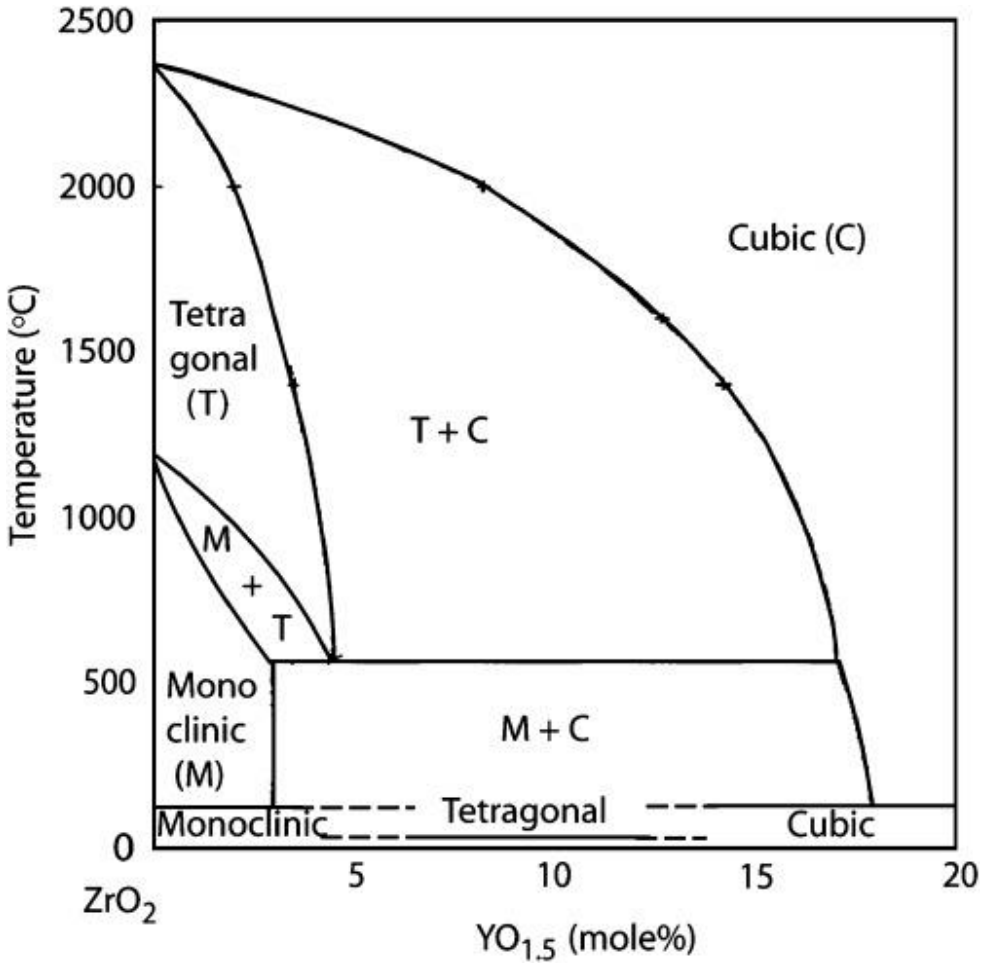


Figure 8: Zirconia-yttria phase diagram. Reprinted with permission from [60].

Lower levels of yttria doping, such as 3YSZ, meaning 3 mol% yttria stabilized zirconia (6 mol% $YO_{1.5}$ in the phase diagram above), yield predominantly tetragonal zirconia at room temperature. Higher yttrium levels, such as 8-YSZ, yield predominantly cubic zirconia at room temperature. The phase stability of YSZ is important for its engineering applications. The temperature or stress induced martensitic transformation from the tetragonal phase to the monoclinic phase can have a positive or detrimental effect on important mechanical properties such as fracture toughness [61]. Furthermore, different coefficients of thermal expansion between the tetragonal and monoclinic phase can lead to cracking of components with two different phases present [62]. The phase stability of YSZ subjected to a new

sintering technique, such as flash sintering, is therefore of interest.

3.3 Flash Sintering

Flash sintering is the densification of a powder compact occurring at a critical combination of electric field and temperature [56], [59]. Flash sintering is characterized by a power surge at constant electric field occurring at this critical combination (the flash event) resulting in full densification of the green body accompanied by shrinkage in just seconds [56], [63]. At this flash event, thermal runaway occurs when the negative temperature coefficient of most ceramics leads to increased power dissipation at higher temperatures leading to further Joule heating in a self-perpetuating process causing rapid sintering [63]. Work conducted before the first flash sintering experiments demonstrated DC electric fields could inhibit coarsening in 3YSZ, suggesting flash sintering can be tuned to provide fine control over resulting microstructure [64]. Furthermore, compared to conventional sintering, which requires a furnace to dwell at much higher temperatures for much longer time periods, flash sintering can be conducted at much lower furnace temperatures — even at room temperature — over a matter of seconds [56], [59], [65]–[67]. Although the furnace temperature is lower, Joule heating causes the specimen to reach a similar temperature to that required for conventional sintering. This gives flash sintering the potential to sinter materials at much lower costs.

3.3.1 Flash Sintering Setups

Three main types of flash sintering setups are commonly found in the literature [25], [56]. The first employs a horizontal tube furnace with a sample suspended horizontally using platinum wires acting as electrodes [56], [59]. The second makes use of a dilatometer or loading frame to apply light pressure to hold a sample in place between electrodes during the flash sintering experiment [56], [59]. The last approach uses a spark plasma sintering or

hot press device to apply low to high pressure across the specimen in an insulating die between two electrodes [56], [59]. The first two approaches usually allow for viewing of the specimen during sintering while the third approach does not. Monitoring specimen temperature during flash sintering is an important consideration when attempting to finely control microstructure, however it proves difficult especially when attempting to measure temperature at the center of a specimen [56].

3.3.2 Flash Sintering Mechanism

Despite the growing interest in flash sintering, there is no consensus regarding the underlying mechanisms that cause flash sintering to occur. Debate hinges around the following question: can flash sintering be sufficiently explained by thermal runaway caused by Joule heating, or are additional mass transport pathways from defects necessary for a full description?

Several research groups conclude flash sintering behavior can be sufficiently described solely by Joule heating [68]. Joule heating results from resistive losses converting the energy of electric current into heat in an ohmic material [68]. Todd *et al.* demonstrate that flash sintering in 3YSZ can be modeled using the measured inverse Arrhenius relationship between temperature and resistivity [63]. The study concludes a Joule heating model can correctly account for the following phenomena: the delay of the flash event following field application, the relationship between field and sintering temperature, heat localization during the flash event, the dependence upon powder particle size, and the evolution of electrical properties of the sample during flash sintering [63]. The relationship between field and sintering temperature derived from this study yields flash event criterion predictions similar

to observation [69]. Similar work conducted by Zhang *et al.* and Dong *et al.* yield other Joule heating predictive expressions [70], [71].

Research efforts, mainly headed by Raj *et al.*, argue that in addition to Joule heating, the formation of large defect populations and their diffusion contributes to flash sintering [56]. Raj *et al.* postulate the applied fields during flash sintering form Frenkel defects, and this elevated defect concentration enhances self-diffusion in the specimen lattice resulting in increased mass transport and decreased sintering times [72], [73]. However, Raj also acknowledges an insufficient understanding of how an electric field may provide the necessary energy to create the large concentration of Frenkel defects requisite to improve diffusion [73]. Furthermore, an additional study by Ji and Todd demonstrates that the rapid heating schedule of flash sintering may account for the small timescales of a flash sintering event [68]. By comparing conventional sintering and sintering using exothermic powder reactions and furnace insertion, which replicate the rapid heating involved in flash sintering, the study shows a significant increase in sintering rate [68]. Thus accelerated Joule heating, as opposed to defect concentration, stands as the more rigorously demonstrated theory. High resolution microstructural characterization of flash sintered YSZ could help further explore the question of the mechanism(s) causing rapid densification during flash sintering. Therefore the next several sections will explore high resolution microstructural characterization of first YSZ sintered using more established techniques before discussing recent advances in the characterization of flash sintered YSZ.

3.4 High Resolution YSZ Microstructural Characterization

3.4.1 TEM/STEM Grain Boundary Analysis

Several studies have analyzed chemical segregation to grain boundaries and multi-junctions in conventionally sintered YSZ. Studies of high purity YSZ powders, some with deliberate SiO_2 and Al_2O_3 additions, show particular boundaries are more susceptible to segregation than others [74]–[79]. HRSTEM studies indicate both cubic and tetragonal YSZ systems contain two main types of grain junctions: clean structured boundaries and amorphous regions [74]–[79]. In specimens made from as-received high purity powder, amorphous regions only exist at a few triple points [74], [76], [78], [79]. These amorphous regions are the only microstructural features with silicon segregation above measurement sensitivity threshold using EDS and electron energy loss spectroscopy (EELS) [75]. Al_2O_3 strongly segregates to both amorphous boundaries and clean structured boundaries displaying crystallinity from selected area diffraction patterns (SADP) [78], [79]. HRSTEM studies analyzing specimens with varying levels of Al_2O_3 doping conclude that Al_2O_3 effectively scavenges SiO_2 from grain boundaries to amorphous zones at triple pockets and multi-junctions [75]. It is important to note that EDS studies of this material system suffer from partial peak overlaps of the Si-K, Y-L, and Zr-L peaks, limiting quantitative analysis of results from the technique [74].

As an ionic conductor of oxygen anions, oxygen content at microstructural features (such as grain boundaries) is an important consideration, especially for applications such as solid-state electrochemical devices. One study tackling this consideration was conducted by Feng *et al.* and aimed to determine the behavior of oxygen vacancies at several model high angle

YSZ grain boundaries formed by bicrystal bonding [80]. By using the Cliff-Lorimer method, the concentration of oxygen along lines parallel to grain boundaries in a STEM EDS map was measured, indicating a rise in oxygen concentration at the grain boundary cores, and a resulting deficiency in oxygen vacancies [80]. These EDS results contrast sharply with EELS results from other studies [81], [82]. In a study conducted by Frechero *et al.*, a 33 degree [001] tilt boundary in a bonded bicrystal was investigated using STEM EELS [82]. Unlike the EDS study conducted by Feng *et al.*, the grain boundary showed an oxygen deficiency at the boundary (oxygen vacancy enrichment) [82]. The grain boundary studied using EELS does not possess the same geometric parameters as the EDS study; however, a similar study conducted by Jihwan *et al.* studied a $\sum 13$ grain boundary, one of the boundaries probed in the EDS study [81]. This study also demonstrated an oxygen deficiency at the grain boundary [81]. The EDS study proposes incoherent atomic configurations in the type of boundaries probed creates a local positive charge at the grain boundary core which repels oxygen vacancies and attracts yttrium [80]. The EELS study conducted by Frechero *et al.* uses DFT to demonstrate oxygen vacancies are favored at and surrounding grain boundaries, validating the EELS results [82]. Furthermore, the Frechero *et al.* study also verified specimen thickness has no effect on reported trends [82]. Thus, the discrepancy remains unexplained. The EELs studies, however, are supported by a long-standing theory describing grain boundary charge and chemistry, the space charge theory.

A space charge develops at grain boundaries and surfaces in ionic solids due to an inherent difference in free energy of formation and therefore concentration of cation and anion vacancies [83]. YSZ possesses excess oxygen vacancies due to the lower valence of dopant

yttrium, and these vacancies segregate to grain boundaries [83]. These anion vacancies cause a positive potential to form at the grain boundary core which facilitates yttrium segregation, as the lower valence charge of yttrium ions gives them an effective negative charge within the zirconia lattice [84]. However, the yttrium segregation is insufficient to neutralize the positive grain boundary core charge, and a positive potential at the grain boundary core persists [84]. This positive core potential is neutralized by a depletion of oxygen vacancies within a space charge layer surrounding the grain boundary core [84]. This space charge layer has a significant effect on grain boundary impedance and other electrical properties [78], [83].

Work conducted by Matsui *et al.* used STEM EDS to study yttrium segregation in 2.9 mol% YSZ sintered between 1100°C and 1650°C [85]. The study demonstrates differences in yttrium composition at differing sintering temperatures. At lower sintering temperatures (<1200°C), when particles are still individual crystals of YSZ, yttrium is evenly distributed throughout the grains [85]. However, as the intermediate stage of sintering begins at higher temperatures (1200-1350°C), grain boundaries begin to form and yttrium segregates uniformly to these boundaries [85]. Yttrium within grain interiors remains evenly distributed [85]. As the intermediate phase concludes and the final stage begins at even higher temperatures (>1500°C), yttrium begins to segregate to newly forming cubic regions growing out of yttrium rich grain boundaries [85]. The authors dub the formation of these cubic regions as the Grain Boundary Segregation-Induced Phase Transformation Model (GBSIPTM), and schematics corresponding to each step in the transformation process can be seen in Figure 9 [85].

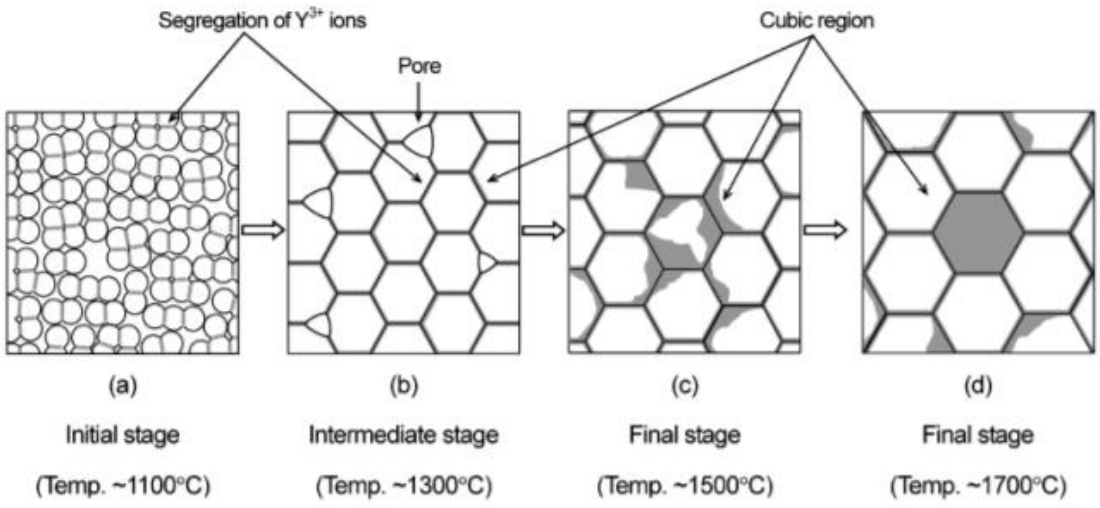


Figure 9: Schematics demonstrating yttrium distribution within YSZ microstructure at different temperatures. a) represents the microstructure during the initial stage of sintering, b) represents the microstructure during the intermediate stage of sintering, c) demonstrates the microstructure during the final stage of sintering when occurring at ~1500°C, and d) represents the final stage of sintering when conducted at a higher temperature of ~1700°C. Reprinted with permission from [85].

The study also employed x-ray diffraction (XRD) to demonstrate an increase in cubic phase fraction with increasing sintering temperature, further validating the theory [85]. Many studies report yttrium segregation to grain boundaries; however very few attempt to compare yttrium segregation levels to grain boundary character [74], [75],[76], [85], [86]. The study conducted by Matsui compares several special CSL boundaries. However no study attempts to characterize random boundaries in polycrystalline material to study the effect of grain boundary type on segregation [85].

3.4.2 TEM/STEM Analysis of Bulk YSZ Chemistry and Structure

A combined STEM HAADF and DFT study of 3.7 mol% YSZ electron-beam physical vapor-deposited (EBPVD) on alumina substrates and annealed for 24 hours conducted by *Wang et al.* demonstrates intragranular oxygen vacancies which in turn lead to a distorted cation lattice within regions of bulk YSZ cubic crystals [87]. DFT modelling of a yttrium enriched structure, assuming charge compensation with one oxygen vacancy when two

yttrium atoms replace two zirconium atoms, yielded a simulated lattice in agreement with STEM HAADF observation [87]. The study demonstrated yttrium enrichment is not limited to only boundaries and surfaces but is expected and observed within grains. Another study conducted by Krogstad *et al.* examines the formation and development of yttrium non-uniformities in EBPVD 3.5 mole percent YSZ [88]. The YSZ coatings were deposited on alumina substrates and annealed for time periods ranging from a quarter of an hour to ~240 hours [88]. Using dark field TEM, the annealed specimens exhibited a modulated structure of alternating light and dark contrast regions [88]. EDS and HRTEM demonstrate the modulations begin as coherently ordered yttrium rich and yttrium deficient cuboids oriented normal to {111} type planes; the contrast is caused by differing tetragonality due to differing yttrium composition [88]. Upon further annealing, the cuboids merge into oriented lamellas and lose coherency [88]. The modulated structure was described as two alternating types of tetragonal phase, Y-lean and Y-rich [88]. The origin of this modulation can be explained by examining the YSZ phase diagram in Figure 10 [60].

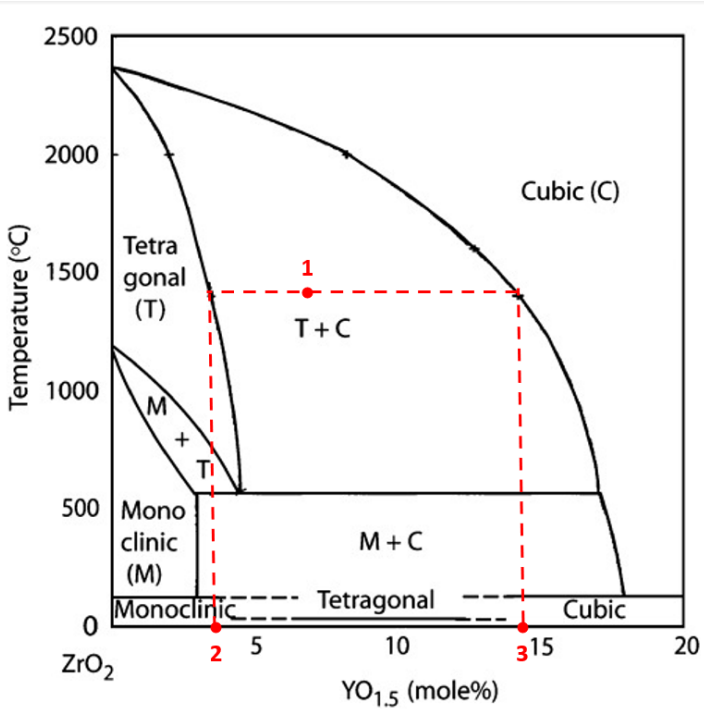


Figure 10: YSZ phase diagram illustrating locations corresponding to modulated yttrium content in Krogstad *et al.* study [88]**. 1 refers to the deposited YSZ at annealing temperature. 2 refers to the Y-lean tetragonal phase formed. 3 refers to the Y-rich tetragonal phase formed [88]. Adapted from [60].**

Region 1 indicates the coating during annealing. As it cools, the tetragonal portion of the mixed phase region cools into a Y-lean tetragonal phase while the cubic portion cools into a Y-rich tetragonal phase [88]. The longest annealing times yielded cubic yttrium rich regions and yttrium depleted monoclinic regions. The tetragonal to cubic transformation was more consistent with a spinodal decomposition model, however the possibility the transformation occurs via nucleation and growth cannot be discounted [88]. During the earlier stages of the yttrium segregation, the cuboids are too small compared to the TEM lamella thickness for compositional measurement [88].

3.4.3 APT Analysis of YSZ

Analysis of zirconia using APT is rather sparse in the literature, likely due to the relatively recent introduction of laser assisted APT. One early study characterized spinel precipitates

within bulk 3YSZ [89]. The study found aluminum and yttrium segregation to 3YSZ grain boundaries as well as aluminum dissolved within grains [89]. However, due to a need to optimize experimental parameters, quantitative analysis of these qualitative features was not reported [89]. Atom maps demonstrating Al and Mg enriched grains within a zirconia matrix can be seen in Figure 11.

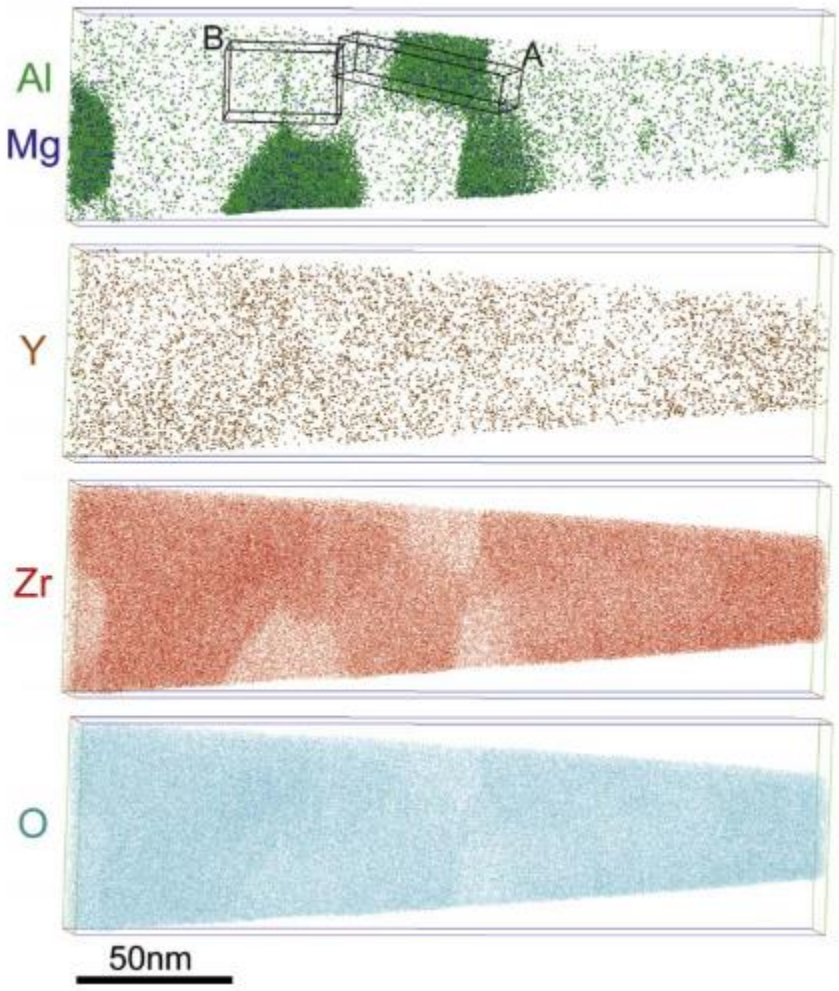


Figure 11: Three dimensional atom maps of zirconia matrix with Mg and Al enriched grains. Reprinted with permission from [89].

A subsequent study conducted by Hono *et al*. once again demonstrated the feasibility of ceramic investigation by APT, achieving high spatial resolution and near stoichiometric reconstruction of YSZ [90]. The scarcity of literature analyzing YSZ using APT also

indicates a scarcity of information regarding optimal experimental conditions and artefacts that can arise during the analysis of these materials.

3.4.4 Flash Sintered YSZ TEM/STEM Characterization

Zirconia is arguably the best studied flash sintered ceramic; in fact it was the first ceramic to be successfully flash sintered to full density [56], [91]. Flash sintered YSZ samples demonstrate unique microstructures when compared to conventionally sintered samples. For example, YSZ has been successfully sintered using both AC and DC fields, with a study conducted by Conrad and Yang concluding AC fields resulted in reduced grain growth [92]. DC fields have been shown to result in asymmetric microstructures across the specimen, with similarly reduced grain growth occurring near the specimen anode and often near the center of the specimen [93]. Field induced reduced grain growth was probed in a study by Conrad, which concludes that the retardation of grain growth caused by an applied field is the result of an interaction between the field and grain boundary space charges (discussed in section 3.4.1) [94], [95].

As opposed to grain size reduction near the anode in flash sintered YSZ samples, a study conducted by Qin *et al.* demonstrates significantly larger grains in DC field specimens at the cathodic side of the specimen [93]. It has been postulated that the difference arises due to vacancy buildup at the cathodic end; however quantitative characterization of vacancies was not carried out by the study [56], [93]. Furthermore, a study conducted by Dong *et al.* demonstrated 8-YSZ and 3YSZ grain growth is facilitated by either a chemically reducing environment or an electrically reducing environment caused by increased cation kinetics facilitated by reduction induced oxygen vacancies [96]. These results, however, contradict

TEM studies of flash sintered YSZ conducted by Wang *et al.* which found sintering in argon gas inhibited grain growth despite providing a stronger reducing environment [97]. However, this discrepancy may be explained by conductivity. The argon and air sintered samples were flash sintered by applying a constant voltage across the sample and slowly heating the furnace until the flash event was observed [97]. The increased prevalence of oxygen vacancies in the argon samples promoted conductivity, which led to a lower sintering temperature and resulting smaller grain size [97]. The same study used dark field imaging to characterize grain clusters in flash sintered samples with low angle grain boundaries [97]. The authors theorize that these clusters indicate grain boundary rotation and alignment may play a role in grain growth mechanisms during flash sintering [97].

Alongside differences in mobility and grain growth during flash sintering, studies have demonstrated flash sintering may result in differences in phase composition. In situ XRD experiments have demonstrated the existence of a purported previously undiscovered cubic phase forming during flash sintering and disappearing 10-30 minutes following the end of power application [98]. The authors theorize this phase forms as a result of a high concentration of defects caused by flash sintering which diffuse apart once power application ceases [56]. However, there may exist a simpler explanation. The reduction occurring during flash sintering can form lower valence zirconium cations (Zr^{3+} or Zr^{2+}) and oxygen vacancies [99], [100]. These two reduction phenomena can stabilize the cubic phase at lower temperatures, and therefore the observed XRD cubic phase is expected. Upon cooling, the cubic phase is expected to become tetragonal, accounting for the disappearance of the XRD peak and phase.

Prolonged periods of current exposure under DC fields can produce another unique phase, zirconium oxynitride [101], [102]. After holding at the flash event current for an hour, a study by Morisaki *et al.* noted yellowish metallic regions formed on the specimen [101]. These regions were investigated using HRTEM and EELS to demonstrate elevated nitrogen levels (~80 at%) and a selected-area-diffraction pattern indicative of a slightly deformed zirconium oxynitride *Fm3m* NaCl structure [101]. The one-dimensional ionic flow of charge resulting from DC field application is thought to create excess oxygen vacancies resulting in the formation of the oxynitride [101], [102]. This effect has been suppressed by sintering using an AC field instead of a DC field, and no evidence of nitridation was found when investigated using XRD and HRTEM EELS [102].

Finally, studies have reported grain boundaries may show unique properties when formed by flash sintering. By measuring the defect chemistry of grain boundaries in both conventionally sintered and flash sintered YSZ using impedance spectroscopy, M'Peko *et al*. concluded that flash sintering resulted in thinner boundaries with higher oxygen vacancy concentrations near these boundaries as well as higher conductivity and permittivity [103]. Wang *et al.* observed dislocation arrays close to grain boundary triple junctions and postulate high rates of mass transport near these junctions cause high local stresses and result in dislocation arrays [97]. The same study also used STEM EDS to qualitatively demonstrate yttrium segregation and zirconium depletion at grain boundaries; consistent with conventionally sintered samples [97].

3.5 Conclusions

Flash sintering of YSZ is a promising new consolidation technique capable of sintering dense specimens with the potential of achieving significant cost saving. However, high resolution characterization of the resulting microstructure from flash sintering is limited in literature. Further work needs to be conducted to determine what mechanisms contribute to rapid sintering during YSZ flash sintering and what type of microstructural differences, if any, exist between flash sintered and conventionally sintered YSZ.

4 Flash Sintered SiC

4.1 Engineering Relevance

Silicon carbide is a ceramic with a wide array of applications ranging from abrasives tools, bulletproof armor, crucibles, semiconductor devices, nuclear fuel particle cladding, and much more [104]. The strong covalent bonds constituting SiC crystals lead to sintered bodies with high hardness and flexural strength but make sintering a difficult task [104]. Like the motivation driving the YSZ research in this thesis, the effective and economic sintering of SiC is of high interest to both academics and industrialists. In this section, literature relevant to the microstructural characterization of pressureless flash sintered SiC will be presented.

4.2 Crystal Structure

SiC crystals are formed by the ordered stacking and layering of SiC_4 (or C_4Si) tetrahedra sharing common vertices [104], [105]. Unique crystal structures can be formed by varying the order of stacking in a phenomenon called polytypism [104]. The Si-C tetrahedron along with crystal structure schematics of three common SiC polytypes, 2H, 6H (α-SiC), 4H, and 3C (β-SiC) can be found in Figure 14.

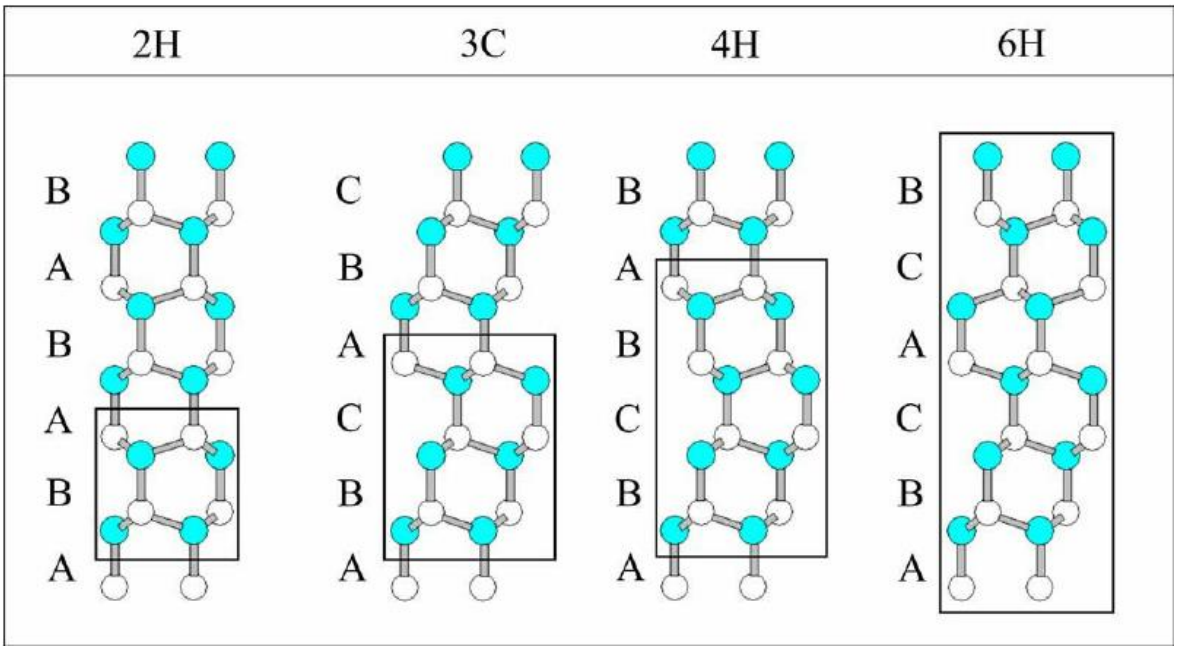


Figure 12: Stacking sequences for 2H, 3C, 4H, and 6H SiC polytypes. Reprinted with permission from [106].

A polytype thermal stability diagram can be seen in Figure 13.

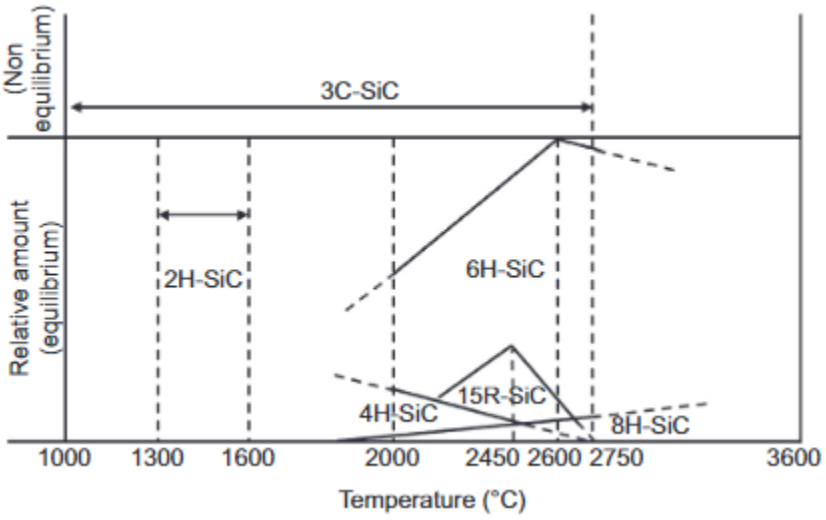


Figure 13: Polytype thermal stability diagram. Reprinted with permission from [107].

The most common polytypes observed at room temperature are 2H, 3C, 6H, 4H, and 15R [104]. The sintering conducted in this thesis occurs between 2200ºC and 2250ºC, and therefore specimens at sintering temperature should contain 4H, 6H, 15R, 3C, and 8H

polytypes [107].

4.3 Role of Carbon and Boron in SiC Sintering

Due to the nature of the covalent bonds constituting the SiC crystal structure, sintering SiC is quite difficult [108]. Liquid phase sintering aids such as alumina/yttria are commonly used to facilitate densification [109]. However, liquid phase sintering can lead to weak intergranular phases following sintering without post processing and is undesirable for certain applications, such as armor and high temperature applications [110], [111]. Solid state sintering of SiC proved elusive at industrially economic temperatures until 1973 when Prochazka used low weight percent doping of carbon and boron to solid state sinter SiC without pressure at 2100ºC [112]. The optimal amount of boron and carbon were investigated in a later study and found to be 0.5 wt% C and 0.36 wt% B [113].

As all the specimens examined in this thesis were sintered using boron and carbon additives, it is useful to briefly review the mechanistic role of each species. Soon after Prochazka's first experiments sintering SiC using carbon and boron, it was generally accepted carbon facilitated sintering by reducing SiO_2 from the surface of SiC powder particles thereby increasing surface energy and enabling densifying mass transport and the formation of grain boundaries [113]–[116]. Later work analyzing the effect of varying carbon wt% doping on oxygen content, porosity, weight change, and microstructure found carbon doping also inhibits vapor transport and surface diffusion, two mass transport pathways that inhibit sintering at elevated temperature [116] [2]. Carbon doping thus maintains dispersed, surface-oxide free SiC particles up to temperatures at which boron can facilitate pore closure and densification [2], [116]. Stobierski *et al.* studied the effect of varying amounts of boron

doping on the pressureless sintering of SiC. The study concluded three wt% regimes of boron doping resulted in three different sintering effects. Boron doping below 0.2 wt% leads to grain rearrangement and very little densification [117]. Boron doping between 0.2 wt% and 0.5 wt% promotes solid state sintering from bulk diffusion by lowering grain boundary energy [104], [117]. Finally, boron doping above 0.5 wt% leads to the formation of a Si-C-B liquid phase resulting in viscous flow causing pore closure and liquid phase sintering [117].

4.4 SiC Bimodal Microstructure

Dense sintered silicon carbide can often contain long equiaxed 6H/4H grains alongside smaller equiaxed grains constituting a bimodal microstructure [82], [118], [119]. This type of microstructure has been observed in both solid state sintering and liquid phase sintering [119], [120]. The elongated SiC grains can result in improved toughness by causing crack bridging and deflection in liquid phase sintered samples [121]. Yet if the elongated grains fracture transgranularly, a phenomenon more likely to occur when a weaker secondary phase is not present, crack bridging and deflection effects are minimal [119]. Furthermore, microstructures containing elongated grains demonstrate lower flexural strength compared to small equiaxed microstructures due to larger surface pores present in elongated grain microstructures which act as initiation sites for brittle fracture [121]. The utility of elongated grains is therefore context dependent. A Vickers indent micrograph of solid state sintered SiC with elongated grains demonstrating transgranular fracture can be seen in Figure 14.

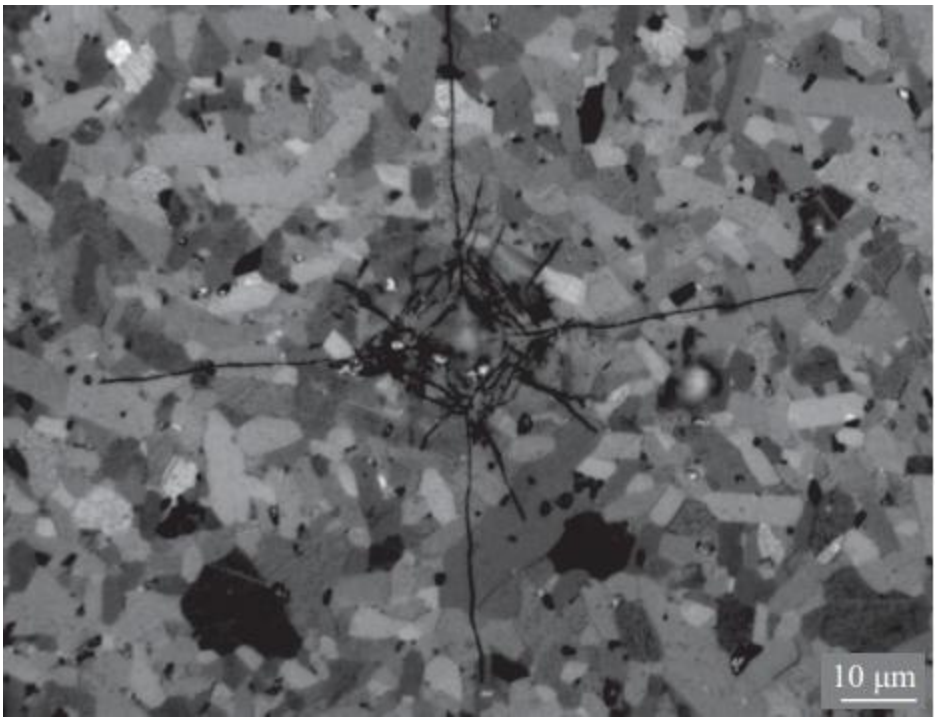


Figure 14: Transgranular fracture in a solid state sintered SiC sample with a bimodal grain structure. Reprinted with permission from [122].

4.5 Flash Sintering and Flash Spark Plasma Sintering of SiC

The first attempt to flash sinter SiC without pressure was conducted by Zapata-Solvas *et al.* using a modified hot press [109]. The only pressure applied to the sample was the weight of the graphite punch above the specimen acting as an electrode [109]. Three different specimen compositions were used in the study including: yttria/alumina doped SiC, additive free SiC, and alumina/boron carbide doped SiC [109]. Although all three chemistries displayed electrical responses indicative of flash sintering, only the yttria/alumina doped specimen achieved near theoretical density (88%) [109]. Thermal decomposition of SiC into silicon and carbon was observed during experimentation, demonstrating evidence of excessive Joule heating [109].

Flash sintering of SiC has also been achieved using spark plasma sintering equipment, albeit

using high pressure. Spark plasma sintering (SPS), also referred to as field assisted sintering technology (FAST) and pulsed electric current sintering (PECS), subjects a powder to pressure within a graphite die before applying a large pulsed DC current through the die [123]. For materials with lower electrical conductivity than the graphite die, such as most ceramics, the current does not flow through the specimen but instead only flows through the more conductive path of the die, externally heating the powder [109], [123]. For materials more conductive than graphite, the DC current flow through the powder compact causing Joule heating [123]. In this case, the pulsed DC current may cause spark plasma between particles leading to short time scale heating which in turn leads to purification of particle surfaces and more effective mass transport [123].

Using a modified SPS setup, Grasso *et al*. conducted the first successful flash sintering experiment on boron carbide doped SiC in a process they named flash (or ultra-rapid) spark plasma sintering (FSPS) [124]. By replacing the graphite die of an SPS apparatus with graphite felt, current flow through the graphite felt causes Joule heating at low temperatures [124]. This preheating allows the SiC sample to reach a sufficient temperature for the SiC resistivity to fall and cause current to flow through the sample [124]. The sample then experiences Joule heating leading to thermal runaway and flash sintering to relative densities of 96% in under one minute [124]. The resulting microstructure displayed elongated grains and evidence of a solidified liquid phase [124]. Similar experiments were conducted by Olevsky *et al.* using a sacrificial copper collar to promote preheating before melting and allowing current to flow through the SiC sample causing flash sintering [125]. Using an asymmetric top punch/electrode under pressure, the study concluded applied pressure led to

higher FSPS densities by achieving a more uniform temperature distribution while promoting pressure driven mass transport [125]. FSPS experiments have also been used to create porous textured microstructures, demonstrating the capability of flash sintering to create unique microstructures tailored to use-cases [126]. Finally mechanical testing comparisons demonstrate FSPS specimens achieve lower flexural strength both at room temperature and at 1600^{o}C when compared to traditional SPS specimens [127].

As flash sintering (or FSPS) is a relatively new densification method for SiC, detailed microstructural characterization down to the nanoscale will be necessary before flash sintered SiC can be used for critical engineering applications. As this type of characterization is sparse in the literature for flash sintered SiC samples, a review of high-resolution characterization of more conventionally sintered SiC follows.

4.6 High Resolution SiC Bulk Analysis

Much interest in high resolution bulk characterization of SiC stems from its prevalent use in nuclear power systems and electronic devices. Ion implantation studies can elucidate the effect of doping for electronic devices as well as study the effect of high energy particle interactions in nuclear power environments [128]. The observed formation of secondary phases and defects caused by ion implantation and irradiation could help clarify formation mechanisms and the effect on properties of any bulk microstructural features seen during the analysis of flash sintered SiC.

Studies analyzing the distribution of erbium and germanium implanted 6H/4H SiC demonstrate the significantly different clustering behavior of chemically disparate species

following annealing [129], [130]. Erbium atoms tend to segregate into lines, planes, and then three dimensional clusters, while germanium atoms tend to cluster into compact three-dimensional particulates immediately following annealing [129], [130]. Both species tend to form clusters at interstitial loop defect sites formed from the initial ion implantation [129], [130]. Aluminum, a species commonly used as a liquid phase sintering aid in SiC, has been observed to form intragranular clusters of Al_4SiC_4 or Al_4Si_2C upon annealing if doping saturates the SiC grains beyond the Al solubility limit [131]. Boron, an important sintering aid used to densify the samples in this thesis, has also been observed to form clusters in boron implanted and annealed 3C-SiC [132]. Combined STEM/SIMS analysis demonstrates implantation causes the clustering of point defects which upon annealing lead to the formation of boron rich $B_{13}C_2$ precipitates [132]. The radius of the precipitates was approximately 50 nm and their precipitation led to the formation of stacking faults possibly to facilitate stress relaxation [132]. Prolonged high energy electron irradiation from a TEM was demonstrated to lead to the formation of Si-Si bonds and silicon clusters in 6H-SiC grains [128]. The Si-Si bonds were the result of carbon displacement from the high energy electron beam [128]. Finally, intragranular secondary phase formation is not limited to solely ion implanted and irradiated SiC. Hot pressed SiC with ABC liquid phase additives were studied using HRTEM revealing intragranular aluminum and boron rich precipitates [133]. Electron diffraction studies of the precipitates identified them as the following phases: $Al_8B_4C_7$, Al_4C_3, Al_2O_3 enriched in silicon, and a previously unidentified Al-O-B-C crystalline phase [133]. The precipitates were observed as either spherical or elliptical inclusions with radii ranging from 200 nm to 400 nm [133]. The authors postulate the precipitates form at grain boundaries enriched in aluminum, boron, and carbon before being

left behind within SiC grains as more mobile grain boundaries migrate [133].

4.7 High Resolution SiC Grain Boundary Analysis

SiC grain boundaries observed using STEM can be broadly characterized into three categories: clean structured boundaries, disordered layer boundaries, and boundaries with amorphous intergranular layers [111]. High resolution STEM images of each type of boundary can be seen in Figure 15.

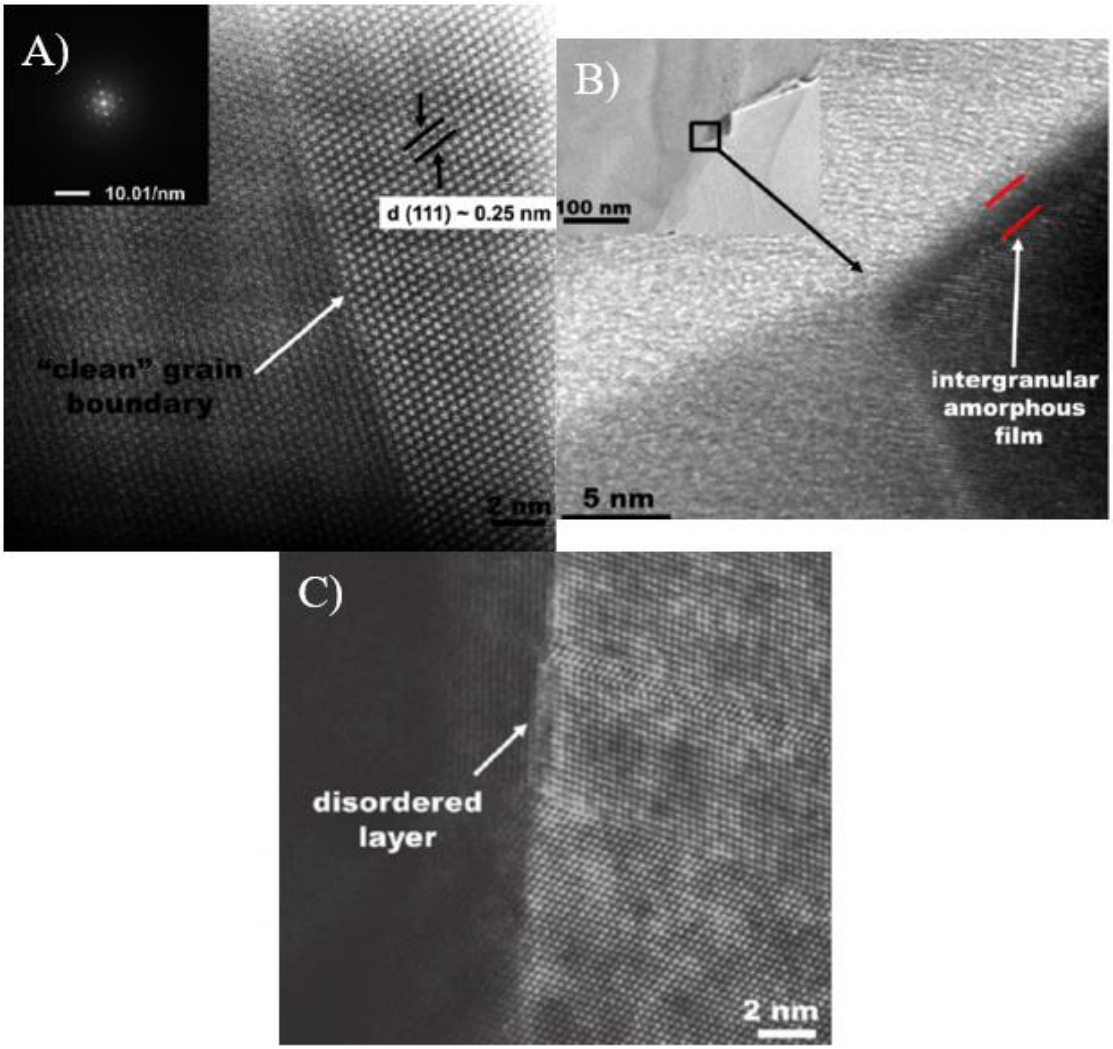


Figure 15: HRSTEM images of A) clean structured grain boundary, B) grain boundary with amorphous film, and C) grain boundary with disordered layer. Reprinted with permission from [111].

Grain boundaries with intergranular amorphous phases are formed from the cooling of liquid phases which facilitate sintering. The resulting amorphous intergranular phases are often enriched in aluminum and oxygen [110], [131], [134]–[136] .These intergranular phases are significantly weaker than the bulk and cause intergranular fracture [119], [120]. Yet studies have demonstrated that annealing can lead to crystallization of amorphous intergranular films and a resulting increase in mechanical properties [110], [131], [134]–[137]. Although boron is commonly a constituent of liquid phase sintered SiC, the EDS analyses used to chemically identify the intergranular amorphous boundaries did not indicate boron segregation, possibly due to EDS limitations [110], [131], [134]–[136]. Observations of disordered layers around solid state sintered SiC grain boundaries using boron and carbon additives have demonstrated regions of disrupted structure approximately 0.5 nm wide [138]. These regions were analyzed for chemical segregation using EELS, and weak oxygen segregation was observed [138]. The regions are believed to form to reduce the high energy of the boundaries [139]. Clean structured boundaries analyzed using EELS have demonstrated significant boron segregation [140], [141]. These boundaries demonstrate unique structure compared to the bulk crystals which extends beyond the thin layer of observed segregation [140], [141]. The observation of boron segregation using EELS when not observed using EDS highlights the importance of choosing an appropriate chemical characterization technique based upon the elements of interest.

4.8 APT Analysis of SiC

Work conducted on carbide inclusions in metals provides guidelines for effective SiC APT analysis. Work conducted by Thuvander *et al*. demonstrates that a reduction in detection efficiency results in a reduction in the detection of multiple hit events and a resultant increase

in compositional measurement accuracy when analyzing carbides [142]. When two or more ions are evaporated at the same time, there are two possible reasons why the second (or third etc.) ion may not be detected. The first mechanism by which the second ion may not be detected is dictated by the nature of the detector. The multi-channel plates which constitute the detector in an atom probe system are composed of openings ions may enter/be detected and spaces between these openings where an ion impact will not result in detection. If a second ion of a multiple hit event strikes the spaces between the openings, it will not be detected. This type of loss is random and species independent. The second mechanism by which ions following an initial hit in a multiple event may not be detected is related to the detector dead time. After the detection of the first ion in a multiple hit event, there is a finite time period (dead time) when a subsequent ion cannot be detected. Due to the high field required to evaporate carbon, potentially caused by a high ionization energy or the strong covalent bonds carbon forms, carbon atoms tend to remain on the specimen surface for numerous pulses and eventually evaporate in large bursts [143]. During these burst events, many of the ions following the first hit are lost due to detector dead time. When an APT system operates at a high detection efficiency, dead-time effects dominate the random species-independent loss caused by detection efficiency. However, when the detection efficiency of the APT system is severely reduced, random loss will dominate. By inserting a physical mesh between the specimen and detector in an APT system, Thuvander *et al*. severely reduced the detection efficiency of the system and therefore reduced the effect dead-time loss has on the measurement of carbon during experiments [142]

Larger peaks are more susceptible to this detector dead-time systematic loss effect, due to a

higher probability of being present in a burst event [143]. It is therefore possible to use smaller isotopic peaks, such as C-13 instead of C-12, to quantify carbon in an APT specimen and report more accurate compositional measurements [143].

Early attempts to analyze SiC using green laser-pulsed APT resulted in poor mass-to-charge (m/q) spectra with broad peaks as seen in Figure 16 [143].

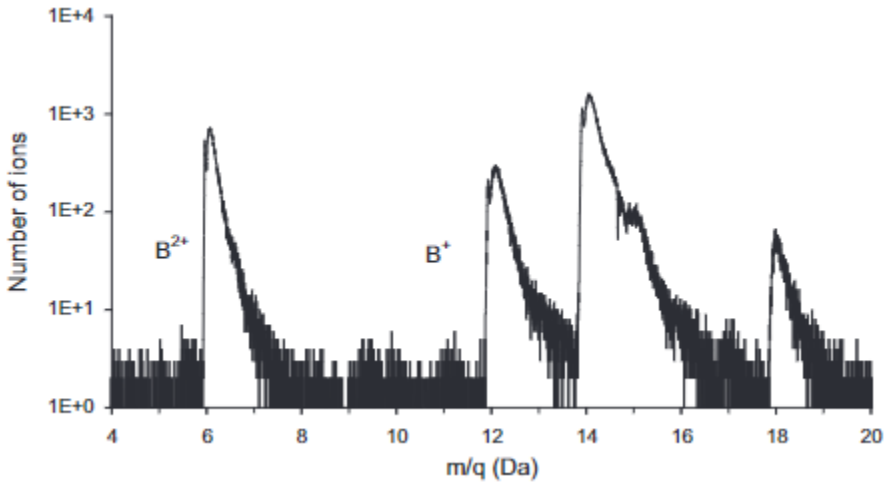


Figure 16: SiC APT m/q spectra analyzed using a green laser demonstrating low m/q resolution. Reprinted with permission from [143].

These effects can likely be mitigated by using a more modern UV laser. APT has been successfully applied to the analysis of ion implantation induced Fe nanoparticles in SiC, yielding high fidelity chemical characterization of nanoscale inclusions [144]–[147]. Finally, successful SiC APT analysis (indeed the first three-dimensional atom probe analysis of bulk SiC) has been conducted on interstellar formed SiC grains providing information regarding APT experimental conditions [148]–[150].

4.9 Conclusions

Pressureless flash sintering of SiC to near full density has yet to be reported in literature, and therefore the microstructural characterization in this thesis is novel analysis of a

consolidation technique with considerable potential when applied to SiC. Microstructural characterization of more conventionally sintered SiC samples inform what type of microstructural features to focus analysis on and highlight the difficulty of analyzing a material doped with a light element (boron) and constituted of carbon.

5 APT Analysis of Ceramics

Early ceramic APT analysis of thin-film oxide layers and thicker deposited metal-oxide films reported metal to oxygen ratios in strong agreement with stoichiometric values [151]. Investigation of zirconia/spinel nanocomposite ceramics by Chen *et al.* was claimed to be the first analysis of a bulk insulating ceramic [89]. The study reported chemical ratios differing from material stoichiometry, but noted that a thorough analysis of running conditions, specifically laser energy, could help achieve more stoichiometric results [89]. A subsequent study conducted by Hono *et al*. once again demonstrated the feasibility of ceramic investigation by APT achieving high spatial resolution and near stoichiometric reconstruction of yttria stabilized zirconia [90]. A study conducted on ZnO and MgO compared the performance of green and UV lasers and concluded the UV laser was capable of producing a high quality m/q spectrum while the green laser was not [152].

Due to the low thermal conductivities of oxides, asymmetric heating of ceramic APT tips is common and can lead to asymmetric heating/evaporation between the side closest to the laser (bright side) and the side opposite (shadow side) [153]. This asymmetry not only leads to asymmetric tip evolution but also reduced mass resolution, particularly from the bright side of the tip [153], [154]. Because the bright side reaches a higher temperature than the shadow side, it takes longer to cool back to its original cryogenic temperature [154]. This

gives bright side atoms a longer evaporation time window and a higher spread of mass-to-charge in the resulting mass spectrum (lower mass resolution) [154]. Shadow side ions may take longer to achieve a temperature suitable to facilitate field evaporation due to low thermal conductivity resulting in delayed evaporation and more spread in time-of-flight for a given species (lower m/q resolution) [153], [155]. Due to asymmetric tip evolution, tip geometry varies between the bright and shadows side of a tip. This leads to a difference in effective field between the two sides of the tip and a difference in CSRs of the same atom [153]. Tip asymmetry can also leads to increased multiple ionization events when more than one atom evaporates during a pulse and results in data loss [153]. These phenomena were all experimentally demonstrated by a study conducted by Seol *et al.* on single crystal bulk MgO, along with a novel solution: metal capping [153]. TEM images of an MgO tip following APT analysis demonstrating laser illumination caused asymmetry can be seen in Figure 17.

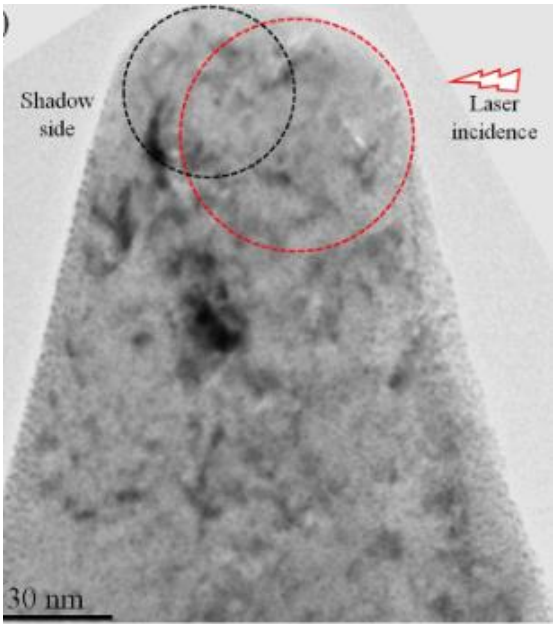


Figure 17: MgO tip following APT analysis, the two circles demonstrate the difference in radius of curvature between the two sides of the tip. Reprinted with permission from [153].

The study demonstrated that by applying a thin silver layer to the shank of a MgO specimen, the thermal energy resulting from laser illumination was better distributed between the shadow and bright side of the tip [153]. This led to increased mass resolution, higher signal-to-noise ratios, and a reduction in multiple ionization events [153].

Several studies have been conducted on ceramic materials systems using APT to study chemistry at grain boundaries. One such study conducted by Clark *et al*. investigated the grain boundaries of yttrium-doped barium zirconate [156]. This study mounted specimens onto an experimental apparatus suitable for TEM and APT analysis, using pre-run TEM to isolate grain boundaries near the tip apex [156]. The study demonstrated local enrichment of Y coupled with Zr and O depletion at grain boundaries [156].

Another study conducted by Diercks *et al.* investigated grain boundary chemistry of perovskite ceramics (BCZY27) doped with small amounts of NiO [157]. Once again TEM was used pre-APT to isolate grain boundaries at the specimen tip [157]. However, post-APT TEM was also conducted to analyze tip evolution during APT to aid in geometrically accurate APT reconstruction [157]. The study concluded the grain boundaries showed little compositional difference compared to the bulk material with a slight increase in yttrium content [157]. Several grain boundaries did however contain NiO rich particles [157]. Finally, a study investigating grain boundaries in Nd doped ceria concluded high angle grain boundaries demonstrate high oxygen depletion coupled with high Nd segregation [158].

Instead of using a more time intensive grain boundary targeting technique, like TEM, a novel

approach developed by Babinsky *et al.* utilizes transmission electron backscatter diffraction, or transmission Kikuchi diffraction (TKD), to isolate and characterize grain boundaries before APT analysis [159]. TKD allows for in situ boundary characterization of APT specimens in properly fitted dual beam FIB/SEM systems. TKD is preferred to EBSD as it provides the higher spatial resolution necessary to study grain boundaries in APT size-suitable specimens [159].

APT analysis of GaN, an important semiconductor for optoelectronic applications, demonstrates key considerations for analyzing non-metal samples. When analyzed using APT, the resulting chemistry of GaN often differs from the expected 1:1 ratio of gallium to nitrogen [160]. The electric field the tip experiences during evaporation has a strong effect on the measured composition and can be affected by the morphology of the tip, the standing DC voltage, laser energy, and other parameters [161]. The effect of the electric field (as measured by the ratio of detected Ga^{++} ions to Ga^{+} ions) on the measured concentration of Ga and N can be seen in Figure 18.

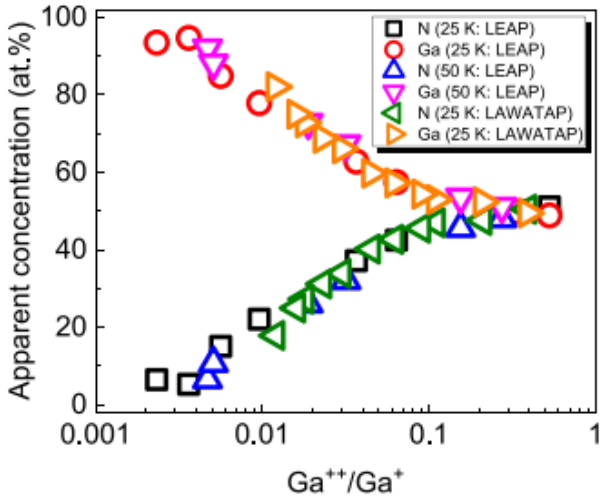


Figure 18: Dependence of measured Ga and N on electric field (as measured by the ratio of detected Ga^{++} ions to Ga^{+} ions). Both a Local Electrode Atom Probe (LEAP) and Laser Assisted Wide-Angle Tomographic Atom Probe (LaWaTAP). Reprinted with permission from [161].

The discrepancy between measured and expected stoichiometry has been attributed to two phenomena [160]. Nitrogen deficiency is caused by the formation of neutral uncharged nitrogen atoms/molecules after evaporation which are not detected, while gallium deficiency is caused by DC evaporation of gallium occurring between pulses and contributing to noise [160]. Careful tuning of experimental parameters can result in more accurate analysis. Recent advances in extreme ultraviolet APT, or EUVAPT, have demonstrated more consistent compositional measurements across different electric field values, demonstrating the emergence of a promising new APT technology for the analysis of nonmetals [162].

6 Conclusions

In this section, relevant literature to the four areas of focus of this thesis has been summarized and critiqued. It is evident high-resolution characterization of each materials system will not only help fill gaps in the existing literature but contribute towards mechanistic understandings of each material system necessary for employment in critical engineering environments. Furthermore, the relative dearth of APT experiments on the three ceramics of

interest to this thesis leaves room for parameter optimization and investigation of APT measurement artefacts that may affect data quality.

Chapter III

Materials and Methods

1 Powder Processing and Sintering

1.1 Alumina

Alumina samples were fabricated using commercially available high purity α-alumina TM-DAR powder (Taimei Chemicals Co., Ltd., Tokyo, Japan) with a mean particle size of 150 nm and purity >99.99%. The impurities found in the alumina powders can be seen in Table 2.

Table 2: Impurities found in alumina powder

Impurity	Maximum Parts per Million
Na	15
K	10
Fe	20
Ca	5
Mg	5
Si	25

Many of the specimens were doped with 0.25 wt% MgO to promote sintering as described in Chapter II. Carbon-doped specimens were doped using synthetic graphite (TIMCAL TIMREX KS6, Germany) at three different wt%: 0.02%, 0.05%, and 0.1%. Doped or pure alumina powders were placed into polyethylene bottles along with ethanol and Al_2O_3 milling

balls before being ball milled for 24 hours. Slurries were then dried using a rotary evaporator (IKA RV10, Jencons, Germany). The dried powders were then passed through a 150 µm sieve to break up agglomerates. The powders where calcined at 250ºC to remove any residual ethanol or plastic from the bottles used for milling. Powders were pressed into discs with 25 mm diameters and 4 mm thicknesses using a uniaxial press at 50 MPa and then a cold isostatic press at 200 MPa. The resulting green bodies were sintered without pressure at 1500ºC for 1 hour using heating and cooling rates of 10ºC per minute in a vacuum furnace (Lenton, UK) under a graphite powder bed. Some specimens were also sintered without a graphite bed and in air to probe the effect of a reducing environment. Upon completion of sintering, the density of each specimen was measured using Archimedes' method. Samples were baked for 2 hours at 100ºC for two hours before measuring a dry mass (m_{dry}). Then the samples were submerged in boiling water for 1 hour to fill pores before a submerged mass measurement (m_{wet}) was made. Finally, the surfaces of specimens were dried, and a saturated mass ($m_{saturated}$) was determined. The density of each specimen was calculated using the following equation.

$$\rho = \frac{m_{dry}}{m_{saturated} - m_{wet}} \times \frac{\rho_{H_2O}}{\rho_t} \times 100\%$$

ρ_{H_2O} is the density of distilled water (1 g/cm^3) while ρ_t is the theoretical density of alumina (3.98 g/cm^3) [163]. All the alumina specimens studied in this thesis demonstrated a relative density of 99.6% or higher.

1.2 3YSZ

Powder processing, flash sintering, and density measurements of 3YSZ samples were performed by Yasuhiro Kubota and Dr Yinsheng Li.

1.2.1 Powder Processing

The powder processing methods were identical for each type of specimen. Specimens were fabricated using 3 mole percent yttria stabilized zirconia powder (TZ-3Y-E Tosoh, Shuanshi, Japan) with a mean particle size of 60 nm as reported by the producer. The powder's elemental composition in atomic percent as reported by the manufacturer can be found in Table 3.

Table 3: Powder stoichiometry as reported by powder manufacturer

Chemical Species	Atomic Percent
O	66.3
Zr	30.4
Y	1.93
Hf	1.03
Al	0.32
Na	0.05
Si	0.03
Fe	<0.01

The powder was mixed with distilled water and Dispex A40 dispersant with the following weight percentages: 55 wt% 3YSZ, 43 wt% distilled water, 2 wt% Dispex A40. An ultrasonic probe was used to break up agglomerates before the slurry was slip cast into bar shaped molds on porous gypsum bases. The green bodies were cold isostatically pressed at 200 MPa before drying in an oven at 70°C. For the flash sintered specimens, holes for platinum wire electrode insertion were drilled into the compacted green bodies, and thin

stripes of platinum paste was spread on the electrode/green body interface to aid in conduction. The final dimensions of the pre-sintered green bodies can be found in the following schematic.

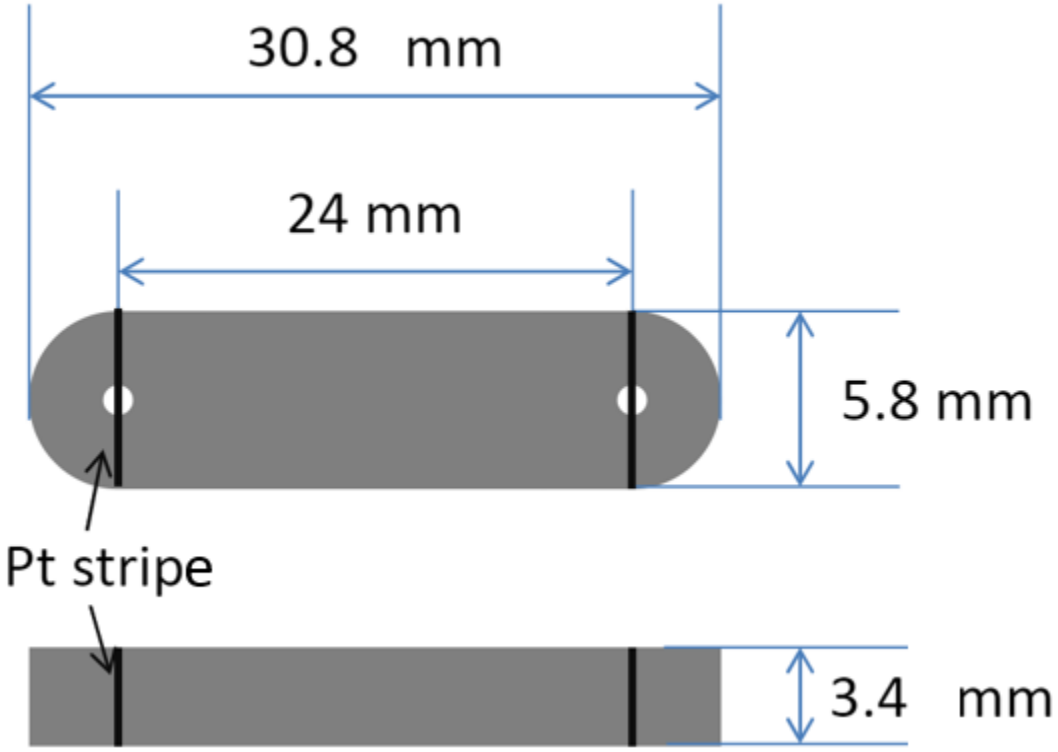


Figure 19: Compacted green body ready for flash sintering with representative dimensions (dimensions will vary between different green bodies). Green bodies for conventionally sintered specimens had identical dimensions without Pt strips and drilled holes.

Once the specimen had been formed, it was placed into a furnace and heated to 800°C for 1 hour to burn out the Dispex organic material.

1.2.2 Sintering

1.2.2.1 Conventional Sintering

Conventionally sintered specimens were heated in an alumina tube furnace. The furnace was heated to 1350°C from room temperature at a rate of 5°C/min. The samples were held at 1350°C for 2 hours before being cooled at 5°C back down to room temperature.

1.2.2.2 Flash Sintering (FS C and FS A)

Pt wires serving as electrodes were fed into the green body drilled holes. The specimen/electrode assemblies were then lowered into an alumina powder bed within an alumina crucible to minimize radiative heat loss. The assembly was placed into a box furnace and the furnace temperature was raised to 900°C at a rate of 6.6°C/min and held at the final temperature for 30 minutes to ensure temperature uniformity. A commercial DC power supply (360 V, 15 A, 1500 W, Elektro-Automatik, Viersen, Germany) was used to create a field of 100 V/cm at a limiting current density value of 80 mA/mm^2. Once the system reached this limiting current value, the current flowed for 60 seconds before the power source was shut off. The specimen was cooled back to room temperature at the same rate as during heating. The FS C specimen was cut from the final 25% of the specimen interior to the hole connecting the platinum cathode electrode to the specimen, while the FS A specimen was cut from the final 25% of the specimen interior to the platinum anode.

1.2.2.3 Flash Sintering Reduced (FS C R)

Pt wires were similarly used as electrodes for the FS C R sample and were fed into the green body's drilled holes. The specimen was then suspended in the furnace and the temperature was raised to 900°C at a rate of 6.6°C/min and held at the final value for 30 minutes. The same power supply as above was used to create a field of 50V/cm at a limiting current density value of 100 mA/mm^2. This field was maintained for 5 minutes to further reduce the specimen as compared to FS C and FS A samples. After 5 minutes the power supply was turned off, and the specimen was cooled at the same rate as during heating down to room temperature. The specimen was cut from the final 25% of the sample interior to the cathode.

1.2.2.4 Flash Sintering He (FS C He/FS A He)

FS C He and FS A He specimens were sintered using identical electrical characteristics to the FS C R specimens. However, the sintering was conducted in a sealed tube furnace with chemically pure grade helium gas being passed through the sealed tube for the duration of the heating and sintering process. Helium gas is used to create an oxygen deficient environment and promote sample reduction. Samples from both the cathodic (FS C He) and anodic (FS A He) ends were studied. The samples were cut from the final 25% of the sample interior to each electrode.

1.2.2.5 Flash Sintering He 1 Hr (FS C He 1 Hr)

The FS C He 1Hr specimen was sintered in an identical environment to the FS A He and FS C He specimens, however the sample was subjected to the sintering current for one hour to strongly electrochemically reduce the specimen. The specimen was cut from the final 25% of the sample interior to the cathode.

1.2.3 Density Measurement

The densities of the sintered specimens were measured using the Archimedes method. A density of 6.05 g/cm^3 as reported by the powder manufacturer (TOSOH Corporation Japan) for well sintered samples was used as a comparison value. The relative densities of the specimens can be found in Table 4.

Table 4: Relative densities of sintered YSZ samples

Specimen	Relative Density (%)
C	99.6
FS A	99.1
FS C	99.1
FS C R	99.5
FS A He	98.8
FS C He	97.9
FS C He 1 Hr	96.5

1.3 SiC

1.3.1 Powder Processing

Powder processing, flash sintering, density measurements, and hardness measurements of SiC specimens were conducted by Andrew Gibson. SiC specimens were fabricated from commercially available STARCERAM S rtp Grade SQ powder (H.C. Starck, Germany). The powder mix consists of 96.2 wt% α-SiC and 3.3 wt% carbon along with 0.5 wt% boron as sintering additives. Polyethylene glycol/polyvinyl alcohol (PEG/PVA) binder is also present in the powder mix which is spray dried into ~60 μm granules. The powder was uniaxially pressed into bars like those shown in Figure 19 with the following dimensions: 22 x 6 x 2 mm before being cold isostatically pressed at 200 MPa. Electrode holes were drilled into the specimen green bodies that were to be flash sintered.

1.3.2 Sintering

1.3.1.1 Fire 1

Fire 1 specimens were conventionally sintered without applied pressure in flowing argon gas. A furnace ramp rate of 5ºC/min was used to achieve a sintering temperature of 2200ºC which was held for 2 hours before the specimen was cooled back down to room temperature at a rate of 5ºC/min.

1.3.1.2 Fire 2

Fire 2 specimens were sintered in an identical manner to Fire 1 specimens, however a sintering dwell time of 5 minutes as opposed to 2 hours was used.

1.3.3.3 FS

FS samples were suspended in a tube furnace using tungsten wires as electrodes and heated to a furnace temperature of 1500ºC using a ramp rate of 5ºC/min. Thirty minutes before sintering was to begin, the flowing gas in the tube furnace was switched from nitrogen to helium. An initial electric field of 30 V/cm was applied across the sample using a commercial DC power supply (Elektro-Automatik Bench Power Supply, Germany). The electric power was then ramped up to 400 W at a rate of 5 W/min and held for 5 minutes. Following flash sintering, the furnace and power supply were shut off and allowed to cool to room temperature.

1.3.3.4 FS Hard

FS Hard samples were subjected to a similar sintering treatment as the FS samples. Following the 5 minute dwell at 400 W, the power across the sample was then ramped to 550 W at a rate of 5 W every 5 minutes. The sample was held at 550 W for one minute before the furnace and power supply were shut off and the sample was allowed to cool.

1.3.3 Density and Hardness Measurements

Density measurements were made using the Archimedes method. Vickers hardness measurements of each sample type were made using a load of 5 kg on a Future Tech Vickers Hardness Tester (Model 110 B, Japan). Additionally, the temperature the flash sintering specimens reached was estimated using a black body radiation model [164]. The relative density (compared to the manufacturer reported value of 3.18 g/cm^3), estimated or actual sintering temperature, and the hardness of each sample type can be found in Table 5.

Table 5: Sintering temperature, density, and Vickers hardness of each SiC sample type

Type	Sintering Temperature (ºC)	Relative Density (%)	Vickers Hardness (GPa)
Fire 1	2200	98	24.6 ± 0.5
Fire 2	2200	97	24.1 ± 0.4
FS	2200	90	23.1 ± 1.1
FS Hard	2250	94	28.0 ± 0.3

2 Atom Probe Tomography

2.1 Experimental Principles

APT is a sub-nanometer three-dimensional chemical characterization technique with the potential for a parts per million sensitivity for all elements [165]. A schematic demonstrating the basic setup of an atom probe along with a visualization of an experiment can be found in Figure 20.

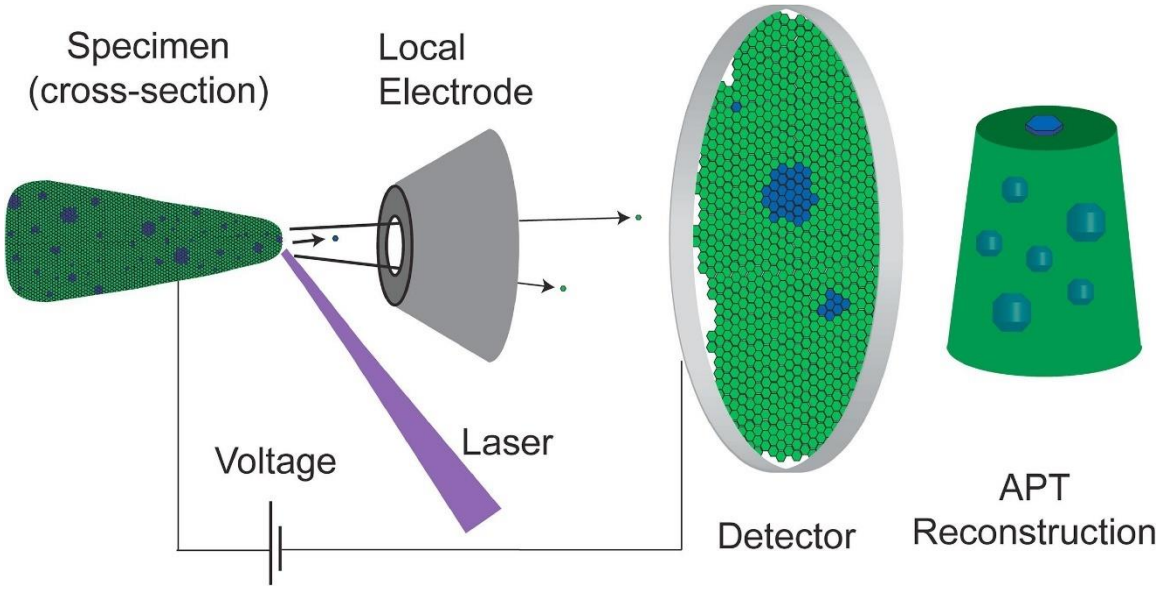


Figure 20: Schematic demonstrating principles of APT analysis and experimental setup. Reprinted with permission from [166].

A needle shaped specimen with an apex radius of approximately 50 nm is cooled to cryogenic temperature (20 K to 80 K) and placed in an ultra-high vacuum ranging from 10^{-8} Pa to 10^{-9} Pa [165], [167]. The specimen is brought within tens of microns to millimeters away from a counter electrode and a standing DC voltage ranging from 1-15 kV is applied [165], [167]. The sample is then either subjected to voltage pulse (lasting a few nanoseconds) or a laser pulse (usually a femtosecond UV pulse) triggering field evaporation of ions from the specimen surface. The field evaporated ions then travel towards a detector consisting of a microchannel plate and an anode [167]. The microchannel plate triggers an electron cascade signaling the time of arrival of the ion, and the anode creates electric signals that travel along three delay lines to calculate the position of the ion on the detector [165]. Some atom probes are equipped with energy compensating devices called reflectrons. Reflectrons act as electrostatic mirrors that deflect the flight path of evaporated ions, correct energy deficits caused by high voltage pulses, and result in higher resolution m/q spectra [168].

The physics of laser-assisted field evaporation is proposed to be a thermally assisted process [169]. It is believed ions are singly charged once they leave the specimen surface, and can be ionized into a higher charge state when near the specimen surface under the high electric field as an electron tunnels back into the specimen [170]. For semiconductors and non-conductors, a high proportion of multiple evaporation events are detected, when one voltage or laser pulse creates two or more detection events [171]. The high proportion of multiple hits originating from low conductivity samples is believed to result from rearrangement of surface charge following field evaporation of an ion which in turn causes the rapid evaporation of a successive ion [167]. Differences in carrier mobility or density between metals and non-conductors may explain this difference [167].

The analysis of ceramic systems often results in the evaporation of complex molecular ions instead of single charged atoms [165]. For example, 3YSZ experiments often result in large peaks corresponding to ZrO charged ions. The prevalence of complex ions can increase the likelihood of peak overlaps occurring, as the spectra contain more total peaks. Therefore, careful peak overlap consideration is necessary when analyzing specimens yielding many complex ion peaks.

Integrated Visualization and Analysis Software (IVAS) was used to reconstruct the experimental data using a reverse-projection algorithm [172]. The point projection model assumes ions fly along straight trajectories towards the detector, the ion trajectories begin from a single point along the specimen long axis, the specimen tip is hemi-spherical, and makes small angle approximations [172]. IVAS makes uses of more advanced iterations of

the point projection model which do not make small angle approximations [173]. The x and y positions of the ions in the specimen are reconstructed from the x and y positions of impact on the detector, while the z position of ions is based upon the order of evaporation of ions accounting for a finite detection efficiency [165]. The chemical identity of detected ions is found by measuring the time-of-flight from pulsing to detection and calculating a corresponding mass-to-charge-state ratio [167]. The identity of peaks in the resulting m/q spectra are manually assigned by the experimentalist. The combination of the position of the ion from the specimen along with its chemical identity results in a three-dimensional point cloud of the atoms constituting the specimen.

2.2 Specimen Preparation

All of the samples analyzed in this thesis were created using a gallium source FIB/SEM lift out method detailed in literature [29]. Two instruments were used, a Zeiss NVision 40 (Zeiss, Germany) and a Zeiss Crossbeam 540 (Zeiss, Germany). Before FIB/SEM preparation, samples were polished using diamond suspensions and finished with a colloidal silica suspension. The key steps in the FIB/SEM specimen preparation workflow can be seen in Figure 21.

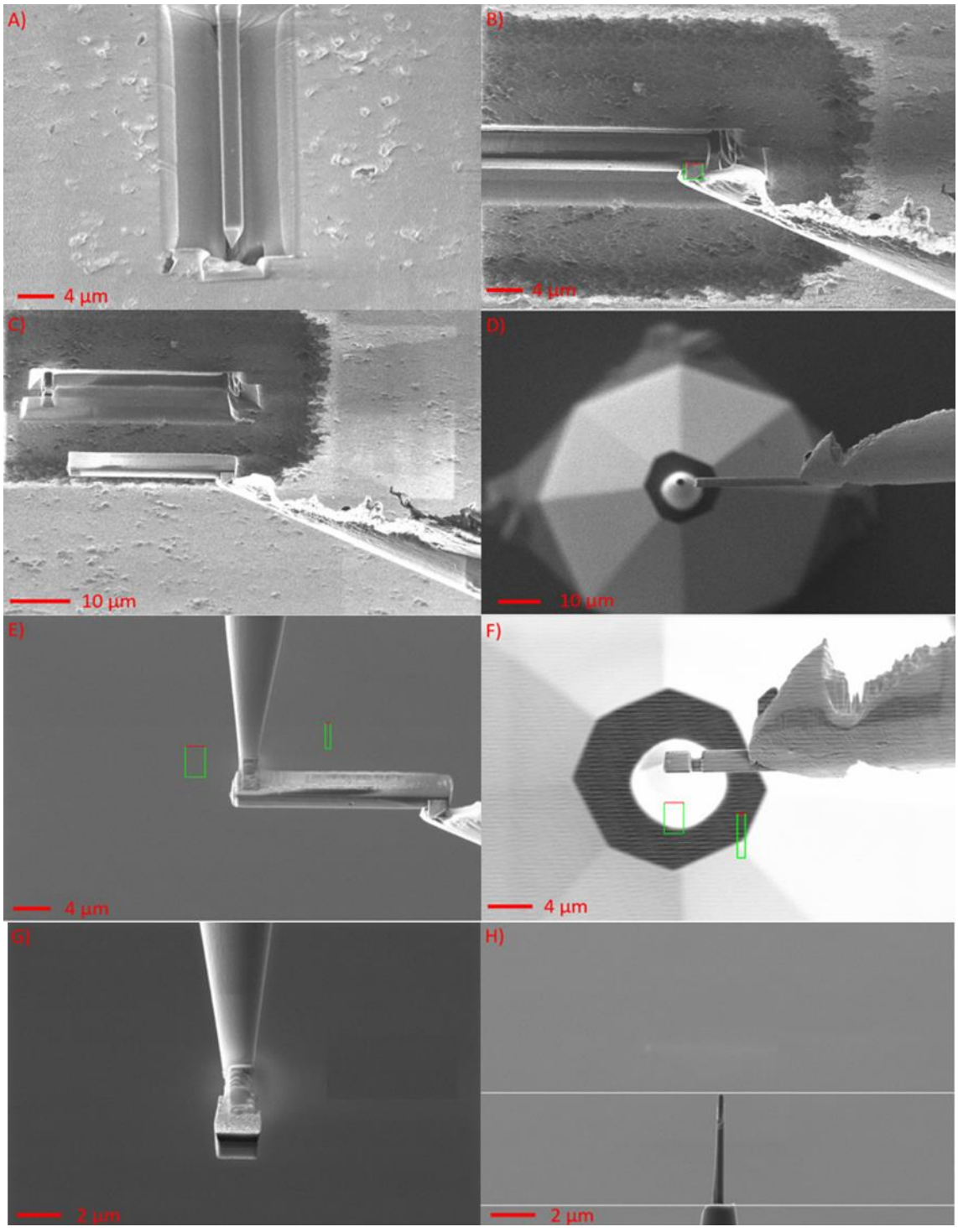


Figure 21: FIB/SEM APT specimen preparation

First, a protective layer of amorphous platinum or tungsten is FIB deposited onto the specimen surface, and trenches are cut along the edges of the bar. The bar is then undercut

exposing a suspended cantilever as seen in A). A micromanipulator is then attached to the cantilever and lifted out of the bulk specimen as seen in B) and C). The cantilever is then deposited atop commercially available silicon microposts using FIB deposition as seen in D) through G). Finally, the wedges were sharpened using annular milling into APT suitable tips. Most FIB milling was conducted using an accelerating voltage of 30 kV; however a final stage polish was conducted at 5 kV or 2 kV to minimize gallium implantation damage in the final specimen.

2.3 APT Data Analysis Tools and Techniques

2.3.1 Peak Identification and Ranging

As previously mentioned, the identification of peaks in an APT m/q spectrum is performed by the experimentalist. In this thesis, an algorithm developed by Haley *et al*. was used to enumerate the possible identities of peaks and the likelihood of each possible identity to help guide peak identification [174]. The width around the peak maximum used to define counts under the peak is also determined by the user in a process referred to as ranging. A novel reproducible ranging technique was developed in this thesis and will be discussed in Chapter IV.

2.3.2 Compositional Measurements

Measuring the composition of features within the APT 3D point-clouds is a process often referred to as peak decomposition. The m/q spectra corresponding to regions of interest (ROI) are first treated with two background corrections, one global and one local. The global background correction is a constant background noise level subtracted from the entire spectrum. Local background corrections are required to deal with the asymmetric tails present off the right side of m/q spectra peaks due to incomplete energy acquisition of a

voltage pulse in voltage pulsed mode and delayed evaporation during slow cooling in laser pulsed mode [165]. If the counts under a peak found within the tail of another peak are to be quantified, a power law curve is fitted to the tail and this curve is used to subtract background counts from the following peak [175]. Once the counts under a peak have been quantified, it is important to also consider the effects of peak overlaps caused by species with similar m/q values. In this thesis a MATLAB package, AtomProbeLab v0.2.2, was used to decompose m/q spectra and solve peak overlaps by studying the relative size of isotopic peaks to calculate the individual contributions of different species to the total counts under a given peak. This process will be explained in greater detail in Chapter IV.

2.3.3 Concentration Profiles

Concentration profiles are used to measure the relative change in composition spatially across microstructural features of interest in the three-dimensional point clouds. Rectangular or cylindrical ROIs across the features are subdivided into smaller ROIs, and the composition of each ROI is calculated using AtomProbeLab.

2.3.4 Isoconcentration/Isodensity Surfaces and Proxigrams

IVAS is used to isolate regions of the reconstructions which have specified concentrations of elemental or ionic species of interest using isoconcentration surfaces. The dataset being studied is first voxelized into discrete voxels before a delocalization algorithm is applied [176]. Voxels with a desired concentration are then identified. Adjacent identified voxels are then combined to form isosurfaces. Isosurfaces can be further analyzed using proximity histograms or proxigrams. Proxigrams are histograms calculated by measuring the composition of shells with identical morphology to the original isosurface but formed at increasing distances away from the original surface. This allows for the composition a

distance normal to the interface of a feature to be probed regardless of the complexity of the surface being analyzed.

2.3.5 Volume Renderings

Volume renderings of concentration or density were formed using IVAS to visualize three-dimensional concentration or density fluctuations throughout a sample. Following delocalization, the concentration of each voxel in a specimen is assigned a normalized color value to create a three dimensional heat map of local concentration or density [176]. The opacity of each voxel can be varied to clarify visualization.

2.3.6 Binomial Analysis

The binomial analysis is a type of grid-based frequency distribution analysis to study the ordering of a chemical species within a material. The binomial analysis compares the distribution of a species in a material to the theoretical distribution of the species if it were randomly distributed within the material [165]. To conduct a binomial analysis, the ions in a data set are portioned into a three-dimensional grid of voxels each containing a given number of ions, *n*. The experimental frequency distribution (*e(n)*) of a given species, *A*, is compared to a binomial probability distribution (proxy for a random distribution). This binomial probability distribution, $f_b(n)$ can be described by [177], [178]:

$$f_b(n) = NP_b(n) = N\frac{n_b!}{N!\,(n_b-n)!}{X_A}^n(1-X_A)^{(n_b-n)}$$

N is the total number of voxels in the data set, X_a is the concentration of A in the material, and n is the number of ions of species A in a voxel. A χ^2 value can be used to measure the deviation from a binomial distribution of an experimental dataset [165], [179]:

$$\chi^2 = \sum_{n=0}^{n_b} \frac{(e(n) - f_b(n))^2}{f_b(n)}$$

Using a null hypothesis of a random distribution of species A and n_b as the degrees of freedom, a probability value, P, for the veracity of the null hypothesis can be found. However, a χ^2 value is very sensitive to the size of a dataset, and due to the very large number of ions present in APT data sets and the variation in size between experiments, χ^2 values are not particularly well suited to comparing between experiments. Therefore, the Pearson coefficient is preferred [179]. The Pearson coefficient (μ) normalizes χ^2 values to the number of sampled voxels [180]:

$$\mu = \sqrt{\frac{\chi^2}{N + \chi^2}}$$

A Pearson coefficient of zero indicates a binomial distribution, whilst a value of 1 indicates complete association of species A. It is important to note that n_b must be kept constant when comparing between datasets.

2.3.7 Clustering Analysis

Solute clustering was observed in select SiC samples in this thesis, and therefore clustering analysis was conducted to isolate the material found in clusters for further analysis and characterization. The core-linkage method was employed in this thesis, which is briefly summarized below [181]–[183].

1. The solute species, or the species thought to be present in clusters (boron in this thesis) is identified.
2. A maximum separation value (D_{max}) is chosen which denotes the maximum distance around a solute ion to search for another solute ion.

3. Using an order number (O) determined by the experimentalist, the O closest solute ions nearest a starting solute ion are identified. If the farthest of these ions is within D_{max} of the starting ion, these ions form a cluster.
4. The clustering algorithm repeats its search using each ion in the cluster, and if the total number of solute ions in the cluster exceeds a minimum value, N_{min}, it is identified as a cluster. N_{min} is used to remove small clusters that are likely the result of random statistical fluctuation.
5. All the ions within a distance (envelope distance or L) of the cluster solute ions are identified as part of the cluster.
6. All atoms within a distance (erosion distance or E) are omitted from the cluster to help eliminate matrix ions that are incorrectly incorporated onto the surface of the cluster by the enveloping step.

The clustering parameters (D_{max}, N_{min}, L, E, and O) are defined by the experimentalist. D_{max} values were chosen in accordance with a technique described by Kolli and Seidman [184]. The value of D_{max} is swept and the number of clusters identified upon application of each D_{max} value is plotted. The D_{max} value that corresponds to the first local minimum is chosen as it is believed to be large enough to not erroneously divide large clusters and small enough to not link unclustered solute ions together [184]. N_{min} values were also swept, and a sufficiently large N_{min} value was chosen that the number of clusters became relatively stable as N_{min} increases. Order values of three were used for all datasets, and L and E values half the value of D_{max} were used.

2.3.8 Gibbsian Interfacial Excess

The concentration at a grain boundary can be reported as a measurement of segregation, yet

a more thermodynamically rigorously defined Gibbsian interfacial excess (Γ), is often preferred [185]. Gibbsian excess denotes the excess atoms of a particular species found within a feature as compared to the surrounding matrix [185]. A robust method for calculating Γ from APT data was developed by Hellman *et al.* [185], [186]. In this thesis, methods and code developed by Jenkins based upon Hellman *et al.*'s work were used to calculate Gibbsian excess [187], [188]. A concentration profile was drawn across an interface of interest. The concentration profile was not constituted of bins with identical volumes, but instead volumes containing identical ion counts to minimize the effects of density related artefacts at grain boundaries observed in this thesis. The edges of the interface were then defined assuming a Poisson distribution of the segregating species in the matrix. The distribution of the segregating species present in the bins of the concentration profile corresponding to the matrix were used to calculate a threshold value [188]. This threshold value was defined as a statistically unlikely high ($p < 0.05$) number of counts of the segregating species observed in a bin. The interface was then defined as the first and last instance of this threshold value count of the segregating species. As the composition of the species of interest can differ to either side of the boundary, different interface edges can be calculated based upon which grain is used. In this analysis, both cases were calculated, and upper and lower limits of the Γ were reported. Gibbsian interfacial excess can be calculated using the following equation [188].

$$\Gamma_i = \frac{N_{total}(C_i - C_{i(\alpha)}\xi - C_{i(\beta)}(1-\xi))}{A\eta}$$

N_{total} is the total number of ions detected in the studied region, C_i is the concentration of species *i* in the entire studied region, $C_{i(\alpha)}$ and $C_{i(\beta)}$ are the concentrations of element *i* in grain alpha and beta respectively, A is the area of the interface being studied, and η is the detection

efficiency (proportion of evaporated ions striking the detector that are successfully detected) of the atom probe used. It is important to note key limitations of reporting Gibbsian interfacial excess. Firstly, if the distribution of the segregation species is not uniform in the bulk, the concentration in both grains may not be accurately calculable using concentration profile bins [187]. Secondly, the distribution of segregating impurities across the length of a boundary may vary, and a narrow concentration profile may not reflect this variability [187].

3 Electron Microscopy

3.1 Scanning Electron Microscopy Imaging

SEM enables imaging of the surface of bulk specimens using a variety of electron signals formed from an electron beam rastered over a bulk specimen surface. Two main types of electron signals were focused upon in this study: backscattered electrons and secondary electrons. Secondary electrons are removed from their atomic orbit by the energy of an incident electron and obtain an energy below 50 eV [189]. Secondary electrons only escape the specimen from a near surface region and yield high spatial resolution images [189]. Backscattered electrons are electrons that originate from the electron gun and are scattered by the atoms in the specimen at high angles before re-emerging from the specimen [189]. These electrons give phase contrast, as heavier atoms create higher back scattered signals.

3.1.1 Linear Intercept Grain Size Measurement

Alumina samples were prepared for grain size measurement by cross sectioning using a precision diamond saw (Isomet 5000, Buehler, Germany) before being polished using diamond and colloidal silica suspensions. The specimens were then thermally etched at 1450 ºC for 15 minutes in either vacuum or air. Specimens were then platinum sputter coated

using a high vacuum sputter coater (Leica EM ACE600, Germany) with a target thickness of 10 nm. Grain size measurements of samples were conducted using SEM secondary electron imaging and the following equation [190].

$$G = 1.56 * \left(\frac{L}{N}\right)$$

G is the grain size of the sampled region, *L* is the length of a line drawn across the image, and *N* is the number of grain boundaries the line intercepts. 1.56 is a correction factor to account for the three dimensional nature of grains versus the two dimensional image used for measurement [190].

3.1.2 Percentage of Transgranular Fracture Characterization

The percent of alumina fracture surfaces demonstrating transgranular versus intergranular fracture was probed using secondary electron imaging. Bulk alumina samples were cut into rectangular bars and notched using a high precision saw. The samples were then bent and fractured before the resulting fracture surfaces were platinum coated. Secondary electron images of the fracture surfaces were collected, and a regular grid was overlaid atop the images. The intersection points of the grid which fell atop regions of transgranular fracture were tallied and divided by the total number of grid points to estimate the propensity of a sample to experience transgranular versus intergranular fracture. Ten micrographs with 468 points of intersection per micrograph were analyzed per specimen type.

3.2 Energy Dispersive X-ray Spectroscopy

EDS analysis relies on incident beam electrons to excite electrons in the inner shells of atoms near the specimen surface [191]. The excited electrons may gain sufficient energy to be ejected from their orbitals creating electron holes. These electron holes will then be occupied

by higher energy shell electrons, which give off energy in the form of X-rays [191]. The energy of these X-rays is characteristic of the difference in orbital energies of the atom, and therefore characteristic of the element [191]. The energies of the X-rays formed by the sample are measured by an energy dispersive spectrometer providing chemical identification of the specimen surface. EDS analysis of SiC was conducted at a working distance of 5 mm, an accelerating voltage of 10 kV, and a beam current of 5 nA.

3.3 Electron Backscatter Diffraction

Electron backscatter diffraction makes use of backscattered electrons to determine the orientation and phase of the crystal grains present near the surface of a polished specimen. A schematic diagram of an EBSD experiment can be found in Figure 22.

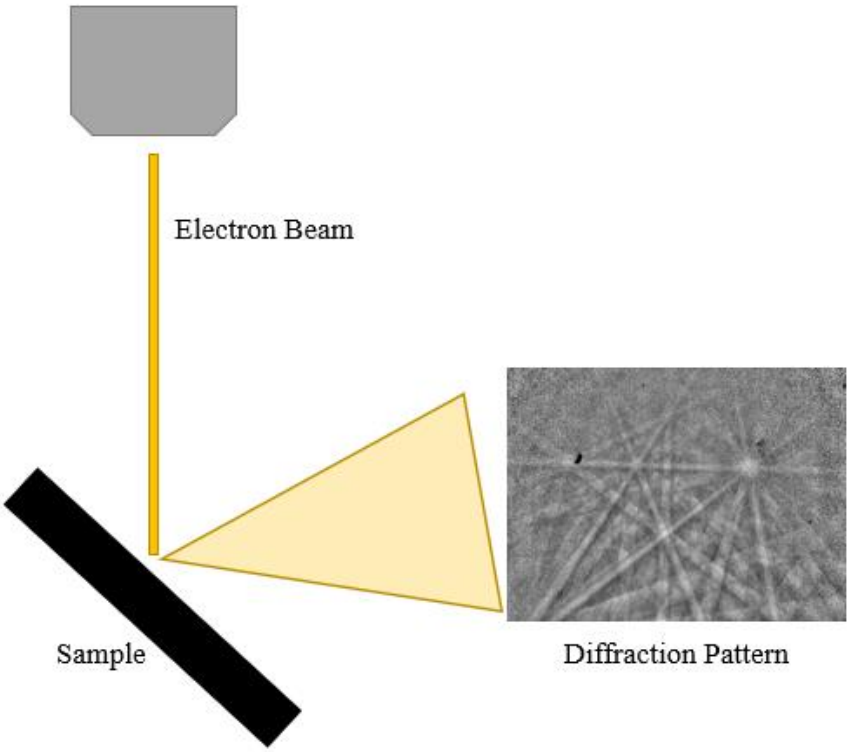


Figure 22: EBSD schematic

The electron beam is focused onto a region of interest on a sample tilted at approximately

70°. The atoms near the surface inelastically scatter some of the incident electrons, forming a divergent source of electrons [192]. Some of these electrons are incident on atomic planes at angles satisfying the Bragg equation and are diffracted to form pairs of large angle cones corresponding to each diffraction plane that has been interacted with [192]. These cones of electrons illuminate a phosphor screen and form Kikuchi bands of high intensity characteristic of the crystal structure and orientation [192]. These Kikuchi patterns are indexed and compared to libraries to identify the crystal phase and orientation of grains near the specimen surface. EBSD analysis of SiC was conducted at an accelerating voltage of 30 kV, a beam current of 80 nA, and a working distance of 10 mm.

3.4 Transmission Kikuchi Diffraction

TKD, or transmission EBSD, is similar in principle to EBSD, however the electron beam is focused on an electron transparent sample, and the scattered electrons originate from the back surface of the tilted sample [193][194]. A schematic demonstrating the basic principle of TKD can be found in Figure 23.

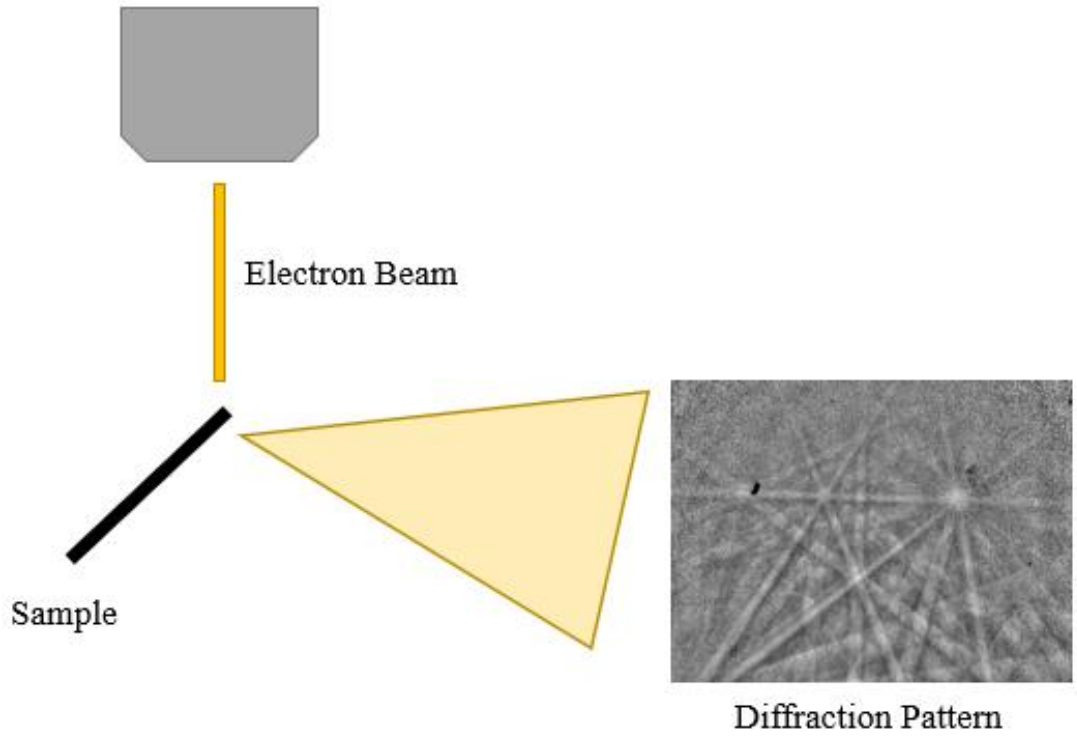


Figure 23: TKD schematic

The diffraction pattern is formed from a smaller volume of the sample and results in improved spatial resolution compared to EBSD [193][194]. TKD was first adapted for use on APT specimens by Babinsky *et al.* [159]. In this thesis, TKD was used to target and characterize the misorientation of grain boundaries found in APT specimens. Grain boundaries were located within the height of sharpened APT tips using TKD. TKD on all three materials was conducted using an accelerating voltage of 30 kV and a working distance of 10 mm. YSZ TKD was conducted using a beam current of 40 nA, while 90 nA was used for SiC and alumina. The tips were then further sharpened using a low (5 kV) accelerating voltage until the grain boundaries were within 100 nm of the tip apex. Misorientation values, phase identification, and grain orientations were found using Aztec^{TM} software.

3.5 Scanning Transmission Electron Microscopy

STEM images are formed by focusing a high energy nanometer-sized electron beam onto a thin electron transparent specimen. Annular dark-field (ADF) images are formed by fore-scattered electrons impacting a detector outside the direct path of the high energy incident electron beam [195]. ADF images provide atomic number contrast at the atomic scale [195]. Annular dark-field imaging of carbon-doped alumina samples was conducted by Dr. Weixin Song using a JEOL ARM-200F (JEOL Ltd., Japan) STEM operating at an accelerating voltage of 200 kV. STEM systems can also perform chemical analysis such as EELS and STEM EDS [195].

4 Grain Boundary Relative Energy Measurement

Grain boundary relative energy measurements of carbon-doped and undoped alumina samples were made. Alumina samples were polished using polycrystalline diamond and colloidal silica suspensions. The unpolished sides of each specimen were also ground to ensure flat surfaces [49]. The samples were then thermally grooved at 1400°C for five, ten, and fifteen hours with a ramp and cooling rate of 10°C/min. AFM was used in contact mode and alternating current atomic force microscopy mode (ACAFM) to measure thermal groove geometry. In contact mode, the AFM cantilever makes contact with and is dragged across the sample surface [196]. A small constant force is exerted on the cantilever by varying the cantilever's height using a piezo actuator and a feedback circuit [196]. In ACAFM mode, the cantilever is oscillated at or near its resonant frequency before being lowered to begin tapping on the specimen surface [196]. The tip's interaction with the specimen surface reduces the amplitude of the tip's oscillation. The reduction of the tip's amplitude is kept constant using a feedback loop and lowering/raising the height of the cantilever [196].

AFM was conducted using an Agilent 5400 AFM (Agilent Technologies, USA) calibrated by the parent company. The AFM apparatus sat on a granite slab suspended by bungee cords within an anti-vibrational chamber to minimize measurement interference. Pyramidal silicon probes with a reflective coating were used for measurement (Bruker NCHV-A, Bruker Corp. USA). The tips had a front angle of 25°, a back angle of 15°, a side angle of 22.5°, a tip radius of 8 nm, a resonant frequency of 320 kHz, and a spring constant of 40 N/m. AFM measurement parameters were adapted from previous publications studying alumina grain boundaries [49], [53]. To achieve enough lateral resolution for grain boundary thermal groove measurement, a step size of 10 nm was chosen with a scan frequency of 101 Hz. As much of the surface specimen as possible was measured to maximize the dataset.

AFM data was post-processed using Gwyddion software to eliminate any overall slope inherent to the specimen [197]. AFM data treatment was consistent with previous work conducted on alumina and other ceramics [49], [53], [198]. Three profiles were found for each measured groove. The width (W) and depth (d) of each groove were then found from the average of the three measurements. Each side of a groove was treated independently assuming symmetry. Using W and d, the ratio of the grain boundary energy (γ_{gb}) to the surface energy (γ_s) can be found using the following equation [51].

$$\frac{\gamma_{gb}}{\gamma_s} = 2\sin\left(\tan^{-1}\left(m\left(\frac{d}{2W}\right)\right)\right)$$

m is the slope of the groove at its lowest point. For smaller values of d/W, Mullins demonstrated $m = 4.73$ [51]. For larger values of d/W, m deviates from 4.73. However, a relationship between m and d/W for larger d/W values was developed by W.M. Robertson and this correction was used [50]. For each sample type, a minimum of 150 boundaries was

analyzed and the results were reported in cumulative distribution plots to compare different specimen types.

AFM image convolution due to finite tip size is a well-known issue [49]. Thermal grooves with a width equivalent to or above 1 μm do not require any tip convolution correction [49], [53]. However, in this study, grooves with widths equivalent to or larger than 250 nm were measured. To correct for tip convolution, blind tip estimation was used. Blind tip estimation uses carefully chosen surface data to create an image of the tip using an established algorithm [199]. Finally, approximations inherent to the equation used to calculate relative energy are important to consider and have a strong influence on data interpretation. The equation assumes the surface energies on either side of a groove are equal, the grain boundary is normal to the surface plane, and finally that differences between grain boundary and surface energies are negligible [53]. These three assumptions are not representative of reality and therefore, in accordance with previous studies, many grooves were measured and the distribution of measurements was reported [49], [53], [198].

FIB cross sectioning and imaging has also been used to directly image and measure the angle of grain boundary grooves formed between an alumina substrate and aluminum/nickel metal layers [200]. This analysis does not rely upon the assumptions necessary to calculate grain boundary relative energy from groove depth and width measurements yet is much more time intensive.

Chapter IV

APT Operating Conditions and Compositional Comparison Considerations

1 APT Experimental Conditions Sweep

Experiments on each materials system were conducted using a LEAP 5000XR (equipped with a reflectron) and a LEAP 5000XS (straight flight path). The performance of both machines for each materials system was analyzed to highlight strengths and weaknesses of atom probe instrumental design, i.e., reflectron versus the straight flight path. Due to the electrically insulating nature of the ceramics investigated, experiments were almost exclusively conducted using the UV femtosecond pulsed laser mode. Considering the relatively recent advent and proliferation of laser assisted APT, literature is still sparse regarding optimal analysis conditions for ceramics. Therefore, for each materials system studied in this thesis, a laser energy sweep was conducted to study the effect on resulting data. Additionally, one successful voltage mode run was conducted on a SiC specimen, and measurements from this experiment were compared to a laser mode run.

When comparing different experimental parameters, the effects on several metrics of data quality were considered. The first metric was the measured composition of grains in the specimens as a function of analysis condition. During an APT experiment, it is preferable for only one atom to be ionized and evaporated per laser pulse. This type of event is known as a single hit event. However, it is common during atom probe experiments for multiple

ions to evaporate at once. The detection of more than one ion correlated to a single voltage or laser pulse is known as a multiple hit event. Significant levels of multiple hits can prove problematic due to detector dead time. Some chemical species, such as carbon, require high electric fields to field evaporate. As such, these species can build up on the specimen surface and eventually evaporate as multiple hit events [201]. The combination of this species dependent specimen build-up phenomenon and the detector dead time can lead to non-random measurement losses of these elements [165]. Furthermore, high rates of multiple hits can also serve as evidence of complex ion dissociation, another source of systematic loss [171]. Therefore, the proportion of multiple hits detected during an experiment is an important consideration when choosing experimental parameters. Thus, the percentage of single hits yielded using varied experimental parameters was studied. Finally, the m/q resolution dependence (as defined by peak width) upon operating conditions was studied by comparing normalized peaks of the most prevalent species evaporating from tips for each material. The m/q resolution was reported using APT literature convention, by dividing the m/q, Dalton (Da), value of the peak by the peak width. As such, larger values correspond to narrower peaks and higher resolution.

A key factor affecting measured composition, single hit evaporation, and m/q spectrum resolution is the electric field inducing evaporation. The applied electric field inducing evaporation is affected by all the varied experimental parameters: laser energy, atom probe instrument design, and voltage versus laser pulsing. As such, indication of the electric field inducing evaporation for each analysis condition is necessary to conduct a consistent comparison. The ratio of a given chemical species evaporating at two different charge states

can give an indication of the field strength at the tip apex during field evaporation using post-ionization theory predictions made by Kingham and Haydock [202]. These CSRs were used as comparison metrics whenever comparing two data sets collected using different analysis conditions.

2 APT Composition Comparison Considerations

Several factors need to be considered when quantifying chemical composition differences between different samples, and even within disparate regions of the same sample. These factors which can influence composition measurements include: the effect of mass spectrum peak ranging and peak overlaps, a continuously blunting tip throughout duration of the experiment, laser illumination proximity, and sample size. Before chemical composition comparisons were made, each of these factors were isolated and their effect on compositional measurements was noted.

2.1 Ranging of the Mass Spectra

The first factor considered is how to consistently range m/q spectra. When analyzing APT data, it is up to the user to assign the chemical identity of a given peak in the m/q spectrum. As mentioned in Chapter III, an algorithm developed by Haley *et al.* was used to enumerate the possible identities and likelihood of each peak in the spectrum using expected chemistry from the powder manufacturer and isotopic abundance [174]. Once the identity of a peak is determined, there remains the question of what width around the peak maximum to include in the range and how to consistently range between different m/q spectra. Narrow range definitions can increase the resulting signal to noise ratio, while wide range definitions increase counting statistics. Therefore, ranging choices and resulting effects on the analysis should be considered carefully during experiment planning. Consistency can be achieved by

defining the bounds of a range as when the spectrum reaches a specific percentage of the peak maximum. However, this approach can fail when analyzing spectra with small peaks where the peak height does not reach significantly far above the level of noise, when analyzing spectra with peaks of differing morphology, and when analyzing peaks with large thermal tails. This issue can be addressed by employing peak fitting. By fitting the m/q peaks with analytic curves, and then defining ranges as when the fitted curves achieve a certain percentage of their respective maxima, small peaks can be more consistently ranged. Several types of curves were investigated to determine which best fit the peaks found in the m/q spectra: Gaussian, Cauchy/Lorentzian, and pseudo-Voigt (weighted sum of a Gaussian and Lorentzian). Linear background curves were also fitted to the left and right of each peak. Several types of peaks were considered: relatively large, relatively small, and peaks lying on the thermal tail of a larger peak to its left. Each type of analyzed peak can be found in Figure 24.

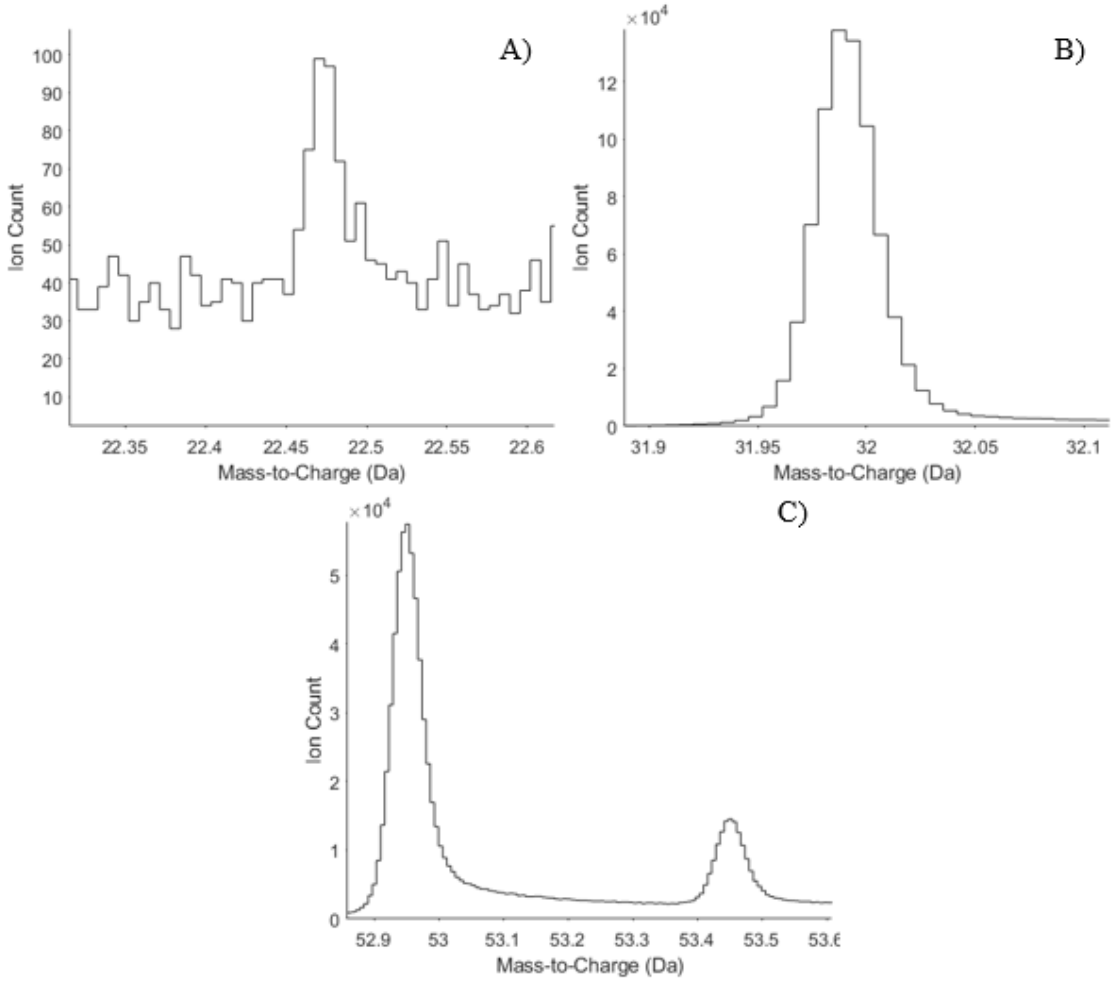


Figure 24: Peaks used to compare peak fit types. A) relatively small peak. B) relatively large peak. C) peak lying on thermal tail of large peak.

Table 6 compares the norm of residuals between the three fit types for the aforementioned peak types coming from a 3YSZ sample. The lowest norm of residuals (best fit) is highlighted in each case.

Table 6: Curve fit norm of residuals comparison.

	Peak		
Fit Type	**22.5 Da**	**32.00 Da**	**53.45 Da**
Cauchy/Lorentzian	0.140	0.261	0.247
Gaussian	0.376	0.153	0.160
Pseudo-Voigt	0.140	0.047	0.094

The pseudo-Voigt curve demonstrates a better fit for all peak types and is therefore the fit employed in this thesis. The fitting was conducted using the GIXSGUI MATLAB library, and the pseudo-Voigt approximation employed by the library comes from a study conducted by Liu *et al.* [203], [204]. Figure 25 demonstrates the improvement in ranging achieved when using a curve fit full width at half maximum range (FWHM) versus a raw data derived FWHM range.

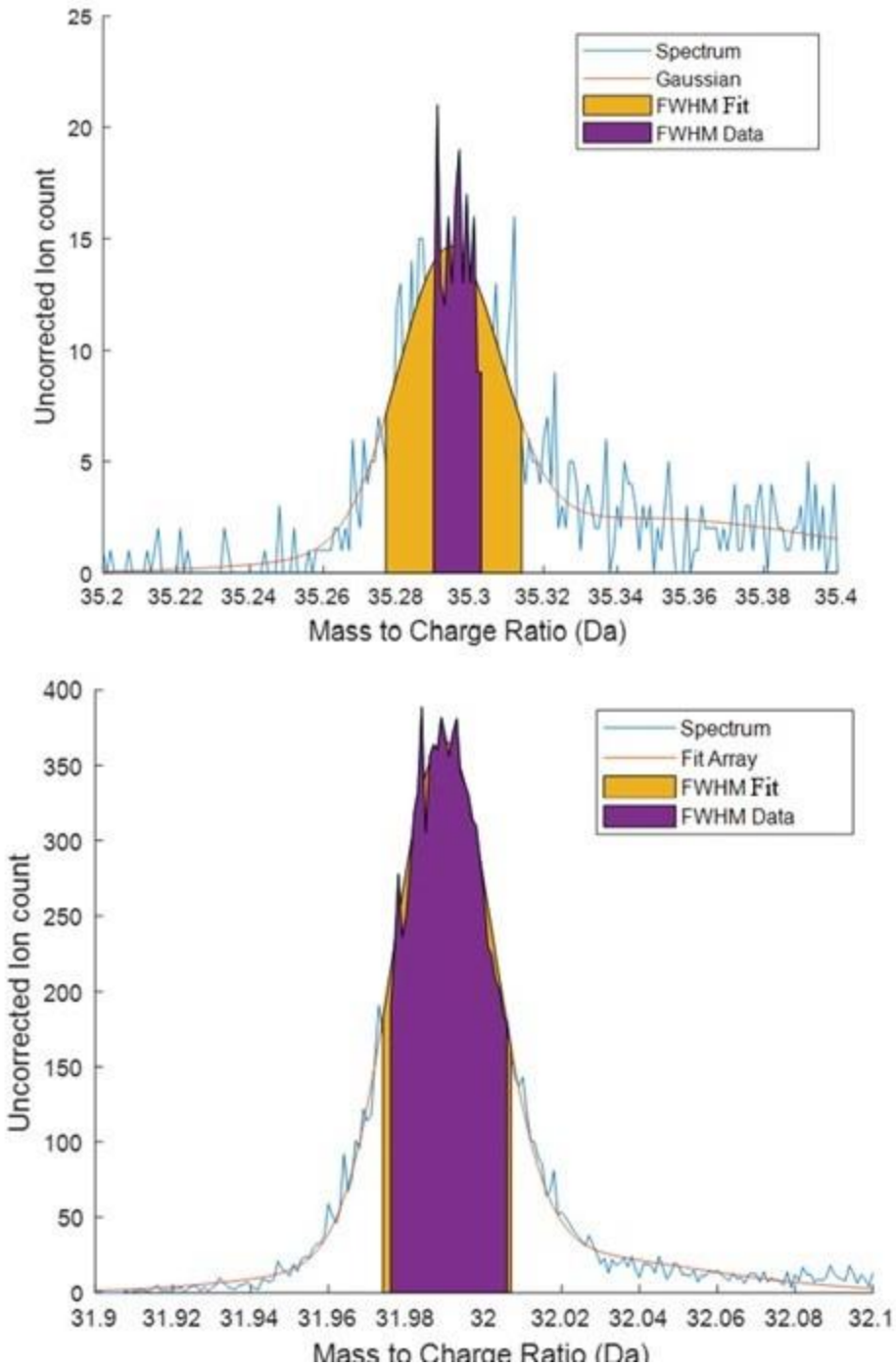


Figure 25: Ranging using the FWHM of a fit curve versus ranging using the FWHM of the raw data

For the larger peak at 32 Daltons, the difference between the fit range and raw data range is minimal. However due to a low peak height compared to noise, a significant difference exists between the fit range and raw range for the smaller peak at 35.3 Daltons, with the peak fitting

approach ranging more than two times the number of ions than the raw ranging approach. However, there remains the issue of determining how wide a range to define around the peak maximum. Large datasets of ten million or more hits with a homogeneous spatial distribution of the incorporated elements for each material were chosen to study the effect range width has on measured composition. Ranges were defined using pseudo-Voigt fitting and these ranges were used to calculate overall composition. This methodology was repeated for several different range width definitions: full width at 75% of peak maximum, full width at 50% of peak maximum, full width at 25% of peak maximum, full width at 5% of peak maximum, and full width at 1% of the peak maximum. The resulting compositions were compared to expected stoichiometry values from the powder manufacturers for each material.

2.2 Peak Overlaps

There exist several peak overlaps due to similar m/q values of constituent ions and complex ions evaporating from the specimen tip in each materials system studied in this thesis. These overlaps can be resolved, and the individual contribution of each overlapping ion calculated, by considering the size of adjacent peaks corresponding to other isotopes of each ion as briefly discussed in Chapter III. This process is effective if at least one of the overlapping ions has an adjacent isotopic peak which does not overlap with another ion. This is the case for many of the overlaps considered in this study, and all compositional measurements in this thesis employ the MATLAB package AtomProbeLab v0.2.2 to report peak overlap solved compositions. The methods employed for peak overlap solving and quantifying the resulting uncertainties are enumerated in publications by London *et al*. [205], [206].

2.2 Tip Blunting

The experiments in this thesis were run using a constant detection rate, or number of ions detected per laser pulse. Previous studies on semiconductors, namely GaN, have demonstrated that as an atom probe experiment progresses, material is removed from the tip and it becomes more blunt. As a result, the electric field necessary to maintain a constant detection rate changes [207]. This changing electric field can have a significant effect on compositional measurement, m/q resolution, single hit percentages, and other data quality metrics. Therefore, a quantitative analysis of how experimental metrics may change as the tip blunts and the electric field compensates during an experiment was conducted for all the studied materials. For each analyzed material, a rectangular ROI running down the center of each data set was extracted, and the effect of tip blunting was studied on the following experimental metrics: the electric field at the tip apex as represented by CSRs, measured composition, m/q resolution, and single hit percentages.

2.3 Laser Illumination Proximity

As discussed previously in Chapter II, variance in proximity to the side of the APT tip illuminated by the laser (bright side versus dark side) can lead to differences in effective field, multiple ionization event likelihood, signal-to-noise ratios, and m/q resolution caused by broader peaks [153], [155], [156]. Therefore, the effect laser illumination proximity has on composition and data quality was probed for each material. Regions of the detector corresponding to ions evaporated from the dark side and the bright side of specimens were isolated, and several parameters were compared. The first parameter investigated was the likelihood of a multiple hit to occur. The second parameter investigated was m/q spectrum resolution. Thirdly, the electric field as estimated by CSRs was investigated. Finally, the

composition moving from the dark side of the tip to the bright side of the tip was measured. For this comparison, an ROI was drawn from the dark to bright side of the tip and concentration profiles of each chemical species were extracted along the ROI's length. Figure 26 displays one such ROI for a 3YSZ specimen.

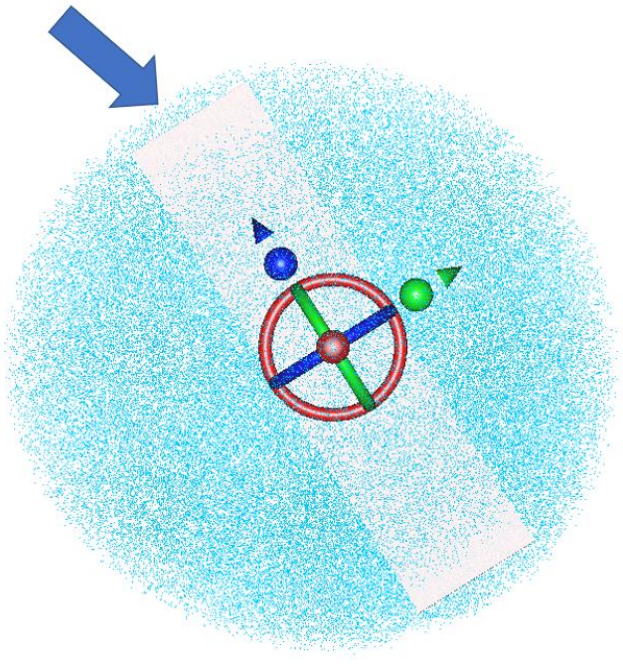


Figure 26: Rectangular ROI measuring composition from dark to bright side of a 3YSZ specimen. The red, green, and blue circles demonstrate the orientation of the rectangular ROI. Blue dots represent O^+ ions. The blue arrow represents the laser illuminating the specimen.

2.4 Correlative Evaporation Histograms

When analyzing insulative complex materials using atom probe tomography, such as oxides and carbides, a significant proportion of evaporation events involve more than one ion being detected per laser or voltage pulse [165]. Often during these multiple hit events, direct statistically significant correlations exist between the type of ions evaporated together [171]. Using correlative evaporation histograms, interesting features of the evaporation phenomenon of a material at given conditions can be probed. Correlative evaporation histograms plot the Dalton values of each atom probe hit that constitutes a multiple hit event.

A correlative evaporation histogram for a silicon carbide specimen with over 50 million hits is found in Figure 27.

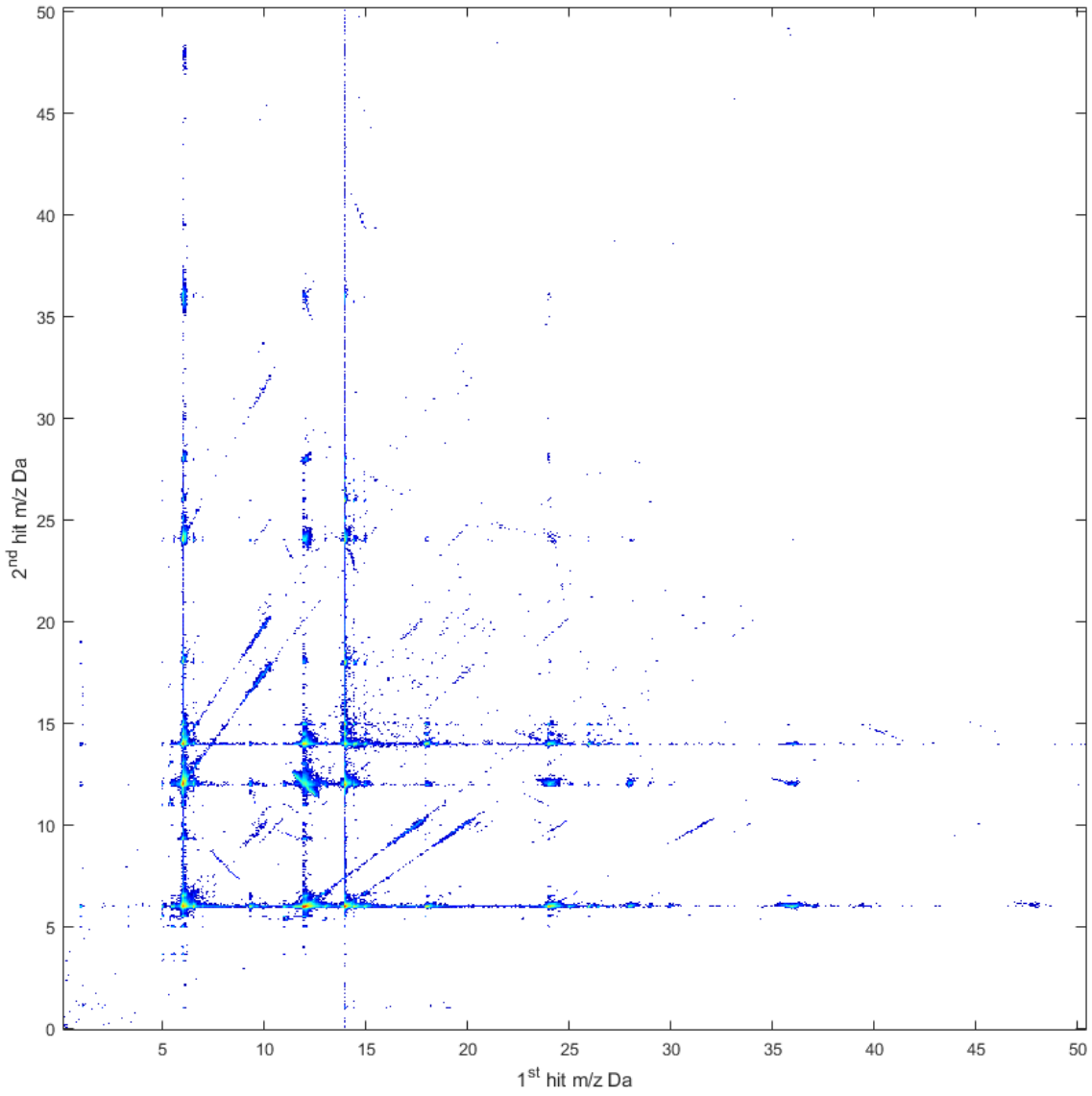


Figure 27: Correlative evaporation histogram for a SiC specimen. Each plotted point corresponds to two ions participating in the creation of a multiple hit event. The color of the plotted regions corresponds to the intensity of multiple hits present at each pair of Dalton values.

The vertical and horizontal lines indicate the evaporation of one of the correlated species at the instant of the pulse followed by the delayed evaporation of the second correlated species. The diagonal lines pointing from the bottom left to the top right of the plot indicate the simultaneous delayed evaporation of the two correlated species. The diagonal, vertical, and

horizontal lines represent the thermal tails present in the m/q spectra of the specimen. Finally, the curved tracks indicate molecular-ion dissociation in route to the detector [171]. Assuming molecular ion dissociation occurs close to the specimen surface, Saxey demonstrates that the deviation in m/q values, and therefore the shape of the curved dissociation tracks, can be plotted using the following relationship:

$$m_1' = m_1\left[1 + \frac{\Delta V}{V_0}\left(1 - \frac{m_1}{m_0}\right)\right]$$

where m_1' represents the shifted measured mass-to-charge ratio of one of the ions formed during dissociation, m_1 represents the mass-to-charge of the same ion if it had not been formed from mid-flight dissociation, ΔV represents the voltage drop that has occurred from the specimen surface to moment of dissociation, V_0 represents the voltage at the moment of evaporation, and m_0 represents the mass-to-charge ratio of the complex ion before dissociation [171]. Curves corresponding to specific m_0, m_1, and m_2 dissociations were plotted over correlative evaporation histograms for each material in this study to identify the ions involved in mid-flight dissociation. Complex ion dissociation can lead to systematic loss of ions for two main reasons. Dissociation occurring far from the specimen surface can lead to altered time of flights that cannot be assigned to a given ion and contribute to spectrum noise [171]. Furthermore, complex ion dissociation can also lead to the formation of uncharged atoms or molecules, neutrals, which are unaffected by the electric field and thus less likely to possess the necessary kinetic energy to reach the detector [171]. Therefore, identifying ions subjected to dissociation for each of the studied materials can help identify sources of systematic loss resulting in compositional measurement bias.

2.6 Sample Size

The effect sampling size has on compositional measurements was probed by determining the measurement uncertainty resulting from varied sample sizes. This analysis can give an indication of the minimum compositional differences that can be discerned when dealing with small features. To study this effect, small rectangular ROIs were placed within regions of data sets away from any distinct microstructural features, such as grain boundaries. The composition of these small rectangular ROIs was calculated, and the size of the ROI was incrementally increased. This increase in dimensions was only executed along directions perpendicular to the analysis direction (tip long axis) to extract data corresponding to evaporation events occurring at similar electric field values. The composition of the larger ROI was then calculated. The uncertainties from each ROI size were finally compared.

3 3YSZ Results

The operating conditions for each proceding analysis can be seen in Table 7.

Table 7: Operating conditions for YSZ analyses

Analysis	Temperature (K)	Pulse Frequency (kHz)	Detection Rate (%)	Laser Energy (pJ)
Laser Energy	40	200	0.5	30, 40, 50, 100
Reflectron	40	200	0.5	30
Tip Blunting	40	200	0.5	30
Laser Proximity	40	200	0.5	30
Correlative Evap.	40	200	0.5	30
Sample Size	40	200	0.5	30

An operating temperature of 40 K was chosen in accordance with studies in the literature on

similar materials systems [157], [208].

3.1 Laser Energy Sweep

Four conventionally sintered 3YSZ samples each containing more than 10 million ions were analyzed at 30 pJ, 40 pJ, 50 pJ, and 100 pJ. Figure 28 demonstrates the results of this laser energy sweep.

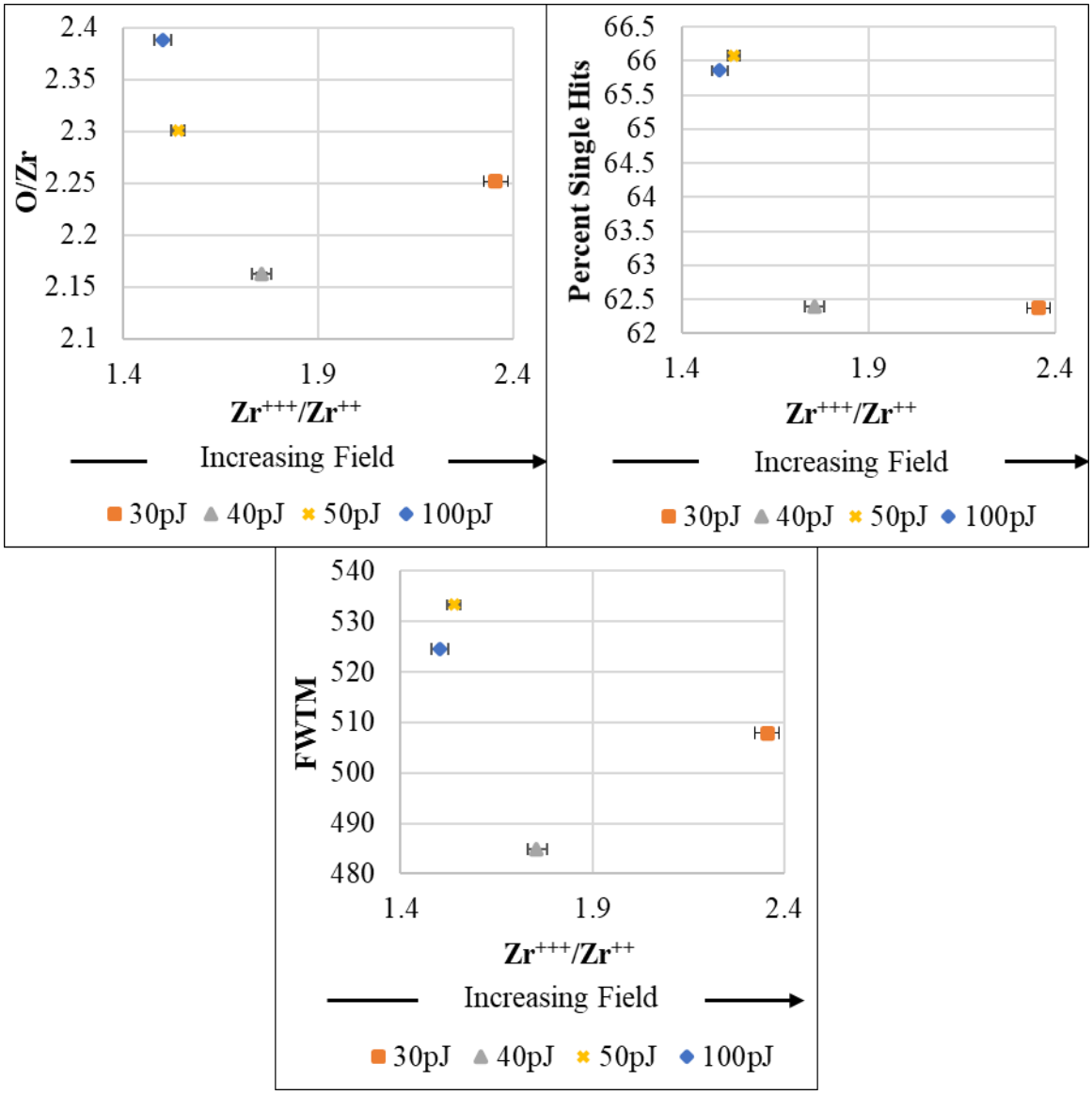


Figure 28: A) Effect of laser energy on measured composition of conventionally sintered 3YSZ APT samples vs. Zr^{+++}/Zr^{++} CSR. B) Percent single hits versus laser energy for 3YSZ samples. C) m/q resolution as measured by full width at tenth of maximum (FWTM) values for the O_2^+ peak versus laser energy value.

3.2 Reflectron (LEAP 5000XR) vs. Straight Flightpath (LEAP 5000XS)

The LEAP 5000XR vs. LEAP 5000XS comparisons were conducted on separate conventionally sintered datasets containing ~10 million ions and can be found in Table 8.

Table 8: LEAP 5000XR vs. LEAP 5000XS for Conventionally Sintered 3YSZ Sample. Values to left and right of central values are uncertainty values.

	LEAP 5000XR			LEAP 5000XS		
Zr^{+++}/Zr^{++}	0.04	1.94	0.04	0.04	1.82	0.04
O/Zr	0.01	2.36	0.01	0.01	2.59	0.01
% Single Hits		65.30			76.08	
FWHM		1103			640	

3.3 Ranging

The effect range width has on 3YSZ compositional measurements using both the LEAP 5000XR and the LEAP 5000XS can be seen in Figure 29.

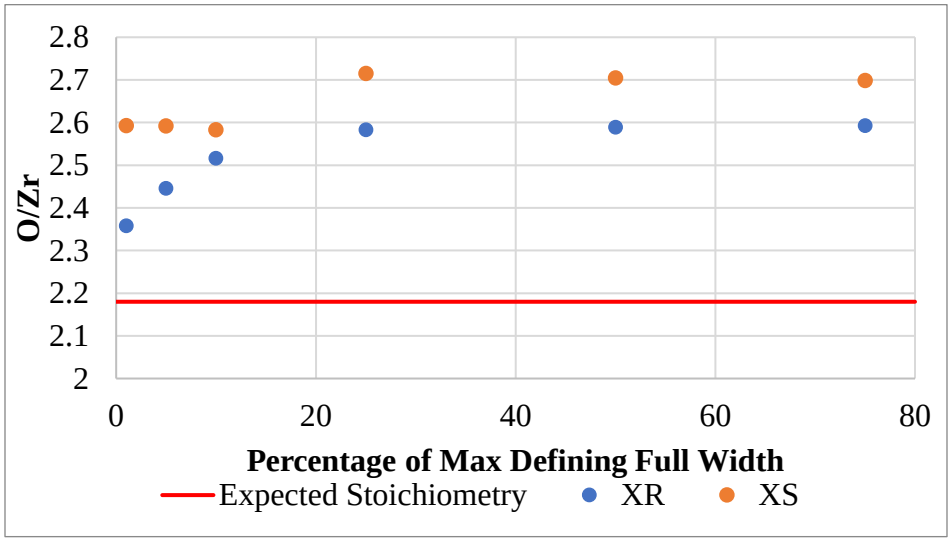


Figure 29: O/Zr vs. ranging for 3YSZ experiments run on both the LEAP 5000XR and LEAP 5000XS

3.4 Peak Overlaps

The peak overlaps considered for 3YSZ samples can be found in Table 9.

Table 9: Overlapping Peaks in 3YSZ m/q Spectra

Dalton Value	Ion 1 and Charge	Ion 2 and Charge	Ion 3 and Charge
22.5	Zr^{++++}	AlO^{++}	SiO^{++}
23	Zr^{++++}	SiO^{++}	
30	Zr^{+++}	Si^{+}	
32	O_2^{+}	Zr^{+++}	
35.6	ZrO^{+++}	YO^{+++}	
45	Zr^{++}	AlO^{+}	SiO^{+}
46	Zr^{++}	SiO^{+}	
53.5	ZrO^{++}	YO^{+}	
61	ZrO_2^{++}	SiO_2^{++}	
61.4	ZrO_2^{++}	YO_2^{++}	
64	ZrO_2^{++}	HfO^{+++}	
106.9	ZrO^{+}	YO^{+}	

A representative ranged m/q spectrum for a 3YSZ specimen can be found in Figure 30. Note, the identities of peaks are consistent across different data sets, however range widths and peak maxima locations may vary slightly.

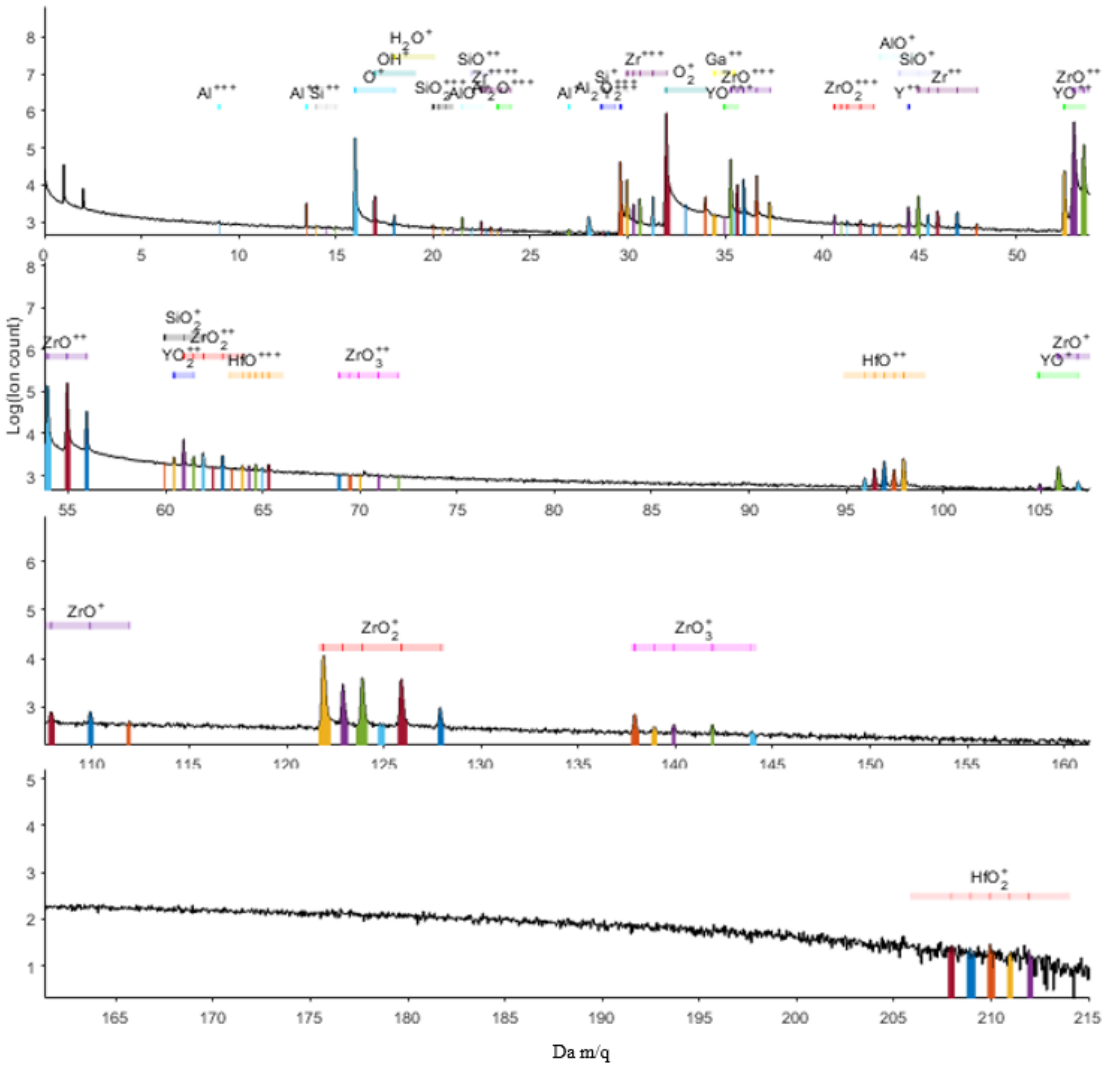


Figure 30: Ranged m/q spectrum for a 3YSZ data set. Figure generated using AtomProbeLab v0.2.2. Note the difference in Log scales across the different panels of the spectrum.

3.5 Tip Blunting

Profiles demonstrating composition across the duration of a 3YSZ analysis as the tip blunts can be found in Figure 31.

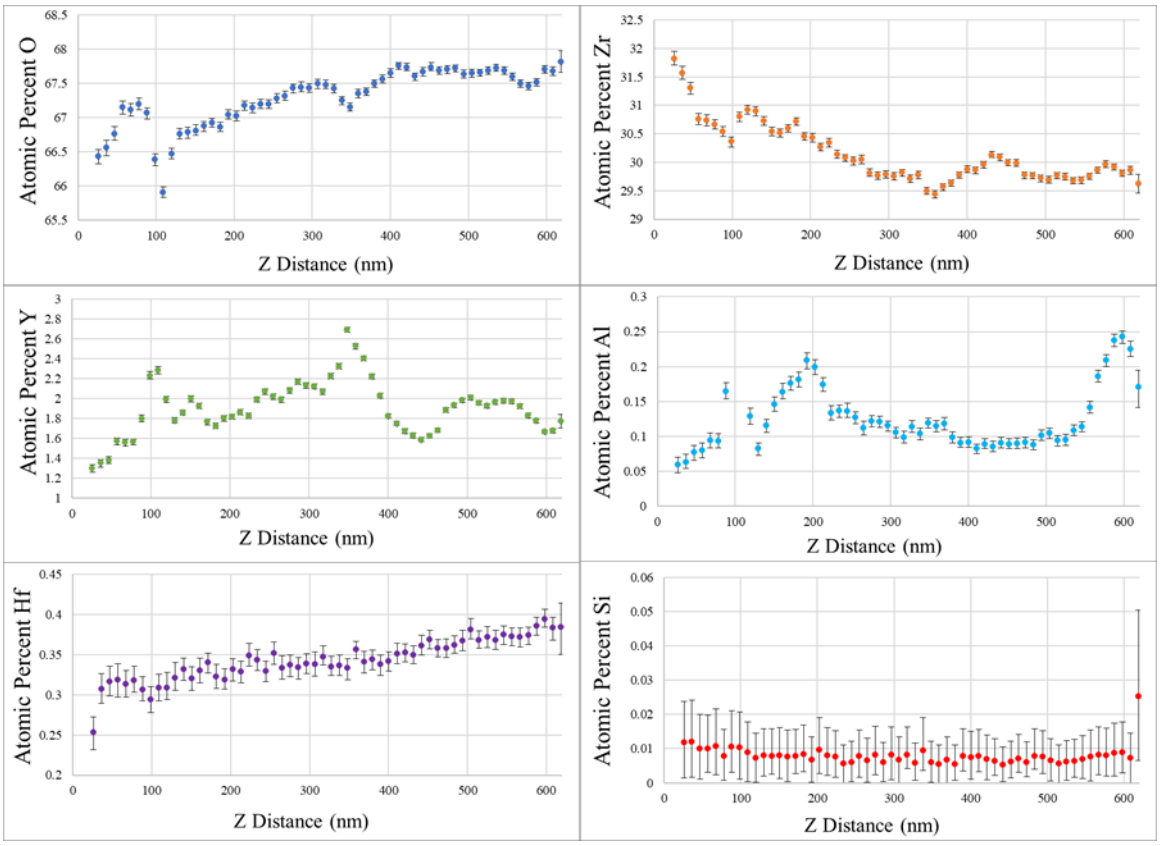


Figure 31: Composition across length of 3YSZ sample

The sudden drops in oxygen and zirconium content and rises in aluminum and yttrium content indicate the location of a grain boundary along the concentration profile. Yttrium composition is not uniform throughout grains (as will be discussed in this thesis), and therefore isolating any tip blunting effect from non-uniformity effects is challenging. Figure 32 demonstrates the effect tip blunting has on the Zr^{+++}/Zr^{++} CSR, percent single hits, and the O_2^+ peak FWTM.

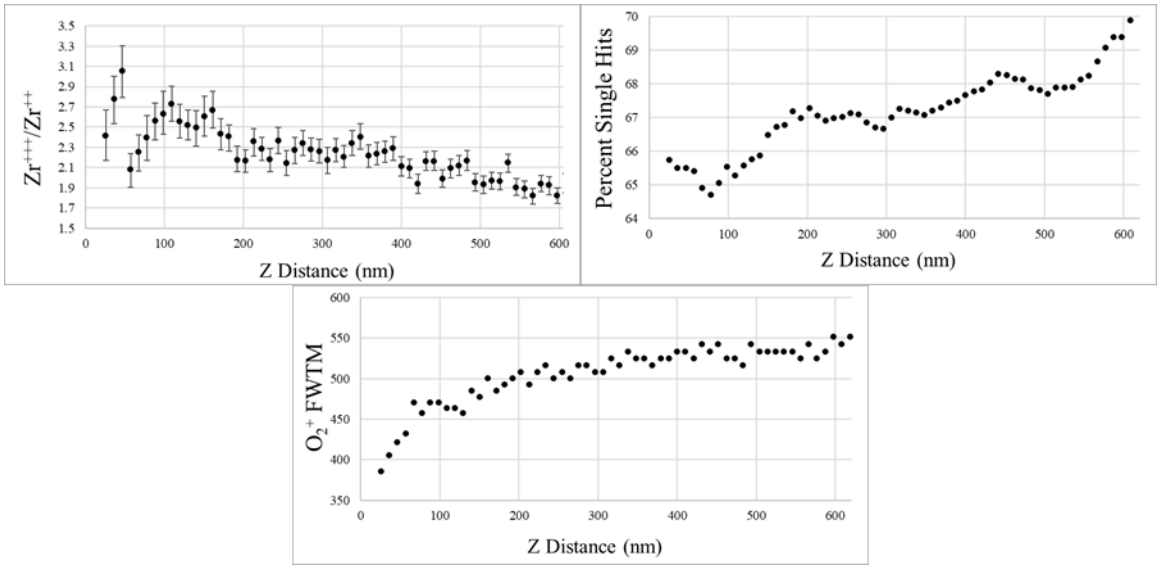


Figure 32: Zr^{+++}/Zr^{++}, percent single hits, and O_2^+ FWTM as the tip blunts during analysis

3.6 Laser Illumination Proximity

Two 3YSZ specimens, specimen A and specimen B, were investigated. For specimen A, the bright side yielded a multiple hit percentage of 26.3%, while the dark side yielded 26.0%. For specimen B, the bright side yielded a multiple hit percentage of 27.4%, while the dark side yielded a multiple hit percentage of 31.7%. Table 10 demonstrates the difference in m/q resolution between the dark and bright sides of tips A and B.

Table 10: FWHM values for specimens A and B from both dark and bright regions of tips

	A			B		
	Bright	**Dark**	**Difference**	**Bright**	**Dark**	**Difference**
O_2^+	1333	941	392	1333	914	419
ZrO^+	1358	897	501	1297	897	400

The effect laser illumination has on measured composition and the Zr^{+++}/Zr^{++} CSR for specimen B is demonstrated in Figure 33.

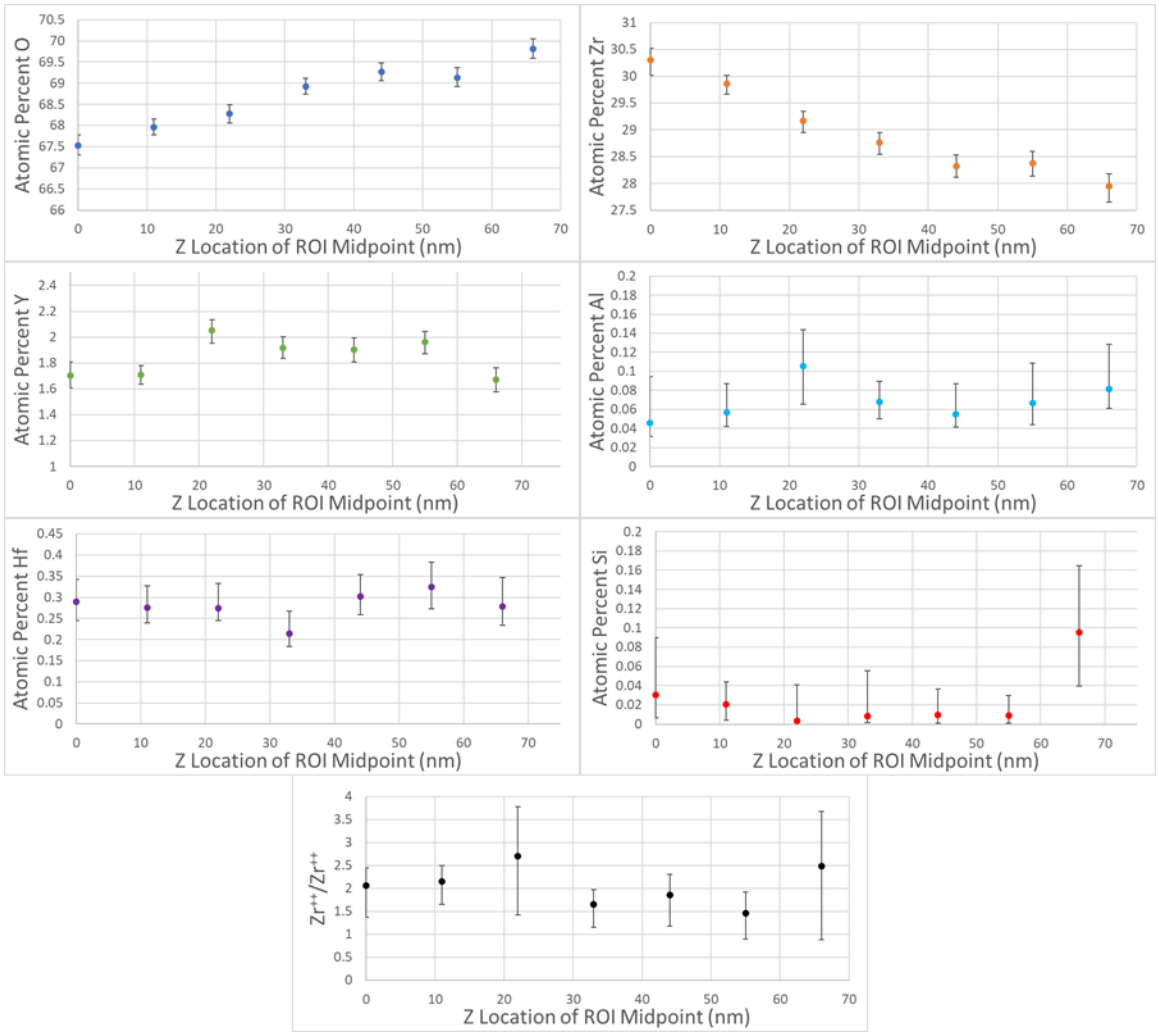


Figure 33: Composition and Zr^{+++}/Zr^{++} CSR moving from dark to light side of tip for specimen B

The left side of each chart indicates the dark side of the specimen while the right side indicates the bright side. Specimen A demonstrated no consistent trend for any of the chemical species and was therefore not plotted.

3.7 Correlative Evaporation Histogram

Figure 34 shows a correlative evaporation histogram for a conventionally sintered 3YSZ sample.

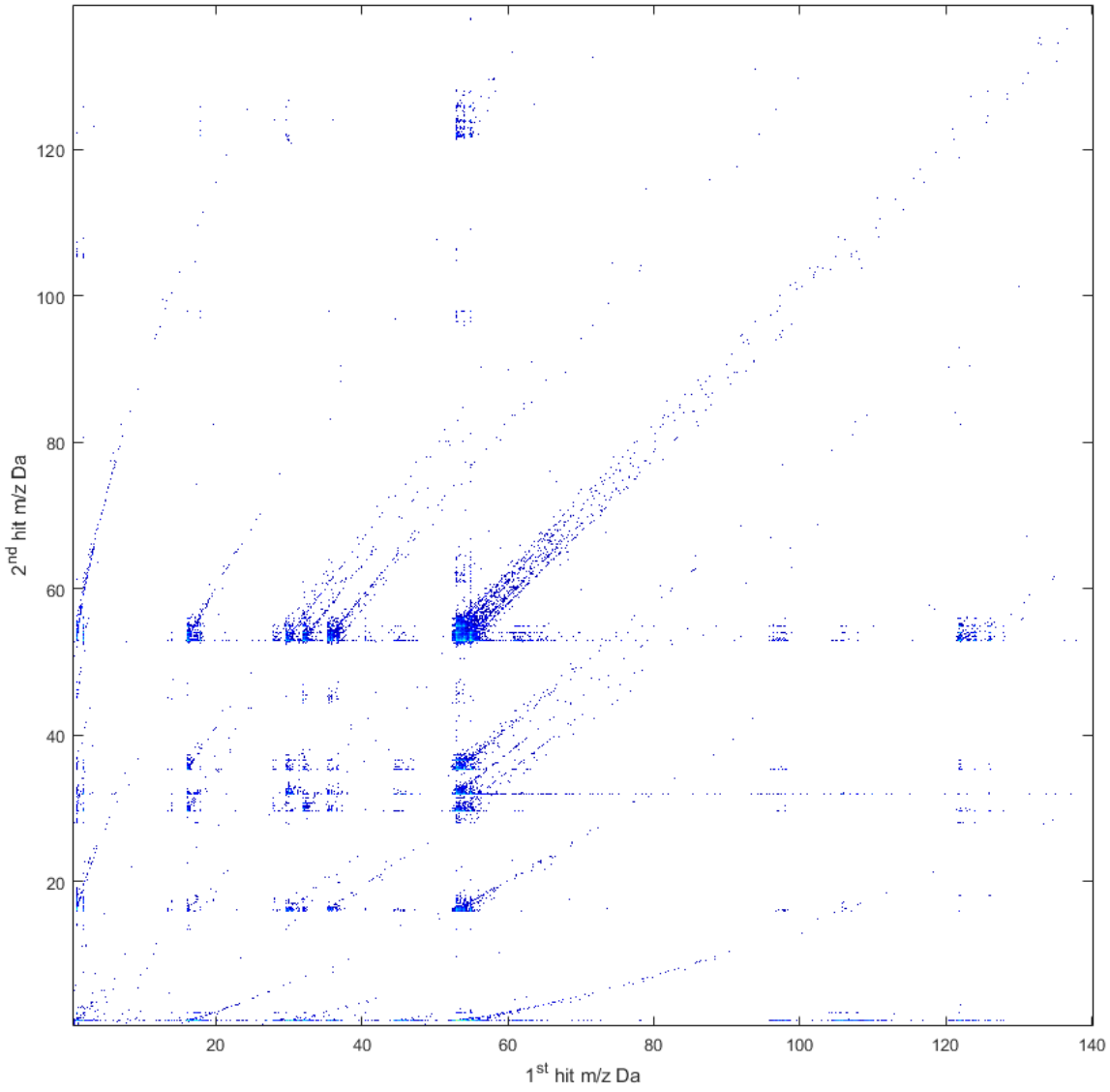


Figure 34: Correlative evaporation histogram for a conventionally sintered 3YSZ sample

The histogram contains relatively weak dissociation tracks which are enumerated in Table 11.

Table 11: Complex ion dissociation mechanisms for a conventionally sintered 3YSZ sample

Coordinates of Track Origin	Ion Dissociation Mechanisms
(32, 44.9)	$ZrO_2^{3+} \rightarrow Zr^{2+} + O_2^{2+}$
(53, 112)	$Zr_2O_3^{3+} \rightarrow ZrO^{2+} + ZrO_2^{+}$
(29.6, 122)	$ZrYO^{4+} \rightarrow ZrO_2^{+} + Y^{3+}$
(16, 122)	$ZrO_3^{3+} \rightarrow ZrO_2^{+} + O^{+}$
(16, 106)	$ZrO_2^{2+} \rightarrow ZrO^{+} + O^{+}$

3.8 Sample Size

Figure 35 demonstrates the dependence of compositional measurement uncertainty on sampling size for each chemical species present in a 3YSZ sample.

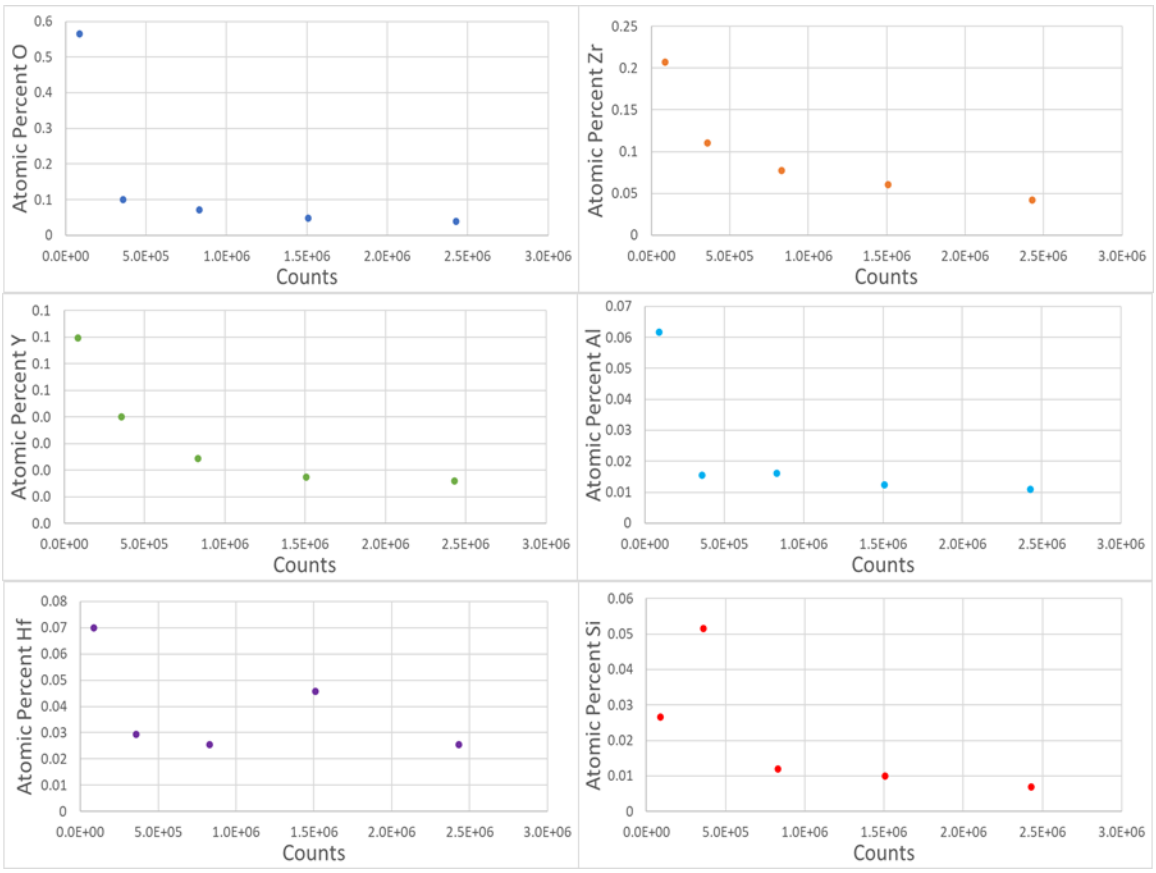


Figure 35: Compositional measurement uncertainty versus sampling size for each chemical species present in 3YSZ samples

4 Alumina Results

The operating conditions for each alumina analysis can be found in Table 12.

Table 12: Operating conditions for alumina analyses

Analysis	Temperature (K)	Pulse Frequency (kHz)	Detection Rate (%)	Laser Energy (pJ)
Laser Energy	60	200	0.5	50, 100, 150
Reflectron	60	200	0.5	30
Tip Blunting	60	200	0.5	30
Laser Proximity	60	200	0.5	30
Correlative Evap.	60	200	0.5	30
Sample Size	60	200	0.5	30

An operating temperature of 60 K was chosen, as early attempts to run alumina samples at lower temperatures yielded little to no data and a high proportion of specimen fractures.

4.1 Laser Energy Sweep

The effect laser energy has on several measurement parameters for alumina samples can be found in Figure 36.

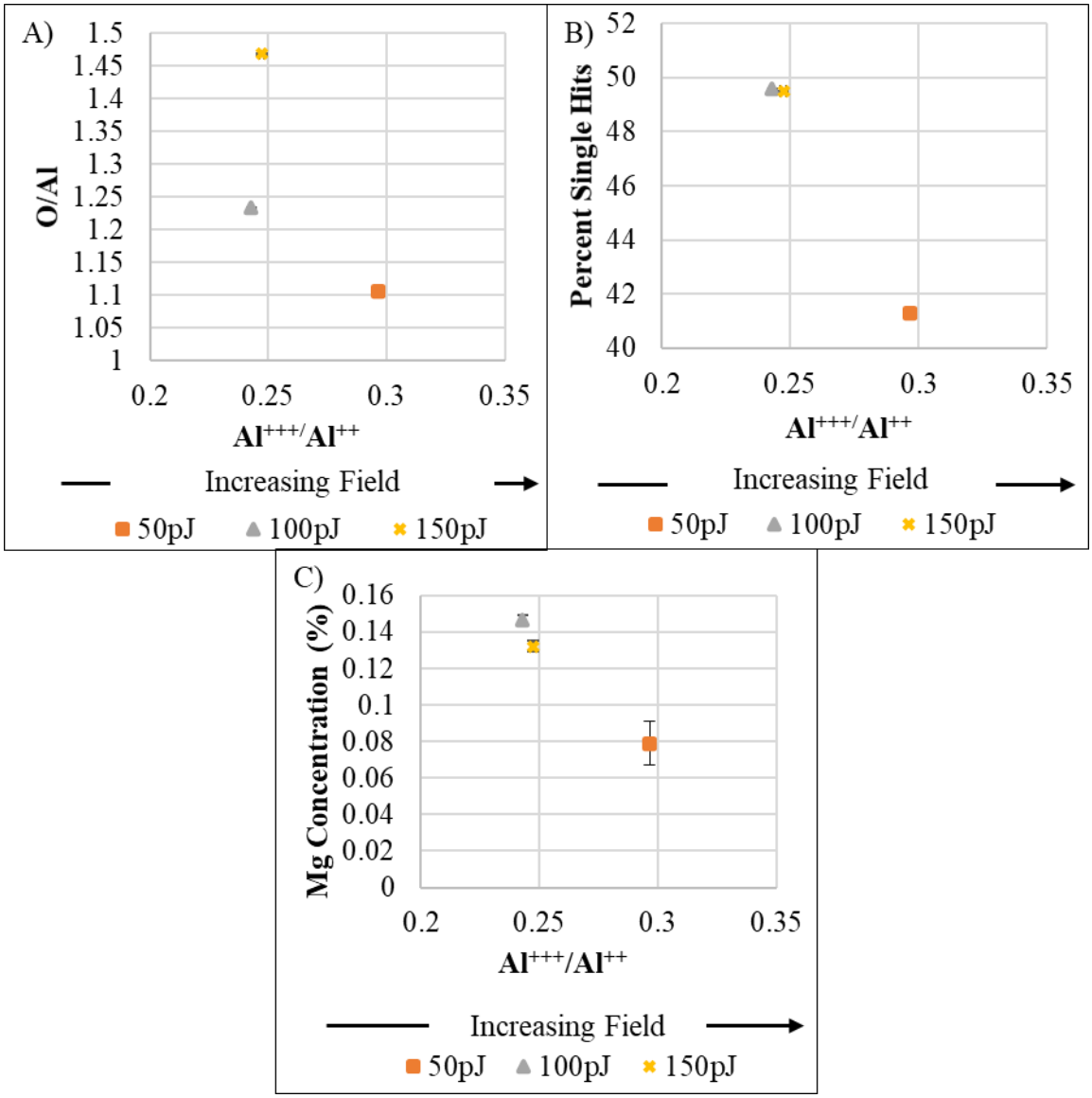


Figure 36: A) Effect of laser energy on measured composition of alumina APT samples vs. Al^{+++}/Al^{++} CSR. B) Percent single hits versus laser energy for alumina samples. C) Mg concentration versus laser energy.

4.2 Reflectron (LEAP 5000XR) vs. Straight Flightpath (LEAP 5000XS)

The LEAP5000XR vs. LEAP5000XS comparisons found in Table 13 were conducted on separate 0.25 weight percent magnesia doped alumina specimens sintered under vacuum, and each data set contained ~50 million ions.

Table 13: LEAP 5000XR vs. LEAP 5000XS for alumina samples. Values to left and right of central values are uncertainty values.

	LEAP 5000XR			LEAP 5000XS		
Al^{+++}/Al^{++}	0.0003	0.25	0.0002	0.0002	0.22	0.0002
O/Al	0.0003	1.21	0.0004	0.0003	1.25	0.0003
% Single Hits		46.7			46.7	
FWHM		1038			435	
Mg at%	0.0019	0.035	0.0018	0.0015	0.047	0.0017

The Al^{+++}/Al^{++} and O/Al measurements include positive and negative uncertainties to the left and right of the absolute values.

4.3 Ranging

The effect range width has on alumina compositional measurements using both the LEAP 5000XR and the LEAP 5000XS can be seen in Figure 37.

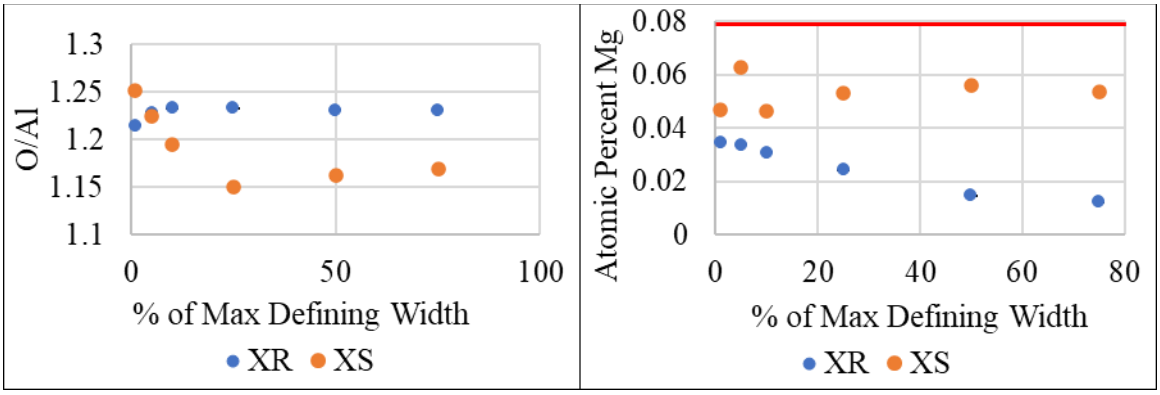


Figure 37: O/Al and Mg concentration vs ranging for alumina samples analyzed using both the LEAP 5000XR and the LEAP 5000XS

4.4 Peak Overlaps

Table 14 presents the peak overlaps of significance considered when analyzing carbon-doped alumina samples.

Table 14: Significant peak overlaps considered when measuring compositions of alumina samples

Dalton Value	Ion 1 and Charge	Ion 2 and Charge
12	Mg^{++}	C^{+}
24	Mg^{+}	C_2^{+}

A representative ranged alumina spectrum can be found in Figure 38.

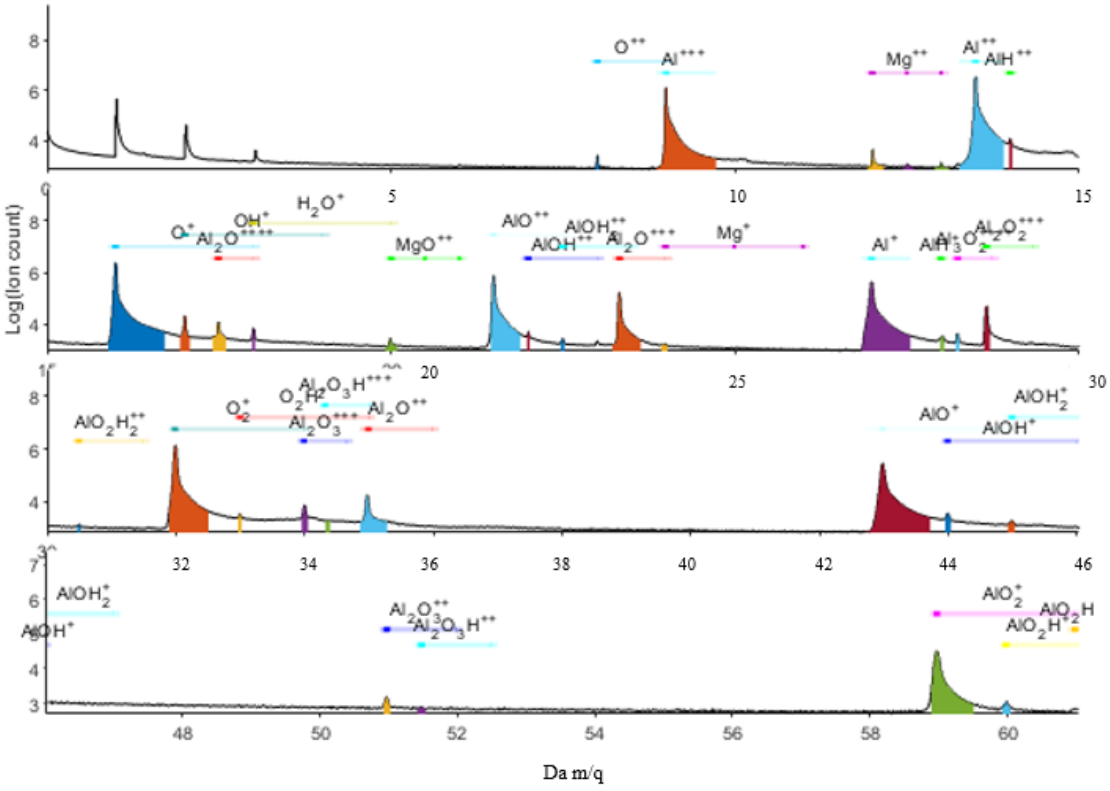


Figure 38: Ranged m/q spectrum for an alumina data set. Figure generated using AtomProbeLab v0.2.2. Note the difference in Log scales across the different panels of the spectrum

4.5 Tip Blunting

Profiles demonstrating composition across the duration of an alumina analysis as the tip blunts can be found in Figure 39. The left side of the charts corresponds to the beginning of the analysis, i.e., the apex of the tip.

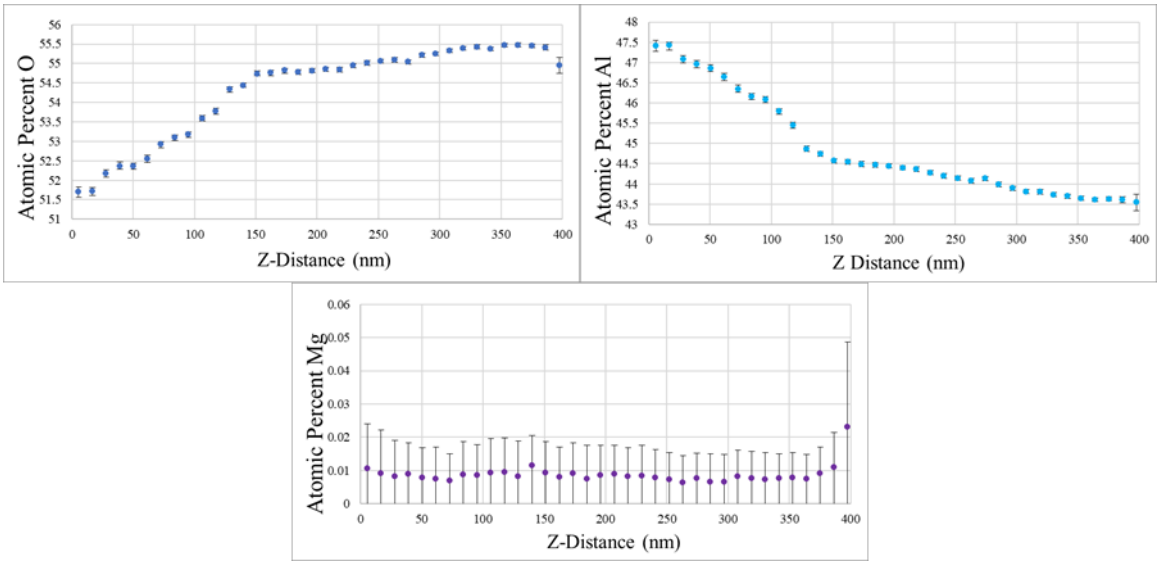


Figure 39: Composition across length of carbon and magnesium doped specimen

These results are consistent with results from another tip analyzed in the same manner. Figure 40 demonstrates the effect tip blunting has on the Al^{+++}/Al^{++} CSR, percent single hits, and the O_2^{+} FWTM.

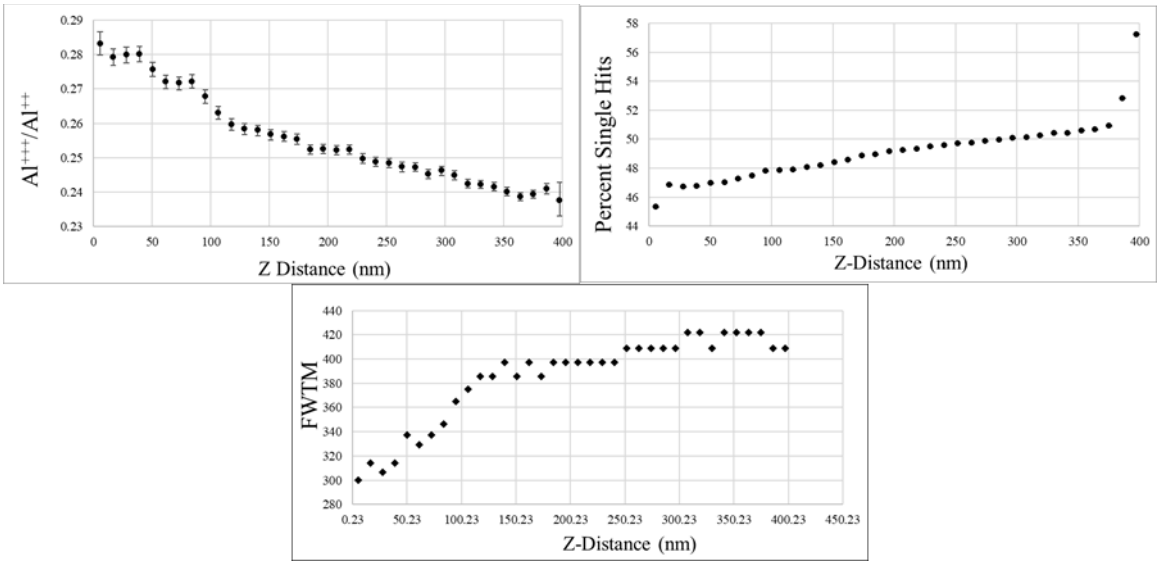


Figure 40: Al^{+++}/Al^{++}, percent single hits, and O_2^{+} FWTM as the tip blunts during analysis

4.6 Laser Illumination Proximity

Two specimens (A and B) doped with 0.25 wt% MgO and 0.02 wt% carbon were

investigated. For specimen A, the bright side of the tip yielded a multiple hit percentage of 57.7% while the dark side yielded 61.1%. For specimen B, the bright side yielded a multiple hit percentage of 40.4% while the dark side yielded a multiple hit percentage of 59.8%. Table 15 illustrates how mass resolution varies between the bright and dark sides of each tip.

Table 15: FWHM values for bright and dark sides of alumina APT tips

	A			B		
	Bright	**Dark**	**Difference**	**Bright**	**Dark**	**Difference**
Al^{++}	1350	794	556	1350	794	556
O^{++}	1143	727	416	1333	762	571

The effect laser illumination proximity has on composition and the Al^{+++}/Al^{++} can be found in Figure 41.

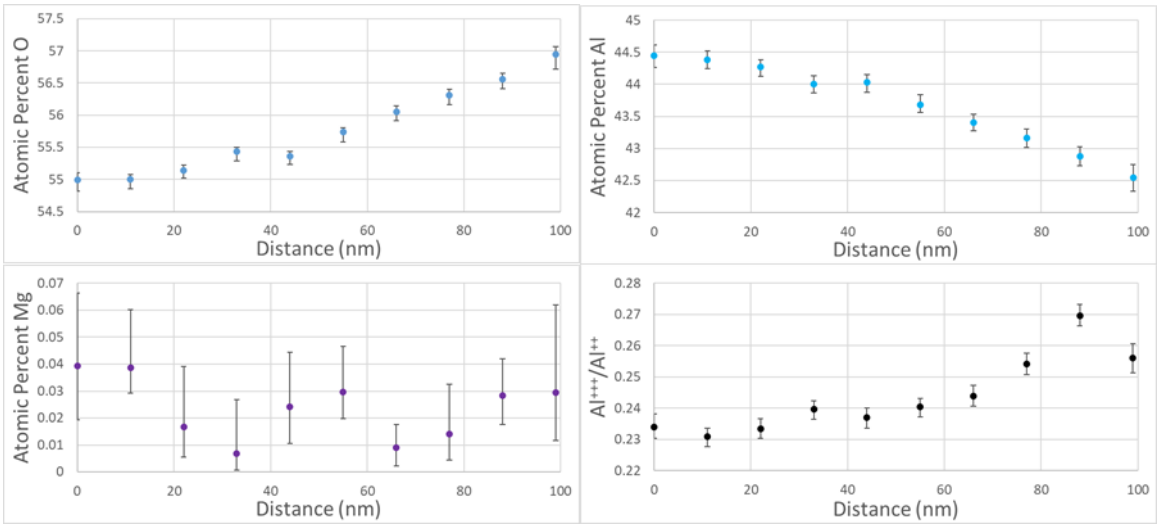


Figure 41: Composition and Al^{+++}/Al^{++} moving from the dark to light side of each tip for specimen B

The left side of each plot corresponds to the dark side of the corresponding tip while the right side corresponds to the bright side of each tip.

4.7 Correlative Evaporation Histogram

Figure 42 shows a correlative evaporation histogram for an alumina sample.

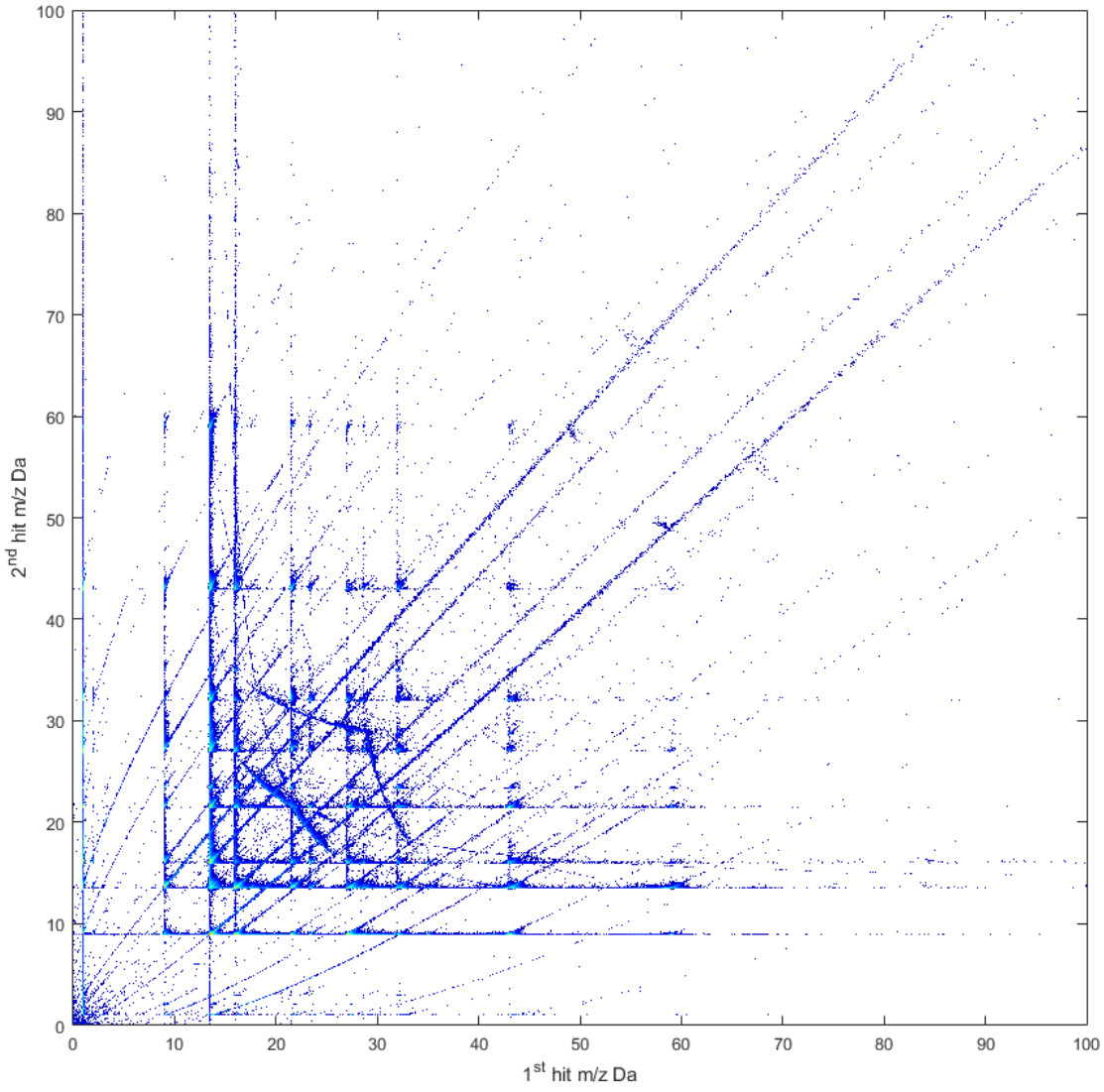


Figure 42: Correlative evaporation histogram for an alumina sample

The histogram contains several dissociation tracks of high intensity which are enumerated in Table 16.

Table 16: Ion dissociation mechanisms for alumina samples

Coordinates of Track Origin	Ion Dissociation Mechanisms
(16, 35)	$Al_2O_2^{3+} \rightarrow Al_2O^{2+} + O^+$
(13.5, 59)	$Al_2O_2^{3+} \rightarrow AlO_2^+ + Al^{2+}$
(13,5, off y-axis - neutral)	$AlOH^{2+} \rightarrow Al^{2+} + OH$
(13,5, 43)	$Al_2O^{3+} \rightarrow Al^{2+} + AlO^+$
(16, 27)	$AlO^{2+} \rightarrow Al^+ + O^+$
(9, 13.5)	$Al_2^{5+} \rightarrow Al^{3+} + Al^{2+}$
(21.5, 27)	$Al_2O^{3+} \rightarrow AlO^{2+} + Al^+$
(21.5, 43)	$Al_2O_2^{3+} \rightarrow AlO^{2+} + AlO^+$
(27, 43)	$Al_2O^{2+} \rightarrow AlO^+ + Al^+$
(27, 32)	$AlO_2^{2+} \rightarrow Al^+ + O_2^+$
(27, 59)	$Al_2O_2^{2+} \rightarrow Al^+ + AlO_2^+$
(27, 33)	$AlO_2H^{2+} \rightarrow Al^+ + O_2H^+$
(16, 86)	$Al_2O_3^{2+} \rightarrow O^+ + Al_2O_2^+$

The third dissociation track from the top is of particular interest, as it demonstrates the formation of an uncharged neutral.

4.8 Sample Size

Figure 43 demonstrates the dependence of compositional uncertainty on sampling size for alumina samples.

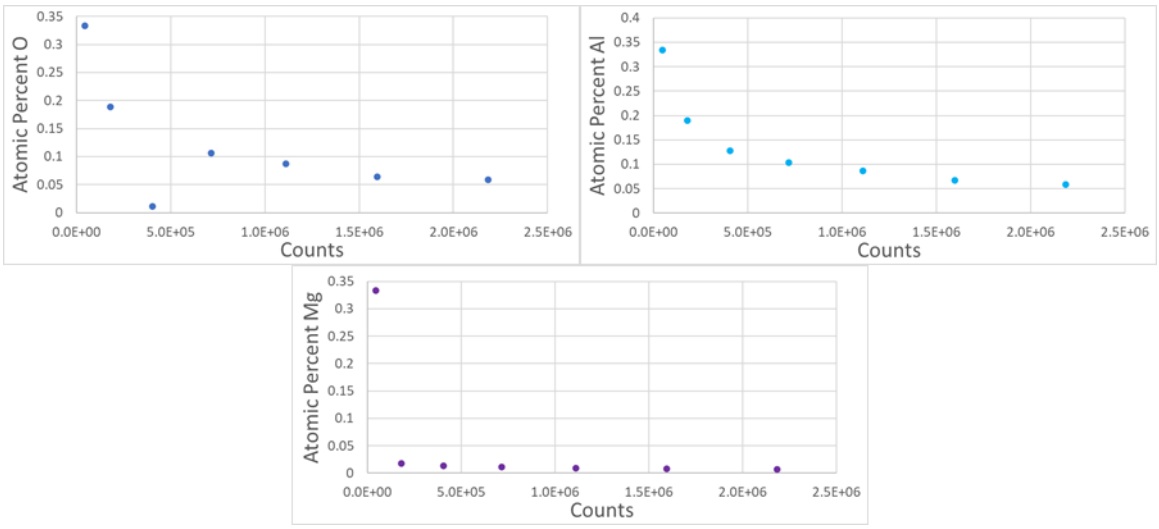


Figure 43: Compositional measurement uncertainty versus sampling size for each chemical species present in alumina samples

5 SiC Results

The operating conditions for SiC analysis are given in Table 17.

Table 17: Operating conditions for SiC analyses

Analysis	Temperature (K)	Pulse Frequency (kHz)	Detection Rate (%)	Laser Energy (pJ)
Laser Energy	50	200	0.5	30, 40, 50, 100
Laser vs Voltage	50	200	0.5	30
Reflectron	50	200	0.5	30
Tip Blunting	50	200	0.5	30
Laser Proximity	50	200	0.5	30
Correlative Evap.	50	200	0.5	30
Sample Size	50	200	0.5	30

The sole voltage mode run used for the laser mode vs voltage mode comparison was run using the following conditions: a constant detection rate of 0.5%, an operating temperature of 60 K, a pulse fraction of 25%, and a pulse frequency of 100 kHz.

5.1 Laser Energy Sweep

Three conventionally sintered SiC samples each containing more than 20 million ions were analyzed at 10 pJ, 30 pJ, and 50 pJ on the LEAP 5000XR, and analysis results can be found in Figure 44.

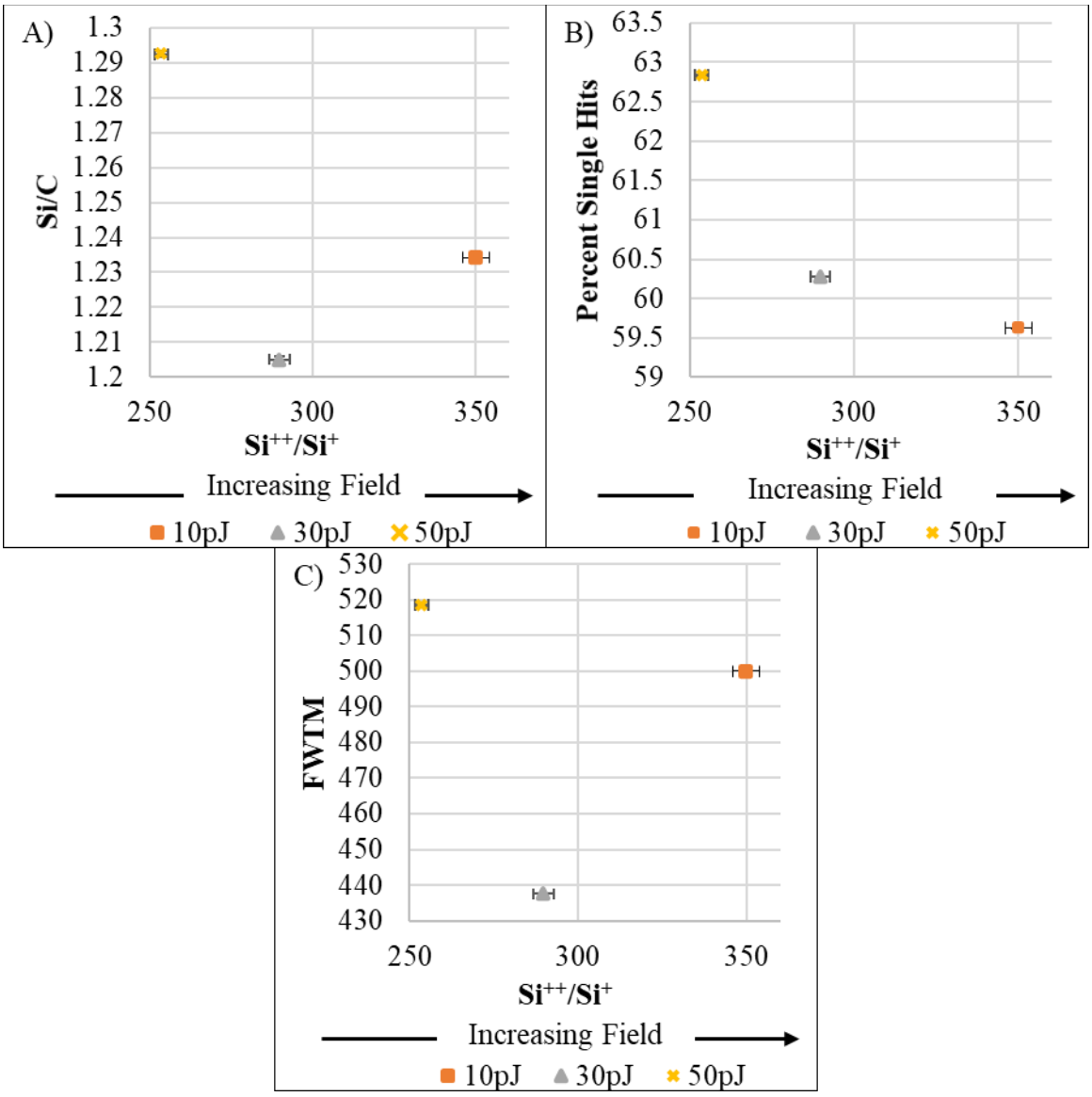


Figure 44: A) Si/C vs. laser energy. B) Percent single hits vs. laser energy. C) M/q resolution vs. laser energy

5.2 Laser Pulsing Mode vs. Voltage Pulsing Mode

The laser pulsing vs. voltage mode comparison seen in Table 18 was conducted on separate conventionally sintered datasets containing ~20 million ions.

Table 18: Laser pulsing vs. voltage pulsing for SiC specimens. Values to left and right of central values are uncertainty values.

	Laser Pulsing			Voltage Pulsing		
Si^{++}/Si^{+}	4.1	274.2	3.3	77.6	1121.6	82.2
Si/C	0.001	1.20	0.001	0.003	1.23	0.003
% Single Hits		59.9			72	
FWHM		1077			875	

5.3 Reflectron (LEAP 5000XR) vs. Straight Flightpath (LEAP 5000XS)

The LEAP 5000XR vs. LEAP 5000XS comparisons found in Table 19 were conducted on separate conventionally sintered datasets containing ~20 million ions.

Table 19: LEAP 5000XR vs. LEAP 5000XS for conventionally sintered SiC sample. Values to left and right of central values are uncertainty values.

	LEAP 5000XR			LEAP 5000XS		
Si^{++}/Si^{+}	4.1	274.2	3.3	2.0	175.7	2.0
Si/C	0.001	1.20	0.001	0.004	1.35	0.005
% Single Hits		59.9			56.7	
FWHM		1077			778	

5.4 Ranging

The effect range width has on SiC compositional measurements using both the LEAP 5000XR and LEAP 5000XS can be seen in Figure 45.

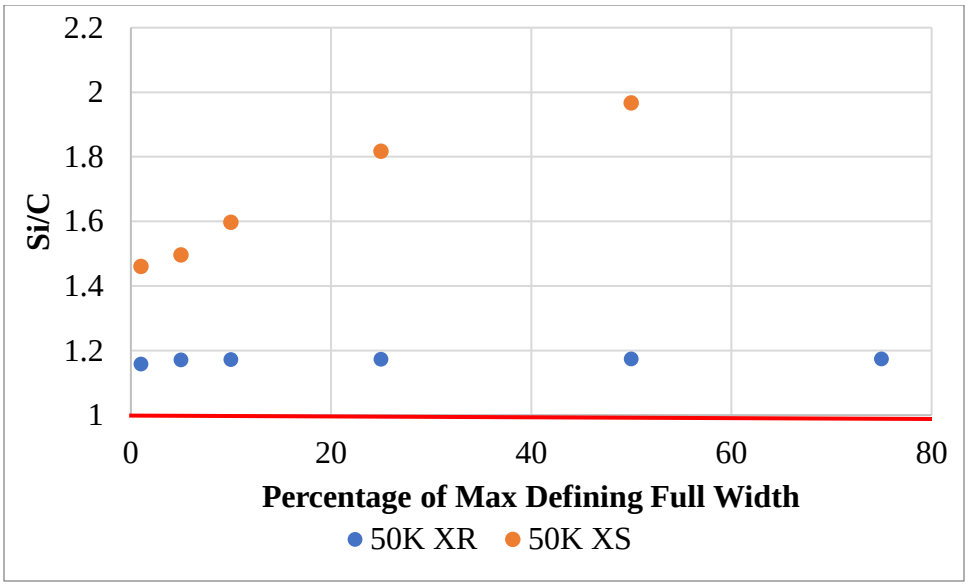


Figure 45: Si/C vs. ranging for SiC experiments run on both the LEAP 5000XS and LEAP 5000XR

5.5 Peak Overlaps

The peak overlaps in Table 20 were considered when calculating the composition of features within SiC samples.

Table 20: Peak overlaps considered when measuring composition of SiC samples

Dalton Value	Ion 1 and Charge	Ion 2 and Charge	Ion 3 and Charge
10.0	Si^{+++}	B^{+}	
18.0	C_3^{++}	O^{+}	
24.0	C_2^{+}	C_4^{++}	CB^{+}
27	Al^{+}	SiC_2^{+}	
28/29/30	Si^{+}	CO^{+}	
50.5	C_4^{+}	SiC_2^{+}	

A representative ranged SiC m/q spectrum can be found in Figure 46.

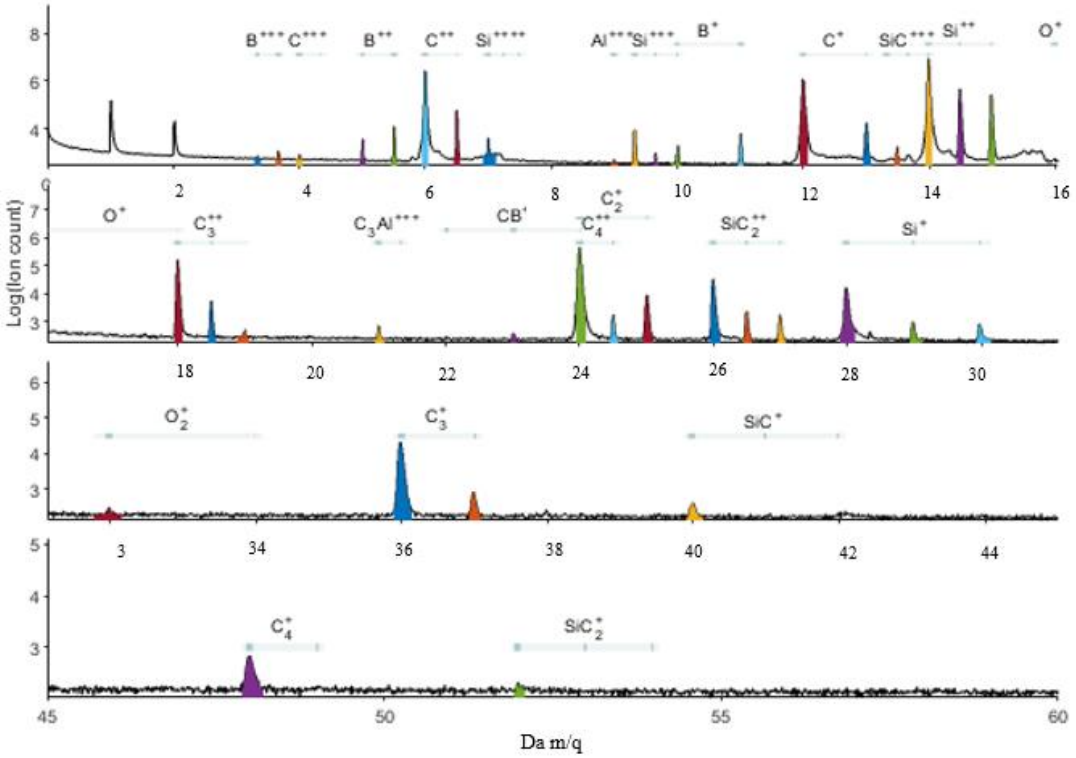


Figure 46: Ranged m/q spectrum for a SiC data set. Figure generated using AtomProbeLab v0.2.2. Note the difference in Log scales across the different panels of the spectrum

5.6 Tip Blunting

Figure 47 demonstrates the effect the blunting of the specimen apex has on compositional measurements.

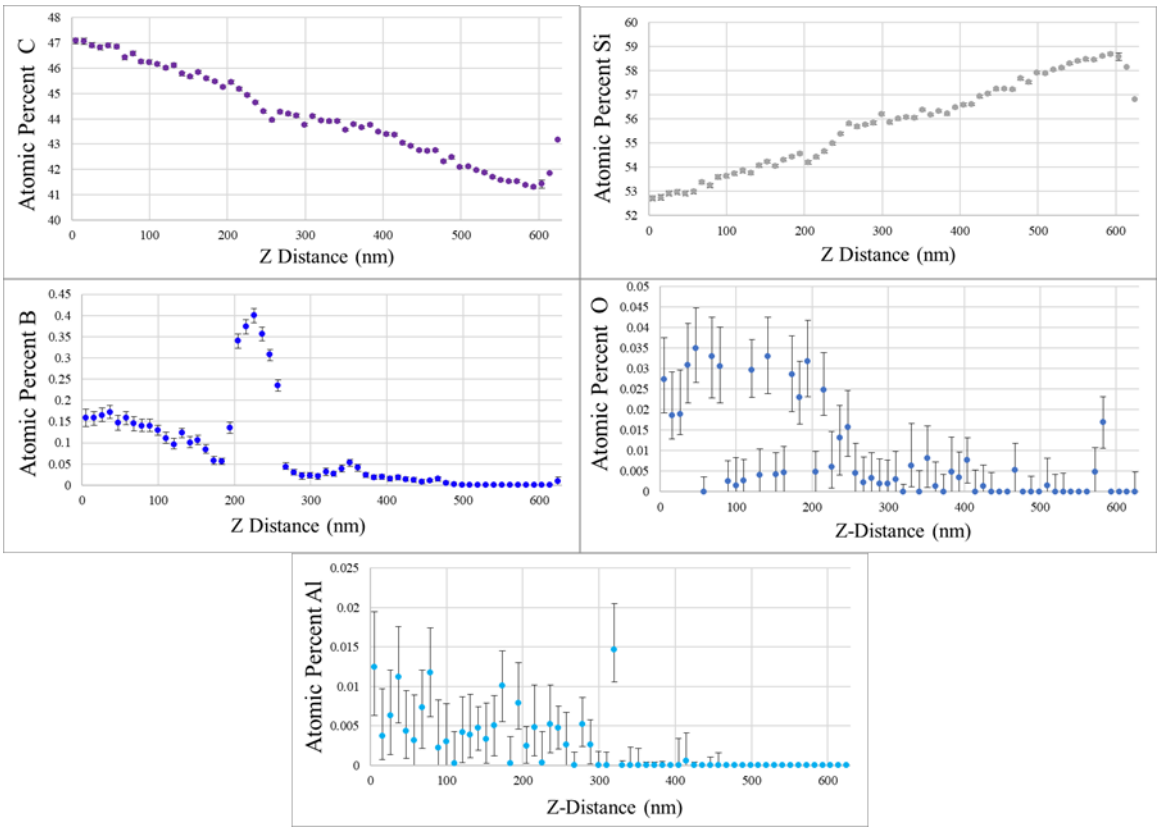


Figure 47: Composition as tip blunts and analysis progresses for SiC specimen

The sharp rise in boron content indicates a grain boundary. Figure 48 demonstrates the effect tip blunting has on the Si^{++}/Si^{+} CSR, percent single hits, and the Si^{++} FWTM.

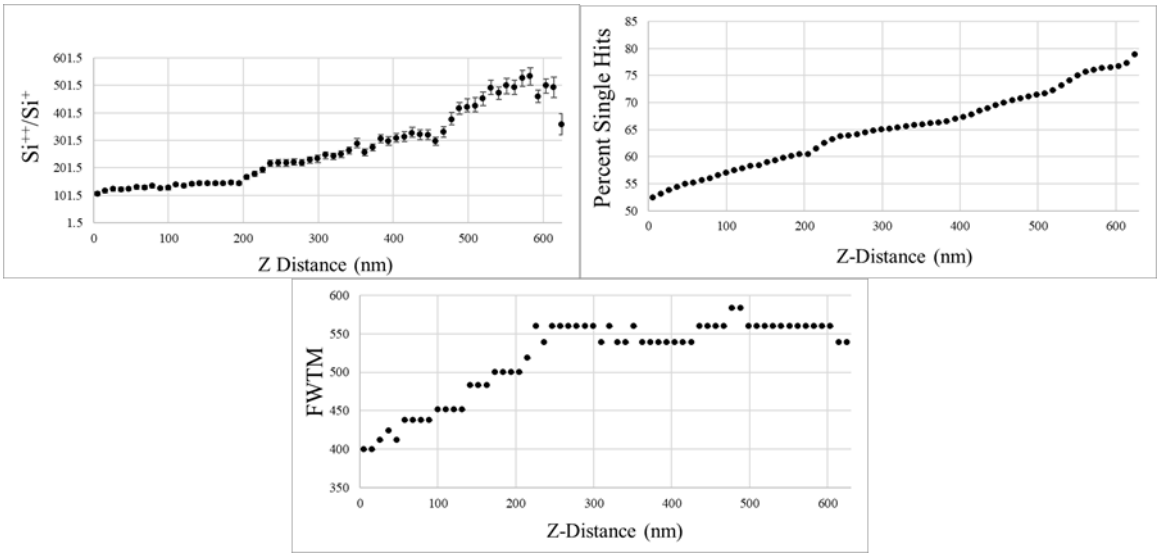


Figure 48: Si^{++}/Si^{+}, percent single hits, and Si^{++} FWTM as the tip blunts during analysis

5.7 Laser Illumination Proximity

Two specimens (A and B) were analyzed to probe the effect of laser illumination proximity on SiC APT analyses. For specimen A, the bright side of the tip yielded a multiple hit percentage of 66.5% while the dark side yielded 66.0%. For specimen B, the bright side yielded a multiple hit percentage of 67.31% while the dark side yielded a multiple hit percentage of 69.96%. Table 21 demonstrates the differences in m/q resolution between the bright and dark sides of specimens A and B.

Table 21: FWHM values for specimens A and B from both dark and bright sides of tips

	A			B		
	Bright	**Dark**	**Difference**	**Bright**	**Dark**	**Difference**
C^{+}	1200	750	450	857	600	257
Si^{++}	1556	1000	556	1167	737	430

The dark sides of both specimens demonstrate lower m/q resolution. The effect laser illumination proximity has on measured composition was also examined, however, neither of the specimens demonstrate clear compositional or field trends moving from one edge of the specimen to another.

5.8 Correlative Evaporation Histogram

A correlative evaporation histogram for a conventionally sintered SiC specimen can be found in Figure 49.

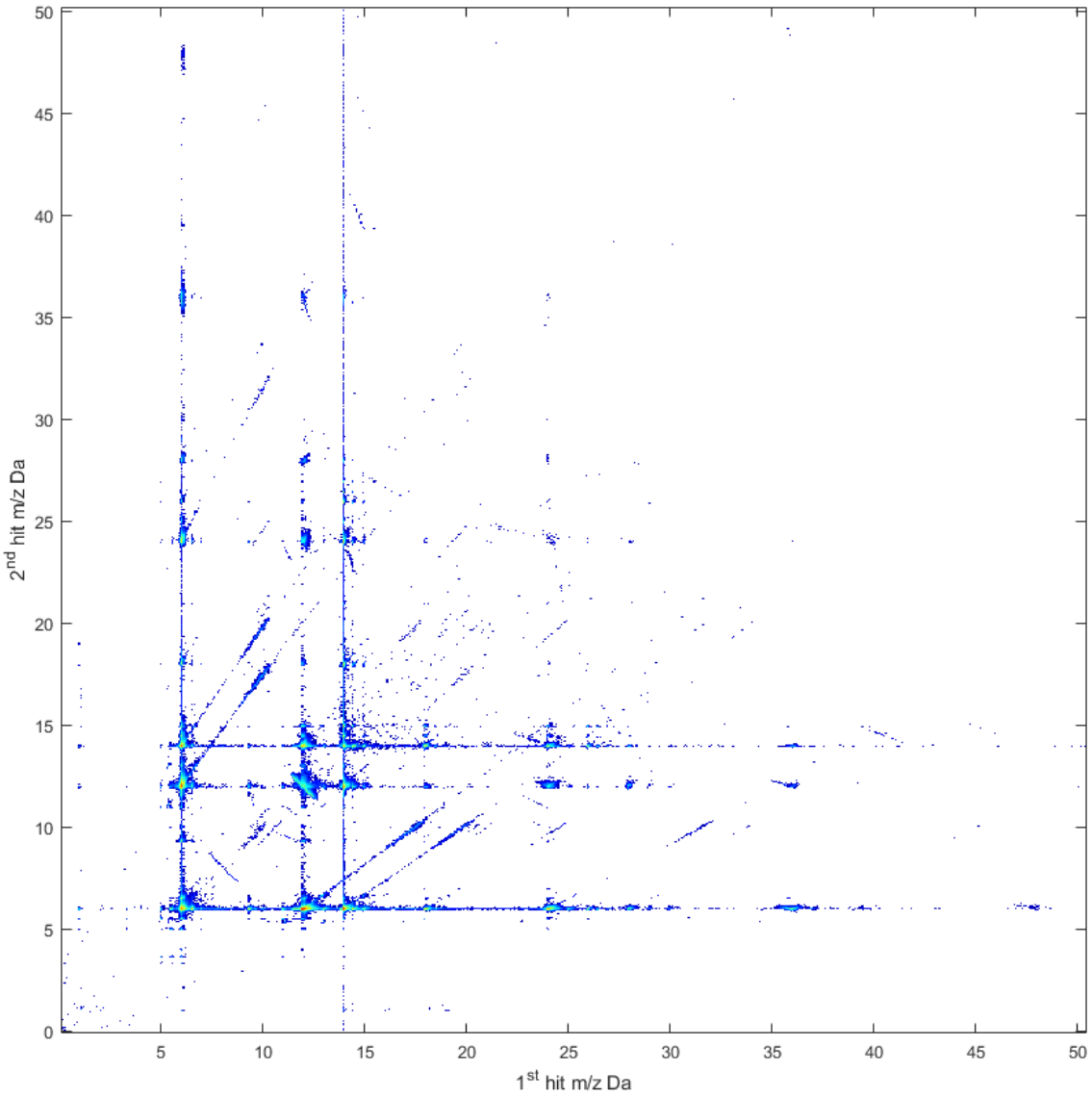


Figure 49: Correlative evaporation histogram for a conventionally sintered SiC specimen

The histogram contains several complex ion dissociation tracks which are enumerated in Table 22.

Table 22: Ion dissociation mechanisms for SiC samples

Coordinates of Track Origin	Ion Dissociation Mechanisms
(6,12)	$C_2^{3+} \rightarrow C^{2+} + C^{+}$
(9.33, 12)	$SiC^{4+} \rightarrow Si^{3+} + C^{+}$
(6, off y-axis – neutral)	$C_2^{2+} \rightarrow C^{2+} + C$
(6, 60)	$C_6^{3+} \rightarrow C^{2+} + C_3^{+}$
(12, 36)	$C_4^{2+} \rightarrow C^{+} + C_3^{+}$
(14, 42)	$Si_4^{4+} \rightarrow Si^{2+} + Si_3^{2+}$
(24, 14)	$SiC_2^{3+} \rightarrow C_2^{+} + Si^{2+}$
(14, 18)	$SiC_3^{4+} \rightarrow Si^{2+} + C_3^{2+}$

The third mechanism from the top of the table is of interest because it provides direct evidence of neutral species formation. The second, third, fourth, fifth, and sixth tracks are of interest because they provide evidence of complex ions that overlap with other species present in the analysis. For example, the tracks demonstrate the presence of C_2^{2+} ions, which have the same m/q value as C^{+} ions. If complete dissolution of these ions does not occur, the resulting overlaps would have an impact on compositional measurements. The overlaps in question are summarized in Table 23.

Table 23: Ion overlaps with direct evidence present in SiC correlative evaporation histogram

Complex Ion	Overlap Ion(s)
SiC^{4+}	B^{+}
C_2^{2+}	C^{+}
C_6^{3+}	C_2^{+}
C_4^{2+}	C_2^{+}

5.9 Sample Size

Figure 50 demonstrates the dependence of compositional uncertainty on sampling size for each of the major chemical species present in the SiC samples.

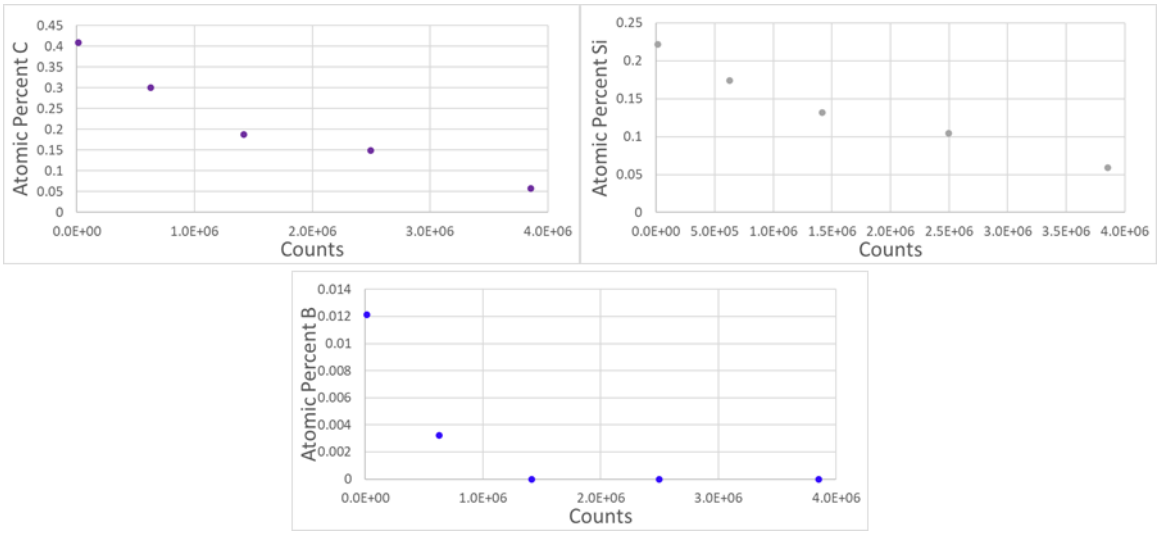


Figure 50: Compositional measurement uncertainty versus sampling size for the major species present in alumina samples

6 Discussion

6.1 Laser Energy Sweep

The laser energy sweeps demonstrate consistent trends for all material systems showing a

decreasing electric field with an increasing laser energy for each material due to an increase in thermal energy at the tip apex. Higher laser energy values also led to higher single hit percentages, possibly due to a decreased likelihood of complex ion dissociation after evaporation. 3YSZ specimens demonstrated increasing mass resolution with increasing laser energy, while SiC and alumina samples showed no discernable trends. The 3YSZ trend is contrary to trends seen in pure copper samples, but consistent with measurements made on magnesium alloys [209], [210]. Thus, the interdependence of laser energy and mass resolving power appears to be material dependent. In alumina samples, higher laser energy values yielded higher magnesium concentration measurements, perhaps due to a decreased likelihood for magnesium DC evaporation (evaporation between laser pulses caused by standing DC field) at lower electric fields. The slightly higher electric field experienced by the 150 pJ alumina sample versus the 100 pJ alumina sample was likely caused by a significant difference in tip morphology [209]. For each material, the laser energy value yielding compositional measurements closest to expected stoichiometry was used as a preferred operating condition: 40 pJ for 3YSZ, 150 pJ for alumina, and 30 pJ for SiC.

6.2 Laser Pulsing vs. Voltage Pulsing

As expected, using voltage pulsing to run SiC samples requires a significantly higher electric field compared to laser pulsing. Voltage pulsing and laser pulsing produced similar Si/C values despite the large field difference. Voltage pulsing detected a much higher proportion of single hits while producing a spectrum with significantly lower m/q resolution, in accordance with literature [165]. There are several other factors to consider when choosing between laser and voltage pulsing. Studies suggest voltage pulsing of electrically insulating materials can cause a morphing of the electric field at the tip apex which in turn broadens

the width of the pulse [211]. However, there exists consensus in the literature that voltage pulsing yields reconstructions with significantly higher spatial resolution due to elevated temperature induced surface migration occurring during laser pulsing [212]. Yet, as demonstrated by the SiC results, laser pulsing produces higher resolution m/q spectra [165]. Voltage pulsing does not suffer from the artefacts introduced by the asymmetry of laser illumination, which literature and preceding results have demonstrated have an effect on compositional measurements [153], [155]. Finally, specimen yield is far greater using laser pulsing, as only one of the sixteen specimens that were run using voltage pulsing survived long enough to produce reconstructions containing over one million ions, while laser pulsing consistently produced reconstructions containing over 10 million ions. This being the case, laser pulsing is the preferred SiC method of analysis for the remainder of this thesis.

6.3 Reflectron (LEAP 5000XR) vs. Straight Flightpath (LEAP 5000XS)

Alumina samples demonstrated more accurate compositional measurements and higher single hit percentages when analyzed using the straight flight path LEAP 5000XS. For all three materials, the LEAP 5000XS subjected specimens to lower electric fields at a given detection rate, likely due to the increased detection efficiency of the straight flight path system. 3YSZ specimens demonstrated higher single hit percentages when using the lower electric field inducing LEAP 5000XS, consistent with laser energy sweep results. Alumina samples displayed no significant difference in single hit percentages between the two machines. The LEAP 5000XS, with its higher detection efficiency and lower electric field, yielded higher magnesium compositional measurements. Although the LEAP 5000XS outperformed the LEAP 5000XR in compositional measurements for alumina samples, the

instrument was introduced to the lab after most of the alumina experiments in this thesis were complete. The LEAP 5000XR yielded spectra with higher m/q resolutions for all studied materials, likely due to its longer flightpath.

Contrary to the oxide results, the LEAP 5000XR made more accurate compositional measurements of SiC with a higher proportion of single hits. These advantages are expected due to the decreased detection efficiency of the LEAP 5000XR. Work conducted by Thuvander *et al*. demonstrates that a reduction in detection efficiency results in a reduction in the detection of multiple hit events and a resultant increase in compositional measurement accuracy when analyzing carbides [142]. Due to the high field required to evaporate carbon, carbon atoms tend to remain on the specimen surface for numerous pulses and eventually evaporate in groups during multiple hit events [143]. However, the combination of the small time periods between the arrival of these carbon atoms and the detector dead time results in a biased loss of carbon atoms [143]. Thuvander *et al*. demonstrated that by reducing the detection efficiency of an atom probe, multiple hit detection also decreases resulting in compositional measurements closer to expected stoichiometry [142]. The same phenomenon can be observed when analyzing SiC samples in this thesis. As such the LEAP 5000XR was the instrument of choice for SiC analysis.

6.4 Ranging

Generally, the most accurate compositional measurements were made when using very wide range definitions. This trend was more pronounced when analyzing using the LEAP 5000XS. This is probably due to the lower m/q resolution of the LEAP 5000XS machine. The broader peaks of the LEAP 5000XS create a more significant difference in counting

statistics when using narrower peaks. Thus, for the remainder of the thesis, wide peak definitions of full width at 1% of the maximum will be used.

6.5 Peak Overlaps

Each of the materials systems studied suffer from several m/q spectra overlaps. Fortunately, most of the overlaps can be solved and resolved. One overlap of note to consider is the carbon and magnesium peak overlap present in carbon-doped alumina specimens, as studying the distribution of carbon at grain boundaries is the motivation for this study. Magnesium is present as three isotopes, with masses of 24, 25, and 26 amu and corresponding natural abundancies of approximately 79%, 10%, and 11% respectively. Carbon is present at two isotopes with 99% present at a mass of 12 amu and 1% present at a mass of 13 amu. By measuring the ratio of the 25 and 26 peak heights to the 24 peak height, the presence of carbon can be detected if the ratios differ from the ratios expected from the magnesium natural abundancies. Furthermore, the studies conducted on SiC indicate that even at high laser energy values, comparable to the values employed to study the alumina samples, a significant proportion of detected carbon evaporates as C^{++} and appears in a m/q spectrum as a peak at 6 Da. This 6 Da peak is another aid in discriminating between magnesium and carbon.

6.6 Tip Blunting

3YSZ and alumina samples demonstrate similar trends when analyzing behavior as the tip blunts. Both materials show that as the tip becomes blunter during the experiment, the electric field necessary to maintain a constant detection rate decreases. This phenomenon is consistent with literature detailing tip blunting of metallic systems run in voltage mode; as the tip blunts, the imaged area increases leading to a higher flux at a given electric field

[165]. Therefore, to maintain a constant detection rate with an increasing imaged area, the electric field must decrease [165]. The decreasing electric field causes increasing O/Zr and O/Al ratios, increasing single hit percentages, and increasing m/q resolution. These results are consistent with trends seen when other experimental parameters decrease the electric field. The increasing O/Zr and O/Al ratios could be caused by a change in the evaporation behavior of either oxygen or Al/Zr, however it is likely the effect is a result of oxygen behavior. Aluminum has a relatively low evaporation field, and therefore would be less likely to experience loss due to DC evaporation as the field decreases [213]. However, the measured aluminum content indeed decreases as the field decreases, thereby indicating the change in O/Al value is an effect of oxygen evaporation behavior. The lower electric field may lead to a smaller probability of molecular ion dissociation and a lower resulting loss of oxygen ions. It is possible 3YSZ samples act similarly.

The Si^{++}/Si^{+} CSR plot for the SiC tip blunting analysis indicates an increasing electric field as the tip blunts, contrary to the results for 3YSZ and alumina tips. The increasing imaged area and increasing flux explanation used to explain 3YSZ and alumina behavior does not account for any thermal effects that may be influenced by a tip becoming blunt. To probe thermal effects and their dependence on the tip radius, two pre-sharpened silicon microtips (PSM) provided by Cameca were run in laser pulsed and voltage pulsed mode, and the Si^{++}/Si^{+} CSRs were tracked with single hit percentages along the duration of the run, as seen in Figure 51. The laser pulsed specimen was run using identical parameters as the tip blunting SiC experiment. The voltage pulsed specimen was run using the following parameters: a 50 K operating temperature, a 20% pulse fraction, a pulse frequency of 200

kHz, and a 0.5% detection rate.

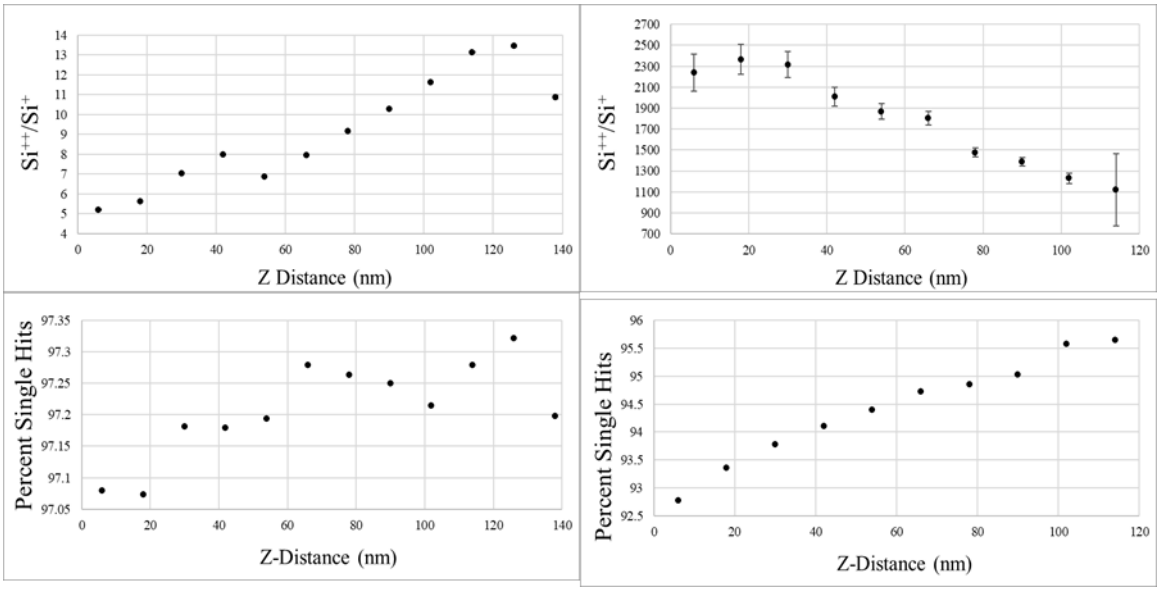


Figure 51: Tip blunting analysis for laser pulsed (left) and voltage pulsed (right) PSM

The contrast in trend between the two PSM specimens indicates thermal effects may be a key factor. Thus, thermal conductivity values for each of the studied materials at 300 K can be found in Table 24.

Table 24: Thermal conductivity values for studied materials

Material	Thermal Conductivity
Predominantly 6H SiC	60 W/m·K [214]
3YSZ	2.5 W/m·K [215]
α-Alumina	16 W/m·K [163]

As the specimen apex radius and shank angle increase, the apex temperature is reduced due to more efficient heat transfer away from the apex caused by a higher cross section and less efficient absorption [216]. For SiC and PSM samples (with higher thermal conductivities than 3YSZ and alumina), as the tip becomes blunt and the shank angle increases, the apex

temperature significantly decreases. Therefore, to compensate for this decreasing specimen temperature, the electric field must increase to maintain a constant detection rate. In the case of the 3YSZ and alumina samples, due to much lower thermal conductivities, the specimen apex does not efficiently conduct heat away from the specimen apex even with a larger radius and cross section. Furthermore, due to the less conductive nature of the specimens, it is likely the tip end-forms become more asymmetric in the case of 3YSZ and alumina samples. This asymmetry results in smaller effective shank angles, causing more efficient absorption of thermal energy from the laser pulse [216]. Therefore, the specimen apex temperature does not significantly drop during the experiment, and the increased flux mechanism dominates necessitating a drop in electric field to maintain the constant detection rate. The increasing proportion of single hits detected as the field increases for SiC samples is inconsistent with the field trends found in the laser energy sweep, yet consistent with the field trend observed when the effective field increases between a laser pulsed experiment and a voltage pulsed experiment. It is possible that there are two competing mechanisms present: the first being an increasing field is more likely to cause complex ion dissociation, and the second being an increasing field is less likely to cause species with high evaporation fields (such as carbon) to build up on the specimen surface and evaporate as multiples. The latter may dominate as the field increases due to a blunting tip.

6.7 Laser Illumination Proximity

Although the CSRs for each material did not demonstrate clear trends moving from the dark to light side of the studied tips, there exists consensus in the literature that the dark side of a laser run tip will yield a higher electric field. This increased field occurs due to blunting of the warmer bright side and a resulting higher shank angle on the dark side [153], [155]. One

of the two 3YSZ specimens studied and one of the two alumina specimens studied demonstrated increased measured oxygen content and single hit percentages moving towards the bright side (ostensibly the direction of decreasing electric field) of the specimen. These trends are consistent with a decreasing electric field as demonstrated by the other analyses in this chapter. However, the m/q resolution increases towards the dark side of these specimens, contrary to expectation as the electric field increases. This is perhaps due to the higher temperatures achieved at the bright side yielding larger thermal tails.

The laser proximity analyses for SiC did not demonstrate as clear trends in terms of multiple hits or composition as the 3YSZ and alumina analyses. This provides further evidence for the theory regarding the difference in field trend as SiC specimens blunt compared to 3YSZ and alumina samples. The less evident differences in composition and single hit percentages between the dark and bright side of SiC tips could be the direct result of less asymmetry due to higher thermal conductivity.

6.8 Correlative Evaporation Histogram

The importance of systematic differences in field and therefore multiple hit propensity is highlighted by the correlative evaporation histogram analyses. Many of the tracks from the oxide histograms yield the formation of either charged oxygen atoms or charged oxygen dimers. Therefore, there exists a distinct possibility for the occurrence of neutral oxygen atom or dimer formation in route to the detector leading to systematic loss [171]. Furthermore, the alumina histogram demonstrates direct evidence of the formation of a neutral containing oxygen. These phenomena could explain the overarching trend of an increasing field leading to a decreasing measured oxygen content for 3YSZ and alumina.

Experimental and theoretical work conducted on GaN analyzed using laser assisted atom probe similarly posit neutral formation contributes to nonstoichiometric reconstructions [160]. However, the trends observed during the GaN analysis do not match the trends observed with the 3YSZ and alumina samples. In the study conducted by Gault *et al.*, the composition of measured nitrogen increases as the field increases, whereas the measured concentration of oxygen decreases as the electric field increases during 3YSZ and alumina analysis [160]. Gault *et al.* propose that nitrogen neutrals formed from dissociation are less likely to be ionized by a weaker electric field after evaporation, and therefore more likely to remain a neutral and not register as a hit after flight [160]. It is possible that there are two competing mechanisms present. Firstly, a higher electric field is more likely to cause molecular ion dissociation leading to the formation of an oxygen or nitrogen neutral. However, a higher electric field is more likely to cause ionization of these oxygen or nitrogen neutrals after evaporation, leading to a registered hit. The first mechanism may dominate in the case of 3YSZ and alumina, leading to a conflicting trend observed during GaN analysis.

The SiC correlative evaporation histogram provides evidence of two sources of carbon loss in addition to pile-up/dead time effects: evidence of neutral carbon atoms resulting from ion dissociation and evidence of C_2, C_3, C_4, and C_6 ions that cause m/q spectrum overlaps. However, due to the relatively weak intensities of the dissociation tracks, it is likely the pile-up/dead time effect dominates.

6.9 Sample Size

Each of the sample size comparison analyses demonstrates a significant decrease in measurement uncertainty values as sample sizes increase. It is important to note, however,

that the estimation of uncertainty used in this analysis is almost certainly an underestimation. The uncertainty reported in this thesis is dominated by the uncertainty resulting from the maximum likelihood estimation used to resolve spectrum peak overlaps [206]. Several other significant sources of uncertainty exist, such as misidentification of peaks, preferential evaporation effects, detector pile-up issues, ion dissociation, and more [160], [174], [206], [217], [218]. These sources of uncertainty, however, are considerably more difficult to quantify.

7 Conclusions

In this chapter, the effects APT analysis conditions have on data quality were probed to develop best practices for analyzing 3YSZ, alumina, and SiC. It is the author's hope that the trends revealed in the study can be applied as guidelines to the analysis of other ceramics/bulk insulators. The ranging and peak overlap considerations and practices are summarized into the following composition measurement procedure:

1. Manually identify the location of peaks in the m/q spectrum of a data set.
2. Use the methodology and software developed by Haley *et al.* to determine the most likely ionic identity of each peak and note potential overlaps [174].
3. Fit each peak using pseudo-Voigt curves.
4. Range each peak using the full width at 1% of the maximum as range bounds.
5. Employ AtomProbeLab v0.2.2 to resolve peak overlaps and determine atomic composition [205], [206].

Unless otherwise stated, this procedure will be used for all compositional measurements in this thesis. The analysis in this chapter also indicates that to quantify subtle differences in composition between different samples, one must carefully consider the systematic effects

tip blunting, laser illumination proximity, and sampling may have on measurement quality and uncertainty. These effects may not always be consistent, as the effects laser illumination proximity and tip blunting have on compositional measurements appear to be specimen-dependent, most likely based upon the morphology of the tip apex formed during FIB milling and specimen thermal conductivity. One effective way to avoid artefact interference during compositional measurement comparisons is to report the electric field, using CSR values, that the ions from a measurement were subjected to during field evaporation. In so doing, a more consistent comparison can be achieved. Additionally, the systematic dependence of aluminum composition in alumina, zirconium composition in 3YSZ, and silicon composition in SiC can be exploited. Because the composition of these elements varies in a systematic and known manner with the electric field at the tip apex, the composition of solute atoms can be reported as a ratio to these elements. For example, the composition of magnesium within in the bulk of an alumina grain can be reported as a Mg/Al measurement instead of an atomic percent of magnesium measurement. This approach would also enable measurements to account for differences in electric field at the tip apex. However, modern atom probe software systems allow data to be collected at a constant CSR instead of at a constant detection rate. The laser energy used during analysis and the detection rate are varied to maintain a chosen CSR. By using these software tools and reporting CSRs of measurements, experimental reproducibility can be enhanced. Therefore, for the remainder of this thesis, whenever the bulk compositions of different ROIs are being compared, the average electric field of the ions in the ROI will also be reported for comparison. The 3YSZ and alumina analyses generally indicate measurements closer to expected oxygen content occur at lower electric fields. Using new CSR tracking features and knowledge of the effect

electric field has on oxygen content, future experiments can operate in electric field regimes conducive to accurate compositional measurements.

Reporting the CSR of a measurement can help mitigate the effects of laser illumination proximity. Additional steps can also be taken. When possible, measurements originating from the center of a specimen, away from the extreme dark and bright side of tips are preferred. Large shank angle specimens facilitate faster cooling of the tip apex, and can therefore lead to less asymmetry [219]. Surface modification of the specimen apex using conductive coating can also lead to more symmetric end forms, but this process is time and resource intensive [153]–[155].

Finally, it is important to note that small ROIs (small sampling) can lead to significant uncertainty in compositional measurements and should be a careful consideration before employing APT to measure subtle compositional differences between small microstructural features.

Chapter V

Alumina Analysis

1 Results

1.1 SEM Characterization

Previous studies have demonstrated a qualitative difference in fracture surfaces between undoped and carbon-doped alumina samples, but a quantitative analysis was not conducted [27], [28]. Therefore, using the grid overlay method detailed in Chapter III, the effect carbon doping has on percent transgranular fracture for alumina samples was investigated to probe the effect of carbon doping on grain boundary strength. The results of this analysis can be seen in Figure 52. Each of the specimens studied also contained 0.25 wt% MgO and were sintered under vacuum in a graphite powder bed.

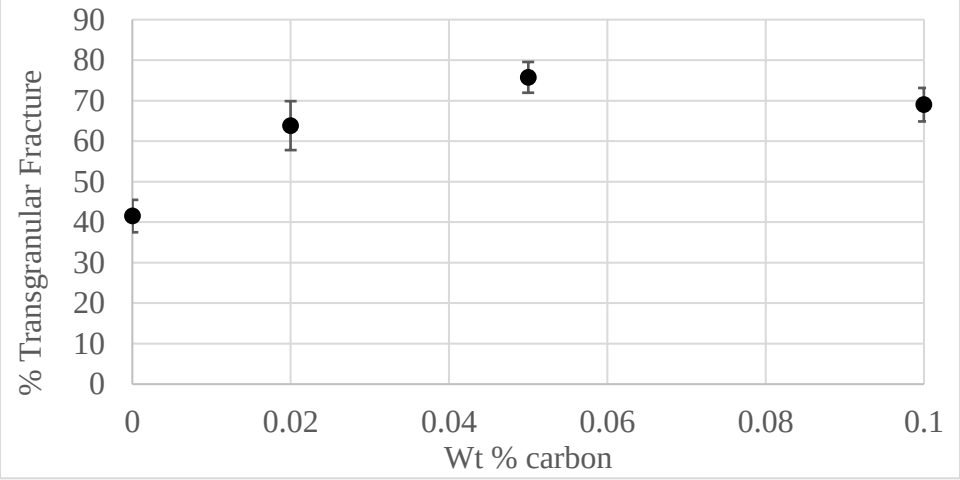


Figure 52: Percent transgranular fracture versus weight percent carbon doping

A maximum percent transgranular fracture exists at 0.05 wt% carbon doping. The sintering environment to which the alumina samples, with and without carbon, were subjected also

had a significant effect on percent transgranular fracture, as evident in Figure 53. Each of these samples also contained 0.25 wt% MgO.

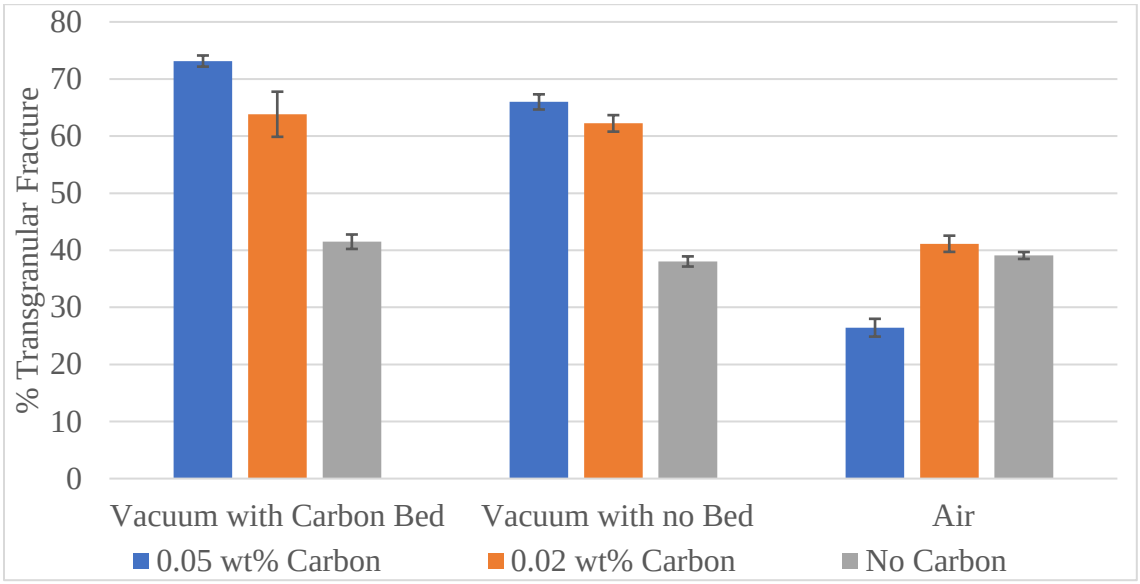


Figure 53: Percent transgranular fracture versus sintering conditions for specimens doped with varying amounts of carbon

The carbon-doped specimens sintered in strong reducing environments show the highest proportion of transgranular fracture. Along with changes in grain boundary strength, dopants can also cause changes in alumina grain boundary mobility, leading to differences in grain morphology following sintering [9], [220]–[224]. Therefore, the effect of carbon doping and sintering environment on grain size was studied, and the results can be seen in Table 25.

Table 25: Effect of doping and sintering conditions on grain size

Specimen Type	Grain Size (μm)
0.25 wt% MgO vacuum	1.47 ± 0.03
0.25 wt% MgO + 0.05 wt% C vacuum	1.65 ± 0.04
0.05 wt% C vacuum	1.59 ± 0.04
pure vacuum	1.72 ± 0.05
pure air	4.61 ± 0.13

Carbon doping along with a reducing environment have significant effects on alumina grain size. Previous studies have shown grain size can have a significant effect on transgranular fracture percentage in alumina [225]. Therefore, it is possible the increased prevalence of transgranular fracture in carbon-doped specimens could be linked to slightly larger grain size achieved when carbon is added to magnesia doped specimens in a vacuum. To probe this possibility, the fracture surfaces of pure alumina samples subjected to sintering times ranging from one hour to five hours at 1500ºC were studied alongside measurements of grain size. This analysis can be found in Figure 54.

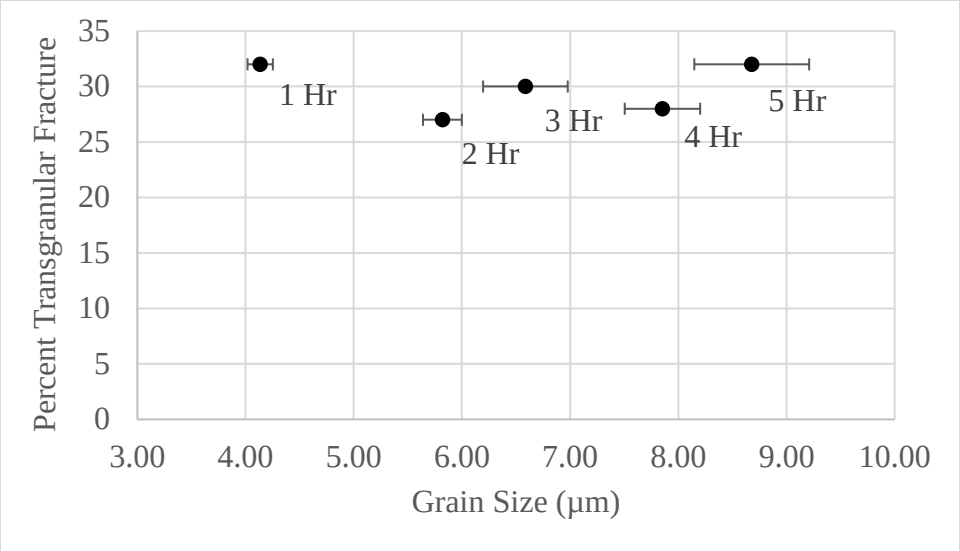


Figure 54: Effect of grain size on percent transgranular fracture for pure specimens sintered in air.

No trend is evident in the grain size regime shown above. Shorter sintering times or lower sintering temperatures would need to be probed to achieve grain sizes comparative to the samples in Table 25 when sintering in air without magnesia. However, careful examination of the results in Table 25 demonstrate that despite having a larger grain size than the carbon-doped specimen, the pure alumina sample sintered in a vacuum did not demonstrate a higher proportion of transgranular fracture. Therefore, the lack of trend seen in Figure 54 may extend into the grain size regime of the carbon-doped and undoped samples sintered in a vacuum.

1.2 Grain Boundary Relative Energy Analysis

Grain boundary relative energy measurements using AFM were conducted on samples doped with 0.05 wt% carbon and 0.25 wt% MgO and samples doped with only 0.25 wt% MgO. Experiments were conducted using both contact mode and ACAFM mode. Experiments were conducted on samples which were polished and thermally etched under vacuum at 1400ºC for 3 hours, 5 hours, and 10 hours using ACAFM mode. Cumulative

distribution plots for these analyses can be seen in Figure 55.

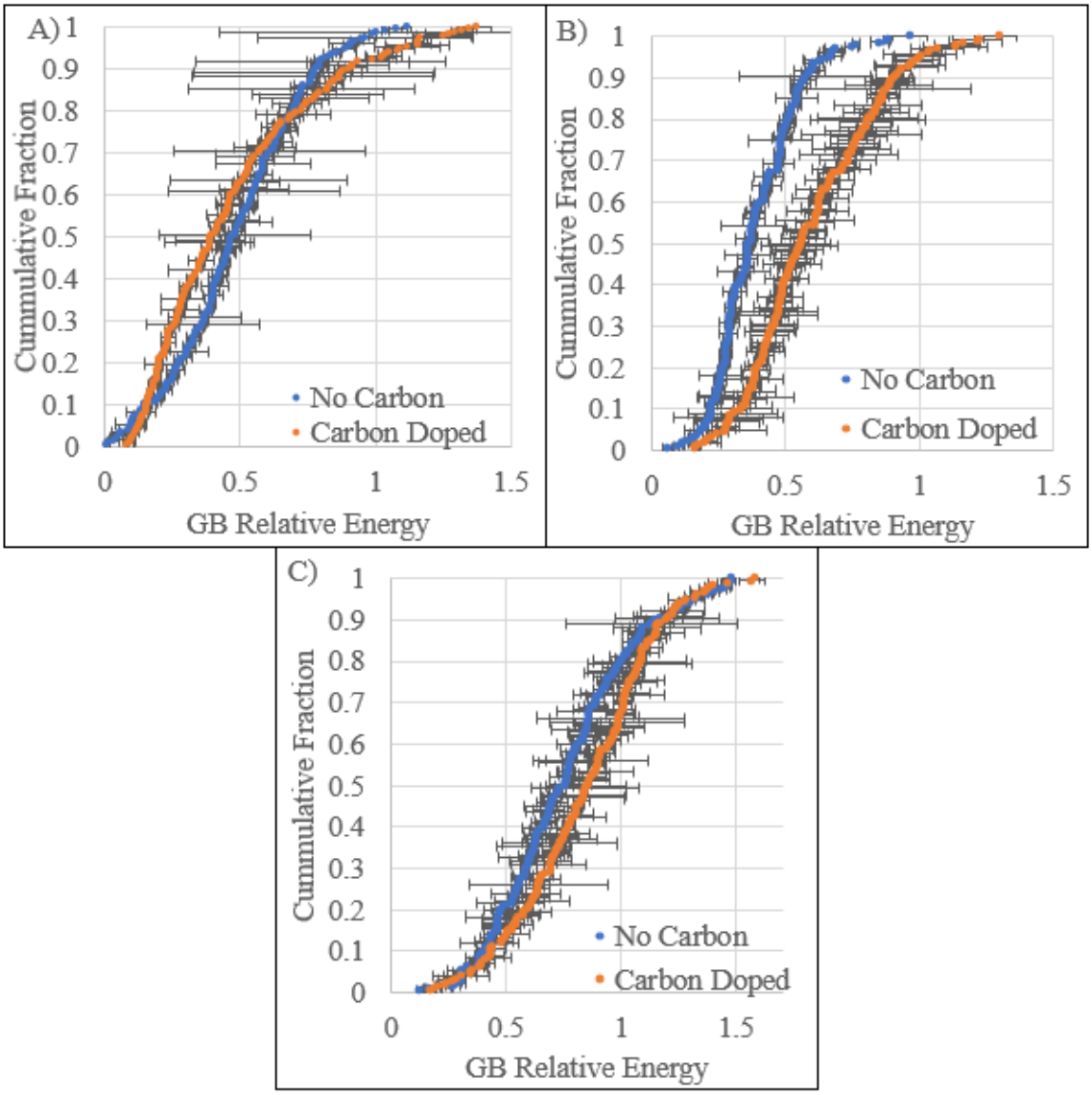


Figure 55: Grain boundary relative energy measurements for specimens doped with only 0.25 wt% MgO and specimens doped with 0.25 wt% MgO along with 0.05 wt% C. A) 3 hour thermal etch, B) 5 hour thermal etch, C) 10-hour thermal etch.

The amount of time the specimens are annealed has a significant effect on the difference in grain boundary relative energy between carbon-doped and non-carbon-doped specimens. The effect of operating mode, contact mode or ACAFM mode, on grain boundary relative energy measurements was also investigated. This comparison for specimens etched for 5 hours at 1400ºC in a vacuum can be found in Figure 56.

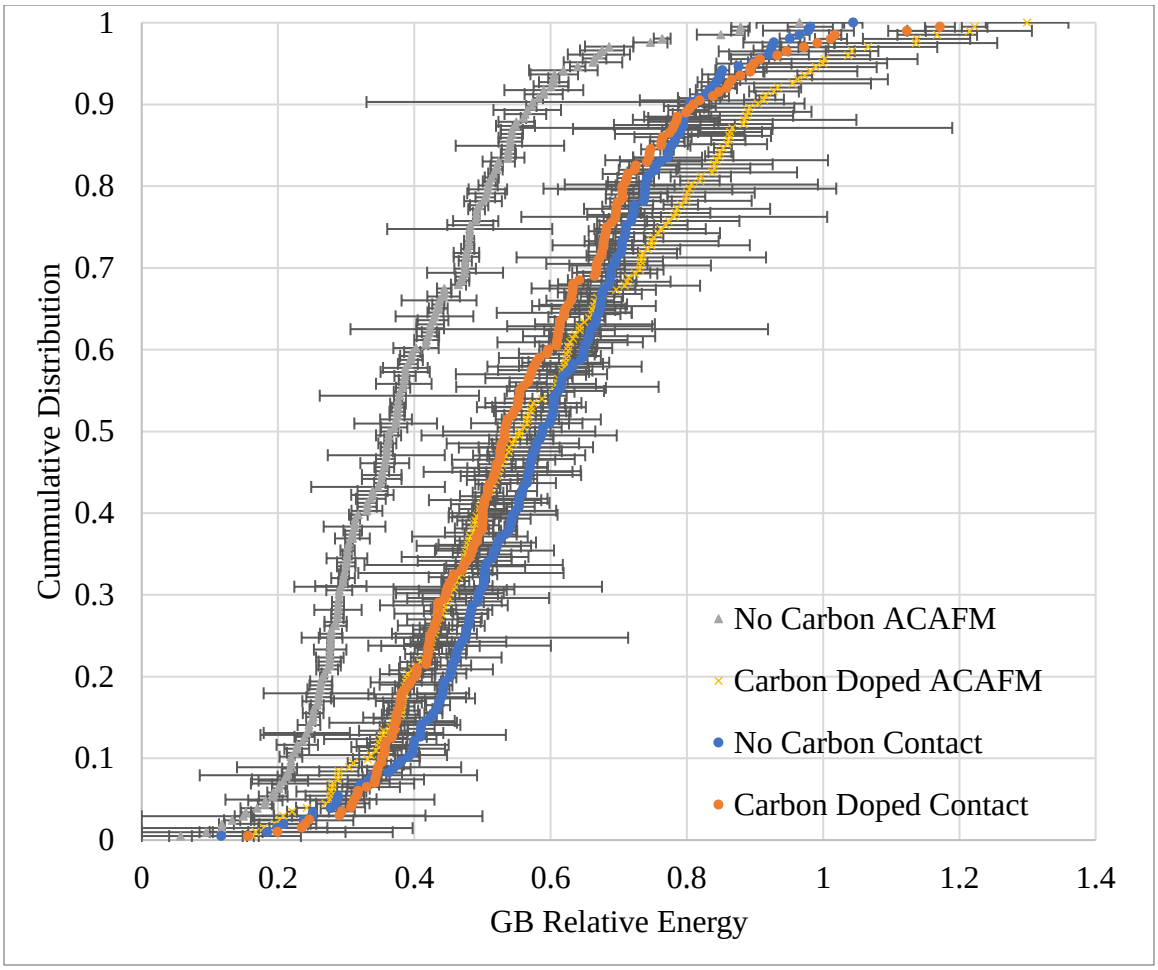


Figure 56: Grain boundary relative energy measurements made using contact mode and ACAFM mode for specimens doped with only 0.25 wt% MgO and specimens doped with 0.25 wt% MgO along with 0.05 wt% C

A significant difference exists between carbon-doped and non-carbon-doped grain boundary relative energy measurements when using ACAFM mode, however the difference becomes insignificant when using contact mode. A comparison in image quality between contact mode and ACAFM mode can be seen in Figure 57.

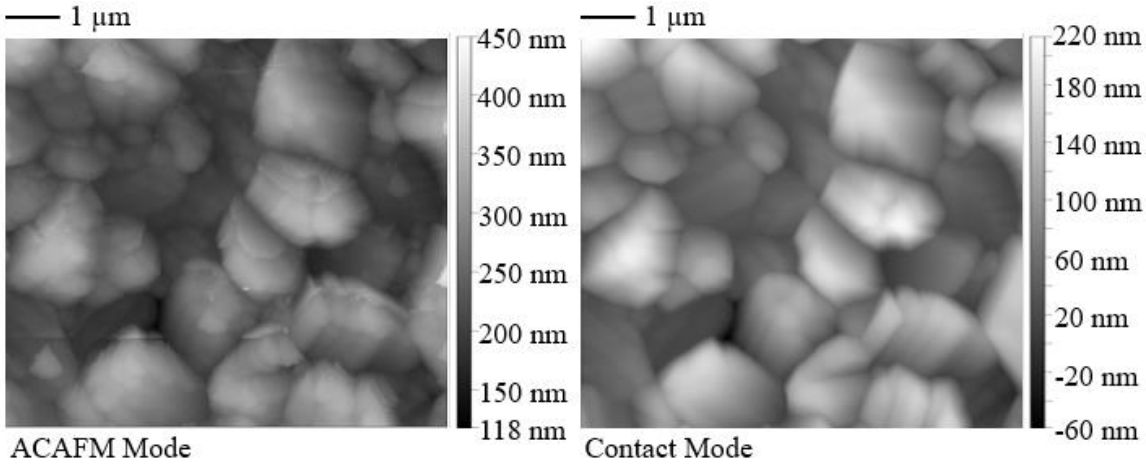


Figure 57: Image quality comparison between ACAFM mode and contact mode

The analysis conducted using ACAFM mode reveals more detail of the specimen surface.

1.3 STEM Analysis

A sample doped with 0.05 wt% carbon and 0.25 wt% MgO sintered in vacuum within a graphite powder bed was analyzed using a JEOL ARM-200F STEM. ADF images of grain boundaries at several magnifications can be seen in Figure 58.

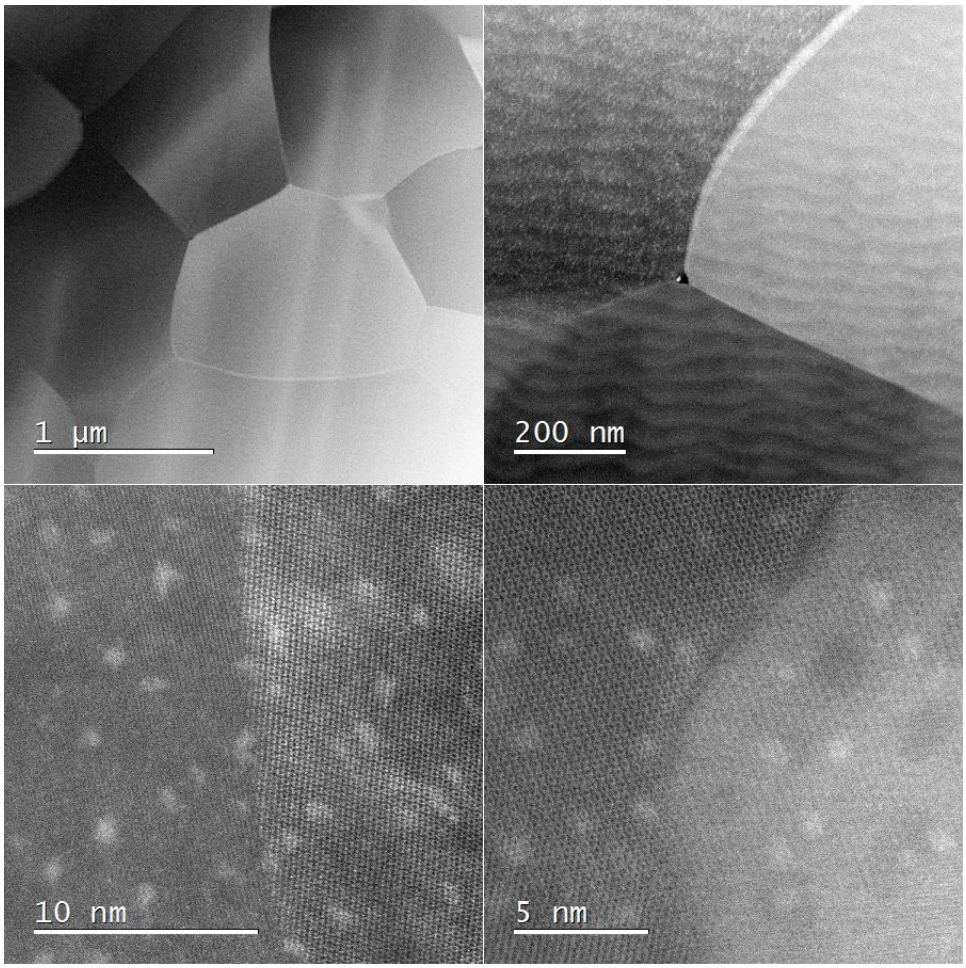


Figure 58: STEM ADF images of grain boundaries in carbon-doped alumina sample

The high contrast regions in the bottom two images are the result of gallium implantation damage from FIB specimen preparation. The samples show no evidence of unique structuring at grain boundaries caused by the carbon doping, such as the formation of thin films. EDS and EELS analysis were also used to study the chemical distribution across grain boundaries, however maps from both techniques showed no significant segregation to grain boundaries.

1.4 Atom Probe Analysis

1.4.1 Bulk Analysis

To measure the bulk composition of grains, rectangular ROIs were positioned away from

microstructural features such as grain boundaries and FIB ion implantation regions. The composition of each ROI was then calculated alongside the Al^{+++}/Al^{++} CSR. The results of this analysis can be seen in Figure 59.

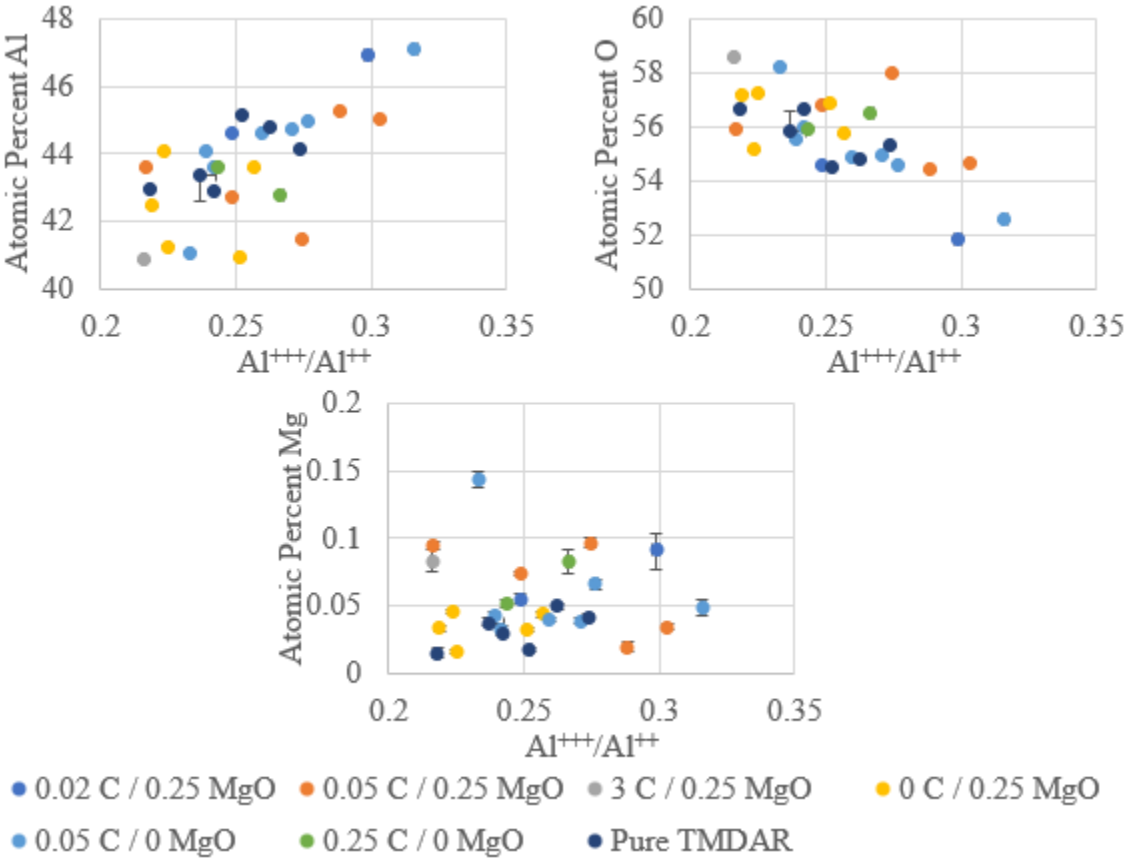


Figure 59: Bulk compositional measurements for alumina samples with varying levels of carbon and MgO doping

No evident trend is visible between specimen doping and bulk composition. The trends observed for oxygen and aluminum content as the aluminum CSR increases are consistent with the trends observed in Chapter IV.

1.4.2 Grain Boundary Analysis

As discussed in Chapter IV, the mass spectrum peak overlap existing between carbon and magnesium peaks is important to consider when analyzing alumina atom probe data, as the distribution of carbon at grain boundaries is the motivation for this study. Therefore, an

analysis was conducted to track the change in peak intensities corresponding to isotopes of magnesium and carbon to probe the likelihood of the presence of carbon alongside magnesium at grain boundaries. Two different types of carbon were used as dopants. The first powder contained carbon with assumed natural isotopic abundance: 98.9 at% C_{12} and 1.1 at% C_{13}. The second powder contained 99 at% C_{13} and 1 at% C_{12}. A grain boundary demonstrating only magnesium segregation would be expected to demonstrate a m/q spectrum with peaks at 12 Da, 12.5 Da, and 13 Da (as well as weaker peaks at 24, 25, and 26 Da) with relative intensities corresponding to the natural isotopic abundancies of magnesium: 79.0 at% at 12 Da, 10.0 at% at 12.5 Da, and 11.0 at% at 13 Da. If a specimen were doped with the graphite powder containing a majority of C_{12}, the intensity of the 12 Da peak would grow in relation to the other peaks, while the 13 Da peak would also gain a small number of counts. If a specimen were doped with the graphite powder containing a majority of C_{13}, the intensity of the 13 Da peak would grow in relation to the other peaks, while the 12 Da peak would gain a small number of counts. In both cases, the peak at 12.5 Da would not significantly change assuming the contribution of a peak created by a C_{12} ion and a C_{13} ion evaporated together with a 2+ charge is insignificant. Therefore, for specimens doped using the majority C_{12} powder, the ratio of counts under the peak at 12.5 Da to the counts under the peak at 12 Da would be expected to be smaller than the ratio if only magnesium was present. For specimens doped using the majority C_{13} powder, the ratio of the counts under the peak at 12.5 Da to the counts under the peak at 13 Da would be expected to be smaller than the ratio if only magnesium is present. These ratios were therefore calculated for ROIs isolating ions found at grain boundaries, and the percent difference between the expected ratio if only magnesium were present can be seen in Table 26. A negative percent

difference would indicate the presence of carbon.

Table 26: Carbon and magnesium grain boundary overlap analysis

C wt%	MgO wt%	% Change 12.5 / 12	% Change 12.5 / 13
0	0.25	40.7 ± 82.7	
0	0.25	100.6 ± 33.7	
0	0.25	-59.9 ± 27.4	
0	0.25	55.0 ± 8.7	
0.05	0.25	34.2 ± 19.2	
0.05	0.25		-48.2 ± 22.3
0.05	0	14.3 ± 14.2	
0.05	0	-20.8 ± 9.4	
0.05	0	43.6 ± 17.9	
0.05	0	4.9 ± 5.7	
0.25	0	-7.4 ± 12.7	
0	0	-14.0 ± 14.1	
0	0	-30.6 ± 11.7	
3	0.25		65.3 ± 37.0

The results in Table 26 do not demonstrate evidence of carbon segregation to grain boundaries in carbon-doped alumina samples. Negative 12.5/12 Da ratios and 12.5/13 Da ratios are not unique to carbon-doped specimens, and many carbon-doped samples show positive ratios. The somewhat random distribution of negative and positive count ratios is likely the result of random fluctuation in the noise contributing to counts under the small peaks at 12.5 Da. Furthermore, none of the grain boundaries studied demonstrated peaks at

6 Da, further evidence that carbon is not present at grain boundaries in alumina samples. The large errors present in this analysis are likely the result of small peak intensities at 12.5 Da compared to local background. Figure 60 demonstrates Gibbsian interfacial excess measurements at alumina grain boundaries. Following the results from the analysis in Table 26, it was assumed no carbon was present at grain boundaries, and the peaks which overlap between carbon and magnesium were assumed to contain only magnesium ions.

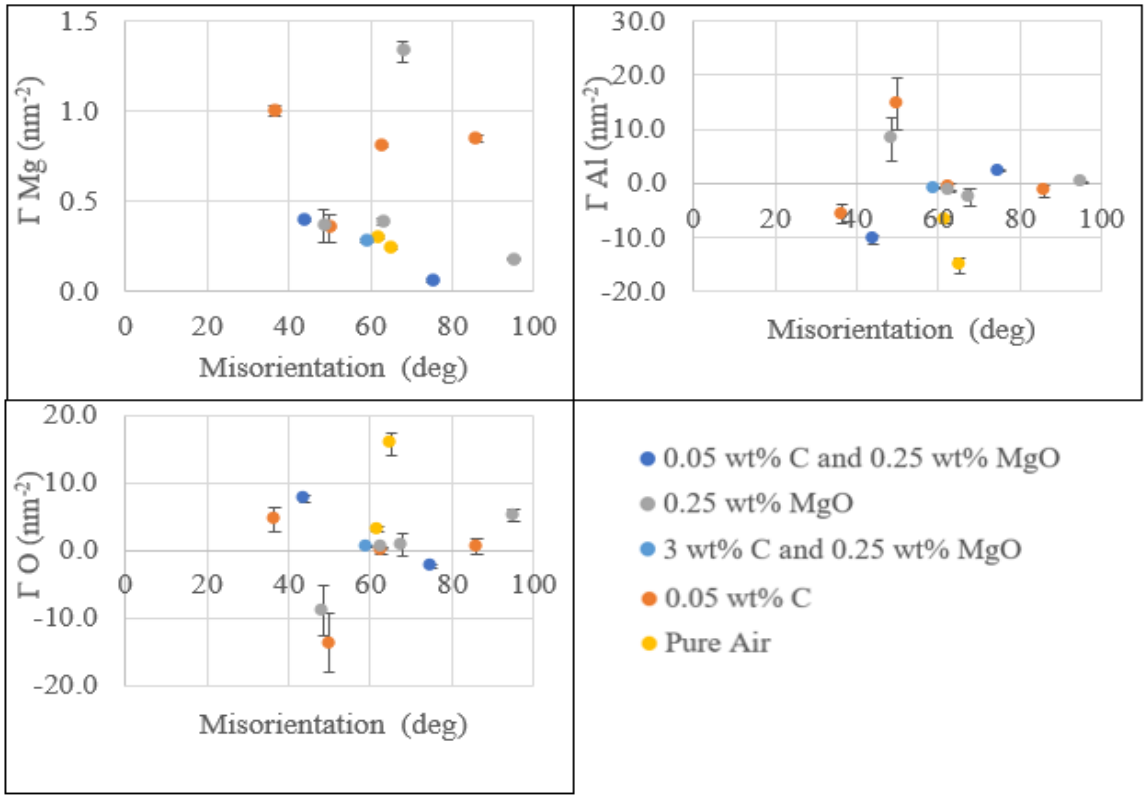


Figure 60: Grain boundary Gibbsian interfacial excess measurments versus grain boundary misorientation in alumina samples

There are no evident trends in the interfacial excess measurements between specimens with different doping levels or between grain boundaries with different misorientation values. All the studied boundaries demonstrate Mg segregation. The two boundaries demonstrating strong oxygen depletion and aluminum enrichment may be special boundaries, yet the software used to analyze misorientiation did not identify them as such.

1.4.3 Triple Point Analysis

One triple point in a specimen doped with only 0.25 wt% MgO was analyzed using APT. The ions at the triple point were isolated using a rectangular ROI, and chemical analysis can be seen in Figure 61.

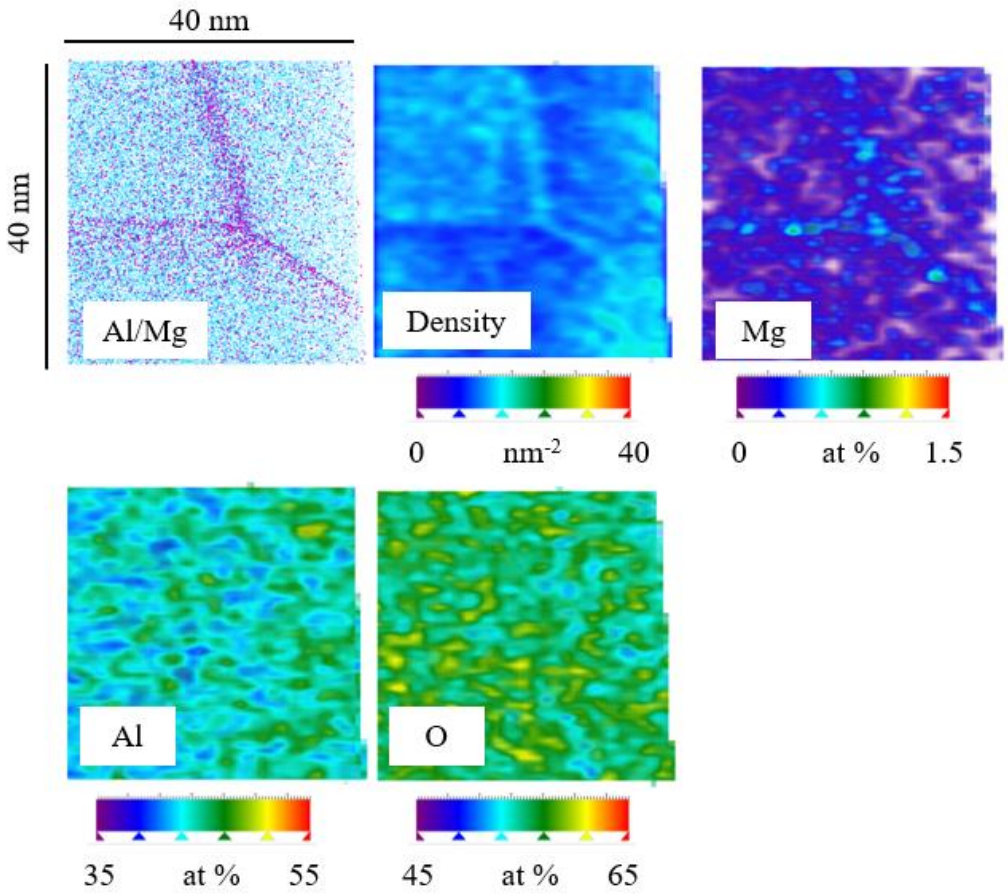


Figure 61: Triple point analysis for a sample doped with 0.25 wt% MgO sintered under vacuum. The depth of the ROI is approximately 50 nm. The ion map shows magnesium ions in purple and aluminum ions in blue. The remainder of the maps are volume renderings of density and chemical species concentration.

The ion map and the magnesium concentration volume rendering demonstrate uniform magnesium segregation to the grain boundaries and the triple point. There is no clear enrichment or depletion of aluminum or oxygen at the triple point.

2 Discussion

2.1 SEM Characterization

Carbon doping significantly increases the likelihood for transgranular fracture to occur in the studied alumina samples. This analysis combined with previous results demonstrating reduced grain pull-out during wear testing and improved microcantilever strength with grain boundaries along the length of the cantilever suggest carbon doping has a strengthening effect on alumina grain boundaries [4], [27], [28]. This conclusion is strengthened by the results shown in Figure 53. The carbon-doped specimens demonstrate higher levels of transgranular fracture when sintered in the strongest reducing atmosphere when the doped carbon is least likely to become oxidized during sintering. The pure samples show little change in transgranular fraction proportion regardless of sintering environment, indicating the sintering environment alone is not the cause of the fracture mode transition.

The average grain size of the carbon and magnesium specimen sintered under vacuum is slightly larger than the grain size of the specimen doped with only magnesium sintered under vacuum. Although previous studies on alumina have demonstrated larger grained alumina is more likely to fracture transgranularly, the results in Figure 54 show no discernable relationship between grain size and percent transgranular fracture [225]. In a study conducted by Mussler *et al.*, the transgranular proportion of fracture decreases more significantly at lower grain sizes than at higher grain sizes, and the grain sizes analyzed in Figure 54 are larger than the specimens doped with carbon and alumina sintered under vacuum [225]. Therefore, it is still possible the transition towards more transgranular fracture in carbon-doped samples is linked to an increased grain size. However, this

phenomenon cannot sufficiently explain the improvements to wear resistance, flexural strength, and fracture toughness demonstrated by carbon-doped specimens. Specifically, microcantilever testing of grain boundaries in carbon-doped and undoped specimens conducted by Noor demonstrated increase strength when carbon-doping has occurred [28]. This phenomenon cannot be explained by a grain size effect.

2.2 Grain Boundary Relative Energy Analysis

The grain boundary relative energy analysis conducted in this thesis demonstrates the importance of carefully considering the suitability of analysis techniques and sample preparation to individual materials systems. The difference in relative energy distributions between carbon-doped and undoped specimens is dependent upon the amount of time specimens are annealed for. No studies in literature were found regarding the effect annealing time has on grain boundary relative energy measurements on magnesium or carbon-doped alumina; however, one study did analyze the effect annealing temperature had on yttria doped alumina [53]. Grain boundary relative energy values of yttria doped alumina increased with increasing annealing temperature due to the formation of secondary yttrium aluminum garnet (YAG) phases depleting yttrium from grain boundaries [53]. The carbon-doped and undoped specimens in this thesis also demonstrate increasing relative energy measurements with increasing sintering time, however SEM and APT analysis found no evidence of secondary phases rich in magnesium or carbon that would cause boundary depletion. This lack of a secondary phase along with an increasing grain size resulting from longer annealing would likely cause increased magnesium or carbon content at grain boundaries [226]. The change in the relative difference in energy distributions between carbon-doped and undoped specimen as the annealing time increases is a potent potential

source of erroneous analysis/conclusion. The analyses conducted on specimens annealed for 3 hours and 10 hours demonstrate an insignificant difference in grain boundary relative energy for carbon-doped and undoped specimens, while the 5 hour annealed specimens demonstrate a significant difference. It is possible a complexion transition occurs at timescales between the different annealing time periods, however the implication for unannealed specimens remains ambiguous. It would therefore be difficult to draw any significant conclusion regarding the effect of carbon doping on grain boundary energy from these results. Many analyses from literature only consider distributions obtained from one annealing temperature and timescale treatment [49], [52], [227]. These studies may suffer from similar ambiguity when analyzed at different annealing timescales. The results in this thesis demonstrate the importance of sensitivity testing of annealing conditions when comparing differently doped samples using AFM grain boundary grooving techniques.

The effect AFM operation mode has on relative energy measurements is also significant. Contact mode is most often employed when making grain boundary relative energy measurements of hard ceramic materials, as it benefits from high scan speeds and higher resolutions [228]. However, Figure 57 demonstrates a slightly more detailed image of grain surfaces resulting from ACAFM mode. When using contact mode, lateral forces due to friction caused by particularly rough surfaces can lead to degraded lateral resolution [228], [229]. The surfaces studied in this thesis are considerably rougher than other AFM grain boundary relative energy studies from literature [6], [49], [52], [53], [198]. Figure 62 showing a two-dimensional AFM image along with a three-dimensional reconstruction of the surface demonstrates the highly faceted nature of the specimens annealed in vacuum.

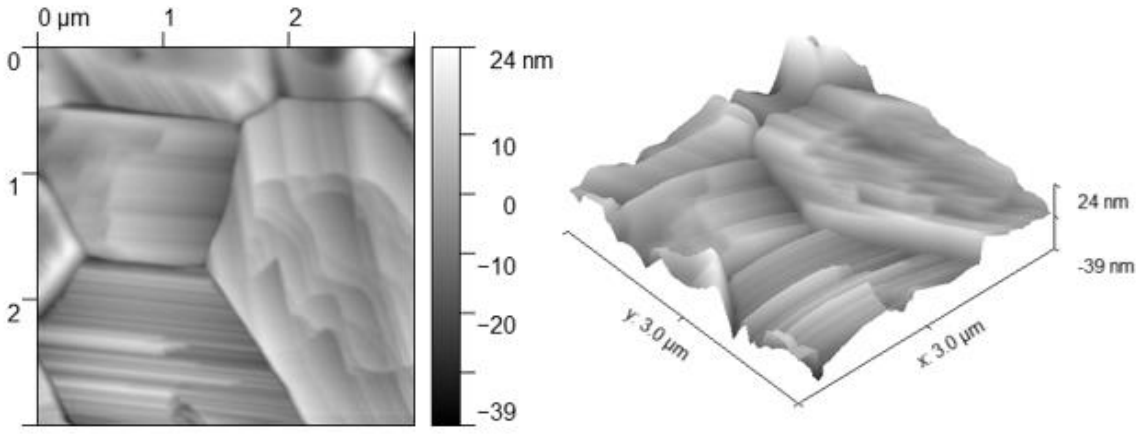


Figure 62: AFM image demonstrating highly faceted surface of alumina grains after annealing in vacuum

Not only is it possible that the highly faceted and rough nature of the grain free surfaces following annealing can affect lateral resolution during AFM inspection, but the surface roughness also contradicts key assumptions of relative energy measurement theory. The equation used to calculate grain boundary relative energy from groove depth and width discussed in Chapter III of this thesis requires several important assumptions [49]. Two of these assumptions are that the surface energy is isotropic and equivalent on either side of the groove [49], [230]. The highly faceted nature of the alumina surfaces demonstrates the invalidity of these assumptions. To overcome this obstacle, it is recommended over 100 boundaries should be examined and mean values along with widths of the distribution, as displayed by cumulative distribution plots, should be used to compare samples. These metrics are reported as reproducible measurements of a sample [230]. It is possible, however, that the extreme anisotropy of the alumina surfaces resulting from thermal grooving in a vacuum requires a significantly higher number of boundaries than one hundred to produce comparable statistics. Or a more extreme conclusion may be that materials undergoing significant surface reconstruction during thermal grooving are not suitable for this type of analysis. It is clear however, sensitivity testing of grain boundary relative energy

measurements to thermal grooving conditions and AFM analysis mode is an important data quality check. These results indicate either any potential difference in relative energy caused by carbon doping is too small for clear characterization using this specific technique, or there exists no significant difference in grain boundary energy when carbon doping occurs.

A novel technique developed by Ni *et al*. used FIB cross sectioning combined with SEM imaging to directly image and measure dihedral angles formed by thermal etching, avoiding inaccuracies introduced by surface faceting [200]. This technique could be applied to the current work, however the time intensive nature of such a process would likely prove unfeasible when considering the large number of boundaries necessary to facilitate a significant comparison.

2.3 STEM Analysis

The STEM/ADF images of carbon-doped boundaries demonstrate no evidence of unique structuring caused by carbon doping. The boundaries observed in the studied foil showed no sign of the thin films often seen in calcia or silica doped alumina samples [41]–[43]. Many STEM/ADF studies of alumina grain boundaries use bonded bicrystals to create special CSL grain boundaries with ordered repeating structures [32]–[34], [36], [86]. The random high angle grain boundaries imaged in this thesis therefore do not share the exact same structure as special boundaries from literature. To make a direct comparison of the structure of two grain boundaries, one un-doped and one carbon-doped, two grain boundaries sharing the same geometric degrees of freedom would need to be compared. Finding two such boundaries in two separate TEM thin foil specimens would require a large sampling of boundaries, a time intensive task. Bonding bicrystals in the presence of carbon would lead

to a much higher probability of observing two boundaries with the same geometric degrees of freedom, however, these may not be representative of the random high angle grain boundaries that dominate the microstructure of the studied alumina samples.

2.4 APT Analysis

The APT bulk composition measurements do not demonstrate a significant relationship between doping levels and bulk composition. The MgO doped specimens do not contain more magnesium within grains than the specimens not doped with magnesia. Previous work demonstrates alumina doped with excess magnesia will result in secondary phase spinel precipitation, and this is likely the sink for excess magnesia in the specimens from this thesis as well [231]–[233]. The trends in oxygen and aluminum content seen as the Al^{+++}/Al^{++} CSR changes are consistent with the results from Chapter IV.

The carbon and magnesium overlap analysis yields no significant evidence of carbon segregation to grain boundaries in carbon-doped specimens. The chemical sensitivity of APT is a few atomic parts per million in ideal cases [234]. The characterization of carbon in a ceramic is indeed not an ideal case, however even assuming a sensitivity a couple of orders of magnitude higher helps validate the conclusion that carbon segregation to alumina grain boundaries either does not occur or occurs at levels below the APT sensitivity level. These results are inconsistent with those published by Marquis *et al.* [1]. There are two possibilities for this inconsistency. It is possible only select grain boundaries in a carbon-doped system demonstrate carbon segregation. Only seven carbon-doped grain boundaries were successfully analyzed using APT, therefore it is possible a grain boundary demonstrating carbon segregation was not randomly sampled. However, the transgranular fracture analysis

in this chapter along with flexural strength, fracture toughness, and wear results from previous studies indicate the strengthening effect is not limited to a select few grain boundaries [4], [27], [28]. Therefore, it is unlikely carbon segregation to grain boundaries is limited to only a few boundaries that were not sampled during the APT analysis in this thesis and causes strengthening. It is also possible the presence of magnesium in the carbon-doped samples was not considered in the original publication. The presence of peaks at 12.5 Da and 13 Da with similar intensities is often a clear and quick way to distinguish between carbon and magnesium in an APT m/q spectrum. However, due to the relatively small amount of magnesium present in the alumina samples studied both in this thesis and the study by Marquis *et al.*, the peaks of magnesium present at 12.5 Da and 13 Da can be indistinguishable from random noise, especially when analyzing a small grain boundary such as that found in the Marquis *et al.* study [1]. The combination of miscommunication between the APT experimentalist and the sample producing ceramicist compounded by low intensity isotopic peaks may have led to a mischaracterization of magnesium segregation as carbon segregation.

The Gibbsian interfacial excess measurements of magnesium, aluminum, and oxygen at grain boundaries show no significant relationship between interfacial segregation and specimen doping. Even the samples that were not doped with MgO powder prior to sintering demonstrated magnesium segregation to grain boundaries. The powder used to produce the samples in this thesis contains approximately 5 ppm magnesium as an impurity. The magnesium segregating to grain boundaries in the undoped specimens is likely from this source. Furthermore, there exists a possibility of contamination between powder processing

experiments despite thorough cleaning using ethanol. Finally, much of the equipment used to process and sinter the samples in this thesis are made of alumina, such as milling media. It is possible these alumina components were sintered using magnesia and contribute to the magnesia content in the samples studied during this thesis. A STEM EDS analysis conducted by Marvel *et al.* studied the grain boundary excess of magnesium at alumina grain boundaries [233]. Excess values reported in this study ranged from approximately 0.5 atoms/nm^2 to 1.5 atoms/nm^2, a range in a good agreement with the excess values reported in this thesis [233].

Finally, the triple point analyzed using APT demonstrated uniform magnesium segregation compared to the grain boundaries constituting the triple junction. There is no evidence of a glassy phase at the triple point, which can develop from impurity silica found in the alumina powder [42], [43]. In fact, no silicon was detected anywhere in the studied samples, likely due to the high purity powder used for sintering. Additionally, there is no evidence of segregation or depletion of aluminum or oxygen at the triple point. It is important to note that only one triple point was analyzed using APT in this thesis, as most targeted triple points fractured before successful analysis.

3 Conclusions

In this chapter, the effect of carbon doping on grain boundary strength, energy, and chemistry was probed using a variety of techniques. The fracture characterization analysis combined with previous mechanical testing indicates carbon doping has a strengthening effect on alumina grain boundaries. The grain boundary relative energy measurements made using AFM were hindered by a highly faceted anisotropic surface and no significant energy

difference could be established between carbon-doped and undoped specimens. Additionally, the STEM and APT analysis yielded no significant difference in grain boundary structure or chemistry between the specimens with and without carbon. Due to the high variability in structure between grain boundaries based upon their geometric degrees of freedom, it is still possible structural differences exist between carbon-doped and undoped specimens. To isolate the effect of carbon doping on grain boundary structure, two grain boundaries with equivalent geometric degrees of freedom would need to be analyzed, one formed in the presence of carbon, the other not. This type of analysis would be easiest to conduct using bonded bicrystals, as fine control over the nature of each grain boundary would be possible. This type of analysis is a strong candidate for future work. Following publication of work by Marquis *et al.*, grain boundary segregation of carbon was thought to contribute to the observed strengthening [1]. However, the results in this section contradict these finding, posing the question what causes the observed strengthening? Structural differences stand as one possible explanation, and bicrystal studies can probe this possibility. Carbon may also have an indirect effect on grain boundary chemistry, by facilitating local reduction. The APT grain boundary characterization in this section does not show evidence of this reduction, however it may be quite subtle and below the technique sensitivity. DFT and other modeling techniques could provide answers to the persistent question of what causes grain boundary strengthening upon carbon doping.

Chapter VI

3YSZ APT Analysis

Each of the measurements made in this chapter, apart from the FS C He 1Hr APT measurements, were conducted using identical experimental parameters: an operating temperature of 40 K, a laser energy value of 30 pJ, a pulse frequency of 200 kHz, and a constant detection rate of 0.5%. Attempts to run FS C He 1Hr specimens using these analysis conditions resulted in 12 consecutive fractures. Therefore, different experimental parameters were used to facilitate higher experimental yield for FS C He 1Hr specimens: an operating temperature of 60 K, a laser energy value of 100 pJ, a pulse frequency of 200 kHz, and a constant detection rate of 0.5%.

1 Results

1.1 Bulk Analysis

1.1.1 Bulk Composition

Bulk compositional measurements were made for each of the specimen types listed in the Materials and Methods chapter. Rectangular ROIs were positioned away from evident microstructural features, such as grain boundaries and phase boundaries. The composition of each ROI was then measured and reported alongside the Zr^{+++}/Zr^{++} CSR of the measurement. Due to the large number of datasets, plots have been split for easier comparison. Figure 63 shows the averaged composition of flash sintered anode specimens along with conventional specimens for reference. For each of the following figures, standard error values are used as error bars.

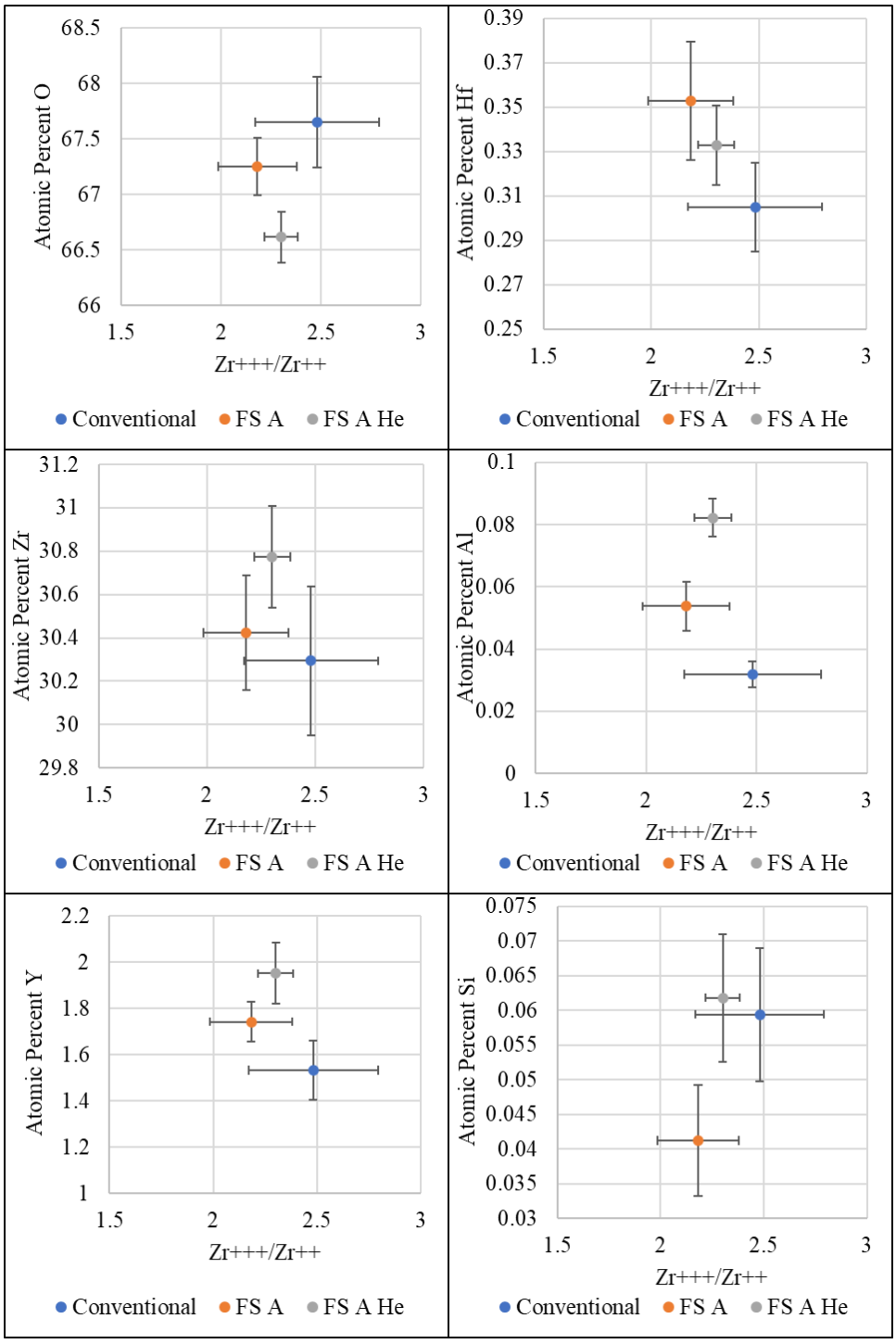


Figure 63: Averaged bulk composition for anode specimens

The FS A He specimens, which are expected to be the most strongly reduced anode specimens, demonstrate lower oxygen contents than the other specimens at similar CSR values. Aluminum content also seems to correlate with order of strongest reducing

atmosphere, with the FS A He samples containing the highest level of aluminum and the conventionally sintered specimens containing the least amount of aluminum. Figure 64 demonstrates the composition of flash sintered cathode samples alongside conventional samples for comparison.

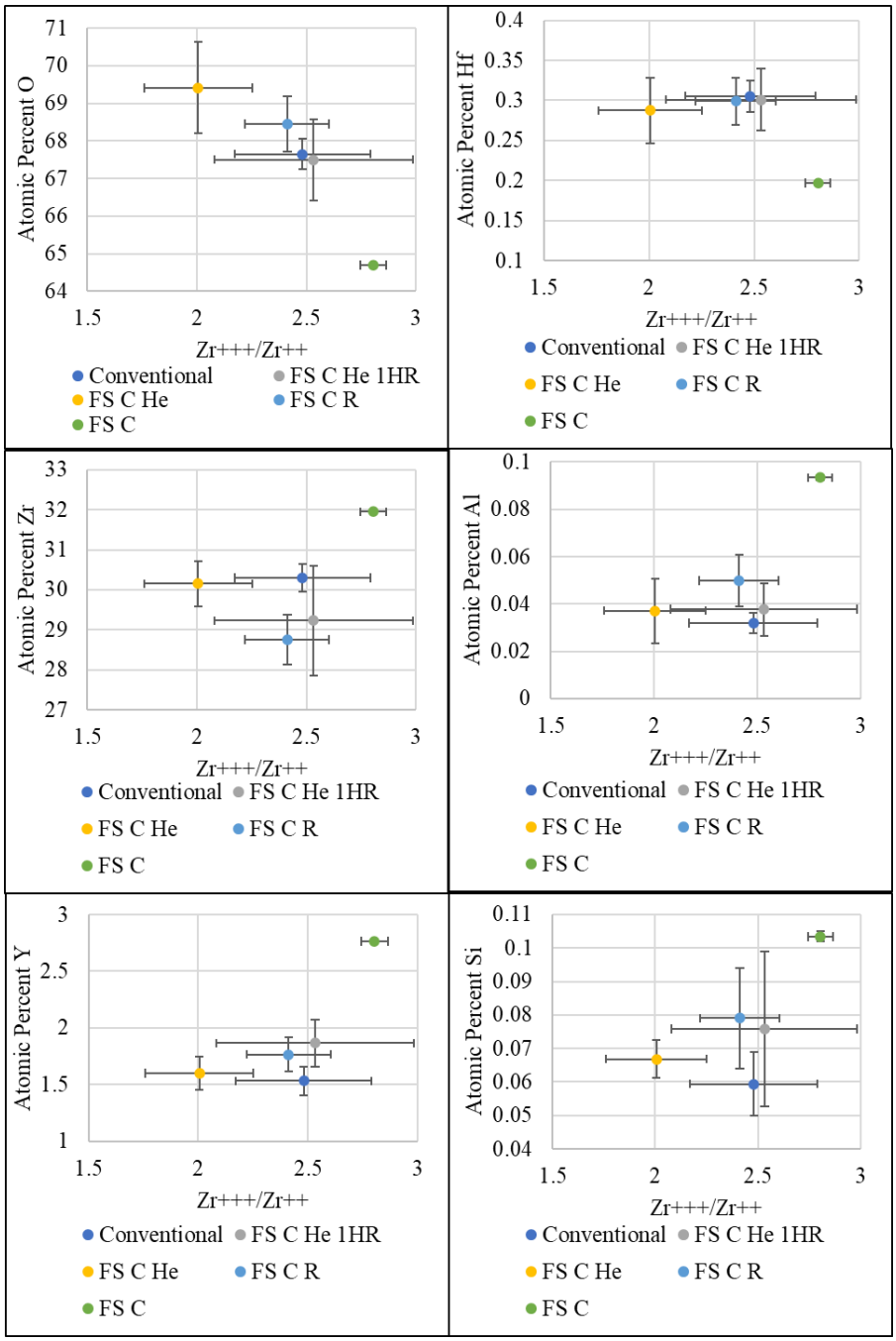


Figure 64: Averaged bulk composition for cathode specimens

Despite being subjected to the strongest reducing environment for the longest period, the FS C He 1Hr specimens demonstrate similar oxygen content compared to the conventionally sintered specimens. The FS C specimens demonstrate significant reduction and elevated aluminum, silicon, and yttrium content. It is also interesting to note that despite being run at higher temperatures using higher laser energy values, there does not seem to be a significant difference in CSR values for the FS C He 1Hr specimens. Comparisons between the anodic and cathodic ends of the same specimens can be found in Figure 65 to demonstrate the local effects of DC current during sintering.

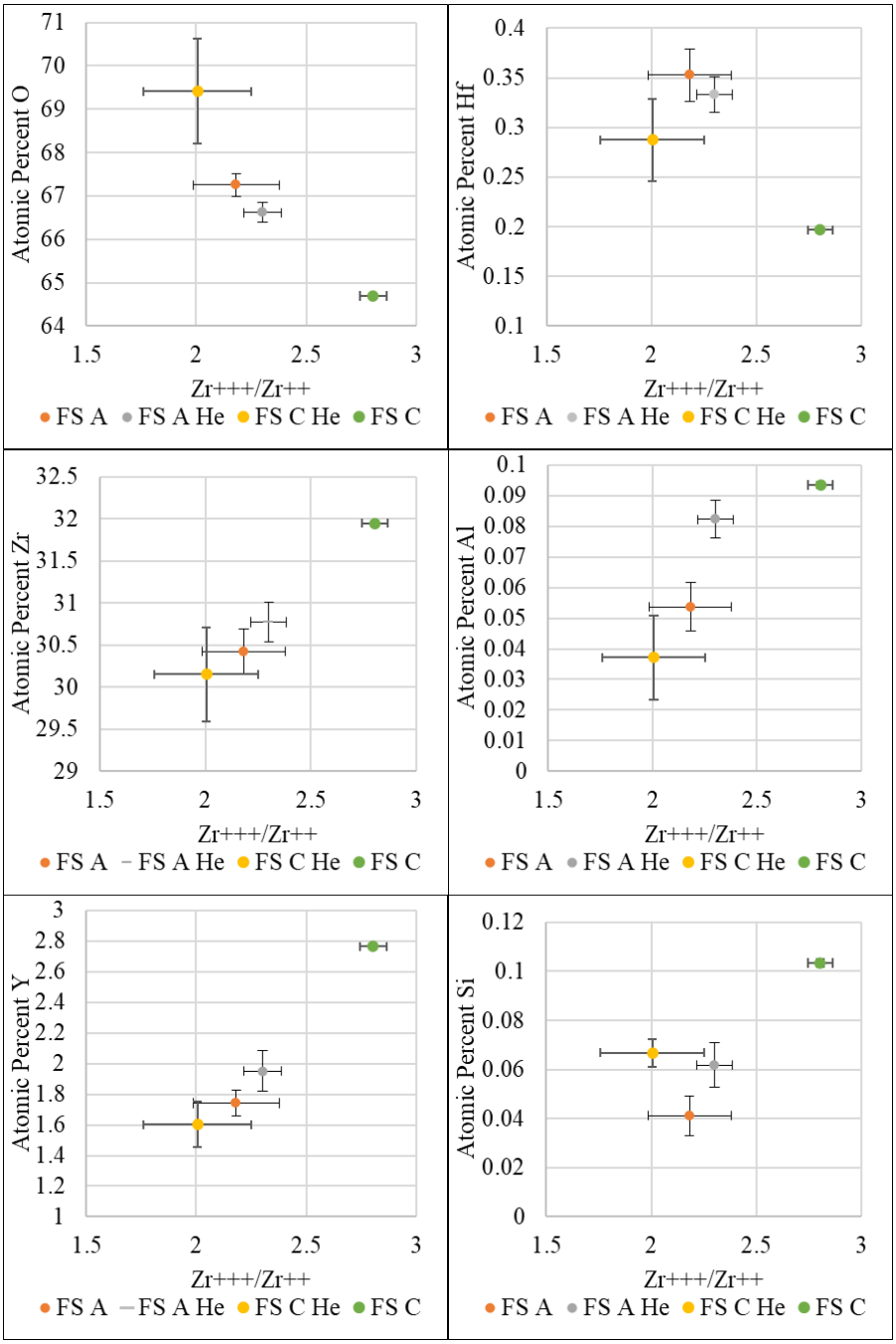


Figure 65: Composition comparisons between anodic and cathodic ends of specimens

The FS C specimens demonstrates local reduction compared to the FS A specimens, however the FS C He specimens demonstrate the opposite effect with a higher oxygen content than its corresponding anode, FS A He. Furthermore, the FS C He specimens demonstrate the highest oxygen content of the compared specimens, inconsistent with the strong reducing

environment these specimens experienced during sintering.

Within the bulk of many 3YSZ APT samples, there exist regions of yttrium inhomogeneity. Three types of inhomogeneity have been observed: round features within the specimen bulk, oriented lath-like features within the bulk, yttrium enrichment bordering grain boundaries, and yttrium depletion bordering grain boundaries. These features are not unique to any specific type of specimen and are found in most of the specimen types studied. However, the density and level of inhomogeneity varies between specimen type. The level of inhomogeneity in each sample will be probed using a binomial grid-based frequency analysis. Additionally, each type of inhomogeneity will be analyzed.

1.1.2 Binomial Grid-Based Frequency Analysis

The same ROIs used for bulk composition measurements were used when conducting the binomial grid-based frequency analysis. The Pearson coefficients of two ions are reported: yttrium ions and yttrium oxide ions, as these ions demonstrated clear visual inhomogeneity when analyzing reconstructions. Binomial analyses were conducted for several other species, including aluminum, silicon, and hafnium. There was, however, little evidence of inhomogeneity when analyzing these elements. The distribution of Pearson coefficients for each measured ROI grouped by specimen type can be found in Figure 66.

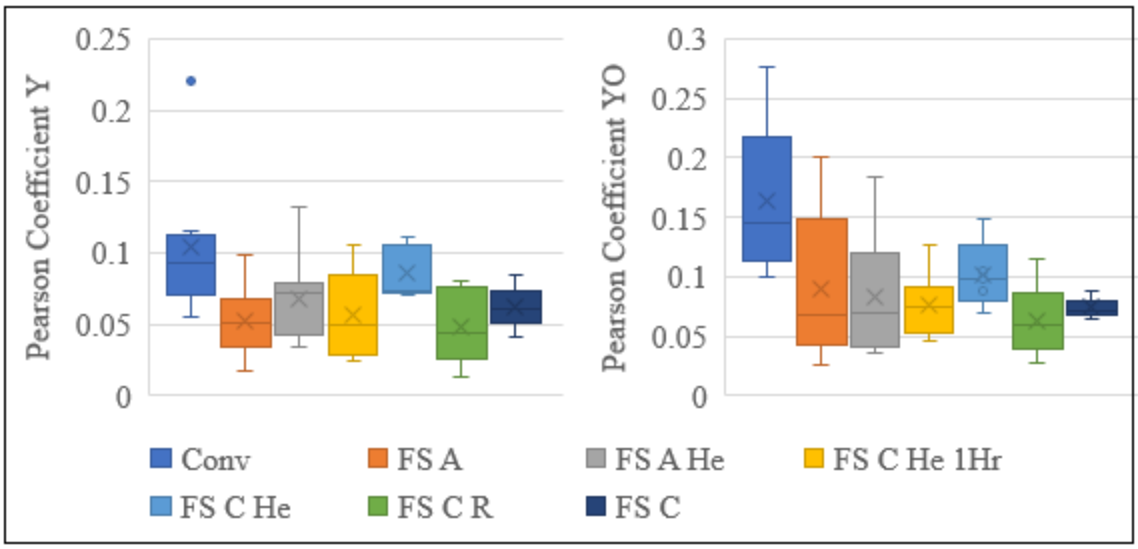


Figure 66: Box and whisker plots of Pearson coefficients for Y and YO ions in 3YSZ samples. The crosses represent the means for each specimen type and the circular points represent outliers. The top whisker corresponds to the maximum value omitting outliers, and the bottom whisker corresponds to the minimum value omitting outliers. The boxes stretch between the interquartile ranges of each distribution (between the first and third quartiles).

These results demonstrate the yttrium distribution in conventionally sintered 3YSZ samples is less random and more inhomogeneous than the flash sintered samples. The distribution of Pearson coefficients for YO ions in conventionally sintered specimens is significantly higher than distributions for the flash sintered samples. Most of the detected yttrium in the datasets comes from YO ions, as opposed to Y ions, as can be seen in the example mass spectrum in Chapter IV.

1.1.3 Round Intragranular Yttrium-Rich Features

Figure 67 displays an example of a round intragranular yttrium-rich feature found in a FS A specimen.

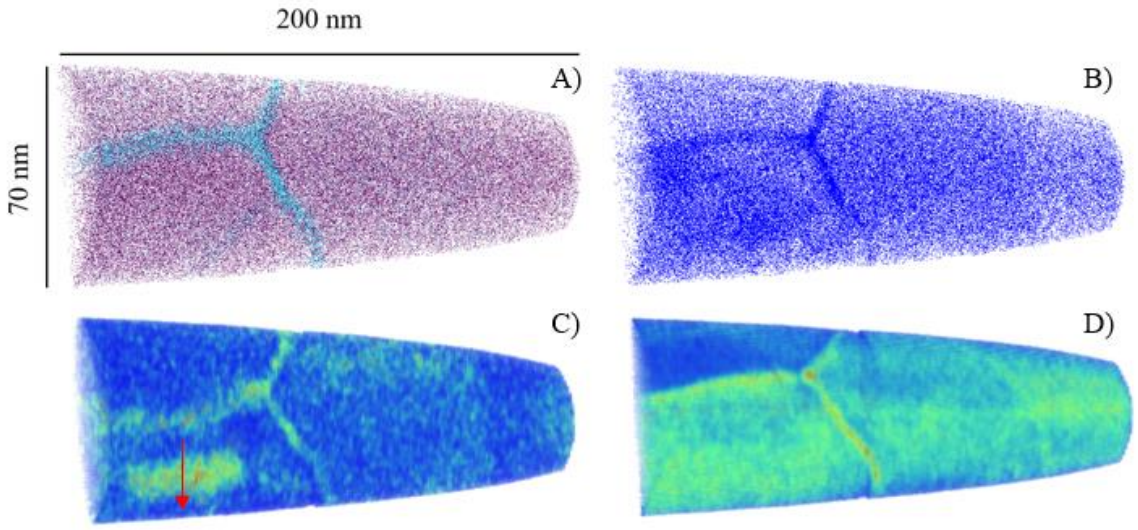


Figure 67: Round intragranular yttrium enriched features in a FS A sample. A) Ion map with purple zirconium ions and blue aluminum ions to highlight the grain boundary. B) Ion map with blue yttrium ions. C) Volume concentration rendering of yttrium concentration. The red line demonstrates where the concentration profile in Figure 68 is measured from. D) Density volume rendering.

The zirconium and aluminum ion map in A) demonstrates that the yttrium feature does not exist at a grain boundary. The feature is difficult to see in the yttrium ion map, B), however it is quite clear in a concentration volume rendering of yttrium found in C). D) demonstrates the increased concentration of yttrium at the feature is not a density related artefact, as the density does not significantly change in the region of the feature. The composition of the feature was probed using a concentration profile, seen in Figure 68, as isolating the material within the features proved difficult using both clustering analyses and isoconcentration surfaces.

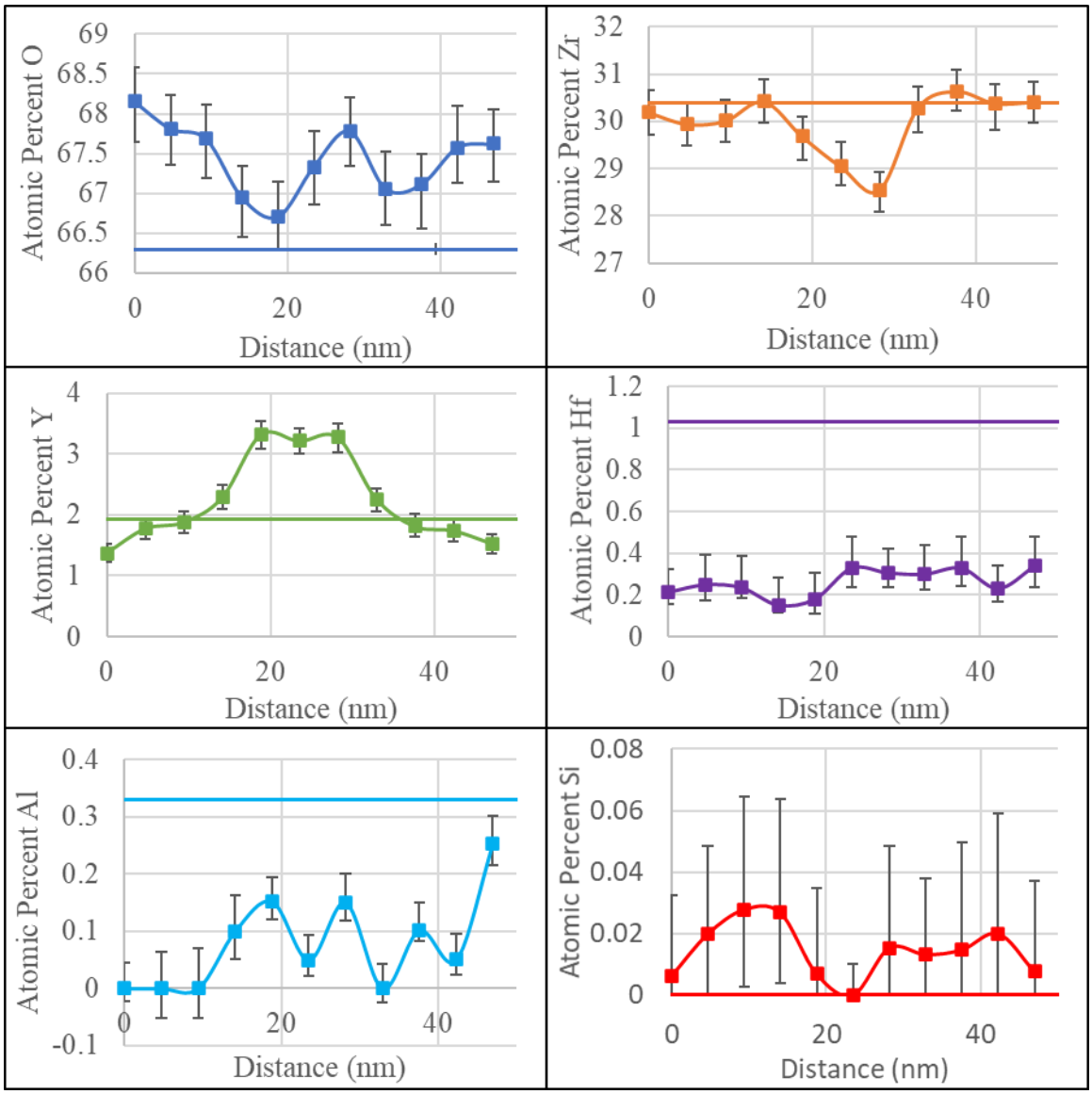


Figure 68: Concentration profiles measuring composition across the length of the round intragranular yttrium rich feature seen in Figure 67. The lines represent the expected concentration of each species from the composition reported by the powder manufacturer.

The feature demonstrates significant yttrium segregation and zirconium depletion. These features were seen in all 3YSZ specimen types.

1.1.4 Lath-like Yttrium Rich Features

Figure 69 displays an example of lath-like features in a conventionally sintered sample.

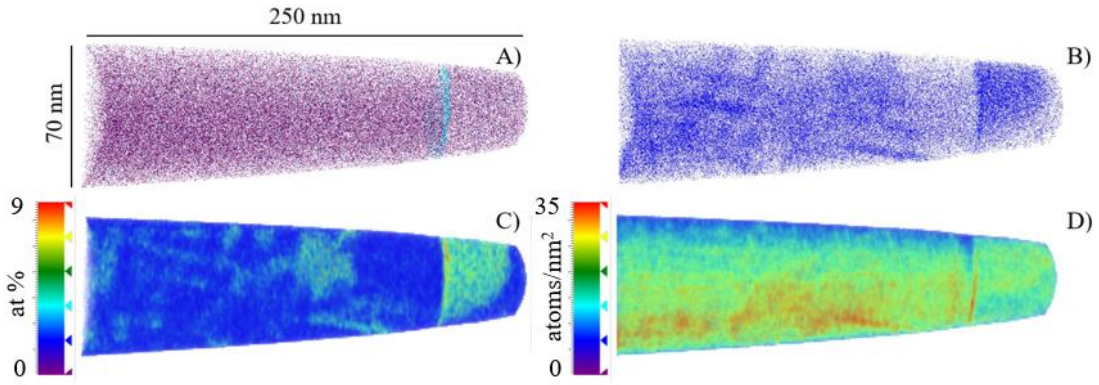


Figure 69: Lath-like yttrium rich features in a conventionally sintered sample. A) Ion map with purple zirconium ions and blue aluminum ions to highlight a grain boundary. B) Ion map with blue yttrium ions. C) Volume concentration rendering of yttrium concentration. D) Density volume rendering.

The features are clearly visible in both the yttrium ion map in B) and the yttrium concentration volume rendering in C). The zirconium and aluminum ion maps in A) demonstrates that these features are not found at grain boundaries, and the density volume rendering in D) demonstrates that these features are not correlated to localized spikes in density. This specimen also contains a grain boundary adjacent region of yttrium enrichment near the specimen apex. These features will be analyzed in a following section. The composition of the lath-like features was probed using a concentration profile as attempts to isolate individual features using clustering analyses and isoconcentration surfaces were not successful. A concentration profile running perpendicular to three laths in the specimen above can be seen in Figure 70.

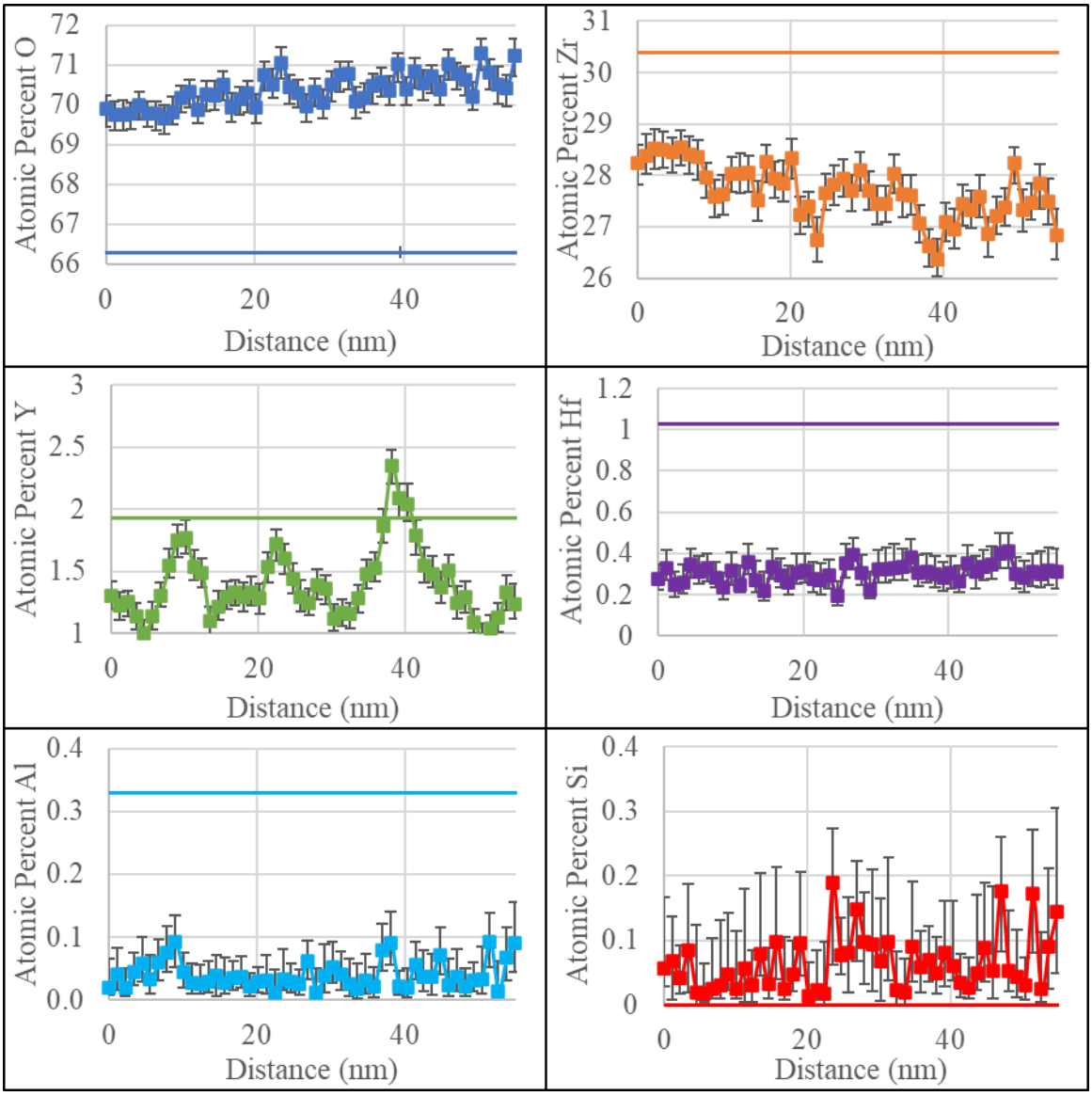


Figure 70: Concentration profile across three lath-like features seen in Figure 69. The lines represent the expected concentration of each species from the composition reported by the powder manufacturer.

The features demonstrate significant yttrium segregation and corresponding zirconium depletion. These features were also found in all the 3YSZ specimen types studied, although more prevalent in conventionally sintered specimens.

1.1.5 Grain Boundary Adjacent Yttrium Enrichment

Figure 71 presents a conventionally sintered specimen showing two grain boundary adjacent regions of yttrium enrichment.

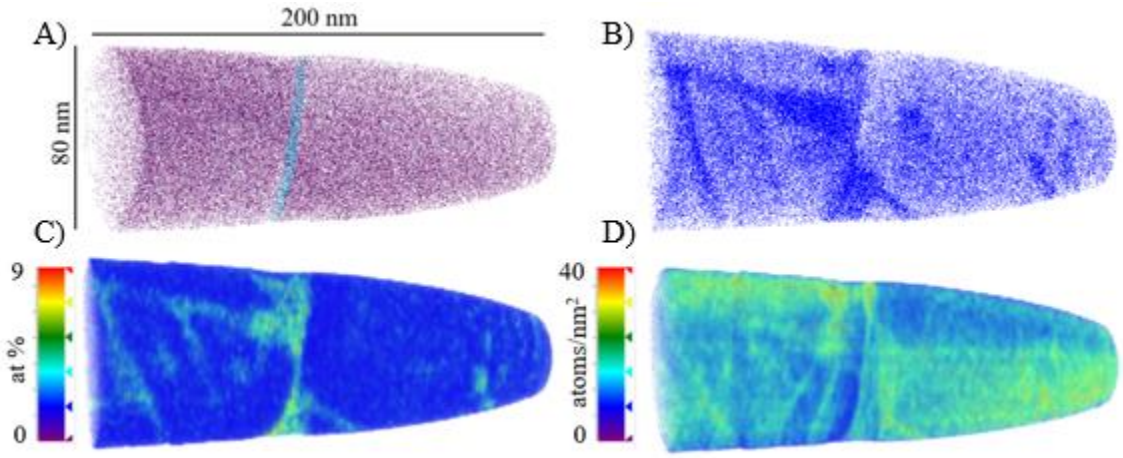


Figure 71: Conventionally sintered specimen with grain boundary adjacent yttrium enrichment regions. A) Ion map with purple zirconium ions and blue aluminum ions to highlight grain boundary. B) Ion map with blue yttrium ions. C) Volume concentration rendering of yttrium. D) Density volume rendering.

The zirconium and oxygen map in A) along with the density map in D) demonstrate evidence of one grain boundary decorated by aluminum ions. The yttrium ion map in B) as well as the yttrium concentration volume rendering in C) demonstrate yttrium segregation to this grain boundary as well as two distinct regions of yttrium enrichment adjacent to the grain boundary, one to the right and one to the left in Figure 71. There is also evidence of lath-like features as discussed in section 1.1.3. A concentration profile containing the feature closest to the top edge of the specimen is shown in Figure 72.

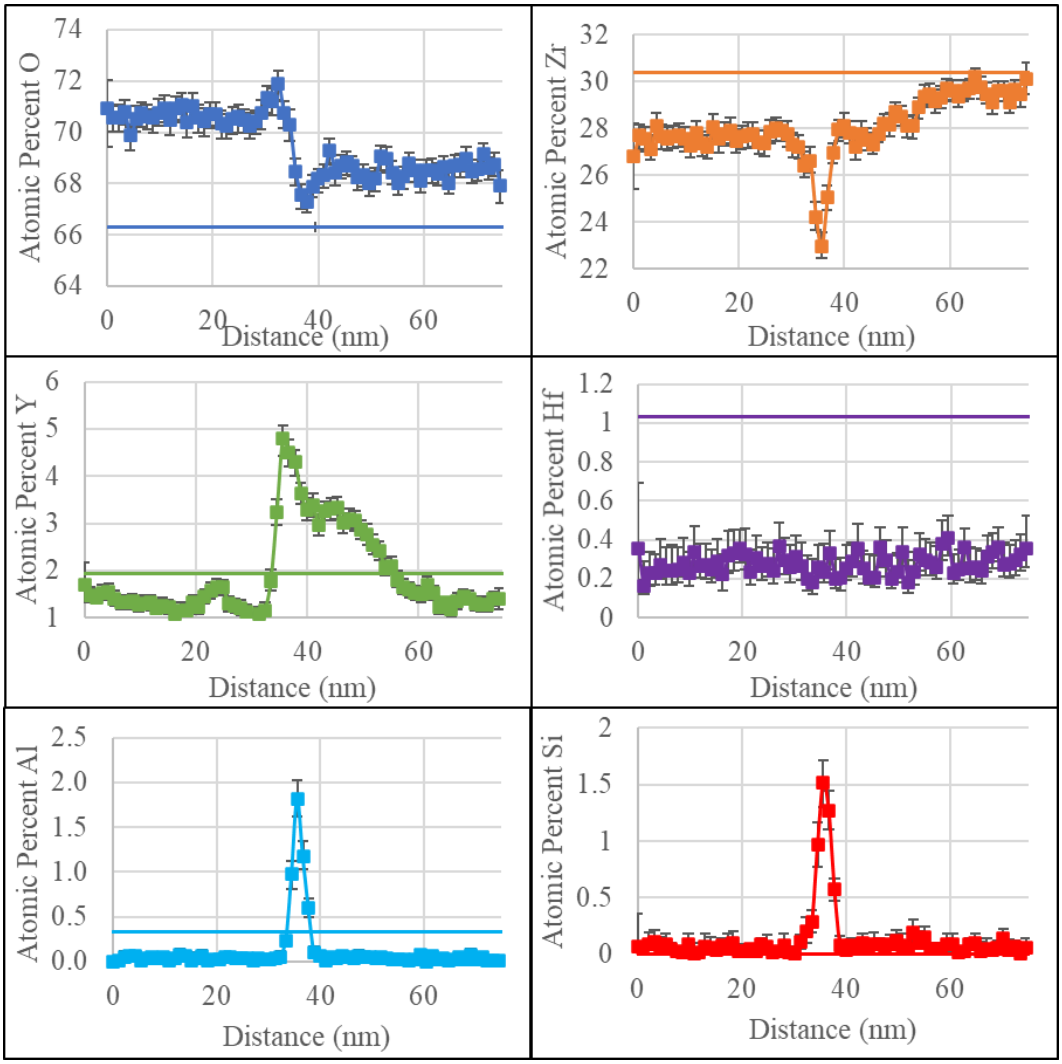


Figure 72: Concentration profiles measuring composition across a grain boundary adjacent yttrium enrichment region in the conventionally sintered specimen shown in Figure 71. The lines represent the expected concentration of each species from the composition reported by the powder manufacturer.

The aluminum and silicon concentration profiles clearly illustrate the location of the grain boundary present in the sample. The yttrium profile demonstrates a peak composition corresponding to the location of the grain boundary followed by a region of lower, yet still above the level of the bulk, concentration. The yttrium enrichment region shows no evidence of any other chemical segregation but does demonstrate oxygen depletion. These features were only present in the two conventionally sintered specimens, those displayed in Figure 69 and Figure 71.

1.1.6 Grain Boundary Adjacent Yttrium Depletion

Figure 73 shows an example of a grain boundary adjacent yttrium depletion region found in a FS C R specimen.

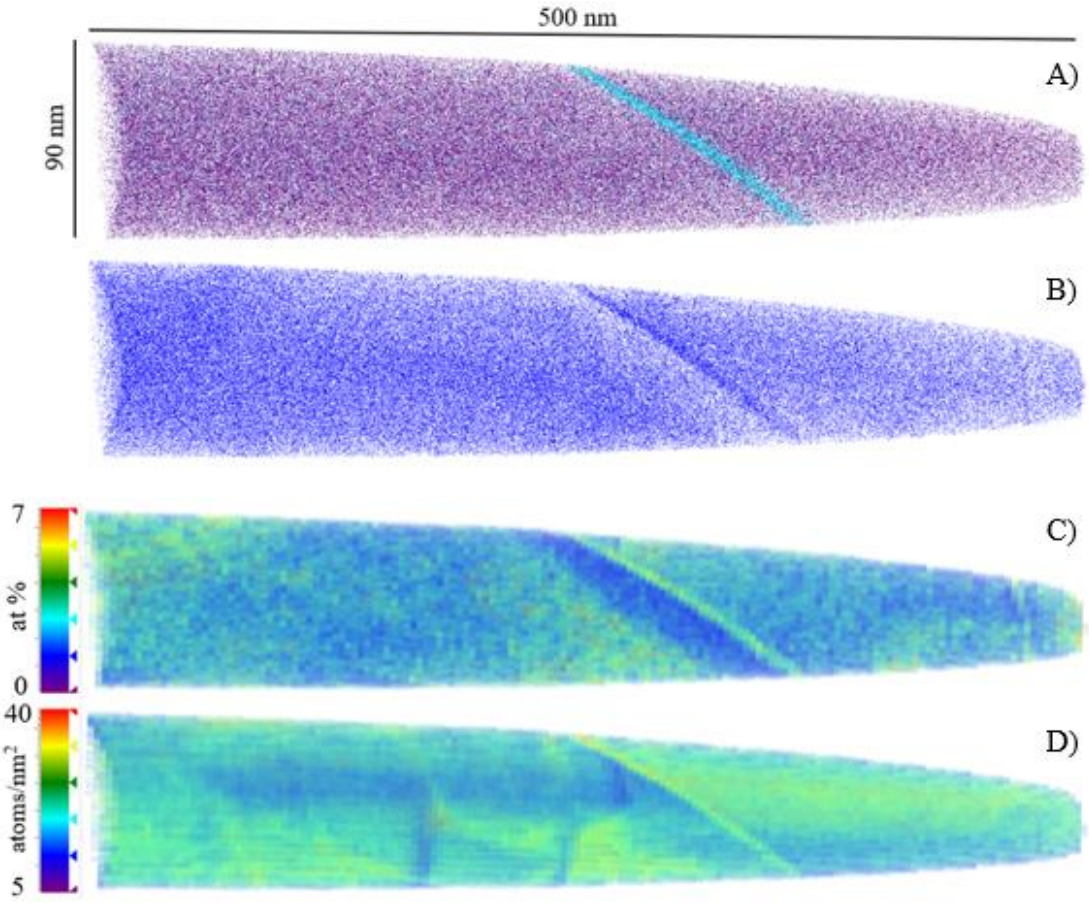


Figure 73: Grain boundary adjacent yttrium depletion region in a FS C R sample. A) Ion map with purple zirconium ions and blue aluminum ions to highlight grain boundary. B) Ion map with blue yttrium ions. C) Volume concentration rendering of yttrium concentration. D) Density volume rendering.

The grain boundary shows clear yttrium and aluminum segregation as evident in A) and B). B) and C) visually demonstrate a region of yttrium depletion immediately to the left of the grain boundary in its orientation shown in Figure 73, while D) demonstrates little evidence that this feature may be a density variation artefact. Concentration profiles running across the grain boundary and the grain boundary adjacent depletion region can be found in Figure 74.

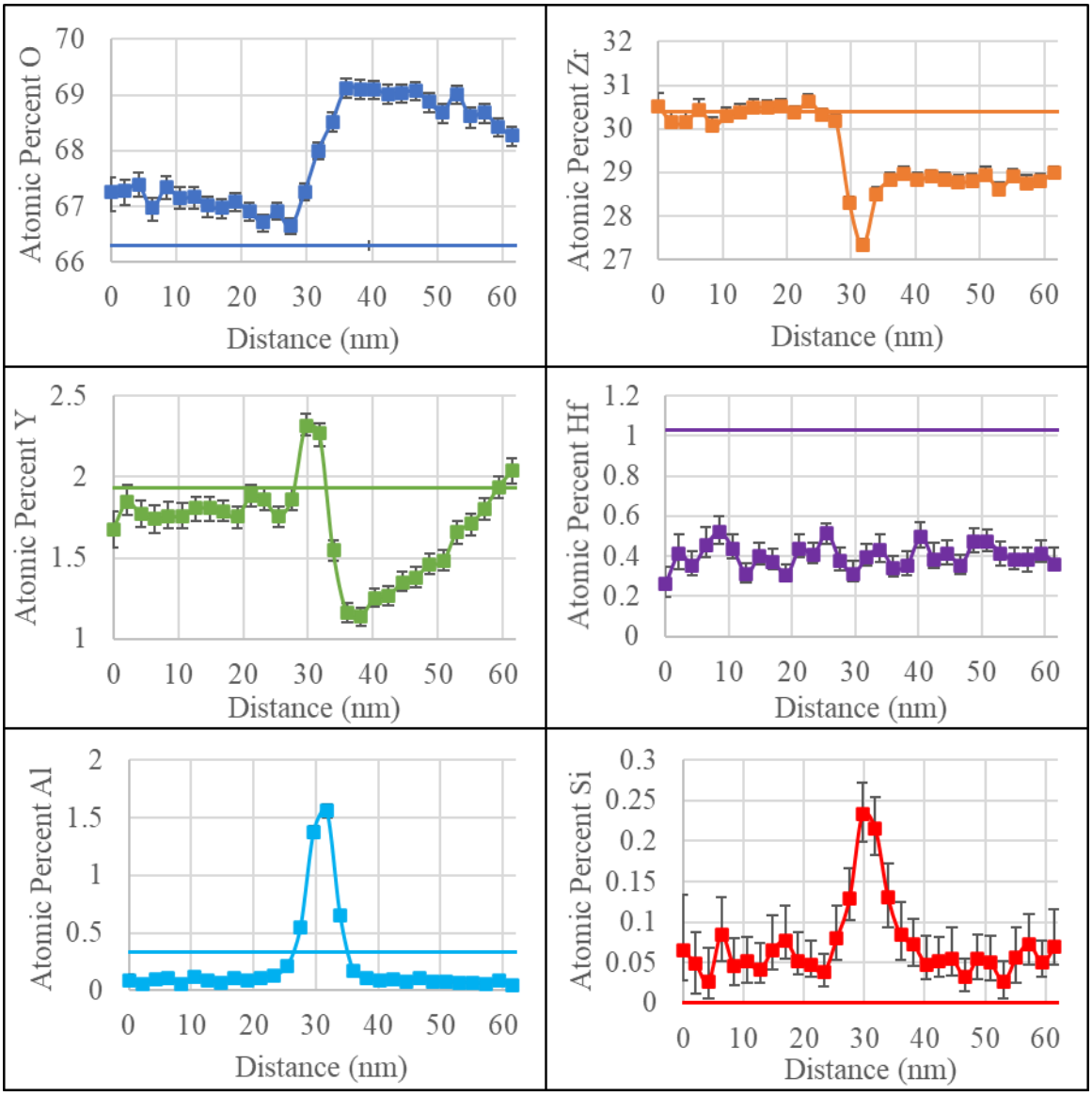


Figure 74: Concentration profiles measuring composition across a grain boundary adjacent yttrium depletion region in the conventionally sintered specimen shown in Figure 73. The lines represent the expected concentration of each species from the composition reported by the powder manufacturer.

The grain boundary is highlighted by significant aluminum, silicon, and yttrium enrichment. Immediately following the grain boundary, a region of yttrium and zirconium depletion exists with a corresponding increase in oxygen concentration. This type of feature was present in both conventionally sintered and FS C R specimens. However, only two specimens in total demonstrated these features, so it is possible they are present in other specimens and were just not sampled. Another interesting bulk feature found exclusively in

the FS C He 1Hr specimens is a carbon rich phase, detailed in the following section.

1.1.7 FS C He 1Hr Carbon Rich Phase

Figure 75 shows ion maps of the FS C He 1Hr specimen containing a carbon rich phase.

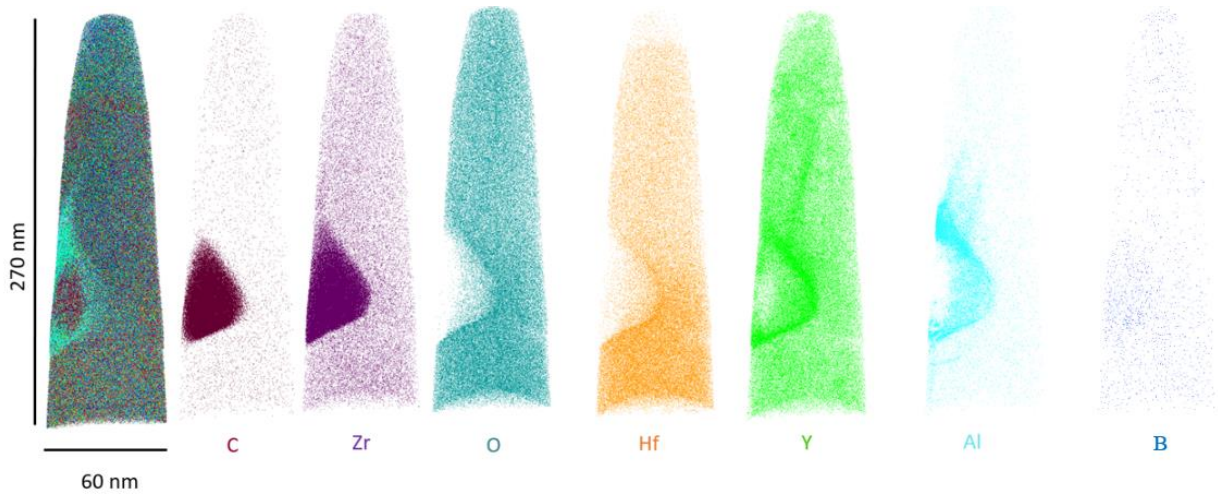


Figure 75: Ion maps of a FS C He 1HR specimen containing a carbon rich phase

Due to the introduction of two new chemical species present within the material, carbon and boron, the mass spectrum needed to be re-analyzed to account for the new species and potential overlaps. The new peak overlaps in addition to those considered in Chapter IV of this thesis can be found in Table 27.

Table 27: Peak overlaps considered when analyzing FS C He 1Hr specimen containing a carbon enriched feature

Dalton Value	Ion 1 and Charge	Ion 2 and Charge	Ion 3 and Charge
18.0	C_3^{++}	O^+	
12.0	C^+	C_2^{++}	C_3^{+++}
24.0	C_2^+	C_4^{++}	
35.33, 36	ZrC^{+++}	ZrO^{+++}	
52	ZrC^{++}	C_3O^+	
53, 54	ZrC^{++}	ZrO^{++}	
114-118	$Zr_2O_3^{++}$	ZrC_2^+	

The labeled mass spectrum for this specimen can be found in Figure 76.

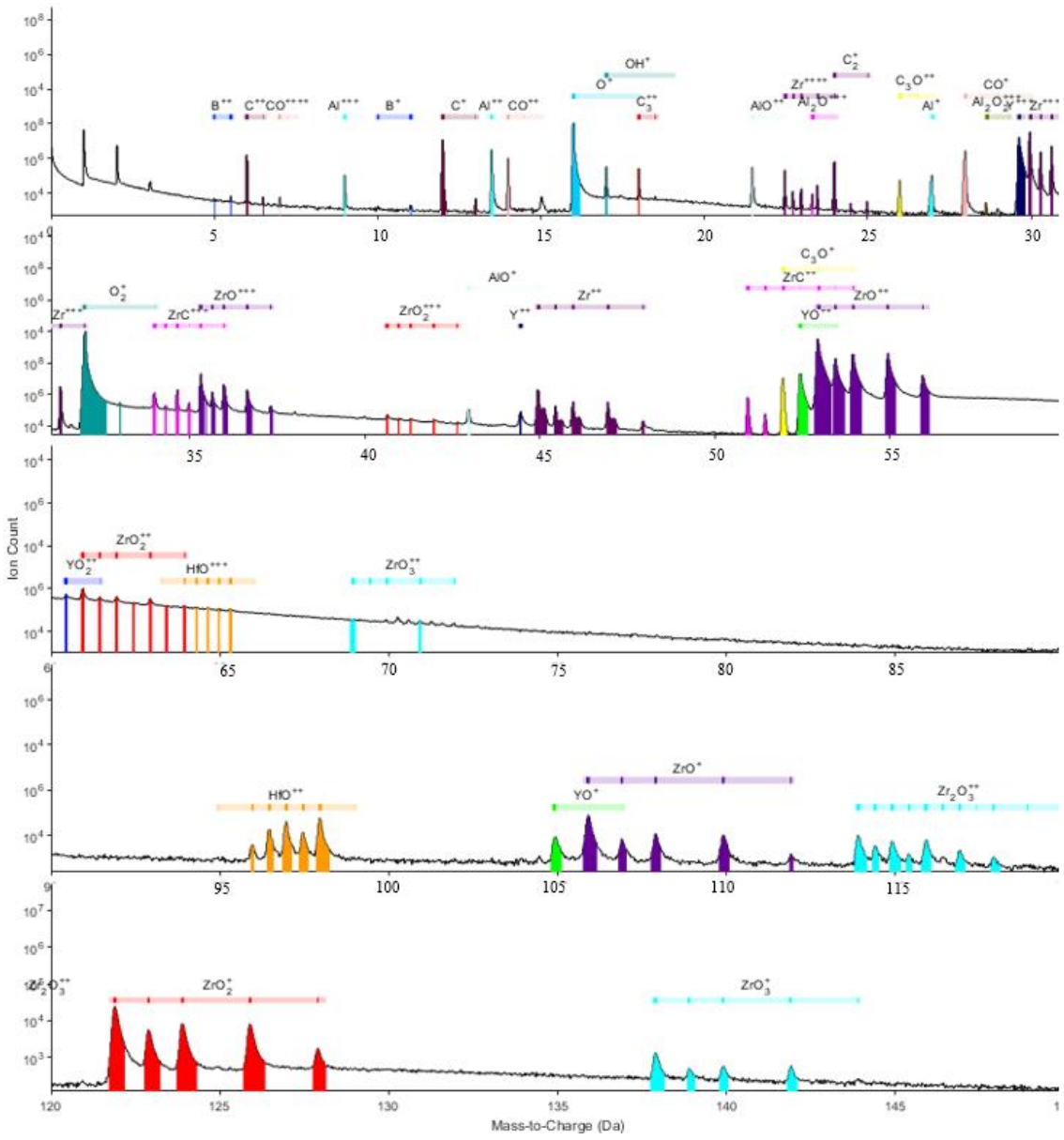


Figure 76: Ranged m/q spectrum for the FS C He 1Hr specimen containing a carbon enriched feature. Figure generated using AtomProbeLab v0.2.2. Note the difference in Log scales across the different panels of the spectrum

To quantify the chemical distribution within and around the carbon enriched feature, a proxigram was plotted from a 25% carbon isoconcentration surface and can be found in Figure 77.

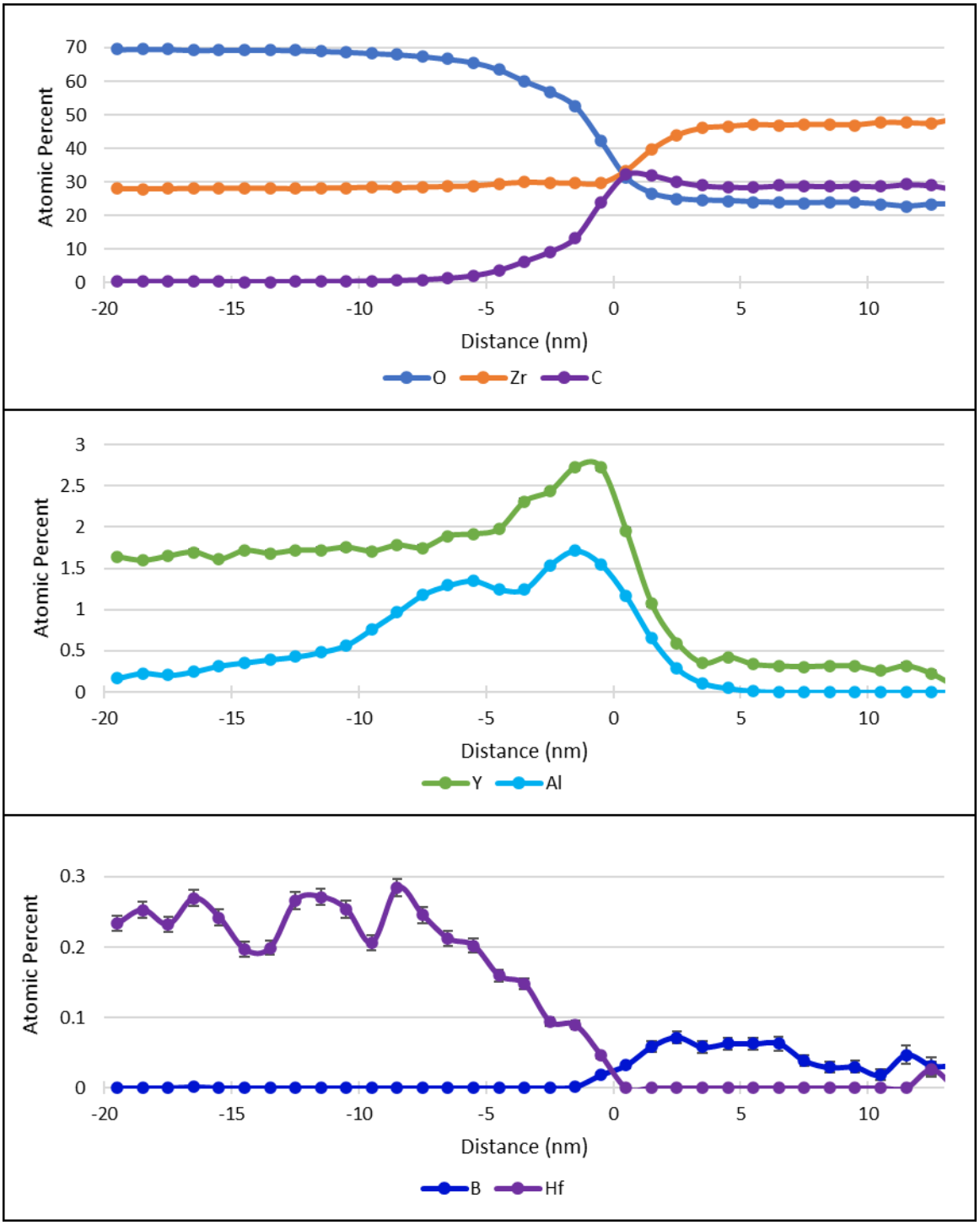


Figure 77: Proxigram analysis of carbon enriched feature

The feature appears to be a zirconium oxycarbide with trace yttrium and boron. The proxigram demonstrates a steady carbon concentration of approximately 29% within the bulk of the carbon enriched feature. It is important to note the proxigram was created using

an IVAS built in feature. However, IVAS does not resolve mass peak overlaps when creating a proxigram, therefore, a spherical ROI was placed within an isoconcentration surface of 29% carbon composition and the composition of this ROI was found using AtomProbeLab v0.2.2 using the standard compositional measurement procedures detailed in Chapter IV. The composition of the zirconium oxycarbide phase can be found in Table 28.

Table 28: Composition of zirconium oxycarbide phase and abutting 3YSZ grain for comparison

Species	Atomic % Oxycarbide	Atomic % 3YSZ
Zr	48.56 ± 0.02	24.0 ± 0.05
C	28.16 ± 0.09	
O	22.81 ± 0.02	65.6 ± 0.06
Y	0.33 ± 0.01	1.84 ± 0.03
Hf	0.11 ± 0.01	0.22 ± 0.02
B	0.04 ± 0.01	
Si		0.13 ± 0.02
Al		0.02 0.01

1.2 Grain Boundary Analysis

1.2.1 Gibbsian Interfacial Excess

Gibbsian interfacial excess measurements of aluminum, silicon, and oxygen can be found in Figure 78. Aluminum and silicon are plotted as they are known segregants to grain boundaries in 3YSZ, and potential oxygen depletion at grain boundaries is a topic of interest related to macro-scale 3YSZ properties. Data for yttrium, another known grain boundary segregant, is not shown, as yttrium is not uniformly distributed within the bulk and therefore

not suitable for Gibbsian excess measurements. Each Gibbsian interfacial excess measurement is plotted versus grain boundary misorientation as calculated by TKD measurements. Misorientation values are used to provide crystallographic characterization of the grain boundary to facilitate a more robust comparison.

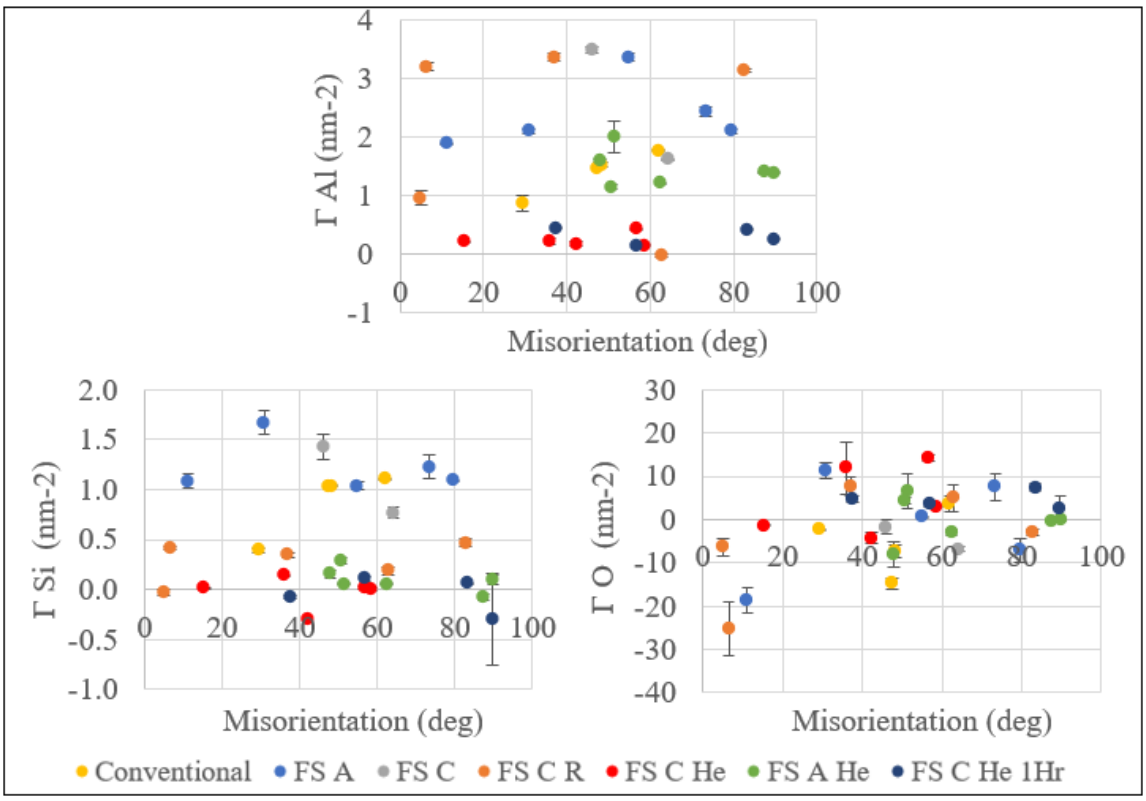


Figure 78: Gibbsian interfacial excess of aluminum, silicon, and oxygen vs grain boundary misorientation for 3YSZ grain boundaries

There is no relationship between grain boundary misorientiation and local chemistry. The two samples exposed to the strongest reducing environment, FS C He and FS C He 1Hr demonstrate significantly lower levels of Al and Si segregation.

1.2.2 Grain Boundary Composition

Due to the inhomogeneous distribution of yttrium within the bulk of the studied 3YSZ specimens, a Gibbsian interfacial excess measurement is not appropriate. Therefore, the yttrium compositions of the grain boundaries studied in section 2.1 are reported. The

Gibbsian interfacial excess analysis yields a repeatable measurement of the width of the studied grain boundary based upon segregation of the strongest impurity (usually Al), and these width values were used to define ROIs around grain boundaries. The yttrium content of these boundaries was then calculated using AtomProbeLab v0.2.2 to account for peak overlaps. Figure 79 shows grain boundary yttrium composition versus grain boundary misorientation.

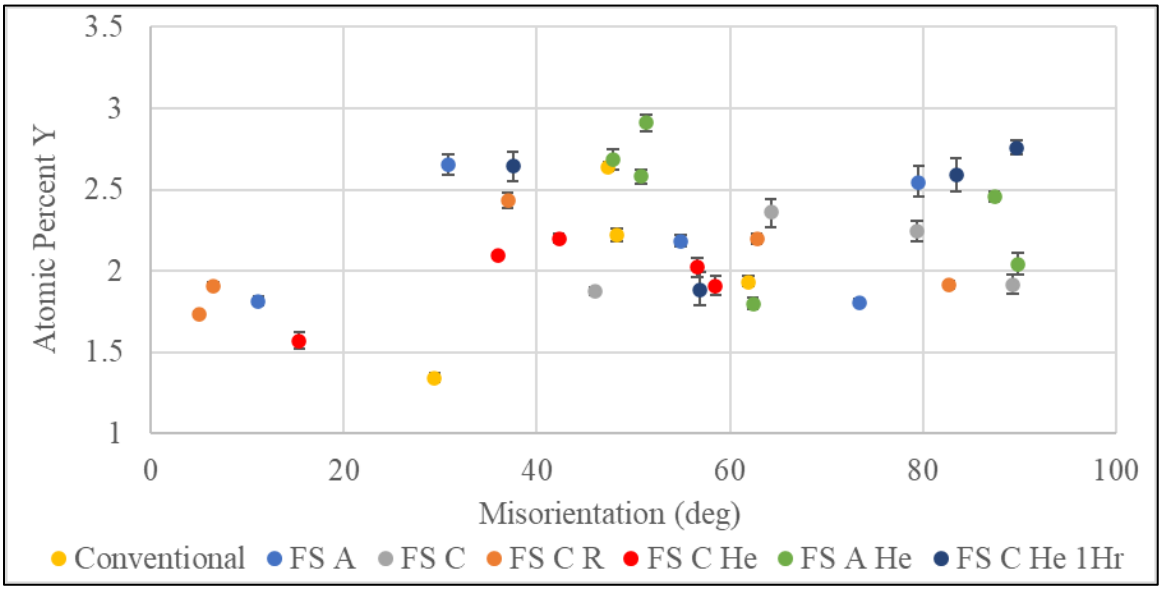


Figure 79: Grain boundary composition of yttrium versus grain boundary misorientation

There exists no evident relationship between yttrium composition and grain boundary misorientation or specimen type.

1.2.3 Grain Boundary Structure

Most of the grain boundaries observed in this thesis consisted of homogeneously distributed species. Two grain boundaries, however, displayed sub-structuring of the segregating species. The first of these grain boundaries was found in a conventionally sintered specimen, shown in Figure 80.

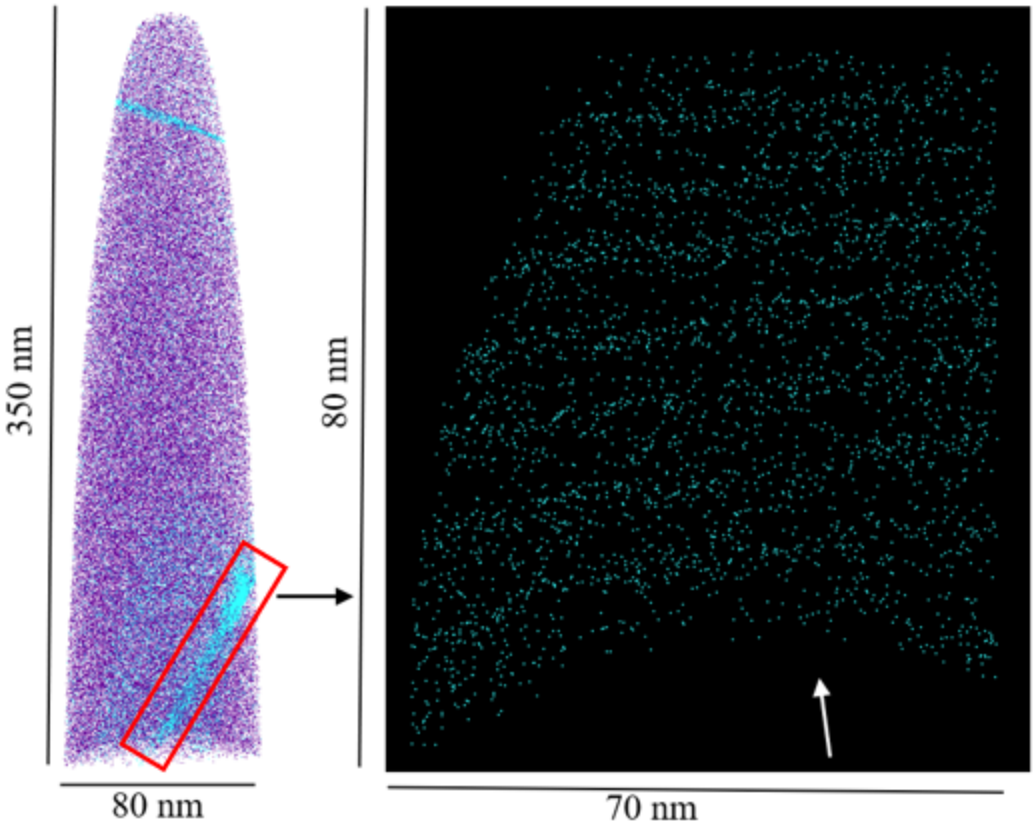


Figure 80: Structured grain boundary from conventionally sintered specimen. The ions constituting the grain boundary outlined with the red box in the left image were isolated, and the resulting image was rotated so that the grain boundary plane is parallel to the page yielding the image on the right. The blue ions in both images are aluminum ions while the purple ions only in the left image are zirconium ions.

Volume renderings of concentration along with a density volume rendering of this grain boundary can be seen in Figure 81.

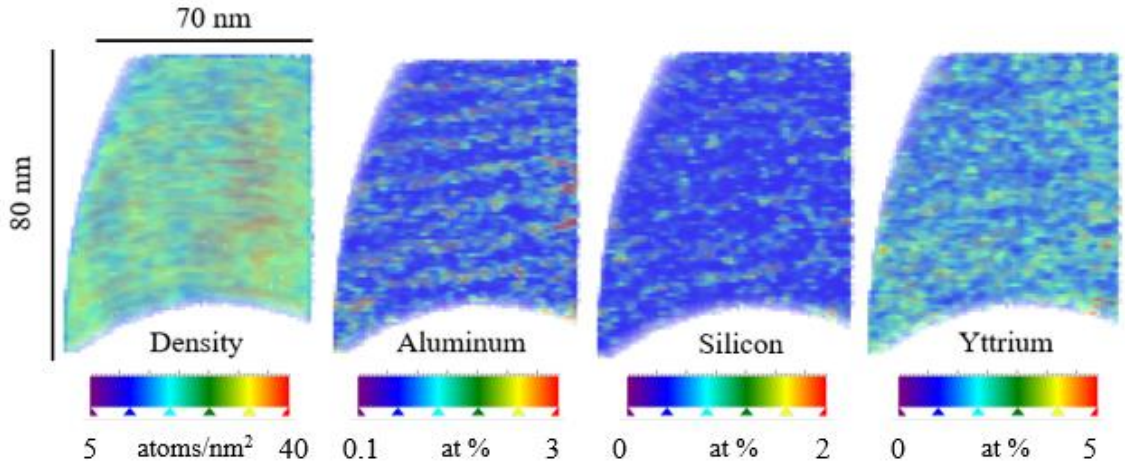


Figure 81: Volume renderings of concentration and density for the grain boundary in Figure 80.

The grain boundary shows evident structuring of aluminum ions and potentially silicon ions. The density volume rendering does not show density spikes at the same locations as high aluminum concentration, providing evidence the banding is not a density related artefact within the APT reconstruction. To quantitatively probe the structuring occurring at this grain boundary, a concentration profile was calculated in the direction of the white arrow in Figure 80 and can be found in Figure 82.

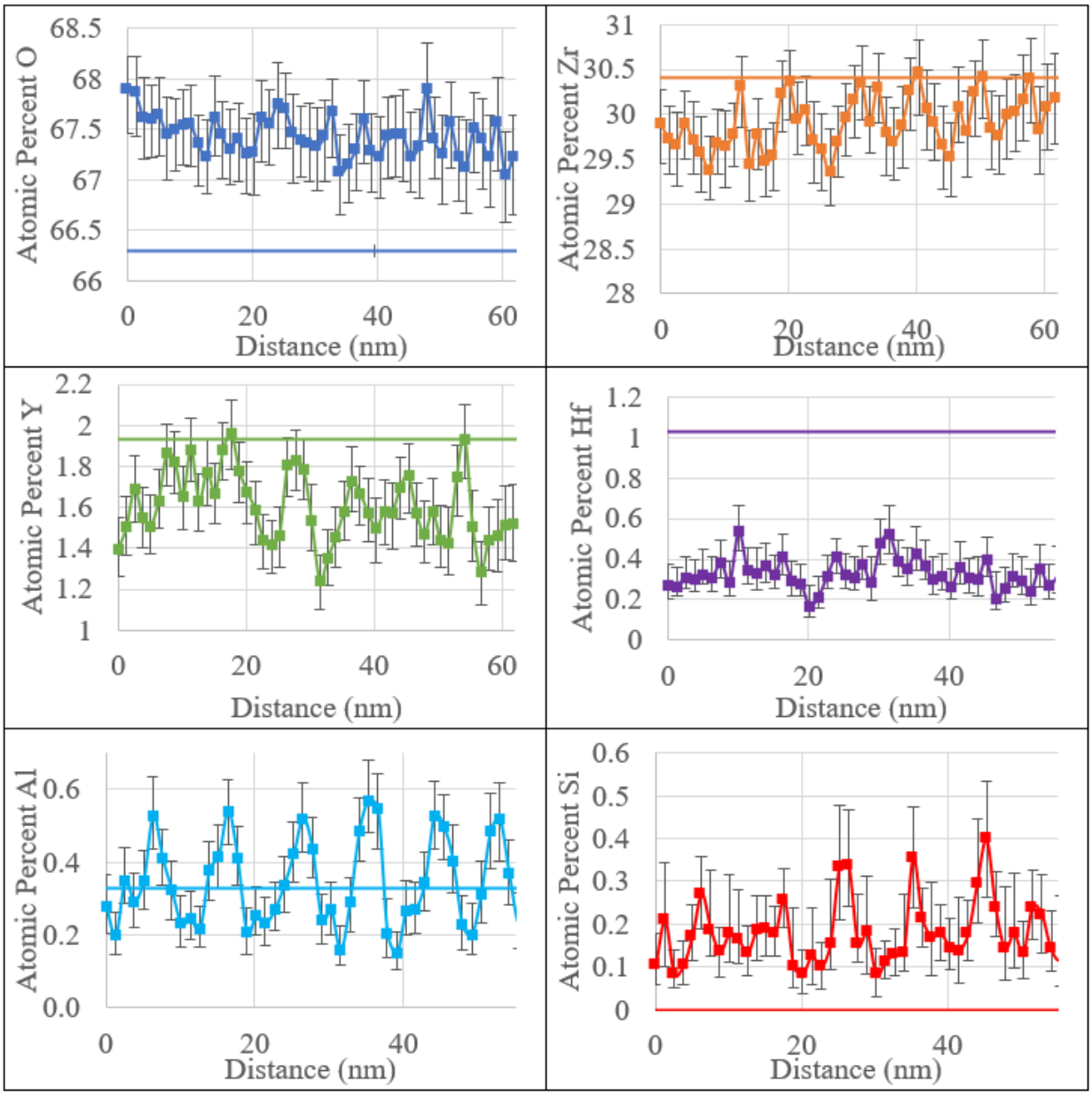


Figure 82: Concentration profiles across the structured grain boundary

The aluminum profile demonstrates clear evidence of alternating bands of high and low aluminum concentration along the length of the grain boundary. The silicon profile shows a similar, albeit weaker trend. The specimen containing this grain boundary was not analyzed using TKD prior to APT, and therefore crystallographic information regarding the boundary

is not available. The second grain boundary demonstrating structure was found in a FS C R specimen, shown in Figure 88.

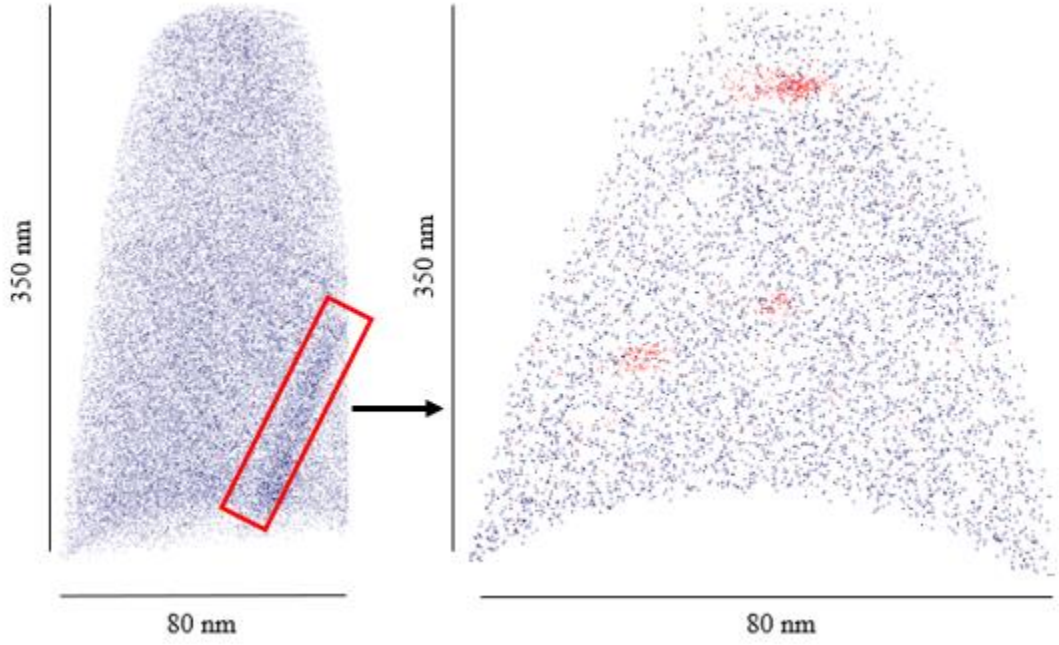


Figure 83: Grain boundary in an FS C R specimen demonstrating sub structuring. Blue ions represent yttrium and red ions represent silicon. The grain boundary outlined in the red box is rotated so that the grain boundary plane is parallel to the page in the image on the right clearly showing silicon clusters.

There exist three silicon clusters along the grain boundary. Volume concentration renderings of several species as well as a volume density rendering can be found in Figure 84.

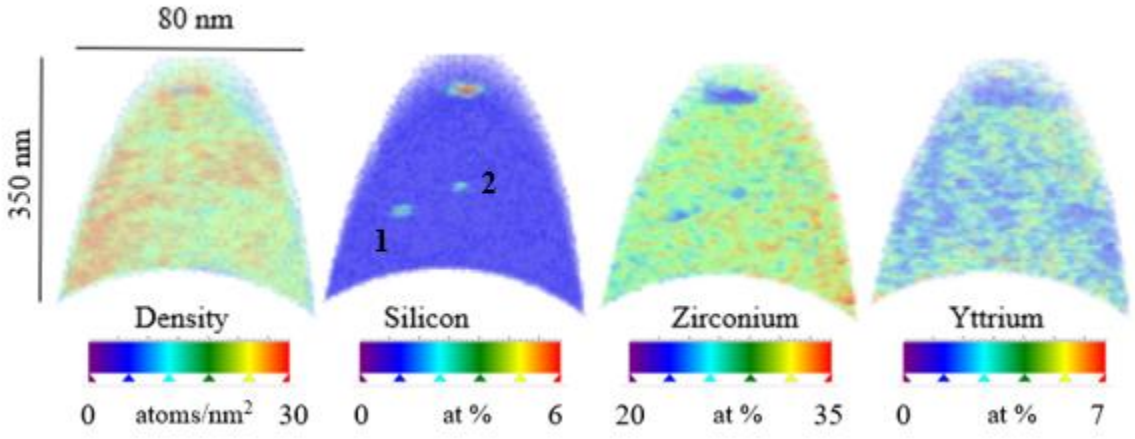


Figure 84: Volume concentration renderings of several species and volume density rendering of FS C R grain boundary demonstrating silicon clustering.

The cluster at the top of the reconstruction, which exists on the surface of the atom probe specimen, does show some weak evidence of an elevated density in the density map. Because of this density fluctuation, and the possibility that the cluster could be some edge-related artefact (such as FIB specimen preparation contamination) no further analysis was conducted on this cluster. The clusters also demonstrate evidence of zirconium depletion. The two lower clusters were isolated using the following cluster search parameters: D_{max} = 1 nm, N_{min} = 10, L = 0.5 nm, E = 0.5 nm. The composition of these clusters can be found in Table 29.

Table 29: Composition of silicon clusters at FS C R grain boundary. Clusters are labeled in Figure 84.

Cluster	H	Si	Y	Zr	O
1	0	57.45	0	6.38	36.17
2	0	71.43	2.86	8.57	14.29

The two clusters demonstrate significantly different compositions, particularly oxygen, silicon, and yttrium content.

1.3 Triple Point Characterization

Triple points observed in the analyzed 3YSZ samples can be categorized into three major types. The first occurs when a triple point is formed when grain boundaries demonstrating significant aluminum, silicon, and yttrium segregation meet. These triple points demonstrate segregation levels like the grain boundaries forming the triple point. An example of this type of boundary from a FS A specimen can be seen in Figure 85.

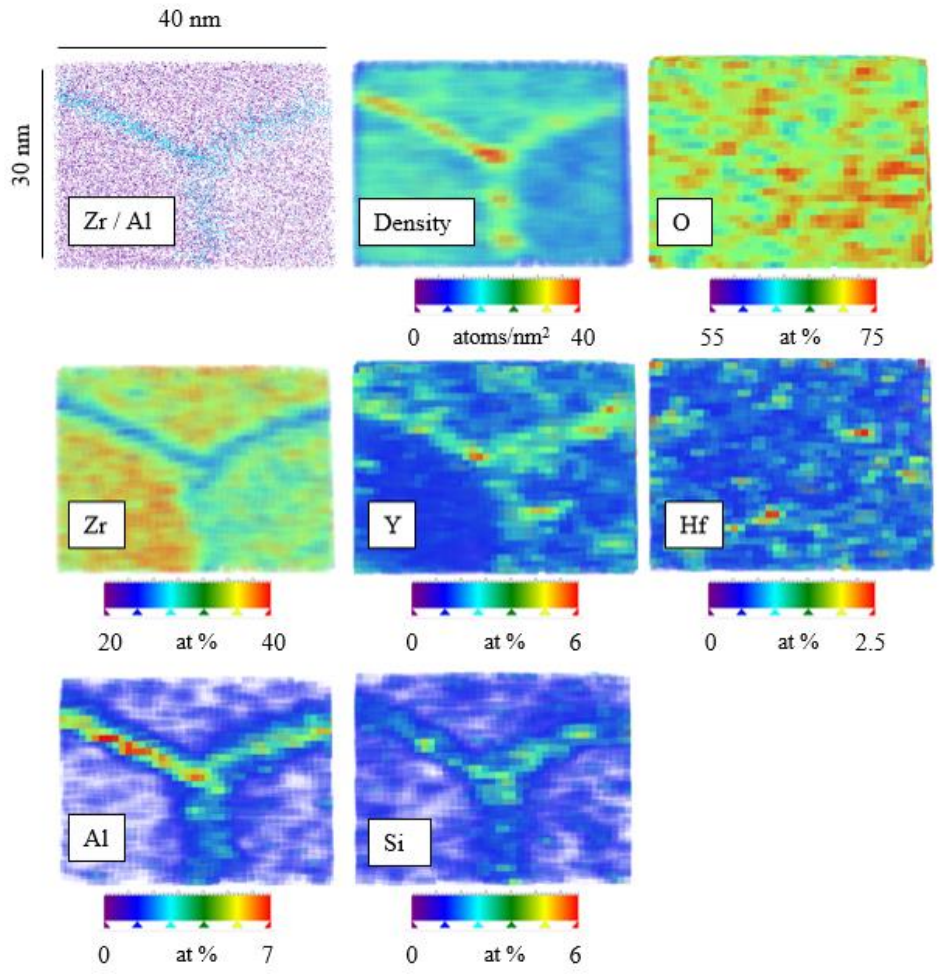


Figure 85: Triple point with segregation levels consistent with the abutting grain boundaries. The ion map shows zirconium ions in purple and aluminum ions in blue. The remainder of the maps are volume renderings of density and chemical species concentration.

Each of the grain boundaries demonstrates segregation of aluminum, zirconium, and yttrium, with the triple point demonstrating similar concentration levels. The second type of triple point also occurs at the intersection of grain boundaries demonstrating aluminum, silicon, and yttrium segregation. However, these triple points demonstrate elevated levels of aluminum and silicon at the triple point compared to the abutting grain boundaries. One such triple point from a conventionally sintered specimen can be seen in Figure 86.

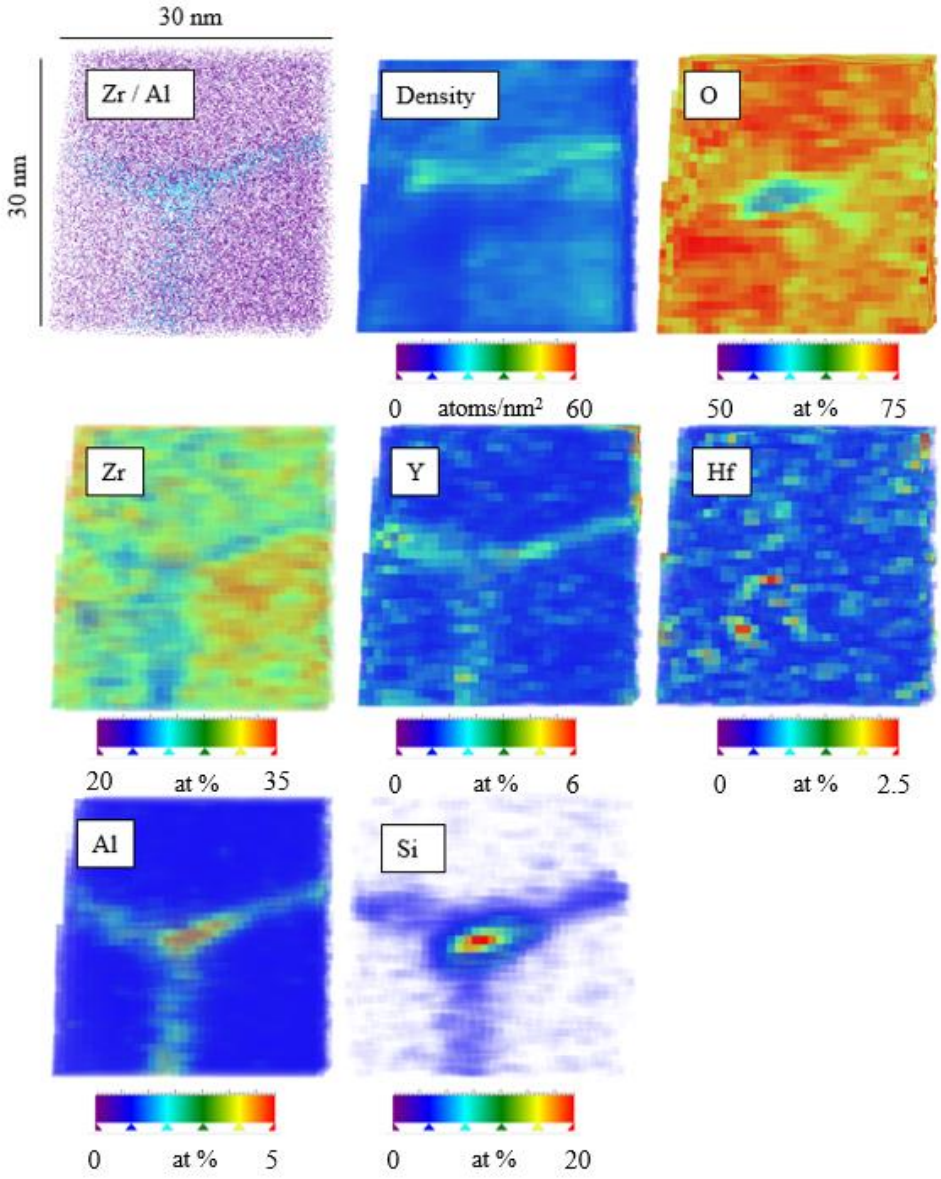


Figure 86: Triple point with segregation levels of aluminum and silicon significantly higher than the abutting grain boundaries. The ion map shows zirconium ions in purple and aluminum ions in blue. The remainder of the maps are volume renderings of density and chemical species concentration. The silicon map was rendered with a lower opacity to make the triple point segregation behavior clearer.

This triple point demonstrates significantly higher silicon and aluminum concentration at the triple point compared to the grain boundaries and the bulk. The triple point also demonstrates very strong oxygen depletion. The material within the triple point was isolated using a 3% isoconcentration surface of silicon. A rotated view of this triple point can be seen in Figure 87.

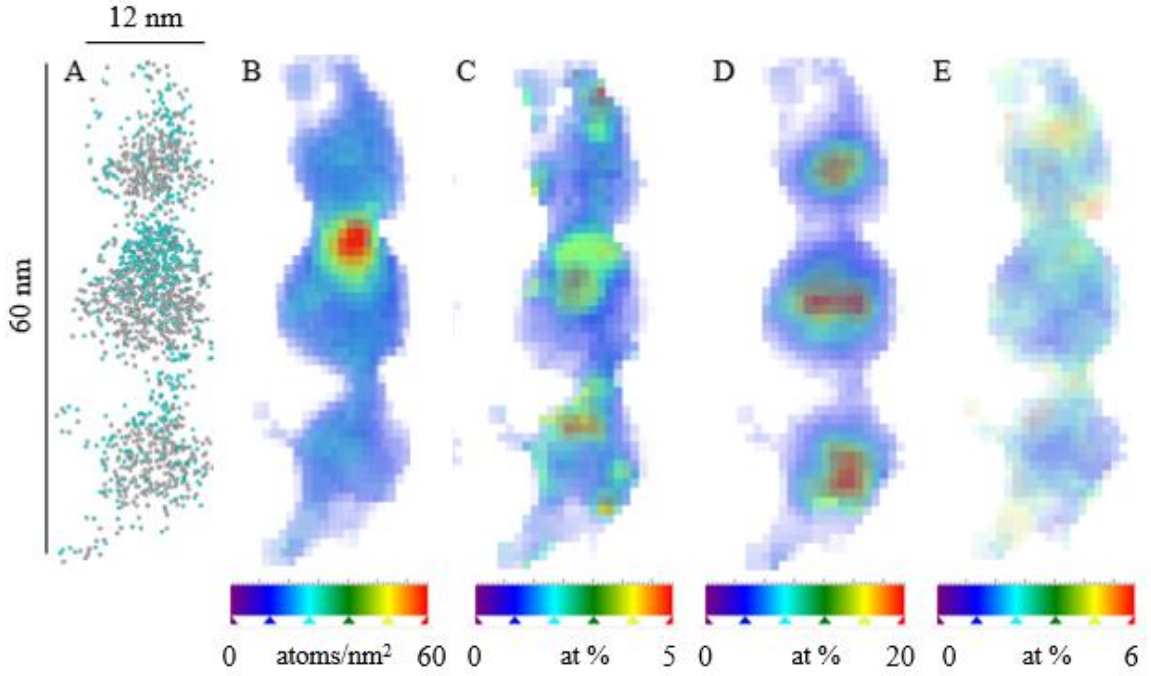


Figure 87: Rotated view along length of triple point in Figure 86. A) Aluminum ions in blue and silicon ions in grey. B) Density volume rendering. C) Aluminum concentration volume rendering. D) Silicon concentration volume rendering. E) Yttrium concentration volume rendering.

Figure 87 clearly demonstrates an inhomogeneous distribution of silicon ions along the length of the triple point, and to a lesser extent, aluminum ions. There exists a density hot spot along the length of the grain boundary, however it does not correlate with the silicon hotspots, demonstrating the silicon clustering may not be a density related artifact. A rotated view of the triple point can be seen in Figure 88.

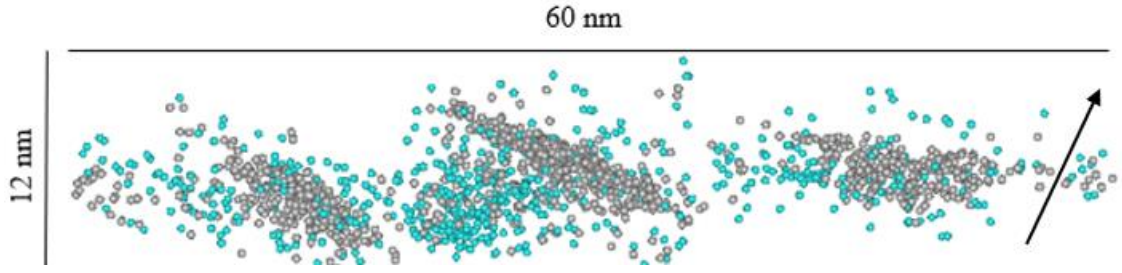


Figure 88: Silicon and aluminum ions at nonhomogeneous triple point seen in Figure 86 and Figure 87. The black arrow points in the direction of analysis towards the bottom of the tip.

The oblate morphology of the silicon clusters is likely a measurement artifact, especially as the long axes of the clusters are perpendicular with the direction of analysis. The difference

in evaporation field of the bulk versus the silicon rich triple point may cause the silicon to evaporate in large bursts, making localized chemical analysis difficult. The third and final type of triple point is like the first but is formed from grain boundaries demonstrating yttrium segregation, very weak aluminum segregation, and no silicon segregation. An example of this this type of triple point can be seen in Figure 89.

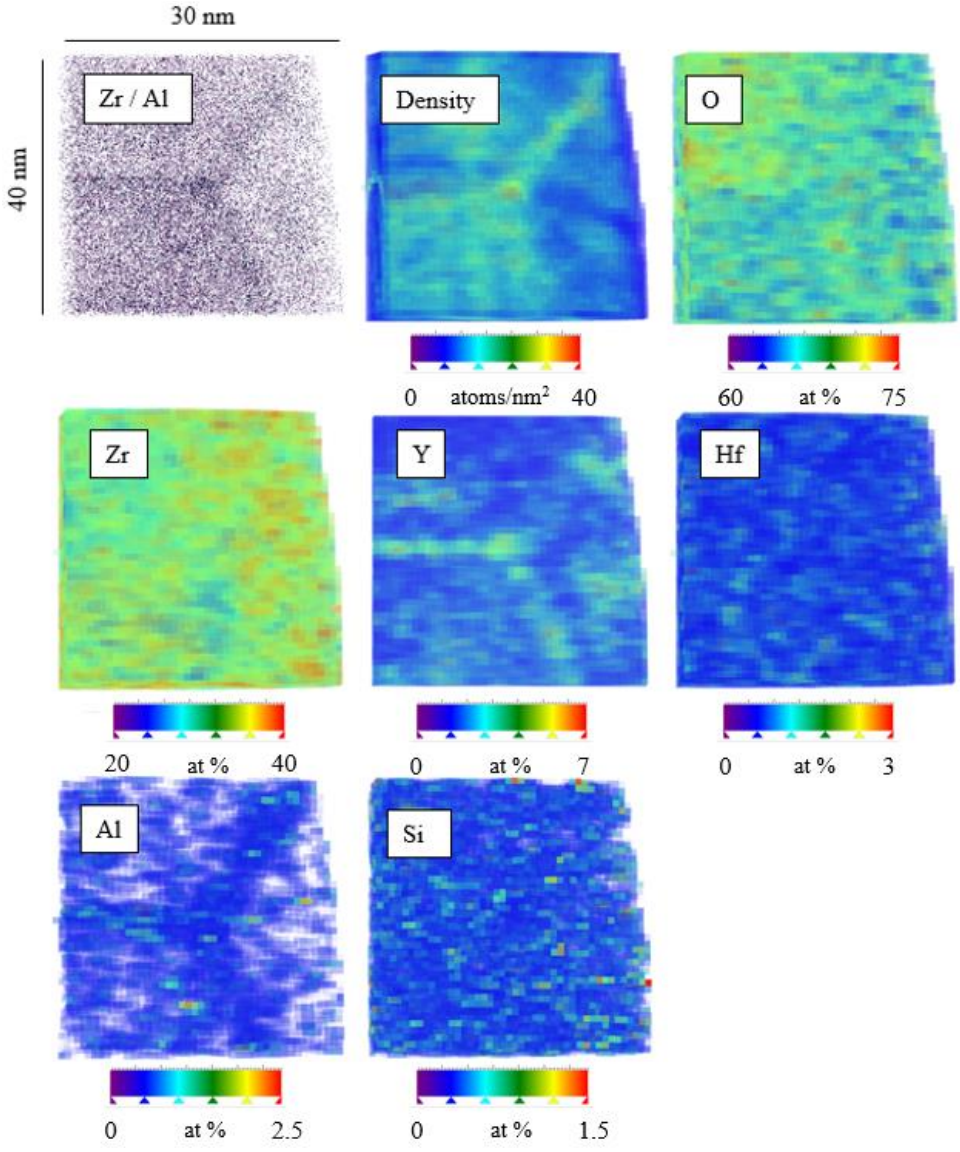


Figure 89: Triple point with segregation levels of yttrium equivalent to the abutting grain boundaries. The ion map shows zirconium ions in purple and aluminum ions in blue. The remainder of the maps are volume renderings of density and chemical species concentration.

This triple point shows similar segregation behavior to the first as well, with a similar

concentration of yttrium at the triple point compared to the abutting grain boundaries. The types of triple point based upon segregation behavior and type of specimen they were found in are summarized in Table 30.

Table 30: Summary of triple points present in 3YSZ APT samples

Specimen Type	Segregation Behavior
Conv: TP 1	Higher Si concentration at triple point than bordering grain boundaries
Conv: TP 2	Higher Si concentration at triple point than bordering grain boundaries
FS A	Similar concentration of Si, Y, and Al at triple point as at grain boundaries
FS C	Higher Si concentration at triple point than bordering grain boundaries
FS C He	Similar concentration of Y and Al at triple point as at grain boundaries. No Si at grain boundaries or triple point
FS C He 1Hr	Higher Si concentration at triple point than bordering grain boundaries

2 Discussion

2.1 Bulk Analysis

The averaged bulk composition measurements do not demonstrate any overwhelming trends relating composition to sintering method. As the field (measured by the zirconium CSR) used to measure the bulk composition increases, the following tend to occur: the measured oxygen concentration tends to decrease, and the measured zirconium, aluminum, and hafnium concentrations tend to increase. These trends are consistent with the analysis reported in Chapter IV. Even when comparing individual measurements from different specimens with CSR values within the error bars of one another, no consistent compositional trends emerge. It is therefore likely that the composition within the grains is equivalent

within the measurement sensitivity of the atom probe system when applied to this material system, considering the artifacts investigated previously in this thesis.

The lack of an oxygen deficiency at the cathodic ends of flash sintered specimens provides information regarding the type of charge carriers responsible for conduction during flash sintering. A quick calculation of the reduction expected at the cathode if all conduction is ionic (oxygen anions), oxygen is fed from the final quarter of the specimen near the cathode, no oxygen is replenished from the environment, and a current density of 100 mA/mm^2 is applied for 5 minutes through a specimen of 1 cm x 1 cm x 1 cm results in an atomic percent reduction of oxygen content of over 65%. These are indeed extreme conditions, however in an a highly oxygen depleted environment (such as the He gas used for this sample), little oxygen replenishment is expected during sintering. Therefore, significant electronic conduction also occurs during flash sintering alongside oxygen anion conduction.

The yttrium inhomogeneity observed in YSZ samples is like inhomogeneity observed in literature. The intragranular modulated lath-like features resemble modulated yttrium enrichment and depletion observed in EBPVD thermal barrier coatings [60], [88], [235]. A metastable yttrium supersaturated tetragonal phase formed by EBPVD demonstrates a modulated yttrium rich and yttrium lean microstructure following annealing and cooling [60], [235]. Sufficiently long annealing can even lead to the formation of cubic and tetragonal domains, while even longer annealing can lead to sufficient depletion of the yttrium lean phases to facilitate the martensitic tetragonal-monoclinic phase transformation [60], [235]. Computer simulation studies demonstrate the transformation is more consistent

with spinodal decomposition models, however may still be the result of nucleation and growth [235]. The annealing performed in these studies is conducted at 1482ºC, higher than the conventional sintering temperature used in this thesis, 1350ºC. Therefore, it is possible the yttrium inhomogeneity observed in the YSZ samples studied in this thesis are early precursors to the same phase transformation of the tetragonal phase into a modulated structure seen in EBPVD studies. The two-hour sintering time used for conventionally sintered samples may be sufficient for a small amount of zirconium and yttrium diffusion to occur and create a modulated structure. The YSZ phase diagram demonstrates that cubic and monoclinic phases are expected to form upon slow cooling of the conventionally sintered 3YSZ, as seen in Figure 90.

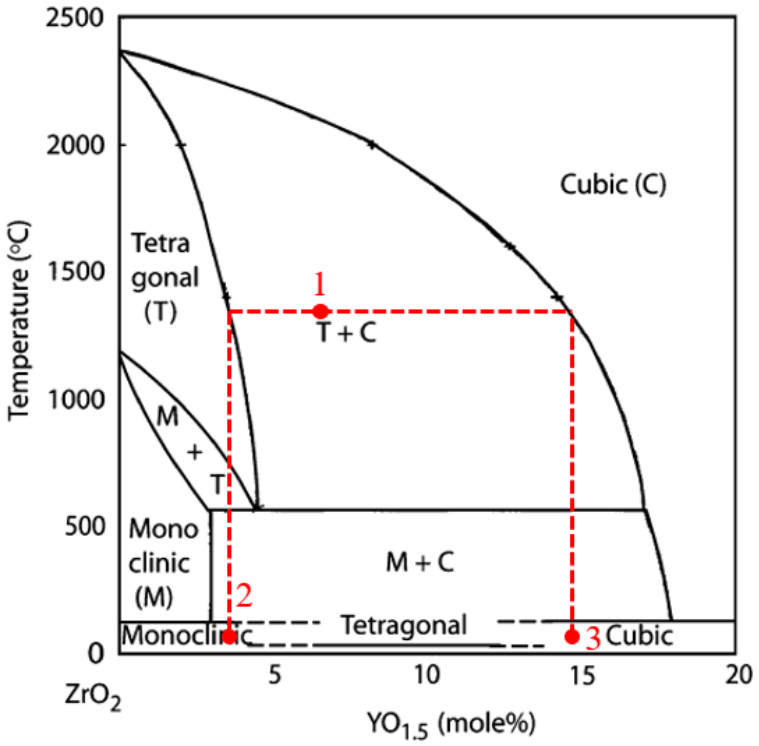


Figure 90: YSZ phase diagram with points indicating steps of slow cooling of 3YSZ. 1 indicates the 3YSZ at sintering temperature with tetragonal and cubic phases present. Upon slow cooling, 2 and 3 indicate both monoclinic and cubic phases should be present. Adapted from [60].

It is expected that the cooling rate of the furnace returning to room temperature along with

the fine grain size of the resulting sintered YSZ samples should be sufficient to stabilize the metastable tetragonal phase for the samples in this thesis [236], [237]. Indeed, the TKD conducted on YSZ samples prior to APT analysis indicates the analyzed grains are tetragonal. However, it is possible that the cooling times are slow enough in conventionally sintered samples that the earliest stages of phase separation into cubic and monoclinic phases are beginning. At high temperature, when the tetragonal phases and cubic phases coexist according to the phase diagram, the yttrium within the tetragonal grains begins to move to regions of the grain where transition to a cubic phase is just starting to begin. Upon cooling, the yttrium does not have enough time nor is it mobile enough to re-homogenize. The preference for cubic formation to begin in some regions of the grain as opposed to others remains a mystery, however it is possible the grain boundary adjacent rich regions begin a cascade of alternating enriched and depleted regions, or that the original powders themselves contain tetragonal grains with weak modulation. APT of the original starting powder would be useful tool in probing this latter possibility. The lathlike morphology may be a result of the minimization of mismatch and therefore strain energy. Literature is sparse regarding observation of a modulated structure in conventionally sintered tetragonal YSZ; however, limitations of conventional characterization techniques may contribute to this scarcity. The very fine scale of the yttrium enriched regions would probably be smaller than a TEM lamella thickness. Therefore, structural imaging of any lattice distortion caused by the alternating yttrium enriched and depleted structure or chemical characterization via EDS or EELS would prove difficult. The advantage of a three-dimensional characterization technique such as APT is once again highlighted.

The grain boundary adjacent yttrium enrichment and depletion regions seen in conventionally sintered specimens are potentially evidence of yet another phase transformation mechanism present in the studied 3YSZ specimens. Work conducted by Matsui *et al*. on 2.9-molar % 3YSZ studied the effect of sintering temperature on yttrium homogeneity [85]. Specimens sintered at the highest studied temperatures, 1500°C and 1650°C, began to show evidence of cubic yttrium enriched regions bordering grain boundaries [85], [238]. These yttrium rich regions eventually develop into distinct cubic grains, leading the authors to conclude the observations are evidence of the GBSIPTM [85], [238]. Matsui *et al.* observed the onset of this phase transformation at sintering temperatures of ~1500°C [85] [238]. However, the conventionally sintered samples displaying grain boundary adjacent yttrium enrichment in this section were sintered at 1350°C. The small size of the features in the atom probe results would likely be difficult to characterize using TEM chemical characterization techniques due to the small feature size versus the finite lamella thickness. As the concentration of yttrium increases at grain boundaries, and eventually cubic regions growing off grain boundaries, the concentration within the tetragonal grains decreases to provide the excess yttrium [238]. The grain boundary adjacent yttrium depletion regions found in the samples studied for this thesis are perhaps the earliest signs of this phenomenon. Like the modulated lath-like yttrium inhomogeneities, the dearth of literature analyzing these features in samples sintered at lower temperatures may be a result of the small size of the features compared to TEM lamella thickness.

Explanations regarding the observation of yttrium inhomogeneities in the YSZ samples have been proposed, however the question remains why these inhomogeneities are more prevalent

in conventionally sintered samples as evidenced by higher Pearson coefficients. One potential explanation is a difference in heating and cooling rates between the flash sintered and conventionally sintered samples. The phase separation occurring in EBPVD samples occurs when the tetragonal phase is annealed at high temperature for extended periods of time. Flash sintered samples spend less time at high temperature, due to rapid heating and cooling. Therefore, the flash sintered samples may demonstrate more homogenous yttrium distributions simply because there is not enough time at high temperature for yttrium to diffuse into a modulated structure within tetragonal grains. Additionally, rapid cooling rates help stabilize the metastable tetragonal phase at room temperature [237]. The cooling rate of flash sintered samples is probably higher than that of the conventionally sintered samples. The sample and furnace are at the same temperature during conventional sintering, and therefore the entire system cools together. During a flash sintering experiment, the furnace is kept at 900ºC while the sample reaches sintering temperature. Upon completion of flash sintering, there is a high temperature gradient between the sample and its environment, and cooling therefore occurs more quickly. The more rapid cooling associated with flash sintering may reduce the likelihood of the early signs of phase separation within tetragonal grains observed more frequently in conventionally sintered samples. It is also possible electrochemical reduction occurring during flash sintering plays a role in suppressing the yttrium inhomogeneity/phase transformation.

Reduction occurs by the formation of oxygen vacancies without electrons in the vacancy when zirconia is doped with yttria to achieve charge balance and accommodate the lower valence of the yttrium cation. However, further electrochemical reduction results from flash

sintering, as first reported in J.A. Downs' doctoral thesis [239]. Reduction occurs when the movement of charge carriers (oxygen anions) in the flash sintered sample outpaces the consumption and incorporation of environmental oxygen in the atmosphere [239]. Reduction often results in blackening of YSZ specimens [240]. Blackening was observed in the flash sintered YSZ specimens studied in this thesis, and the strength of the reducing environment was well correlated with degree of blackening (the FS C R He 1Hr specimen was almost entirely black after sintering). The mode of reduction occurring during the flash sintering of YSZ is not entirely clear, however. The reduction of YSZ could result in several different phenomena: the formation of oxygen vacancies with one or two electrons in the vacancy site (F-centers), oxygen vacancies without electrons present, or non-equilibrium oxidation states of Zr (Zr^{3+} or Zr^{2+}) [241]–[245]. The reduction of YSZ via flash sintering could result in a more homogenous intragranular distribution of yttrium within tetragonal grains for two main reasons. Firstly, the reduction of the YSZ can increase the density of oxygen vacancies compared to conventionally sintered specimens. Molecular dynamic and Monte Carlo simulations show yttrium and oxygen vacancy co-segregation to features such as grain boundaries is energetically favorable [246], [247]. It is possible that with higher levels of oxygen vacancies, and therefore a higher number of energetically favorable sites for yttrium within the flash sintered 3YSZ samples, yttrium is less likely to form yttrium rich features within tetragonal grains serving as precursors to phase transformation.

The second proposed mechanism leading to the more homogenous distribution of yttrium within the flash sintered grains is based upon improved stabilization of the cubic phase at room temperature by the flash sintered samples. Stabilization of the cubic phase at room

temperature is often the result of doping with an oxide containing a cation with a larger ionic radius and lower valency than zirconium (such as Y_2O_3) [87], [248], [249]. The reduction of flash sintered YSZ and formation of Zr^{3+} or Zr^{2+}, with their lower valencies and larger ionic radii than Zr^{4+}, could lead to more stabilized cubic phase present at room temperature [250]. Studies have also demonstrated oxygen vacancies (without cation doping) can stabilize the cubic phase at reduced temperatures by breaking O-Zr bonds, changing local structure, hindering the motion (via vibration modes) of oxygen atoms, and locking the crystal into the cubic phase [99], [100]. The increased stabilization of the cubic phase via either of these two reduction mechanisms could increase the total proportion of separate cubic grains present in flash sintered specimens, relatively deplete yttrium from tetragonal grains, and therefore reduce the likelihood of localized segregation/inhomogeneity within these tetragonal grains. The bulk compositional measurements of the tetragonal grains (as identified using TKD) do not demonstrate depletion of yttrium from flash sintered samples, yet the field dependence of yttrium concentration demonstrated in Chapter IV could overwhelm any subtle compositional difference. An increased proportion of the cubic phase in flash sintered specimens could be verified using quantitative XRD or TKD on TEM foils. Improved tetragonal phase stabilization resulting from electrochemical reduction occurring during flash sintering has also been observed in a study conducted by Dong *et al.* [96]. Dong's study found the martensitic tetragonal to monoclinic phase transformation often observed in large tetragonal grains is suppressed in electrochemically reduced flash sintered samples [96]. The authors postulate the effect may be due to reduction (either caused by the presence of oxygen vacancies or lower valence Zr ions) stabilizing the tetragonal phase, similar to the explanations proposed in this thesis for the suppression of a modulated structure [96].

2.2 Zirconium Oxycarbide Phase

The presence of the zirconium oxycarbide phase in the FS C He 1Hr specimen could be the result of several different factors. Organic additives are present in the powder processing of the YSZ samples as both dispersant agents and binder phases. However, these organics should be removed during an 800°C burnout conducted in air. Incomplete burnout of these organics could account for the carbon found in the oxycarbide phase. Additionally, the furnaces, dies, and presses used to process the 3YSZ green bodies are also used to process B_4C doped SiC specimens. Residual B_4C/SiC powder could account for the carbon which forms the oxycarbide phases in the FS C He 1Hr specimen. This explanation is most likely considering the presence of trace boron within the oxycarbide, as the organic additives are unlikely to contain boron.

Regardless of where the carbon needed to form the oxycarbide phase comes from, the zirconium oxycarbide phases present in the FS C He 1Hr are a novel result, as a review of literature current to the writing of this thesis yielded no other instance of the flash sintering of zirconium oxycarbide. Dense zirconium oxycarbide samples have been successfully sintered using carboreduction at 2023 K for 8 hours followed by SPS at 2460 K under 50 MPa of pressure for 5 minutes [251], [252]. Compared to flash sintering in the absence of applied external pressure for one hour like the FS C He 1Hr specimen, the carboreduction/SPS processes are undoubtedly more energy intensive. Work by Gendre *et al.* reported several zirconium oxycarbide stoichiometries: $ZrC_{0.94}O_{0.05}$, $ZrC_{0.89}O_{0.07}$, $ZrC_{0.79}O_{0.13}$ formed using carboreduction/SPS [252]. The zirconium oxycarbide produced in this thesis incorporates a much higher oxygen content, yielding a chemical composition of

$ZrC_{0.59}O_{0.47}$. The oxycarbide in this thesis also contains trace yttrium, hafnium, and boron. Zirconium oxycarbides are promising materials for electrocatalytic processes, and further examination of the suitability of pressureless flash sintering when applied to zirconium oxycarbides of various compositions could yield optimized results [253] [254].

2.3 Grain Boundary Analysis

Both the Gibbsian excess measurements and the grain boundary yttrium compositional measurement demonstrate no significant relationship between grain boundary misorientation and segregation behavior. Limited sample sizes could play a role in the lack of a pattern. For a given sample type analyzed in this thesis, the highest number of grain boundaries successfully analyzed was only 6 boundaries. However, even with large sampling sizes, grain boundary misorientation does not always demonstrate a clear relationship with chemical segregation [255]. Grain boundary misorientation angle accounts for only one of the five geometric degrees of freedom of a grain boundary [6]. Other studies in the literature demonstrate that the similarity of a grain boundary to a special CSL grain boundary can show better correlation with grain boundary segregation [255], [256]. Using Oxford Instruments HKL Channel 5 software, no CSL grain boundaries were identified in the 3YSZ atom probe tips that yielded grain boundaries in reconstructions. Out of 42 analyzed grain boundaries, none were CSL boundaries as identified by commercial software. Many grain boundary studies of ceramics, especially TEM/STEM studies, analyze segregation and structuring behavior at model CSL boundaries. The work presented in this thesis indicates that in polycrystalline sintered 3YSZ, these boundaries are indeed rare, and model grain boundary studies may not provide significant engineering relevant information.

The two specimens subjected to the strongest electrochemical reducing environments during sintering, FS C He and FS C He 1Hr, demonstrated significantly lower Al and Si segregation values than other specimen types. Several possibilities exist for why these specimens demonstrate lower levels of silicon and aluminum segregation. The first possibility is that the sample size of this study is insufficient, and the low aluminum/silicon levels are just the result of random sampling. Secondly, it is possible an oxygen depleted environment affects the mobility of aluminum and silicon in 3YSZ, and these two species therefore do not segregate to grain boundaries as effectively during sintering. Yet, the bulk compositional measurements do not show elevated intragranular Al or Si concentration for FS C He and FS C He 1Hr specimens. Literature suggests Al scavenges Si from grain boundaries to triple points [16],[17]. Perhaps a strong electrochemically reducing environment promotes this scavenging effect, and the grain boundaries demonstrate lower Al and Si segregation due to higher segregation to triple junctions. The summary of analyzed 3YSZ triple points in Table 30 does not support this finding, though the sample size of triple points is very limited. Triple points very often fractured during APT analysis, therefore increasing sampling would prove to be a tedious and challenging task. A study conducted by Hughes *et al*. concluded that prolonged exposure to high temperature through annealing of 3YSZ led to the accumulation of silicon on the specimen surface and depletion of silicon at grain boundaries [257]. If a reducing environment increases silicon mobility in 3YSZ, maybe silicon is leached from the grain boundaries to the surface more effectively.

Regardless of why the FS C He and FS C He 1Hr specimens demonstrate lower Si and Al segregation to grain boundaries, and assuming the effect is not dictated by random sampling,

the engineering implications are significant. High levels of silicon at grain boundaries create amorphous phases that increase grain boundary ion resistivity far above the levels within bulk 3YSZ [75], [257], [258], [79]. For applications such as solid oxide fuel cells, the ionic conductivity of 3YSZ is crucial. If flash sintering 3YSZ samples in a strong reducing environment can reduce the presence of silicon rich phases at grain boundaries, and in turn reduce grain boundary resistivity, then the sintering technique may be an important tool for fuel cell manufacturing. Additionally, grain boundary segregation has a significant effect on grain boundary diffusivity in many ceramic systems [259]. Grain boundary diffusivity has a significant effect on phenomena such as high temperature creep and sintering, and similar effects could be present in the flash sintered samples demonstrating reduced segregation [259]. There were no evident relationships between sintering method and grain boundary oxygen or yttrium content. In broad terms, the grain boundaries observed in all the 3YSZ specimens can be separated into four categories based upon chemical segregation behavior: boundaries with yttrium, aluminum, and silicon segregation, boundaries with only yttrium segregation, boundaries with aluminum and silicon segregation, and boundaries with only aluminum segregation.

The grain boundary structuring observed in Figure 80 and Figure 83 highlights the utility of the three-dimensional resolving power of APT. Low angle grain boundaries in olivine and titanite observed using APT have shown similar structuring to Figure 80 at grain boundary dislocations, and it is possible the structuring seen in 3YSZ is due to similar dislocation segregation [21], [22]. It is also possible that structured grain boundaries demonstrate unique mechanical/electrical/chemical properties. APT could prove to be a powerful tool enabling

grain boundary engineering in 3YSZ systems.

2.4 Triple Point Analysis

The types of triple points present in each specimen type can help provide information relating to the distribution of resistive species within 3YSZ samples. The presence of high concentration Si triple points can be evidence of successful Al scavenging leading to a reduction in grain boundary resistivity within the specimen as a whole [75], [94]. However, the results in section 1.3 indicate that the highly localized differences in conductivity and evaporation field caused by high silicon enrichment can lead to significant measurement artefacts, which in turn have a strong adverse effect on the possibility for high resolution chemical measurements. It is possible that different run conditions could help alleviate the effects of these artefacts. Even so, the high susceptibility of specimen fracture when analyzing triple points further complicates the issue. Other analytical techniques, such as STEM EDS, can characterize these triple junctions, however using EDS analysis suffers from partial peak overlaps of the Si-K, Y-L, and Zr-L peaks, limiting quantitative analysis of results from the technique [74].

3 Conclusions

In this chapter, the effect of sintering conditions on microstructural chemistry of 3YSZ was probed using APT. The bulk analyses demonstrated a lack of trends relating sintering conditions with composition. A binomial grid-based frequency analysis of the distribution of yttrium within specimen grains demonstrated flash sintered specimens yielded more homogenous yttrium distributions than conventionally sintered specimens. A nonhomogeneous distribution of yttrium within the bulk of 3YSZ specimens can lead to unwanted phase transformations. Yttrium rich regions are likely to adopt a cubic structure if

given time, and yttrium lean regions may develop into a monoclinic phase upon cooling [85], [87], [88], [238]. Unwanted phase transformation can lead to significant property changes with serious engineering ramifications, and a greater understanding of the phase transformation mechanism occurring during 3YSZ sintering is crucial. Novel evidence for the flash sintering of zirconium oxycarbide has been shown, opening the door to further experimentation towards efficient oxycarbide sintering.

The grain boundary analysis demonstrates a strong reducing environment may affect the segregation of aluminum and silicon to 3YSZ grain boundaries. Further experimentation is necessary to collect a statistically significant amount of data, however the implications of such an effect are of interest as siliceous phases at grain boundaries can have an adverse effect on important macroscopic properties [75], [94], [257], [258]. Finally, the triple point analyses demonstrate that like grain boundaries in 3YSZ, triple points differ significantly based on what types of boundaries and grains create the junction. There does also exist evidence of sub-structuring along the length of some triple points. However, it is important to consider measurement artefacts when analyzing microstructural features such as these triple points with significantly different evaporation characteristics from the specimen bulk.

Chapter VII

SiC Analysis

All APT results in this chapter were collected using identical experimental parameters in accordance with the optimal parameters as assessed in Chapter IV: an operating temperature of 50 K, a laser energy value of 30 pJ, a pulse frequency of 200 kHz, and a constant detection rate of 0.5%.

1 Results

1.1 Bulk SEM Analysis

1.1.1 EBSD Analysis

Four SiC polytypes were observed in the SiC specimens analyzed in this thesis: 6H, 4H, 3C, and 15R. The distribution and morphology of the polytypes can be seen in the EBSD phase maps found in Figure 96. The phase maps were post-processed using AztecCrystal™ to smooth wild spikes.

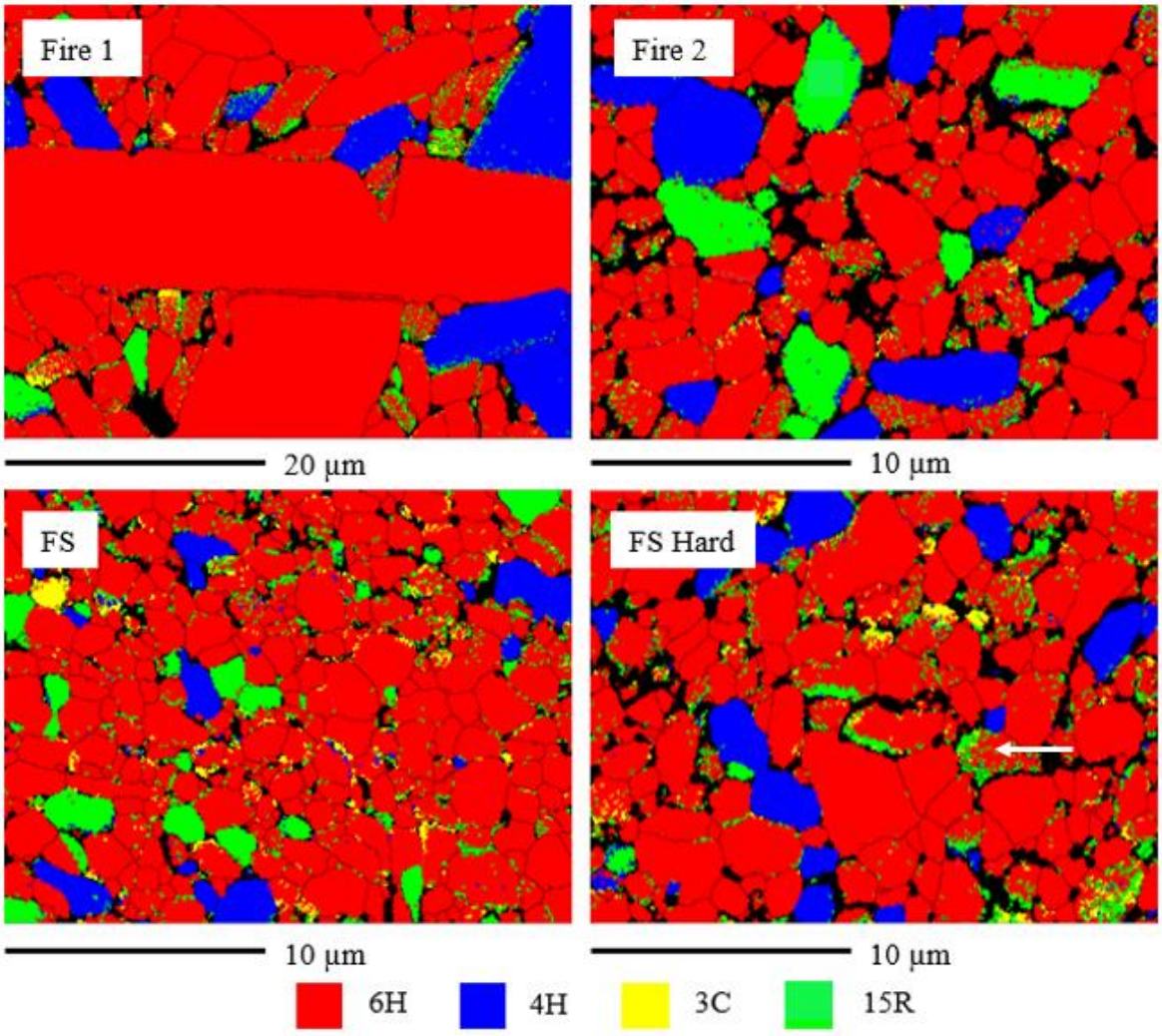


Figure 91: EBSD phase maps of polymorphs present in each type of specimen. Note the difference in scale for the Fire 1 specimen.

The Fire 1 scan demonstrates abnormal elongated 6H and 4H grains. All scans show mixing of the 15R and 6H polytypes within some grains. An example of this mixing can be seen in the grain singled out using a white arrow in Figure 91. The average phase fraction of each polytype for each specimen is summarized in Figure 92. The error bars represent the standard errors of the mean calculations.

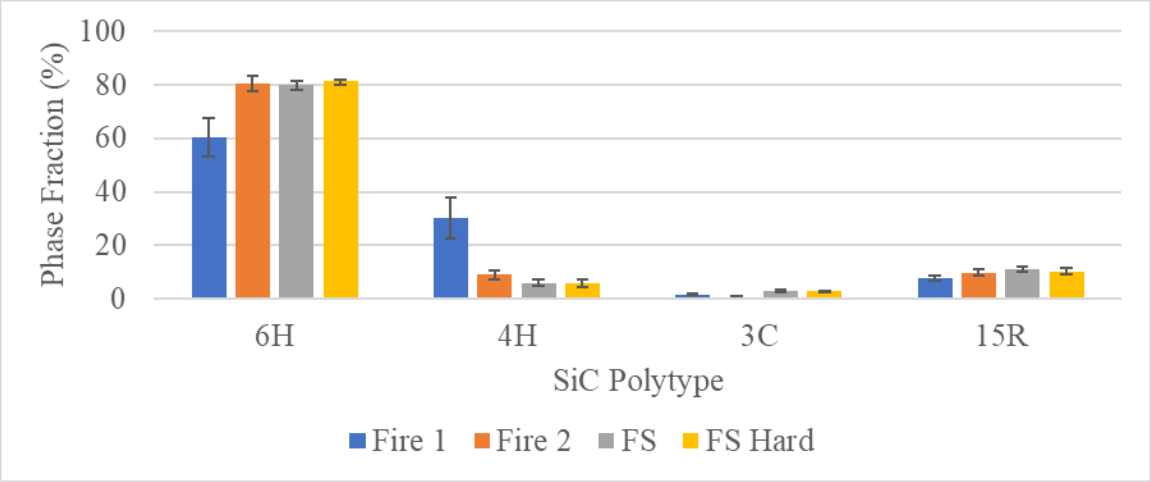


Figure 92: Proportion of polytypes found in each type of SiC specimen

There exists a significant difference in the proportion of 6H and 4H polytypes in the Fire 1 samples compared to the rest of the samples. Using phase contrast images collected during EBSD analysis, the average grain size of each specimen type was found using the linear intercept method. These average grain sizes along with standard error uncertainties can be found in Table 31.

Table 31: Grain size of SiC specimens

Type	Grain Size (μm)
Fire 1	9.9 ± 1.1
Fire 2	3.6 ± 0.2
FS	2.1 ± 0.1
FS Hard	3.1 ± 0.1

The Fire 1 samples demonstrate a significantly larger average grain size than the other specimens.

1.1.2 EDS Analysis

EDS scans of the different specimen types were conducted to examine the distribution of the

two major sintering aids included in the SiC powders used to fabricate specimens: carbon and boron. A representative EDS scan of a Fire 2 specimen can be seen in Figure 93.

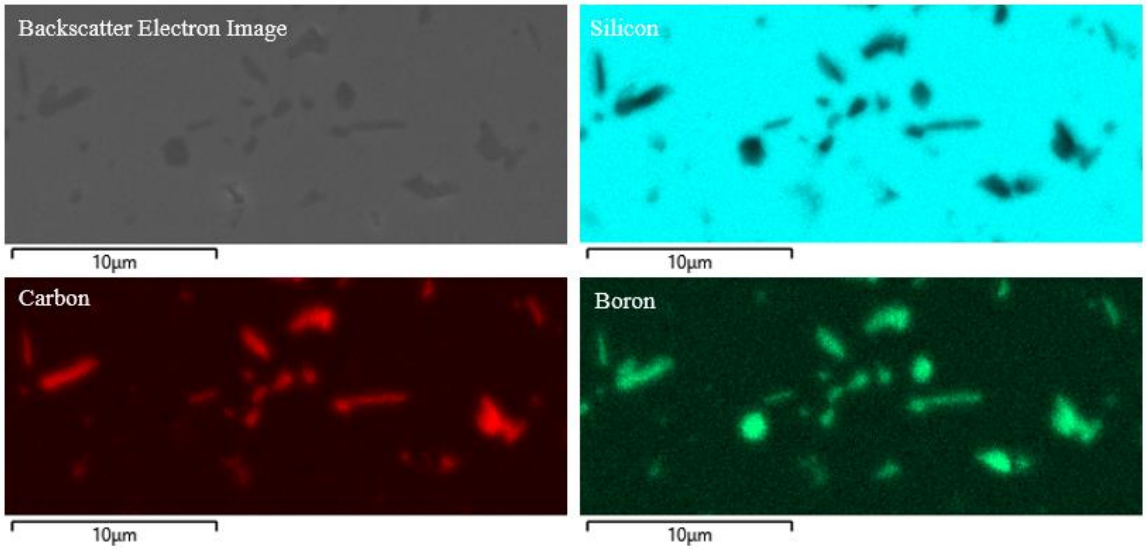


Figure 93: Backscattered electron image and EDS maps of a Fire 2 SiC specimen

The EDS scans clearly demonstrate highly correlated regions of boron and carbon content, which are also clearly distinguishable using backscatter imaging. Additionally, regions demonstrating only boron enrichment or only carbon enrichment were observed. These localized enriched regions were targeted for APT lift out to conduct high resolution chemical analysis discussed in section 1.2.4.

1.2 APT Bulk Analysis

1.2.1 SiC Bulk Composition

To measure the bulk composition of grains, rectangular ROIs were positioned away from microstructural features such as grain boundaries, phase boundaries, and FIB ion implantation regions. The composition of each ROI was then calculated alongside the Si^{++}/Si^{+} CSR. The results of this analysis can be seen in Figure 94.

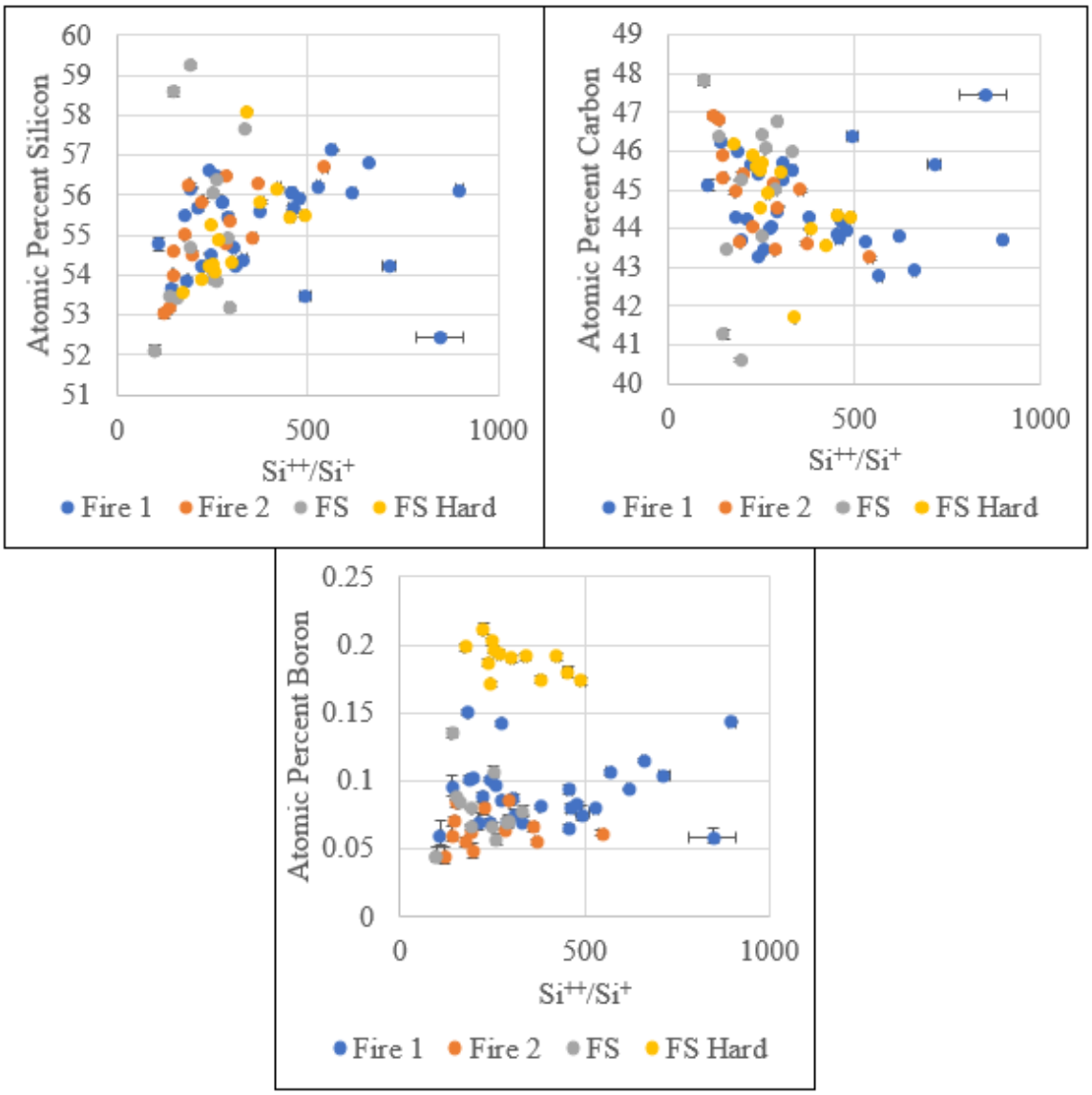


Figure 94: Bulk composition of SiC grains versus Si CSR

All specimens demonstrate some solid solubility of boron within SiC grains, yet the FS Hard specimens demonstrate a significantly higher boron concentration than the other specimen types. Visual inspection of FS Hard specimens demonstrates the clear presence of boron rich clusters, as seen in Figure 95.

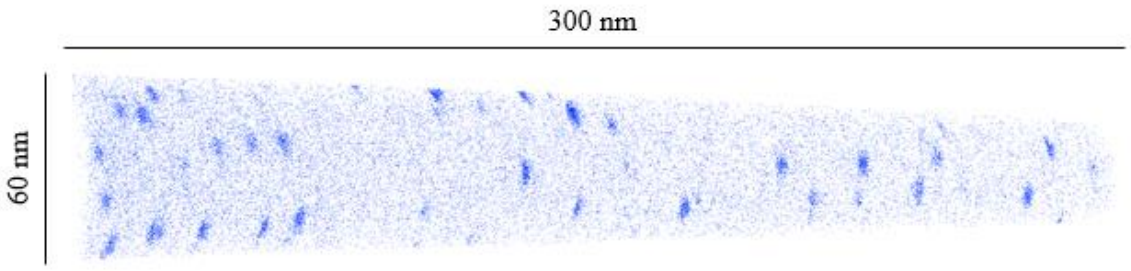


Figure 95: Boron clusters present in a FS Hard specimen. The blue dots represent boron ions.

Boron rich clusters were also observed in the other specimen types, although much less frequently. To quantitatively compare the prevalence of clusters in each type of specimen, a binomial grid-based frequency analysis was used.

1.2.2 Binomial Grid-Based Frequency Analysis

The results of the binomial grid-based frequency analysis for each specimen type can be seen in Figure 96. Additionally, the Pearson coefficient of each analyzed grain was also plotted alongside its corresponding Si^{++}/Si^{+} CSR to probe the possibility of the apparent clustering being an electric field strength artefact.

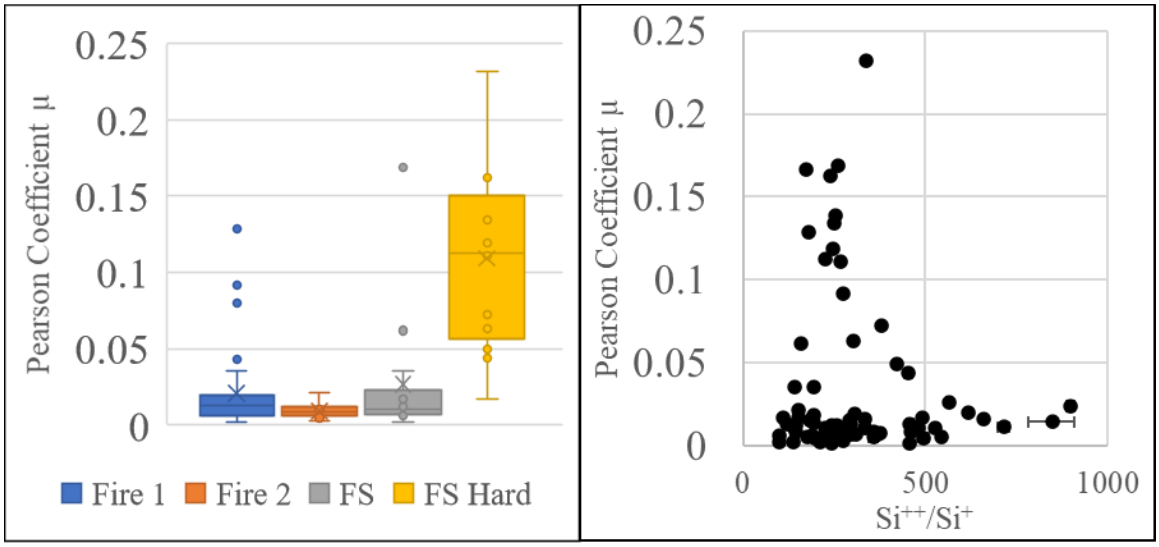


Figure 96: Binomial grid-based frequency analyses for SiC grains

The box and whisker plot shows FS Hard grains demonstrate significantly higher Pearson

coefficients than other specimens, and the scatter plot demonstrates the coexistence of low Pearson coefficient grains and high Pearson coefficient grains at similar electric field values.

1.2.3 Cluster Analysis

Radius of gyration is a commonly used measurement to describe the physical size of clusters found in APT datasets [165]. However, close inspection of the clusters found in SiC datasets shows the clusters are often elongated perpendicular to the direction of analysis, a sign that the morphology of the clusters may be a result of an electric field artefact [262]. As such, the size of the clusters found in the SiC specimens were instead characterized by studying the distribution of the number of ions constituting each of the clusters identified in each specimen. An example of the elongation of clusters along axes perpendicular to the analysis direction as well as a box and whisker plot of the size distribution of clusters in SiC specimens can be seen in Figure 97.

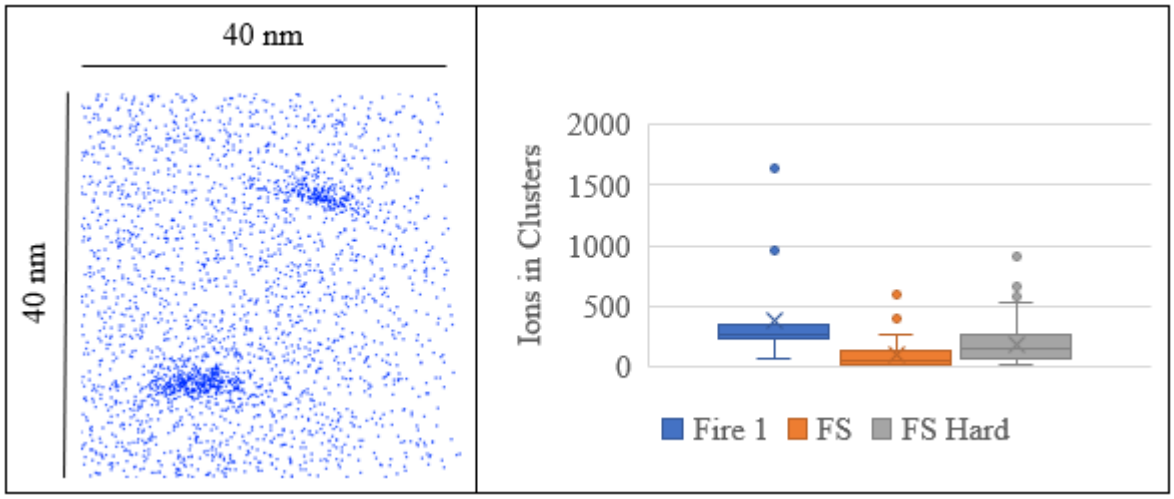


Figure 97: Boron atom maps of two boron clusters and a box and whisker plot of the distribution of cluster sizes for each specimen

There exists no significant difference in the size distribution of clusters between the different types of samples. The boron, silicon, and carbon content of each identified cluster can be seen in the ternary diagrams found in Figure 98.

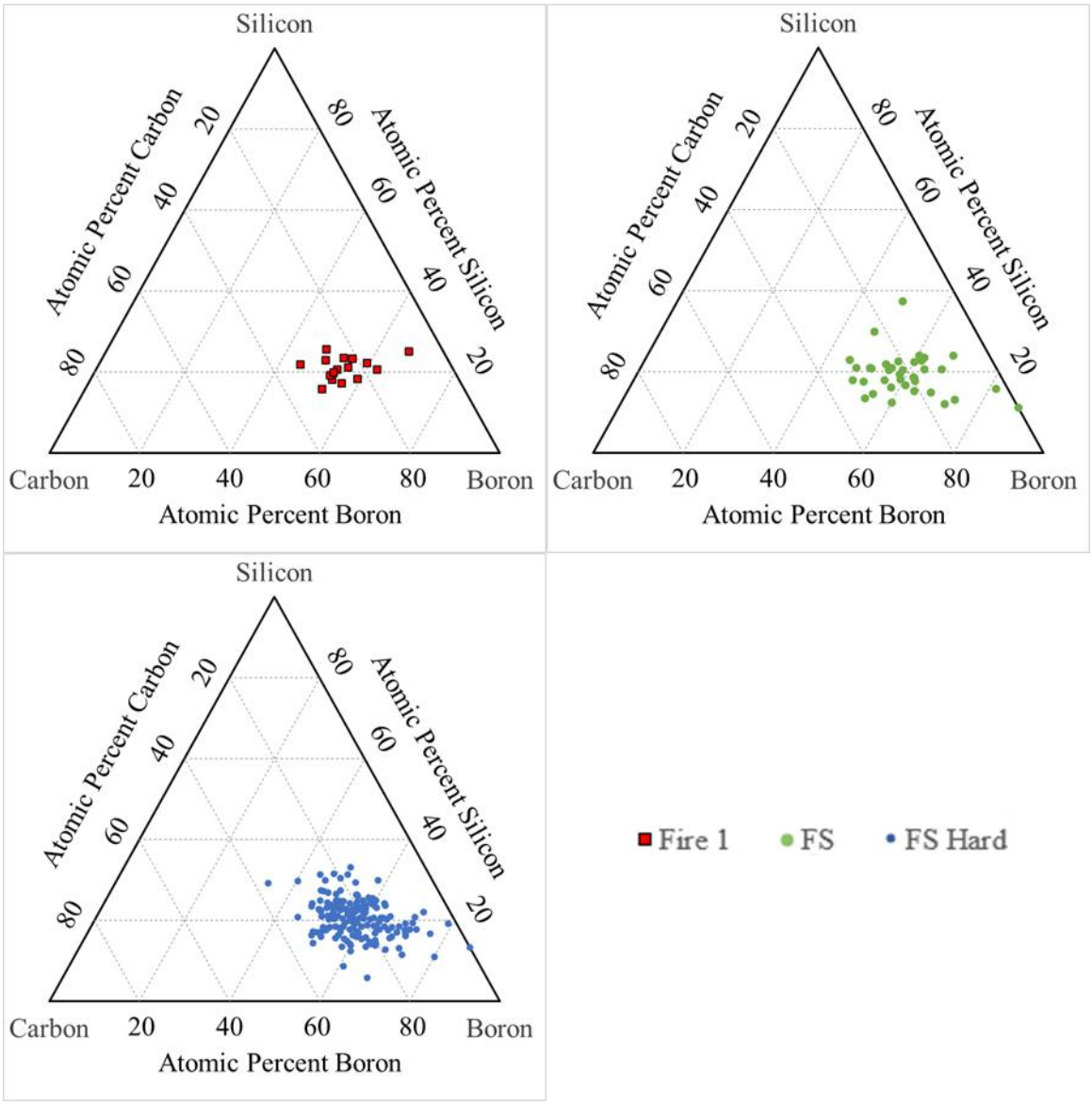


Figure 98: Ternary diagrams demonstrating cluster composition

The averaged composition of clusters for each specimen type can be found in Table 32.

Table 32: Averaged cluster composition for SiC specimens

Type	Silicon	Carbon	Boron
Fire 1	20.8 ± 0.7	24.1 ± 1.5	54.8 ± 1.3
FS	19.4 ± 0.8	20.8 ± 1.3	59.6 ± 1.5
FS Hard	20.6 ± 0.4	21.4 ± 0.5	57.9 ± 0.6

1.2.4 B_4C Bulk Composition

The APT measured composition of the boron/carbon rich features identified in the EDS scans found in section 1.1.2 can be seen in Table 33.

Table 33: Composition of B_4C grain analyzed for each specimen type

Type	B^{++}/B^{+}	B	C	Si	Al
Fire 1	1.13 ± 0.01	78.83 ± 0.02	21.06 ± 0.02	0.08 ± 0.01	0.03 ± 0.01
Fire 1	1.07 ± 0.01	76.50 ± 0.07	23.38 ± 0.06	0.08 ± 0.01	0.03 ± 0.01
Fire 2	1.19 ± 0.01	78.16 ± 0.03	21.77 ± 0.04	0.06 ± 0.01	0.00 ± 0.00
FS	1.00 ± 0.02	77.81 ± 3.38	22.13 ± 3.57	0.06 ± 0.04	0.00 ± 0.00
FS Hard	1.13 ± 0.01	78.10 ± 0.02	21.70 ± 0.10	0.16 ± 0.01	0.01 ± 0.00

The boron to carbon ratios are consistent with expected compositional measurements of B_4C.

1.3 APT Grain Boundary Analysis

1.3.1 Gibbsian Interfacial Excess

As discussed in Chapter V, Gibbsian interfacial excess measurements are not suitable for systems within which the distribution of segregating impurities is not homogenous within the specimen bulk. The presence of boron clusters would therefore preclude Gibbsian interfacial excess measurements of boron in SiC specimens. However, the specimens studied in this thesis demonstrated regions to either side of a grain boundary with no identifiable clustering, as seen in Figure 99.

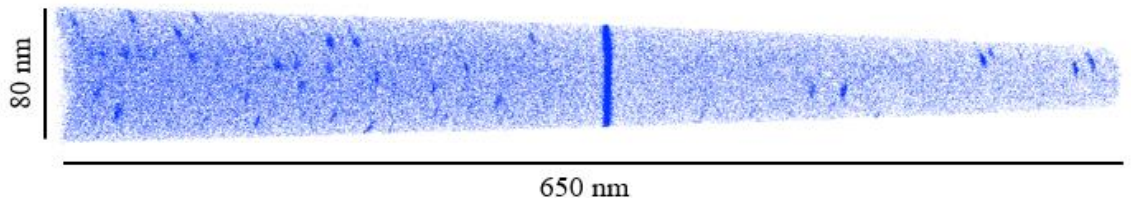


Figure 99: Boron ion map demonstrating distribution of boron clusters in relation to grain boundary

Therefore, if the rectangular ROIs used to isolate the grain boundary and each abutting grain do not extend into the bulk regions containing boron clusters, a Gibbsian interfacial excess measurement is appropriate. Figure 100 shows Gibbsian interfacial excess measurements for Al, B, Si, and C for 29 6H-6H grain boundaries plotted versus grain boundary misorientation.

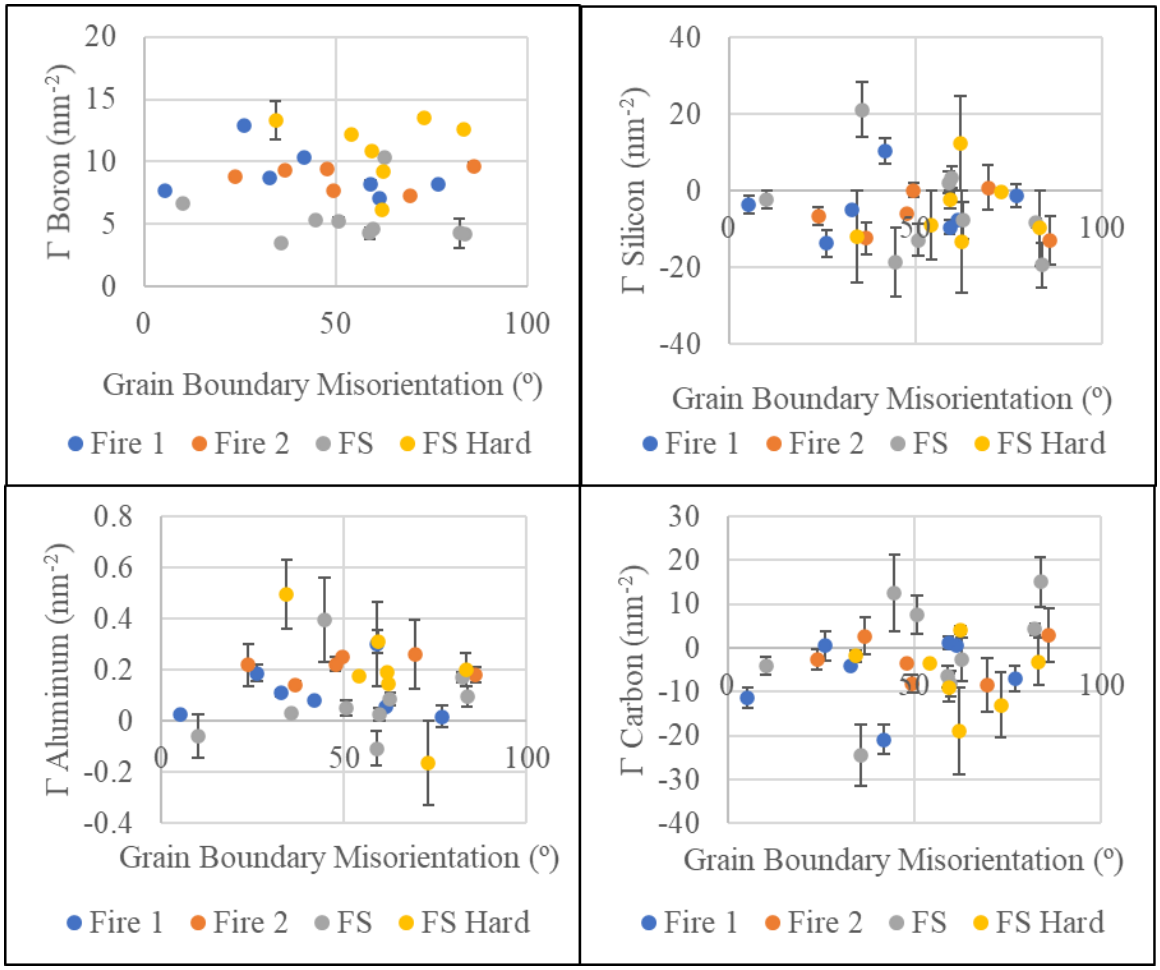


Figure 100: Gibbsian interfacial excess values for chemical species in SiC specimens

No relationship between grain boundary misorientation and segregation is discernable. The

FS samples demonstrate significantly lower boron segregation across a range of misorientiation values.

1.3.2 Polytype Boundary

As well as the 6H-6H grain boundaries analyzed in the previous section, the APT analysis in this thesis also included several 6H-4H polytype boundaries. Gibbsian interfacial excess measurements of boron and aluminum for the 5 polytype boundaries analyzed can be seen in Table 34.

Table 34: Gibbsian interfacial excess values for 6H-4H polytype boundaries

	Γ and Γ error			
Type	**B**		**Al**	
Fire 1	12.87	0.32	0.24	0.04
Fire 1	8.30	0.09	0.12	0.02
Fire 1	9.07	0.19	0.42	0.05
Fire 2	7.43	0.01	0.29	0.06
FS	4.60	0.03	0.17	0.06

Gibbsian interfacial excess measurements for Si an C were not included, as analysis demonstrated a systematic difference in Si and C content between 6H and 4H polytypes. A representative concentration profile across a 6H-4H polytype boundary can be seen in Figure 101.

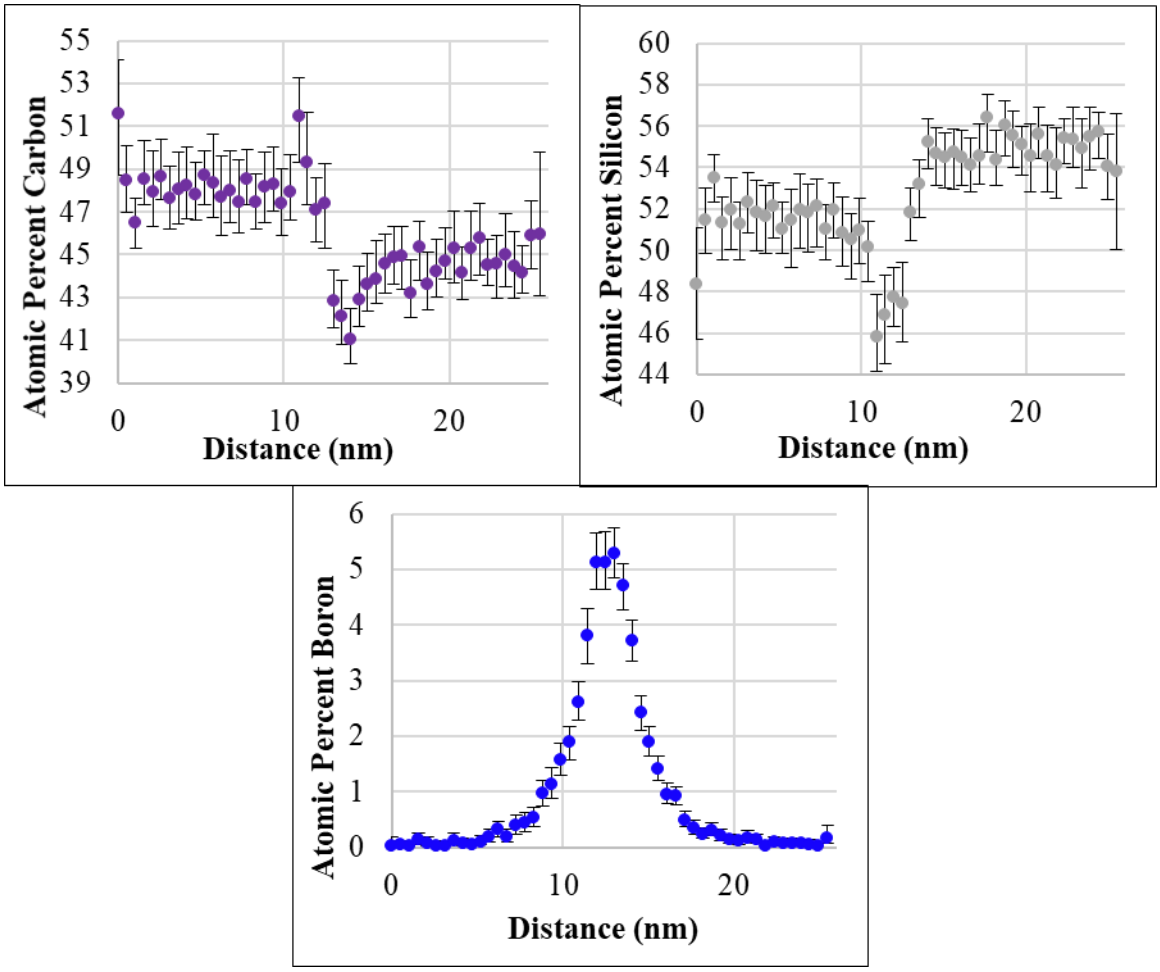


Figure 101: Concentration profile across 6H-4H polytype boundary in Fire 1 sample. The left of the plots corresponds to a 6H polytype while the right corresponds to a 4H polytype

There was no evidence of Al segregation to this polytype boundary, yet clear boron segregation is present like grain boundaries. The 6H polytype grain demonstrates higher carbon content and lower silicon content versus the 4H polytype grain, consistent with analyses done on the other polytype boundaries.

1.4 APT B_4C-SiC Phase Boundary Analysis

The specimens containing B_4C phases isolated for APT analysis using EDS discussed in section 1.2.4 often yielded phase boundaries as well, one of which can be seen in Figure 102.

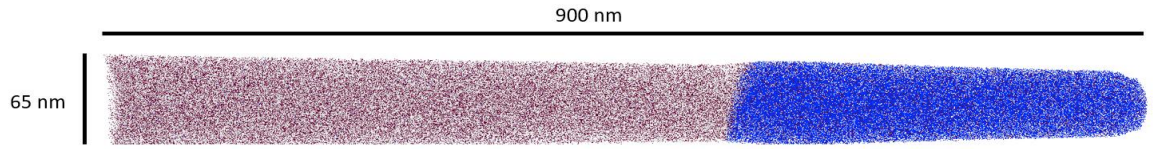


Figure 102: B_4C/SiC phase boundary from a Fire 2 sample. Purple ions represent carbon, grey ions represent silicon, and blue ions represent boron.

This phase boundary was analyzed using a concentration profile which can be seen in Figure 103.

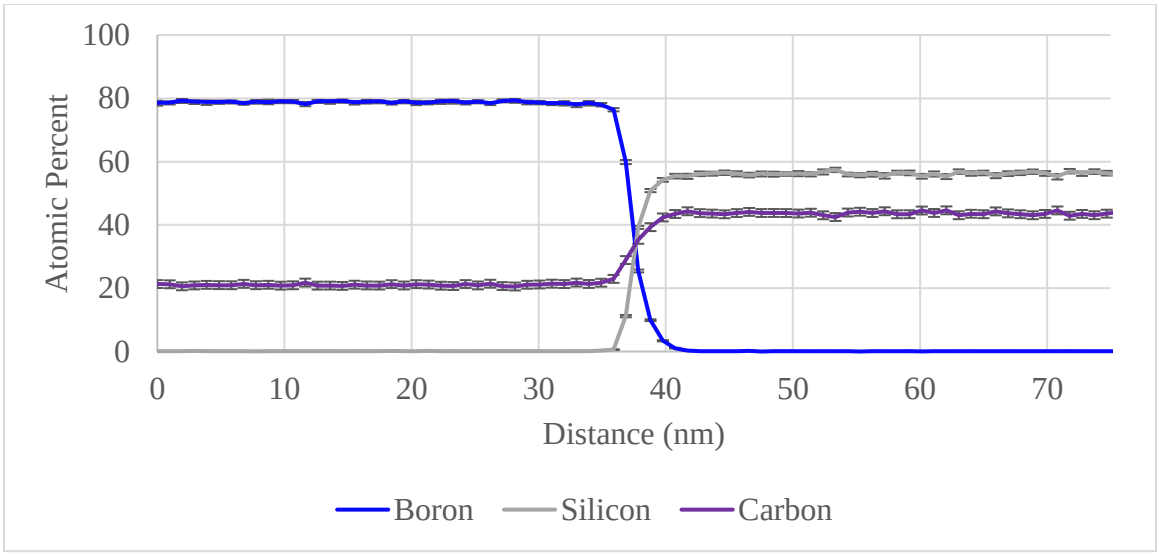


Figure 103: Concentration profile across B_4C/SiC phase boundary in FS Hard specimen

The phase boundary shows no significant impurity segregation and a finite width of approximately 7 nm.

1.5 APT Triple Point Analysis

Triple points were targeted using TKD and analyzed using APT. An ion map, a density map, and concentration maps for a representative triple point from a FS Hard specimen can be seen in Figure 104.

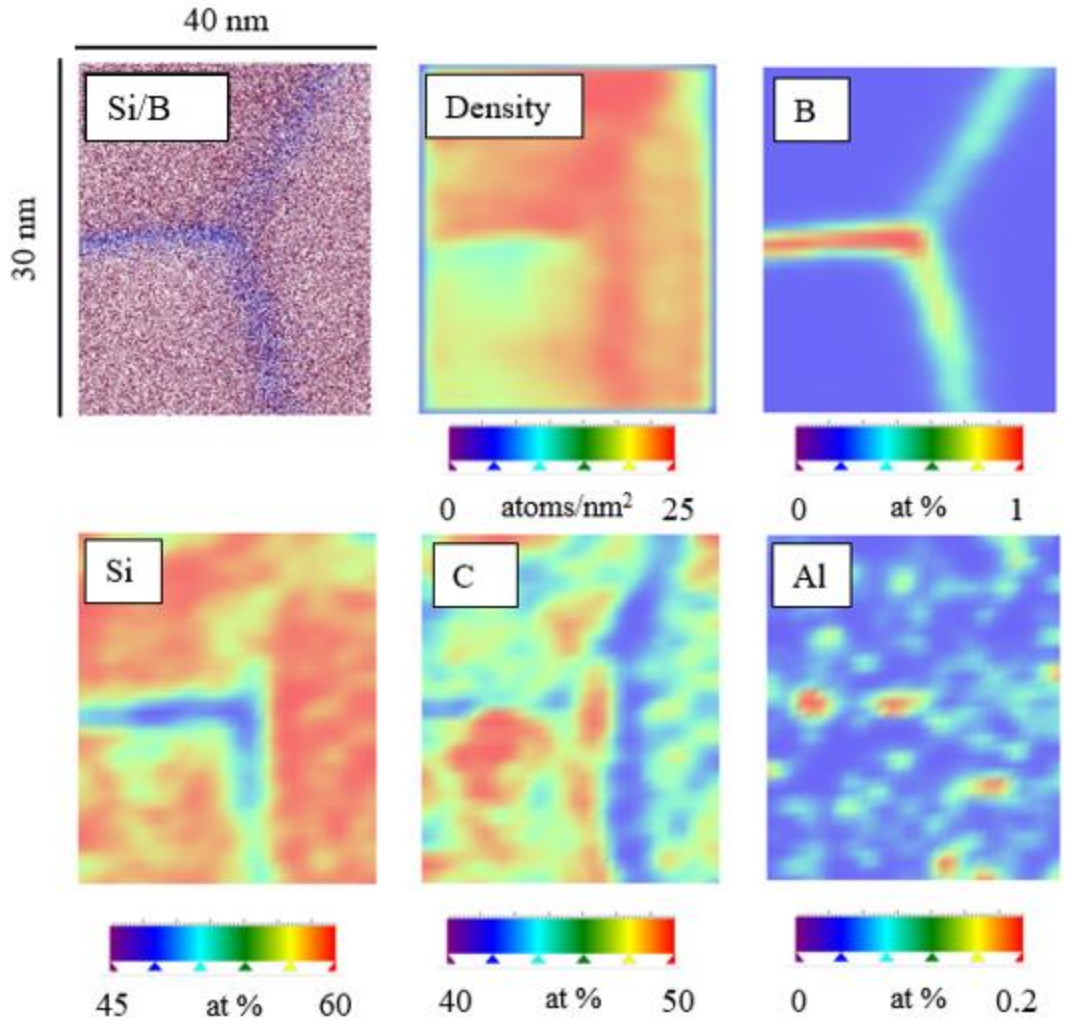


Figure 104: Ion map demonstrating boron (blue) ions decorating triple point with carbon (purple) ions in matrix along with 2D contour plots of density and concentration of chemical species present at triple point.

The triple point shows similar boron content as the grain boundaries forming the junction.

2 Discussion

2.1 Bulk SEM Analysis

The mixed EBSD identification of the 6H and 15R polytypes within grains has also been observed in other studies from literature [3]. This polytype mixing is perhaps due to the similar lattice parameters and stacking sequences of the two polytypes [4]. Most of the grains containing this mixing contain most pixels identified as the 6H polytype, therefore it is likely

that the 15R present in these mixed grains is misidentification of the Kikuchi bands by the analysis software. This erroneous analysis likely causes an overestimation of the 15R present in each specimen type. The elongated grains present in Fire 1 samples are similar to observations in studies from literature on hot pressed SiC specimens after annealing fully dense (>99.5% relative density) specimens at 1950ºC for 4 hours [5]–[7]. Elongated abnormal grains were also found to form when solid state sintering SiC without applied pressure at temperatures above 2100ºC [8]. The Fire 2 and flash sintered specimens do not show evidence of abnormal grains with high aspect ratios. The bimodal grain structure observed in the Fire 1 specimen has been demonstrated to possess higher toughness, as the elongated grains function as a reinforcing phase causing crack bridging and crack deflection [5], [8]–[10]. However, this in situ toughening is reliant upon intergranular fracture, and without a secondary weaker phase present between grains (such as in liquid phase sintering), transgranular cleaving of the elongated grains will occur precluding toughening [9]. Although a bimodal microstructure was not produced using the flash sintering regimes employed in this study, further tuning of flash sintering conditions and timescales could potentially reproduce this bimodal structure.

The only significant difference in polytype content between the different specimen types is the significantly higher 4H content and significantly lower 6H content found in Fire 1 specimens. This disparity is the result of elongated abnormal 4H grains that significantly increase the 4H content of Fire 1 specimens. The large standard errors on phase fraction measurements of 6H and 4H polytype fractions and grain size measurements in Fire 1 specimens are also a result of the large abnormal grains. The grain size measurements are

consistent with expectations based upon sintering time and temperature. Fire 1 specimens demonstrate the largest grain size due to the longest exposure to high temperature sintering conditions. The Fire 2 and FS specimens were subjected to similar sintering temperatures for identical hold times, however the ramp times for the Fire 2 specimen were significantly longer, causing a higher grain size. This difference in temperature ramping can also explain the lower grain size of the FS Hard specimens compared to the Fire 1 specimens. Finally, the higher sintering temperature achieved using a higher electrical power limit for FS Hard specimens compared to the FS specimens can explain the smaller grain size of the FS specimens. The boron and carbon rich features identified using EDS analysis and later determined to be B_4C grains are consistent with previous analyses of solid state sintered boron doped SiC [117], [120], [263].

2.2 APT Bulk Analysis

The composition of carbon, silicon, and boron (omitting the FS Hard data points) is highly correlated to the electric field of collection, demonstrating trends consistent with those found in Chapter IV. Solid solution of boron within SiC grain is quantified between 0.05 and 0.1 at% for most specimen types. The only significant compositional difference between the different SiC specimens is the significantly higher boron content found in FS Hard specimens. This boron enrichment is caused by the boron rich clusters present in these specimens. Boron rich clusters are clearly more prevalent in FS Hard specimens; clustering was observed in 2/34 Fire 1 grains, 0/15 Fire 2 grains, 1/14 FS grains, and 13/13 FS Hard grains. Furthermore, the Pearson coefficient comparison demonstrates significantly more inhomogeneity (clustering) in FS Hard specimens. The Pearson coefficient versus Si^{++}/Si^{+} CSR result in Figure 96 demonstrates the existence of data sets with and without clustering

resulting from experiments subjected to similar APT electric field values. This indicates the clustering is not an electric field induced artefact. Yet, the elongation of the boron clusters in directions perpendicular to the direction of analysis indicates the morphology of the clusters may be distorted. The direction of elongation indicates the clusters are constituted of higher evaporation field phases than the SiC matrix [264]. The cluster size and cluster compositional measurements demonstrated no significant differences between the clusters observed in each type of specimen. The cluster composition ternary diagram demonstrates that the clusters are approximately 60% boron, 20% silicon, and 20% carbon. These results indicate that the clusters are not nanoscale B_4C phases. These compositional measurements may, however, be influenced by atom probe artefacts. Simulation studies conducted by Vurpillot *et al*. demonstrate precipitates possessing a higher evaporation field than the surrounding matrix will lose precipitate atoms from the edge of the precipitate into the matrix near the interface when reconstructed [265]. Therefore, assuming the directional elongation of the clusters along axes perpendicular to the analysis direction is indicative of higher-than-matrix evaporation field clusters, the boron content of the clusters may be underestimated.

A review of boron-doped silicon carbide literature yielded one example of boron clustering in SiC. Following boron ion implantation and annealing, spherical boron clusters with radii of approximately 50 nm were observed in 3C-SiC [132]. These clusters are significantly larger than the clusters found in this thesis and the result of the clustering on mechanical properties was not reported. No literature could be found observing fine scale boron clusters in solid state sintered SiC, perhaps for a few reasons. Boron clusters were much more prevalent in the FS Hard specimen. As pressureless flash sintering of silicon carbide is a

relatively new sintering technique, it is not surprising that microstructural studies of flash sintered SiC are sparse in the literature [109]. Furthermore, the detection and quantification of nanoscale boron features is made difficult by the inefficiency of more conventional characterization techniques, such as STEM EDS, at detecting light element signatures. In addition, the nanoscale dimensions of the boron clusters would probably be smaller than the thickness of a TEM lamella. Therefore, using a TEM chemical characterization technique well suited to light element analysis, such as EELS, would still suffer from overlapping signals from boron clusters and the matrix within the specimen thickness. These issues highlight the strengths of APT and its high-resolution three-dimensional capability to chemically identify light and heavy elements alike. The increased hardness of the FS Hard specimens may be at least partially explained by the presence of boron rich clusters in the SiC matrix. Although precipitation hardening is less well characterized for ceramic systems compared to metallic systems, there do exist examples of precipitation hardening in common ceramic materials systems such as spinel, alumina, and magnesia [266]–[269]. It is possible the boron clusters in the studied SiC specimens play a similar hardening role in SiC systems.

The question remains why the FS Hard specimens demonstrate much higher levels of clustering than the other studied specimens. Consideration of heating and cooling rates along with grain growth occurring during sintering may provide answers. Fire 1, Fire 2, and FS Hard specimens all demonstrate larger grain sizes than FS specimens, and therefore experience more grain growth at high temperature than FS specimens. During grain growth, it is possible the boron rich grain boundaries leave behind boron within SiC grain as the boundaries migrate. As diffusion of boron occurs more slowly within SiC grains compared

to grain boundaries, the rapid cooling and heating of FS Hard specimens leads to insufficient time at high temperature for boron to diffuse to grain boundaries and perhaps B_4C grains [270]. The boron instead tends to form clusters. Yet, conventionally sintered specimens may cool sufficiently slow and spend sufficient time at elevated temperature to allow boron to diffuse to grain boundaries and out of the SiC grains. FS specimens experience minimal grain growth, and therefore less boron is left behind within grains to form clusters upon rapid heating and cooling. This theory would require considerable modeling and simulation to confirm, yet similar formation mechanism have been proposed for aluminum/boron/carbon rich intragranular precipitates in liquid phase sintered SiC [133]. Nonetheless, the prevalence of clustering in flash sintered samples demonstrates the ability of the technique to not only produce fully dense specimens with properties comparable to conventionally sintered specimens, but also complement conventional sintering techniques by providing an avenue to produce unique microstructures.

The APT analysis of the micron-scale scale boron rich features demonstrates a composition consistent with B_4C grains, helping identify the phase. The compositional measurements indicate the B_4C grains contain trace amounts of silicon, which may in fact prove beneficial for the mechanical properties of the B_4C grains. Studies on bulk B_4C have demonstrated silicon doping can help stabilize B_4C from undergoing phase separation into boron and carbon and ensuing amorphization [271]. The silicon found in the B_4C grains may play a similar role in the studied SiC specimens, however the phase transformation occurs under high stress, so mechanical testing would be required to determine if the trace amounts of silicon found in the B_4C grains are sufficient for stabilization to occur [271]. The atomic

percent silicon found in the B_4C in this thesis is two orders of magnitudes lower than those showing improved amorphization behavior, so improved mechanical properties may be unlikely [271]. However, a fine balance between free silicon to stabilize B_4C grains must be considered as silicon can inhibit effective sintering of silicon carbide [115], [263].

2.3 APT Grain Boundary Analysis

All the studied 6H grain boundaries demonstrate significant boron segregation, and most also demonstrate weaker aluminum segregation. Most boundaries show carbon and silicon depletion. The most evident trend present in the Gibbsian excess measurements for different sintering types is the significantly lower boron segregation to FS samples. These samples also demonstrate lower levels of aluminum segregation; however this trend is weaker. There are two potential reasons explaining the lower segregation levels to FS samples. The FS samples have the smallest grain size of all the studied specimen types. Thermodynamic calculations demonstrate segregation of dilute species increases with increasing grain sizes for metals and ceramics [272]. Fire 1 samples, however, demonstrate almost three times larger average grain sizes than the other specimen types but do not demonstrate significantly higher levels of boron or aluminum segregation. This may be caused by the bimodal grain structure of Fire 1 samples. Perhaps a specimen with a unimodal large grain size would demonstrate significantly higher segregation levels. It is also possible the decreased segregation to FS samples is a result of the less advanced sintering evident by the significantly lower relative density of the FS sample. Three-dimensional X-ray microtomography analysis conducted by Okuma *et al.* demonstrated the final stage of sintering begins at a relative density of approximately 90% for viscous glasses and crystalline particles [273]. Studies conducted on tetragonal yttria stabilized zirconia show

grain boundary segregation can continue well into the final stage of sintering [85]. It is therefore possible that the FS samples, with an average relative density of 90%, have not yet undergone the latter stages of sintering and the boron/aluminum segregation accompanying this phase of sintering.

The 4H-6H polytype boundaries demonstrate similar levels of boron and aluminum segregation as 6H-6H boundaries, however the difference in silicon and carbon content between the polytypes is of note. Ab initio pseudopotential calculations of the energies of 3C, 6H, and 4H polytypes with and without vacancies demonstrate silicon vacancies are more energetically favorable in 6H-SiC grains, and carbon vacancies are more energetically favorable in 4H-SiC grains [274]. It is possible the accumulation of silicon vacancies in the 6H grains and carbon vacancies in the 4H grains lead to the observed relative compositional differences in each polytype. It is also important to note local bonding environments have an effect on the field required to evaporate species during an atom probe experiment [165]. The local bonding configuration differs between different polytypes of SiC. This difference in local bonding could cause a difference in the electric field necessary to evaporate species off the specimen tip and cause a systematic artefact seen as an apparent difference in composition between different SiC polytypes.

Finally, it is important to highlight the unresolved structural ambiguity of this analysis. Both structured and amorphous film boron rich grain boundaries have been observed in SiC specimens using high resolution TEM [131], [140]. Amorphous film boundaries were observed in a specimen with significantly higher aluminum content than the specimens in

this thesis. However, the APT results described here do indicate the presence of small amounts of aluminum at grain boundaries. APT cannot determine the presence or lack of structure at grain boundaries, and complementary TEM analysis would be required.

2.4 APT B_4C-SiC Phase Boundary Analysis

The phase boundaries for each material type demonstrated no impurity segregation. There does appear to be a finite thickness to the studied boundaries, where a mixing of the two phases occurs. However, quantification of this mixing layer is possibly affected by spatial resolution artefacts caused by the significant difference in evaporation field of the two phases. This difference in evaporation behavior is highlighted by the voltage histories for runs containing a phase boundary, as shown in Figure 105.



Figure 105: Voltage history across B_4C-SiC phase boundary

The discontinuity occurring before the ten million ion mark indicates the phase boundary transition. This discontinuous voltage curve is evidence of a significant change in evaporation field, which will have a significant effect on the spatial resolution of the APT analysis at the interface [275]. Therefore, the width of the interface between the two phases

as observed in the APT reconstructions may be inaccurate, and chemical mixing at the interface may also be the result of field evaporation induced artefacts

2.5 APT Triple Point Analysis

The triple points observed in the samples studied demonstrate boron and aluminum segregation levels like the abutting grain boundary with the highest level of segregation. The triple points also demonstrate silicon and carbon depletion levels like the abutting grain boundaries.

3 Conclusions

In this chapter, the effect of sintering conditions on the microstructure of SiC samples was probed using several characterization techniques including SEM/EBSD, SEM/EDS, and APT. SEM analysis demonstrates a significant difference in grain morphology between specimens sintered using different techniques and for different amounts of time. A binomial grid-based frequency analysis shows clustering is more prevalent in FS Hard specimens, which may help explain elevated hardness. Literature suggests this increase in hardness may be the result of precipitation hardening caused by boron clustering. Grain boundary analysis demonstrates FS specimens contain grain boundaries with significantly lower levels of boron and aluminum segregation, and literature suggests this may be related to a significantly lower grain size or lower relative density. Phase boundary characterization demonstrates little impurity segregation, yet spatial resolution may be affected by electric field related effects. Finally, SiC triple points demonstrate segregation levels like segregation levels present at grain boundaries.

Chapter VIII

Conclusions

APT Operational Conditions and Compositional Comparison Considerations

A systematic and reproducible procedure for determining the composition of ROIs in ceramic APT data sets was developed and presented. The procedure includes a novel peak fitting ranging procedure that minimizes user input and practically accounts for the asymmetry of laser assisted APT formed spectra. APT operational parameter sweeps were conducted for each of the studied materials. This yielded optimized analysis parameters resulting in compositional measurements approaching expected stoichiometry. The effects on compositional measurements of several important APT artefacts such as laser illumination proximity and a blunting tip during analysis were demonstrated to have a significant effect on compositional measurements. The use of CSRs as a proxy measurement for the applied electric field strength helps isolate field induced artefacts from real compositional differences.

Alumina Analysis

Carbon doping was quantitatively demonstrated to increase the likelihood of transgranular fracture in polycrystalline alumina samples providing further evidence that carbon doping strengthens alumina grain boundaries. Grain boundary relative energy measurements made using AFM demonstrate the need to carefully consider and sweep experimental parameters when choosing to make such measurements. The results also demonstrate the detrimental effect of surface reconstruction on AFM grain boundary relative energy measurements. APT

analysis of carbon-doped and undoped specimens demonstrates no significant chemical changes caused by carbon doping, a convincing result when considering the parts per million chemical sensitivity of the technique [177]. The lack of observed carbon segregation to carbon-doped alumina grain boundaries starkly contrasts work published by Marquis *et al.* [1]. It is likely the observed carbon in the Marquis work is in fact magnesium which has a direct peak overlap with carbon in a m/q spectrum. The mechanism underpinning grain boundary strengthening of carbon-doped alumina therefore remains a mystery, however grain boundary structural changes and local reduction remain possible explanations. APT chemical characterization of grain boundaries and triple points provides quantitative measurements of magnesium segregation to these features.

3YSZ APT Analysis

Conventionally sintered 3YSZ samples demonstrate less homogenous yttrium distribution than flash sintered specimens. The repeating lath-like regions of high and low yttrium concentration found predominantly in conventionally sintered specimens may be early signs of high temperature phase transformation that persists at room temperature following cooling. Flash sintering may inhibit the formation of this modulated structure because of rapid heating and cooling or because of electrochemical reduction occurring during sintering. The increased homogeneity found in flash sintered samples and resulting resistance to undesirable phase transformation demonstrates the potential for flash sintering to produce favorable microstructures in 3YSZ sintered bodies. APT evidence suggests flash sintering of zirconium oxycarbide has been achieved possibly due to contamination of the green body with SiC powder, opening the door for future work into the sintering of a material

of interest for electrocatalytic applications. APT grain boundary analysis demonstrates strong electrochemically reducing flash sintering environments lead to reduced silicon and aluminum segregation to grain boundaries. Finally, APT analysis has yielded evidence of sub-structuring at 3YSZ triple points, yet electric field effects may contribute to these observations.

SiC Analysis

SEM analysis demonstrates flash sintered and conventionally sintered SiC samples with short sintering times demonstrate equiaxed grains compared to samples subjected to longer conventional sintering times with abnormal elongated grains. As the sintering in these specimens is likely to be solid state sintering, small equiaxed grains are preferred as this microstructure tends to create sintered bodies with higher flexural strength due to less large surface porosity [121]. The ability of flash sintering to achieve small equiaxed grains highlights the utility of rapid sintering timescales. EBSD analysis demonstrates no significant difference in polytype composition between specimens, while EDS analysis shows boron and carbon rich features with dimensions ranging from 1 to 2 microns. FS Hard specimens demonstrate higher hardness than conventionally sintered or FS samples. This increase in hardness may be caused by intragranular nanoscale boron rich clusters prevalent throughout FS Hard samples inducing precipitation hardening. The boron rich clusters observed in FS Hard APT samples are dissimilar to any boron rich features found in literature, due to their small size and composition. APT bulk compositional measurements have quantified low levels of solid solubility of boron in SiC. FS samples demonstrate lower levels of grain boundary segregation, potentially due to decreased density or smaller grain

size. As grain boundary chemistry can influence many important properties and processes, the ability to tune grain boundary chemistry using flash sintering is of note. APT analysis of boron/carbon rich microscale inclusions helps verify the identity of these inclusions as boron carbide grains with low levels of solid solution silicon. Lastly, triple point analysis has demonstrated multi-junctions share similar chemistries as abutting grain boundaries.

Chapter IX

Future Work

APT Operating Conditions and Compositional Comparison Considerations

The utility of reporting CSRs to robustly compare compositional measurements made between different samples has been demonstrated in this thesis. New software driving data collection on LEAP 5000 equipment allows the user to run an experiment at a given CSR as opposed to at a constant detection efficiency. This would ostensibly enable more homogenous results across the duration of an experiment and exploring this option would be useful for the analysis of ceramics. An experimental atom probe developed by the National Institute of Standards uses an extreme ultraviolet laser to initiate field evaporation from specimens [162]. Experiments analyzing gallium nitride using this tool have demonstrated Ga:N values near expected stoichiometry regardless of the Ga CSR [162]. Testing this tool on the materials studied in this thesis may prove similarly beneficial. The effect of APT specimen apex morphology was not probed in this study. Correlative APT/TEM to characterize the shape of the tip pre-APT analysis would allow for the development of best practices during FIB specimen preparation of the studied materials.

Alumina Analysis

APT analysis of alumina grain boundaries demonstrated no significant difference in grain boundary chemistry between carbon-doped and undoped specimens. However, the spatial resolution of APT precludes high resolution structural comparison of grain boundaries. Comparing the structure of doped and undoped grain boundaries with identical geometric

degrees of freedom would allow subtle structural effects of carbon on boundary structure to be investigated. Diffusion bonding bicrystals with and without carbon present before conducting HRSTEM studies of the grain boundaries would facilitate such a comparison.

The AFM studies in this thesis suffered from highly reconstructed surfaces. It is possible annealing specimens with aluminum metal melted atop the free surface to protect the surface while etching occurs would minimize surface faceting [200]. The metal could then be chemically removed before AFM analysis.

Lastly, it is possible carbon strengthens grain boundaries by reacting with and removing oxygen from the boundary region. Density functional theory (DFT) calculations may prove useful in exploring this possibility.

3YSZ APT Analysis

The analysis of 3YSZ in this thesis would also benefit from further characterization using diffusion bonded bicrystals. Two possibilities for bicrystal analysis could prove fruitful. The first possibility would entail diffusion bonding a 3YSZ bicrystal under high temperature before cutting the sample in half perpendicular to the grain boundary. High electric current, like the currents achieved during flash sintering, would then be applied across one of the halves. The two samples would then be analyzed using HRSTEM and APT to study the effects of current on the structure and chemistry of the controlled grain boundary. Another possible avenue for bicrystal study would be to bond one bicrystal using conventional heating, while bonding another using flash sintering. It would be important to ensure the two

bicrystals are bonded together using as close to identical geometries as possible. APT and TEM analysis could then be conducted on the two bicrystals. APT analysis of the YSZ powder used to fabricate samples would be useful to investigate the origins of phase separation observed in conventionally sintered samples. Finally, further exploration of the flash sintering of zirconium oxycarbide may prove of interest.

SiC Analysis

The bicrystal studies described in the preceding 3YSZ discussion would likely prove of use in advancing the SiC analysis detailed in this thesis. Recent results in the research group have demonstrated flash sintering specimens using powers exceeding those used to sinter FS Hard samples demonstrate lower hardness. APT analysis of these samples may help validate or disprove the theory that boron clusters strengthen FS Hard samples. Optimizing sintering conditions to produce higher densities of clusters may allow tuning of the observed strengthening effects. TEM analysis near a hardness indent in a FS Hard specimen could allow for direct imaging of dislocation bowing around nanoparticles, verifying the precipitation strengthening theory presented in this thesis.

Lastly, conducting APT analysis of the starting SiC powders would help identify the presence or lack of an oxidized layer on the powder surface. Oxidized layers can inhibit sintering unless successfully removed via reduction, and therefore the presence and chemistry of such layers would be illuminative.

Chapter X

Works Cited

[1] E. A. Marquis, N. A. Yahya, D. J. Larson, M. K. Miller, and R. I. Todd, “Probing the improbable: imaging C atoms in alumina,” *Mater. Today*, vol. 13, no. 10, pp. 34–36, 2010.

[2] M. N. Rahaman, *Ceramic processing and sintering*. CRC press, 2017.

[3] Y.-M. Chiang, D. P. Birnie, W. D. Kingery, and S. Newcomb, *Physical ceramics: principles for ceramic science and engineering*, vol. 409. Wiley New York, 1997.

[4] J. L. Ortiz-Merino and R. I. Todd, “Relationship between wear rate, surface pullout and microstructure during abrasive wear of alumina and alumina/SiC nanocomposites,” *Acta Materialia*, vol. 53, no. 12. pp. 3345–3357, 2005, doi: https://doi.org/10.1016/j.actamat.2005.03.031.

[5] W. Swiatnicki, S. Lartigue-Korinek, and J. Y. Laval, “Grain boundary structure and intergranular segregation in Al2O3,” *Acta Metall. Mater.*, vol. 43, no. 2, pp. 795–805, 1995, doi: https://doi.org/10.1016/0956-7151(94)00256-H.

[6] P. R. Cantwell, M. Tang, S. J. Dillon, J. Luo, G. S. Rohrer, and M. P. Harmer, “Grain boundary complexions,” *Acta Materialia*, vol. 62. pp. 1–48, 2014, doi: https://doi.org/10.1016/j.actamat.2013.07.037.

[7] C. Hammond and C. Hammond, *The Basics of Cristallography and Diffraction*, vol. 214. Oxford, 2001.

[8] M. L. Kronberg, “Plastic deformation of single crystals of sapphire: basal slip and twinning,” *Acta Metall.*, vol. 5, no. 9, pp. 507–524, 1957.

[9] S. J. Dillon, M. Tang, W. C. Carter, and M. P. Harmer, “Complexion: A new concept for kinetic engineering in materials science,” *Acta Mater.*, vol. 55, no. 18, pp. 6208–6218, 2007.

[10] J. G. Fisher and S. L. Kang, “Strategies and practices for suppressing abnormal grain growth during liquid phase sintering,” *J. Am. Ceram. Soc.*, vol. 102, no. 2, pp. 717–735, 2019.

[11] W. E. Lee and M. Rainforth, *Ceramic microstructures: property control by processing*. Springer Science & Business Media, 1994.

[12] R. L. Coble, “Translucent Y3Al5O12 ceramics,” *Mater. Res. Bull.*, vol. 19, no. 12, pp. 1669–1674, 1984, doi: 10.1016/0025-5408(84)90245-9.

[13] R. L. Coble, “Sintering Crystalline Solids. II. Experimental Test of Diffusion Models in Powder Compacts,” *J. Appl. Phys.*, vol. 32, no. 5, pp. 793–799, 1961, doi: 10.1063/1.1736108.

[14] K. A. BERRY and M. P. HARMER, “Effect of MgO Solute on Microstructure Development in Al2O3,” *J. Am. Ceram. Soc.*, vol. 69, no. 2, pp. 143–149, Feb. 1986, doi: https://doi.org/10.1111/j.1151-2916.1986.tb04719.x.

[15] A. H. Heuer, “The role of MgO in the sintering of alumina,” *J. Am. Ceram. Soc.*, vol. 62, no. 5-6, pp. 317–318, 1979.

[16] R. I. Todd and A. Limpichaipanit, “Microstructure-Property Relationships in Wear

Resistant Alumina/SiC" Nanocomposites",” in *Advances in Science and Technology*, 2006, vol. 45, pp. 555–563.

[17] A. J. Winn and R. I. Todd, “Microstructural requirements for alumina–SiC nanocomposites,” *Br. Ceram. Trans.*, vol. 98, no. 5, pp. 219–224, Jan. 1999, doi: 10.1179/096797899680471.

[18] J. Zhao, L. C. Stearns, M. P. Harmer, H. M. Chan, G. A. Miller, and R. F. Cook, “Mechanical Behavior of Alumina–Silicon Carbide „Nanocomposites”,” *J. Am. Ceram. Soc.*, vol. 76, no. 2, pp. 503–510, 1993, doi: 10.1111/j.1151-2916.1993.tb03814.x.

[19] C. N. Walker, C. E. Borsa, R. I. Todd, R. W. Davidge, and R. J. Brook, “Fabrication, characterisation and properties of alumina matrix nanocomposites,” *Nov. Synth. Process. Ceram. Mater. 1 Carlt. House Terrace, London, SW 1 Y 5 DB, UK, 1995.*, pp. 249–264, 1995.

[20] K. Niihara and A. Nakahira, “Particulate strengthened oxide ceramics-nanocomposites,” 1990.

[21] H. Kara and S. G. Roberts, “Polishing Behavior and Surface Quality of Alumina and Alumina/Silicon Carbide Nanocomposites,” *J. Am. Ceram. Soc.*, vol. 83, no. 5, pp. 1219–1225, 2000, doi: 10.1111/j.1151-2916.2000.tb01357.x.

[22] A. Limpichaipanit and R. I. Todd, “The relationship between microstructure, fracture and abrasive wear in Al2O3/SiC nanocomposites and microcomposites containing 5 and 10% SiC,” *Journal of the European Ceramic Society*, vol. 29, no. 13. pp. 2841–2848, 2009, doi: https://doi.org/10.1016/j.jeurceramsoc.2009.03.023.

[23] S. Jiao, M. L. Jenkins, and R. W. Davidge, “Electron microscopy of crack/particle interactions in Al2O3/SiC nanocomposites,” *J. Microsc.*, vol. 185, no. 2, pp. 259–264, 1997.

[24] J. Sedláček, D. Galusek, P. Švančárek, R. Riedel, A. Atkinson, and X. Wang, “Abrasive wear of Al2O3–SiC and Al2O3–(SiC)–C composites with micrometer- and submicrometer-sized alumina matrix grains,” *J. Eur. Ceram. Soc.*, vol. 28, no. 15, pp. 2983–2993, 2008.

[25] A. Boccaccini and G. Gevorkian, *Carbon-fibre reinforced glass matrix composites: Self-lubricating materials for wear applications in vacuum*, vol. 74. 2001.

[26] M. Y. Chen, Z. Bai, S. C. Tan, and M. R. Unroe, “Friction and wear scar analysis of carbon nanofiber-reinforced polymeric composite coatings on alumina/aluminum composite,” *Wear*, vol. 252, no. 7, pp. 624–634, 2002, doi: https://doi.org/10.1016/S0043-1648(02)00021-2.

[27] N. A. Yahya and R. I. Todd, “Influence of C doping on the fracture mode and abrasive wear of Al2O3,” *Journal of the European Ceramic Society*, vol. 32, no. 16. pp. 4003–4007, 2012, doi: https://doi.org/10.1016/j.jeurceramsoc.2012.07.003.

[28] N. A. Yahya, “Mechanical Testing of Carbon Doped Alumina,” Oxford, 2012.

[29] K. Thompson, D. Lawrence, D. J. Larson, J. D. Olson, T. F. Kelly, and B. Gorman, “In situ site-specific specimen preparation for atom probe tomography,” *Ultramicroscopy*, vol. 107, no. 2, pp. 131–139, 2007, doi: https://doi.org/10.1016/j.ultramic.2006.06.008.

[30] A. P. Sutton, “Grain-boundary structure,” *Int. Met. Rev.*, vol. 29, no. 1, pp. 377–404, 1984.

[31] A. S. M. M. S. Seminar, A. S. for Metals., M. S. Division., S. Committee., and M. S. of AIME., “Grain-boundary structure and kinetics : papers,” 1980.

[32] F.-R. Chen, C.-C. Chu, J.-Y. Wang, and L. Chang, “Atomic structure of Σ7 (01 1 2) symmetrical tilt grain boundaries in α-Al2O3,” *Philos. Mag. A*, vol. 72, no. 3, pp. 529–544, 1995.

[33] S. Fabris, S. Nufer, C. Elsasser, and T. Gemming, “Prismatic Sigma 3 (10 (1) over-bar-0) twin boundary in alpha-Al2O3 investigated by density functional theory and transmission electron microscopy,” 2002.

[34] S. Fabris and C. Elsässer, “∑ 13 (1 0-1 4)) twin in α-Al2O3: A model for a general grain boundary,” *Phys. Rev. B*, vol. 64, no. 24, 2001.

[35] Y. Ikuhara, T. Watanabe, T. Saito, H. Yoshida, and T. Sakuma, “Atomic structure and chemical bonding state of sapphire bicrystal,” in *Materials science forum*, 1999, vol. 294, pp. 273–276.

[36] T. Höche, P. R. Kenway, H. Kleebe, M. Rühle, and P. A. Morris, “High-Resolution Transmission Electron Microscopy Studies of a Near Σ11 Grain Boundary in α-Alumina,” *J. Am. Ceram. Soc.*, vol. 77, no. 2, pp. 339–348, 1994.

[37] J. Cho, M. P. Harmer, H. M. Chan, J. M. Rickman, and A. M. Thompson, “Effect of yttrium and lanthanum on the tensile creep behavior of aluminum oxide,” *J. Am. Ceram. Soc.*, vol. 80, no. 4, pp. 1013–1017, 1997, [Online]. Available:

https://www.scopus.com/inward/record.uri?eid=2-s2.0-0031120406&partnerID=40&md5=d3b59e8d7cd36fd47b1b82233f24af82.

[38] H. Yoshida, Y. Ikuhara, and T. Sakuma, “High-temperature creep resistance in rare-earth-doped, fine-grained Al2O3,” *J. Mater. Res.*, vol. 13, no. 9, pp. 2597–2601, 1998, doi: 10.1557/JMR.1998.0362.

[39] R. by P. D. Brown, “Transmission Electron Microscopy-A Textbook for Materials Science, by David B. Williams and C. Barry Carter,” *Microsc. Microanal.*, vol. 5, no. 6, pp. 452–453, 1999, doi: DOI: 10.1017/S1431927699990529.

[40] T. Höche and M. Rühle, “Effect of calcium doping on the atomistic structure of the (1104) twin boundary in alumina,” *J. Am. Ceram. Soc.*, vol. 79, no. 7, pp. 1961–1966, 1996.

[41] D. R. CLARKE, “On the Equilibrium Thickness of Intergranular Glass Phases in Ceramic Materials,” *J. Am. Ceram. Soc.*, vol. 70, no. 1, pp. 15–22, Jan. 1987, doi: 10.1111/j.1151-2916.1987.tb04846.x.

[42] R. Brydson, S. Chen, F. L. Riley, S. J. Milne, X. Pan, and M. Rühle, “Microstructure and Chemistry of Intergranular Glassy Films in Liquid-Phase-Sintered Alumina,” *J. Am. Ceram. Soc.*, vol. 81, no. 2, pp. 369–379, 1998.

[43] M. P. Harmer, “Use of solid-solution additives in ceramic processing,” *Adv. Ceram.*, vol. 10, p. 679, 1984.

[44] S. Blonski and S. H. Garofalini, “Atomistic Structure of Calcium Silicate Intergranular Films in Alumina Studied by Molecular Dynamics Simulations,” *J.*

Am. Ceram. Soc., vol. 80, no. 8, pp. 1997–2004, Aug. 1997, doi: https://doi.org/10.1111/j.1151-2916.1997.tb03083.x.

[45] D. A. Litton and S. H. Garofalini, "Atomistic Structure of Sodium and Calcium Silicate Intergranular Films in Alumina," *J. Mater. Res.*, vol. 14, no. 4, pp. 1418–1429, 1999, doi: DOI: 10.1557/JMR.1999.0192.

[46] S. Blonski and S. H. Garofalini, "Molecular Dynamics Study of Silica−Alumina Interfaces," *J. Phys. Chem.*, vol. 100, no. 6, pp. 2201–2205, Jan. 1996, doi: 10.1021/jp951798p.

[47] I. Povstugar, J. Weber, D. Naumenko, T. Huang, M. Klinkenberg, and W. J. Quadakkers, "Correlative Atom Probe Tomography and Transmission Electron Microscopy Analysis of Grain Boundaries in Thermally Grown Alumina Scale," *Microsc. Microanal.*, vol. 25, no. 1, pp. 11–20, 2019, doi: DOI: 10.1017/S143192761801557X.

[48] K. Stiller *et al.*, "Atom Probe Tomography of Oxide Scales," *Oxid. Met.*, vol. 79, no. 3, pp. 227–238, 2013, doi: 10.1007/s11085-012-9330-6.

[49] D. M. Saylor and G. S. Rohrer, "Measuring the influence of grain-boundary misorientation on thermal groove geometry in ceramic polycrystals," *J. Am. Ceram. Soc.*, vol. 82, no. 6, pp. 1529–1536, 1999.

[50] W. M. Robertson, "Grain-Boundary Grooving by Surface Diffusion for Finite Surface Slopes," *J. Appl. Phys.*, vol. 42, no. 1, pp. 463–467, 1971, doi: 10.1063/1.1659625.

[51] W. W. Mullins, “Theory of Thermal Grooving,” *J. Appl. Phys.*, vol. 28, no. 3, pp. 333–339, 1957, doi: 10.1063/1.1722742.

[52] S. J. Dillon, M. P. Harmer, and G. S. Rohrer, “The relative energies of normally and abnormally growing grain boundaries in alumina displaying different complexions,” *J. Am. Ceram. Soc.*, vol. 93, no. 6, pp. 1796–1802, 2010.

[53] M. N. Kelly, S. A. Bojarski, and G. S. Rohrer, “The temperature dependence of the relative grain-boundary energy of yttria-doped alumina,” *J. Am. Ceram. Soc.*, vol. 100, no. 2, pp. 783–791, 2017, doi: 10.1111/jace.14488.

[54] S. J. Dillon, H. Miller, M. P. Harmer, and G. S. Rohrer, “Grain boundary plane distributions in aluminas evolving by normal and abnormal grain growth and displaying different complexions,” *Int. J. Mater. Res.*, vol. 101, no. 1, pp. 50–56, 2010.

[55] A. R. Krause, P. R. Cantwell, C. J. Marvel, C. Compson, J. M. Rickman, and M. P. Harmer, “Review of grain boundary complexion engineering: Know your boundaries,” *J. Am. Ceram. Soc.*, vol. 102, no. 2, pp. 778–800, Feb. 2019, doi: 10.1111/jace.16045.

[56] C. E. J. Dancer, “Flash sintering of ceramic materials,” *Mater. Res. Express*, vol. 3, no. 10, p. 102001, 2016.

[57] K. Ren, Q. Wang, Y. Lian, and Y. Wang, “Densification kinetics of flash sintered 3mol% Y2O3 stabilized zirconia,” *J. Alloys Compd.*, vol. 747, pp. 1073–1077, 2018, doi: https://doi.org/10.1016/j.jallcom.2018.02.308.

[58] I. Kosacki, C. M. Rouleau, P. F. Becher, J. Bentley, and D. H. Lowndes, “Nanoscale effects on the ionic conductivity in highly textured YSZ thin films,” *Solid State Ionics*, vol. 176, no. 13, pp. 1319–1326, 2005, doi: https://doi.org/10.1016/j.ssi.2005.02.021.

[59] M. Yu, S. Grasso, R. Mckinnon, T. Saunders, and M. J. Reece, “Review of flash sintering: materials, mechanisms and modelling,” *Adv. Appl. Ceram.*, vol. 116, no. 1, pp. 24–60, Jan. 2017, doi: 10.1080/17436753.2016.1251051.

[60] G. Witz, V. Shklover, W. Steurer, S. Bachegowda, and H.-P. Bossmann, “Phase Evolution in Yttria-Stabilized Zirconia Thermal Barrier Coatings Studied by Rietveld Refinement of X-Ray Powder Diffraction Patterns,” *J. Am. Ceram. Soc.*, vol. 90, pp. 2935–2940, Sep. 2007, doi: 10.1111/j.1551-2916.2007.01785.x.

[61] A. Loganathan and A. S. Gandhi, “Effect of phase transformations on the fracture toughness of t′ yttria stabilized zirconia,” *Mater. Sci. Eng. A*, vol. 556, pp. 927–935, 2012, doi: https://doi.org/10.1016/j.msea.2012.07.095.

[62] X. Y. Liu, X. Z. Wang, A. Javed, C. Zhu, and G. Y. Liang, “The effect of sintering temperature on the microstructure and phase transformation in tetragonal YSZ and LZ/YSZ composites,” *Ceram. Int.*, vol. 42, no. 2, Part A, pp. 2456–2465, 2016, doi: https://doi.org/10.1016/j.ceramint.2015.10.046.

[63] R. I. Todd, E. Zapata-Solvas, R. S. Bonilla, T. Sneddon, and P. R. Wilshaw, “Electrical characteristics of flash sintering: thermal runaway of Joule heating,” *J. Eur. Ceram. Soc.*, vol. 35, no. 6, pp. 1865–1877, 2015, doi: https://doi.org/10.1016/j.jeurceramsoc.2014.12.022.

[64] S. Ghosh, A. H. Chokshi, P. Lee, and R. Raj, “A Huge Effect of Weak dc Electrical Fields on Grain Growth in Zirconia,” *J. Am. Ceram. Soc.*, vol. 92, no. 8, pp. 1856–1859, Aug. 2009, doi: 10.1111/j.1551-2916.2009.03102.x.

[65] A. M. Raftery *et al.*, “Onset conditions for flash sintering of UO2,” *J. Nucl. Mater.*, vol. 493, pp. 264–270, 2017, doi: https://doi.org/10.1016/j.jnucmat.2017.06.022.

[66] J. Nie, Y. Zhang, J. M. Chan, R. Huang, and J. Luo, “Water-assisted flash sintering: Flashing ZnO at room temperature to achieve ~98% density in seconds,” *Scr. Mater.*, vol. 142, pp. 79–82, 2018, doi: https://doi.org/10.1016/j.scriptamat.2017.08.032.

[67] J. Luo, “The scientific questions and technological opportunities of flash sintering: From a case study of ZnO to other ceramics,” *Scr. Mater.*, vol. 146, pp. 260–266, 2018, doi: https://doi.org/10.1016/j.scriptamat.2017.12.006.

[68] W. Ji, B. Parker, S. Falco, J. Y. Zhang, Z. Y. Fu, and R. I. Todd, “Ultra-fast firing: Effect of heating rate on sintering of 3YSZ, with and without an electric field,” *J. Eur. Ceram. Soc.*, vol. 37, no. 6, pp. 2547–2551, 2017, doi: https://doi.org/10.1016/j.jeurceramsoc.2017.01.033.

[69] I. J. Hewitt, A. A. Lacey, and R. I. Todd, “A Mathematical Model for Flash Sintering,” *Math. Model. Nat. Phenom.*, vol. 10, no. 6, pp. 77–89, 2015, [Online]. Available: https://doi.org/10.1051/mmnp/201510607.

[70] T. Kumagai, “Rapid Densification of Yttria-Stabilized Tetragonal Zirconia by Electric Current-Activated/Assisted Sintering Technique,” *J. Am. Ceram. Soc.*, vol. 94, no. 4, pp. 1215–1223, Apr. 2011, doi: 10.1111/j.1551-2916.2010.04235.x.

[71] Y. Dong and I.-W. Chen, “Onset Criterion for Flash Sintering,” *J. Am. Ceram. Soc.*, vol. 98, no. 12, pp. 3624–3627, Dec. 2015, doi: 10.1111/jace.13866.

[72] R. Raj, M. Cologna, and J. S. C. Francis, “Influence of Externally Imposed and Internally Generated Electrical Fields on Grain Growth, Diffusional Creep, Sintering and Related Phenomena in Ceramics,” *J. Am. Ceram. Soc.*, vol. 94, no. 7, pp. 1941–1965, Jul. 2011, doi: 10.1111/j.1551-2916.2011.04652.x.

[73] M. Cologna, B. Rashkova, and R. Raj, “Flash Sintering of Nanograin Zirconia in <5 s at 850°C,” *J. Am. Ceram. Soc.*, vol. 93, no. 11, pp. 3556–3559, Nov. 2010, doi: 10.1111/j.1551-2916.2010.04089.x.

[74] L. Gremillard, T. Epicier, J. Chevalier, and G. Fantozzi, “Microstructural study of silica-doped zirconia ceramics,” *Acta Mater.*, vol. 48, no. 18–19, pp. 4647–4652, 2000.

[75] X. Guo, W. Sigle, J. Fleig, and J. Maier, “Role of space charge in the grain boundary blocking effect in doped zirconia,” *Solid State Ionics*, vol. 154, pp. 555–561, 2002.

[76] S. Stemmer, J. Vleugels, and O. Van Der Biest, “Grain boundary segregation in high-purity, yttria-stabilized tetragonal zirconia polycrystals (Y-TZP),” *J. Eur. Ceram. Soc.*, vol. 18, no. 11, pp. 1565–1570, 1998.

[77] J. Lee, T. Mori, J. Li, T. Ikegami, M. Komatsu, and H. Haneda, “Improvement of grain-boundary conductivity of 8 mol% yttria-stabilized zirconia by precursor scavenging of siliceous phase,” *J. Electrochem. Soc.*, vol. 147, no. 7, pp. 2822–2829, 2000.

[78] X. Guo, C.-Q. Tang, and R.-Z. Yuan, “Grain boundary ionic conduction in zirconia-based solid electrolyte with alumina addition,” *J. Eur. Ceram. Soc.*, vol. 15, no. 1, pp. 25–32, 1995.

[79] X. Guo and R. Yuan, “Roles of alumina in zirconia-based solid electrolyte,” *J. Mater. Sci.*, vol. 30, no. 4, pp. 923–931, 1995, doi: 10.1007/BF01178426.

[80] B. Feng, N. R. Lugg, A. Kumamoto, Y. Ikuhara, and N. Shibata, “Direct Observation of Oxygen Vacancy Distribution across Yttria-Stabilized Zirconia Grain Boundaries,” *ACS Nano*, vol. 11, no. 11, pp. 11376–11382, Nov. 2017, doi: 10.1021/acsnano.7b05943.

[81] J. An *et al.*, “Atomic Scale Verification of Oxide-Ion Vacancy Distribution near a Single Grain Boundary in YSZ,” *Sci. Rep.*, vol. 3, no. 1, p. 2680, Dec. 2013, doi: 10.1038/srep02680.

[82] M. A. Frechero *et al.*, “Paving the way to nanoionics: atomic origin of barriers for ionic transport through interfaces,” *Sci. Rep.*, vol. 5, no. 1, p. 17229, 2015, doi: 10.1038/srep17229.

[83] K. L. Kliewer and J. S. Koehler, “Space charge in ionic crystals. I. General approach with application to NaCl,” *Phys. Rev.*, vol. 140, no. 4A, p. A1226, 1965.

[84] X. Guo and R. Waser, “Electrical properties of the grain boundaries of oxygen ion conductors: Acceptor-doped zirconia and ceria,” *Prog. Mater. Sci.*, vol. 51, no. 2, pp. 151–210, 2006, doi: https://doi.org/10.1016/j.pmatsci.2005.07.001.

[85] K. MATSUI, N. OHMICHI, M. OHGAI, H. YOSHIDA, and Y. IKUHARA, “Grain

Boundary Segregation-Induced Phase Transformation in Yttria-Stabilized Tetragonal Zirconia Polycrystal," *J. Ceram. Soc. Japan*, vol. 114, no. 1327, pp. 230–237, 2006, doi: 10.2109/jcersj.114.230.

[86] Y. Ikuhara, H. Nishimura, A. Nakamura, K. Matsunaga, T. Yamamoto, and K. P. D. Lagerlöf, "Dislocation Structures of Low-Angle and Near-Σ3 Grain Boundaries in Alumina Bicrystals," *J. Am. Ceram. Soc.*, vol. 86, no. 4, pp. 595–602, Apr. 2003, doi: 10.1111/j.1151-2916.2003.tb03346.x.

[87] Y. Wang, C. Cai, L. Li, L. Yang, Y. Zhou, and G. Zhou, "Oxygen vacancy ordering induced displacements of cations in yttria-stabilized zirconia," *AIP Adv.*, vol. 6, no. 9, p. 95113, Sep. 2016, doi: 10.1063/1.4963202.

[88] J. A. Krogstad *et al.*, "Phase Stability of t′-Zirconia-Based Thermal Barrier Coatings: Mechanistic Insights," *J. Am. Ceram. Soc.*, vol. 94, no. s1, pp. s168–s177, Jun. 2011, doi: 10.1111/j.1551-2916.2011.04531.x.

[89] Y. M. M. Chen, T. Ohkubo, M. Kodzuka, K. Morita, and K. Hono, "Laser-assisted atom probe analysis of zirconia/spinel nanocomposite ceramics," *Scr. Mater.*, vol. 61, no. 7, pp. 693–696, Oct. 2009, doi: https://doi.org/10.1016/j.scriptamat.2009.05.043.

[90] K. Hono *et al.*, "Broadening the applications of the atom probe technique by ultraviolet femtosecond laser," *Ultramicroscopy*, vol. 111, no. 6, pp. 576–583, May 2011, doi: 10.1016/J.ULTRAMIC.2010.11.020.

[91] M. Cologna, A. L. G. Prette, and R. Raj, "Flash-Sintering of Cubic Yttria-Stabilized Zirconia at 750°C for Possible Use in SOFC Manufacturing," *J. Am. Ceram. Soc.*,

vol. 94, no. 2, pp. 316–319, Feb. 2011, doi: 10.1111/j.1551-2916.2010.04267.x.

[92] H. Conrad and D. Yang, “Effect of the strength of an AC electric field compared to DC on the sintering rate and related grain size of zirconia (3Y-TZP),” *Mater. Sci. Eng. A*, vol. 559, pp. 591–594, 2013, doi: https://doi.org/10.1016/j.msea.2012.08.146.

[93] W. Qin, H. Majidi, J. Yun, and K. van Benthem, “Electrode Effects on Microstructure Formation During FLASH Sintering of Yttrium-Stabilized Zirconia,” *J. Am. Ceram. Soc.*, vol. 99, no. 7, pp. 2253–2259, Jul. 2016, doi: 10.1111/jace.14234.

[94] H. Conrad, “Space Charge and Grain Boundary Energy in Zirconia (3Y-TZP),” *J. Am. Ceram. Soc.*, vol. 94, no. 11, pp. 3641–3642, 2011, doi: 10.1111/j.1551-2916.2011.04823.x.

[95] A. Tsoga and P. Nikolopoulos, “Surface and grain-boundary energies in yttria-stabilized zirconia (YSZ-8 mol%),” *J. Mater. Sci.*, vol. 31, no. 20, pp. 5409–5413, 1996.

[96] Y. Dong, H. Wang, and I.-W. Chen, “Electrical and hydrogen reduction enhances kinetics in doped zirconia and ceria: I. grain growth study,” *J. Am. Ceram. Soc.*, vol. 100, no. 3, pp. 876–886, Mar. 2017, doi: https://doi.org/10.1111/jace.14615.

[97] H. Wang *et al.*, “Key microstructural characteristics in flash sintered 3YSZ critical for enhanced sintering process,” *Ceram. Int.*, vol. 45, no. 1, pp. 1251–1257, 2019, doi: https://doi.org/10.1016/j.ceramint.2018.10.007.

[98] J.-M. Lebrun, T. G. Morrissey, J. S. C. Francis, K. C. Seymour, W. M. Kriven, and R. Raj, “Emergence and Extinction of a New Phase During On–Off Experiments Related to Flash Sintering of 3YSZ,” *J. Am. Ceram. Soc.*, vol. 98, no. 5, pp. 1493–1497, May 2015, doi: 10.1111/jace.13476.

[99] S. Fabris, A. T. Paxton, and M. W. Finnis, “A stabilization mechanism of zirconia based on oxygen vacancies only,” *Acta Mater.*, vol. 50, no. 20, pp. 5171–5178, 2002, doi: https://doi.org/10.1016/S1359-6454(02)00385-3.

[100] P. Kalita *et al.*, “Oxygen vacancy mediated cubic phase stabilization at room temperature in pure nano-crystalline zirconia films: a combined experimental and first-principles based investigation,” *Phys. Chem. Chem. Phys.*, vol. 21, no. 40, pp. 22482–22490, 2019, doi: 10.1039/C9CP02121C.

[101] N. Morisaki, H. Yoshida, K. Matsui, T. Tokunaga, K. Sasaki, and T. Yamamoto, “Synthesis of zirconium oxynitride in air under DC electric fields,” *Appl. Phys. Lett.*, vol. 109, no. 8, p. 83104, Aug. 2016, doi: 10.1063/1.4961624.

[102] T. Kurachi, Y. Yamashita, T. Tokunaga, H. Yoshida, and T. Yamamoto, “Suppression of nitridation of yttria-doped zirconia during flash sintering,” *J. Am. Ceram. Soc.*, vol. 103, no. 5, pp. 3002–3007, May 2020, doi: 10.1111/jace.16990.

[103] J.-C. M’Peko, J. S. C. Francis, and R. Raj, “Impedance Spectroscopy and Dielectric Properties of Flash Versus Conventionally Sintered Yttria-Doped Zirconia Electroceramics Viewed at the Microstructural Level,” *J. Am. Ceram. Soc.*, vol. 96, no. 12, pp. 3760–3767, Dec. 2013, doi: 10.1111/jace.12567.

[104] H. Tanaka, “Silicon carbide powder and sintered materials,” *J. Ceram. Soc. Japan,*

vol. 119, no. 1387, pp. 218–233, 2011.

[105] N. W. Jepps and T. F. Page, “Polytypic transformations in silicon carbide,” *Prog. Cryst. Growth Charact.*, vol. 7, no. 1, pp. 259–307, 1983, doi: https://doi.org/10.1016/0146-3535(83)90034-5.

[106] S. Mitridis, “Physics of Advanced Materials Winter School 2008 Determination of lattice site location of impurities in compound semiconductors, by transmission electron microscopy,” Mar. 2011.

[107] D. Chaussende and N. Ohtani, “5 - Silicon carbide,” in *Woodhead Publishing Series in Electronic and Optical Materials*, R. B. T.-S. C. of E. M. Fornari, Ed. Woodhead Publishing, 2019, pp. 129–179.

[108] M. Ohyanagi, “Chapter 5 - Simultaneous transformation and consolidation of stacking-sequence disordered SiC without sintering additives,” G. Cao, C. Estournès, J. Garay, and R. B. T.-S. P. S. Orrù, Eds. Elsevier, 2019, pp. 127–152.

[109] E. Zapata-Solvas, S. Bonilla, P. R. Wilshaw, and R. I. Todd, “Preliminary investigation of flash sintering of SiC,” *J. Eur. Ceram. Soc.*, vol. 33, no. 13, pp. 2811–2816, 2013, doi: https://doi.org/10.1016/j.jeurceramsoc.2013.04.023.

[110] R. W. Carpenter, W. Braue, and R. A. Cutler, “Transmission electron microscopy of liquid phase densified SiC,” *J. Mater. Res.*, vol. 6, no. 9, pp. 1937–1944, 1991, doi: DOI: 10.1557/JMR.1991.1937.

[111] F. Cancino-Trejo, D. J. Navarro-Solis, E. López-Honorato, J. Rabone, R. C. Walker, and R. Salomon, “Grain boundary complexions in silicon carbide,” *J. Am. Ceram.*

Soc., vol. 101, no. 3, pp. 1009–1013, Mar. 2018, doi: https://doi.org/10.1111/jace.15300.

[112] S. Prochazka, "Sintering of silicon carbide," *Ceram. high-performance Appl.*, pp. 239–252, 1974.

[113] S. PROCHAZKA and R. M. SCANLAN, "Effect of Boron and Carbon on Sintering of SIC," *J. Am. Ceram. Soc.*, vol. 58, no. 1–2, p. 72, Jan. 1975, doi: https://doi.org/10.1111/j.1151-2916.1975.tb18990.x.

[114] W. Van Rijswijk and D. J. Shanefield, "Effects of carbon as a sintering aid in silicon carbide," *J. Am. Ceram. Soc.*, vol. 73, no. 1, pp. 148–149, 1990.

[115] S. Prochazka, "Sintering of silicon carbide," in *Mass transport phenomena in ceramics*, Springer, 1975, pp. 421–431.

[116] L. Stobierski and A. Gubernat, "Sintering of silicon carbideI. Effect of carbon," *Ceram. Int.*, vol. 29, no. 3, pp. 287–292, 2003, doi: https://doi.org/10.1016/S0272-8842(02)00117-7.

[117] L. Stobierski and A. Gubernat, "Sintering of silicon carbide II. Effect of boron," *Ceram. Int.*, vol. 29, no. 4, pp. 355–361, 2003, doi: https://doi.org/10.1016/S0272-8842(02)00144-X.

[118] D. C. Jana, P. Barick, and B. P. Saha, "Effect of Sintering Temperature on Density and Mechanical Properties of Solid-State Sintered Silicon Carbide Ceramics and Evaluation of Failure Origin," *J. Mater. Eng. Perform.*, vol. 27, no. 6, pp. 2960–2966, 2018, doi: 10.1007/s11665-018-3397-4.

[119] N. P. Padture, “In Situ-Toughened Silicon Carbide,” *J. Am. Ceram. Soc.*, vol. 77, no. 2, pp. 519–523, Feb. 1994, doi: https://doi.org/10.1111/j.1151-2916.1994.tb07024.x.

[120] M. S. Datta, A. K. Bandyopadhyay, and B. Chaudhuri, “Sintering of nano crystalline α silicon carbide by doping with boron carbide,” *Bull. Mater. Sci.*, vol. 25, no. 3, pp. 181–189, 2002.

[121] C.-S. Lee, Y.-W. Kim, D.-H. Cho, H.-B. Lee, and H.-J. Lim, “Microstructure and mechanical properties of self-Reinforced alpha–Silicon carbide,” *Ceram. Int.*, vol. 24, no. 7, pp. 489–495, 1998, doi: https://doi.org/10.1016/S0272-8842(97)00047-3.

[122] L. R. Vargas-Gonzalez, “Microstructural optimization of solid-state sintered silicon carbide,” Georgia Institute of Technology, Ann Arbor, 2010.

[123] M. Tokita, “Chapter 11.2.3 - Spark Plasma Sintering (SPS) Method, Systems, and Applications,” S. B. T.-H. of A. C. (Second E. Somiya, Ed. Oxford: Academic Press, 2013, pp. 1149–1177.

[124] S. Grasso, T. Saunders, H. Porwal, B. Milsom, A. Tudball, and M. Reece, “Flash Spark Plasma Sintering (FSPS) of α and β SiC,” *J. Am. Ceram. Soc.*, vol. 99, no. 5, pp. 1534–1543, May 2016, doi: https://doi.org/10.1111/jace.14158.

[125] E. A. Olevsky, S. M. Rolfing, and A. L. Maximenko, “Flash (Ultra-Rapid) Spark-Plasma Sintering of Silicon Carbide,” *Sci. Rep.*, vol. 6, no. 1, p. 33408, 2016, doi: 10.1038/srep33408.

[126] S. Grasso *et al.*, “Ultra-Rapid Crystal Growth of Textured SiC Using Flash Spark

Plasma Sintering Route," *Cryst. Growth Des.*, vol. 16, no. 4, pp. 2317–2321, Apr. 2016, doi: 10.1021/acs.cgd.6b00099.

[127] D. Demirskyi and O. Vasylkiv, "Hot-spots generation, exaggerated grain growth and mechanical performance of silicon carbide bulks consolidated by flash spark plasma sintering," *J. Alloys Compd.*, vol. 691, pp. 466–473, 2017, doi: https://doi.org/10.1016/j.jallcom.2016.08.234.

[128] N. Asaoka, S. Muto, and T. Tanabe, "Formation of Si clusters in electron-irradiated SiC studied by electron energy-loss spectroscopy," *Diam. Relat. Mater.*, vol. 10, no. 3, pp. 1251–1254, 2001, doi: https://doi.org/10.1016/S0925-9635(00)00453-2.

[129] U. Kaiser, D. A. Muller, J. L. Grazul, A. Chuvilin, and M. Kawasaki, "Direct observation of defect-mediated cluster nucleation," *Nat. Mater.*, vol. 1, no. 2, pp. 102–105, 2002, doi: 10.1038/nmat729.

[130] U. Kaiser, D. A. Muller, A. Chuvilin, G. Pasold, and W. Witthuhn, "The Formation of Clusters and Nanocrystals in Er-Implanted Hexagonal Silicon Carbide," *Microsc. Microanal.*, vol. 10, no. 2, pp. 301–310, 2004, doi: DOI: 10.1017/S1431927604040449.

[131] D. Chen, M. E. Sixta, X. F. Zhang, L. C. De Jonghe, and R. O. Ritchie, "Role of the grain-boundary phase on the elevated-temperature strength, toughness, fatigue and creep resistance of silicon carbide sintered with Al, B and C," *Acta Mater.*, vol. 48, no. 18, pp. 4599–4608, 2000, doi: https://doi.org/10.1016/S1359-6454(00)00246-9.

[132] C. Patricia *et al.*, "Boron-doping of cubic SiC for intermediate band solar cells: a scanning transmission electron microscopy study," *SciPost Phys.*, vol. 5, no. 3, pp.

1–17, 2018.

[133] X. F. Zhang, M. E. Sixta, and L. C. De Jonghe, “Secondary Phases in Hot-Pressed Aluminum-Boron-Carbon–Silicon Carbide,” *J. Am. Ceram. Soc.*, vol. 84, no. 4, pp. 813–820, Apr. 2001, doi: https://doi.org/10.1111/j.1151-2916.2001.tb00746.x.

[134] X. F. Zhang, M. E. Sixta, and L. C. De Jonghe, “Grain Boundary Evolution in Hot-Pressed ABC-SiC,” *J. Am. Ceram. Soc.*, vol. 83, no. 11, pp. 2813–2820, Nov. 2000, doi: https://doi.org/10.1111/j.1151-2916.2000.tb01637.x.

[135] R. O. Ritchie, X.-F. Zhang, and L. C. De Jonghe, “On the Role of Grain-Boundary Films in Optimizing the Mechanical Properties of Silicon Carbide Ceramics,” *MRS Proc.*, vol. 818, p. N1.1.1, 2004, doi: DOI: 10.1557/PROC-818-N1.1.1.

[136] X. F. Zhang and L. C. De Jonghe, “Thermal Modification of Microstructures and Grain Boundaries in Silicon Carbide,” *J. Mater. Res.*, vol. 18, no. 12, pp. 2807–2813, 2003, doi: 10.1557/JMR.2003.0391.

[137] X. F. Zhang and L. C. DeJonghe, “Aluminum-containing intergranular phases in hot-pressed silicon carbide,” *J. Mater. Res.*, vol. 19, no. 8, pp. 2510–2516, 2004, doi: 10.1557/JMR.2004.0320.

[138] S. Tsurekawa, S. Nitta, H. Nakashima, and H. Yoshinaga, “Grain boundary structures in silicon carbide: Verification of the extended boundary concept,” *Interface Sci.*, vol. 3, no. 1, pp. 75–84, 1995, doi: 10.1007/BF00203983.

[139] Y. Ikuhara, H. Miyazaki, H. Kurishita, and H. Yoshinaga, “Grain boundary structure and strength of SiC bicrystals,” *J. Ceram. Soc. Japan*, vol. 97, no. 1132, pp. 1511–

1516, 1989.

[140] H. Gu, Y. Shinoda, and F. Wakai, “Detection of Boron Segregation to Grain Boundaries in Silicon Carbide by Spatially Resolved Electron Energy-Loss Spectroscopy,” *J. Am. Ceram. Soc.*, vol. 82, no. 2, pp. 469–472, Feb. 1999, doi: https://doi.org/10.1111/j.1551-2916.1999.tb20089.x.

[141] H. Gu and Y. Shinoda, “Structural and Chemical Widths of General Grain Boundaries: Modification of Local Structure and Bonding by Boron-Doping in β-Silicon Carbide,” *Interface Sci.*, vol. 8, no. 2, pp. 269–278, 2000, doi: 10.1023/A:1008720404554.

[142] M. Thuvander, A. Kvist, L. J. S. Johnson, J. Weidow, and H.-O. Andrén, “Reduction of multiple hits in atom probe tomography,” *Ultramicroscopy*, vol. 132, pp. 81–85, 2013, doi: https://doi.org/10.1016/j.ultramic.2012.12.005.

[143] M. Thuvander *et al.*, “Quantitative atom probe analysis of carbides,” *Ultramicroscopy*, vol. 111, no. 6, pp. 604–608, 2011.

[144] L. Diallo, L. Lechevallier, A. Fnidiki, J. Juraszek, M. Viret, and A. Declémy, “Characterization of nanostructure in low dose Fe-implanted p-type 6H-SiC using atom probe tomography,” *J. Magn. Magn. Mater.*, vol. 481, pp. 189–193, 2019.

[145] M. L. Diallo *et al.*, “Fe-implanted 6H-SiC: Direct evidence of Fe3Si nanoparticles observed by atom probe tomography and 57Fe Mössbauer spectroscopy,” *J. Appl. Phys.*, vol. 117, no. 18, p. 183907, May 2015, doi: 10.1063/1.4921056.

[146] L. Diallo *et al.*, “6H-SiC-Fe Nanostructures Studied by Atom Probe Tomography,”

IEEE Magn. Lett., vol. 9, pp. 1–3, 2018, doi: 10.1109/LMAG.2018.2829109.

[147] L. Zhang *et al.*, "Probing the origins of magnetism in 2 at% Fe-implanted 4H-SiC," *Scr. Mater.*, vol. 188, pp. 157–163, 2020, doi: https://doi.org/10.1016/j.scriptamat.2020.07.030.

[148] P. R. Heck *et al.*, "Atom-probe tomographic analyses of presolar silicon carbide grains and meteoric nanodiamonds–first results on silicon carbide," 2010.

[149] J. B. Lewis, D. Isheim, C. Floss, E. Groopman, F. Gyngard, and D. N. Seidman, "Isotopic composition and trace element abundances of a presolar SiC AB grain reconstructed by atom-probe tomography," *LPICo*, vol. 77, no. 1800, p. 5367, 2014.

[150] J. B. Lewis, C. Floss, D. Isheim, and D. N. Seidman, "Study of Asymptotic Giant Branch Stars and Type II Supernovae Via nm-Scale Isotopic Analyses of Presolar Silicon Carbide by Atom-Probe Tomography," in *81st Annual Meeting of the Meteoritical Society*, 2018, vol. 81, no. 2067, p. 6269.

[151] D. J. Larson *et al.*, "Analysis of Bulk Dielectrics with Atom Probe Tomography," *Microsc. Microanal.*, vol. 14, no. S2, pp. 1254–1255, 2008, doi: DOI: 10.1017/S1431927608083657.

[152] Y. M. Chen, T. Ohkubo, and K. Hono, "Laser assisted field evaporation of oxides in atom probe analysis," *Ultramicroscopy*, vol. 111, no. 6, pp. 562–566, 2011.

[153] J.-B. Seol, C.-M. Kwak, Y.-T. Kim, and C.-G. Park, "Understanding of the field evaporation of surface modified oxide materials through transmission electron microscopy and atom probe tomography," *Appl. Surf. Sci.*, vol. 368, pp. 368–377,

2016, doi: https://doi.org/10.1016/j.apsusc.2016.01.196.

[154] S. Koelling, N. Innocenti, A. Schulze, M. Gilbert, A. K. Kambham, and W. Vandervorst, “In-situ observation of non-hemispherical tip shape formation during laser-assisted atom probe tomography,” *J. Appl. Phys.*, vol. 109, no. 10, p. 104909, May 2011, doi: 10.1063/1.3592339.

[155] C.-M. Kwak, Y.-T. Kim, C.-G. Park, and J.-B. Seol, “Understanding of Capping Effects on the Tip Shape Evolution and on the Atom Probe Data of Bulk LaAlO3 Using Transmission Electron Microscopy,” *Microsc. Microanal.*, vol. 23, no. 2, pp. 329–335, 2017, doi: 10.1017/S1431927617000149.

[156] D. R. Clark *et al.*, “Probing Grain-Boundary Chemistry and Electronic Structure in Proton-Conducting Oxides by Atom Probe Tomography,” *Nano Lett.*, vol. 16, no. 11, pp. 6924–6930, Nov. 2016, doi: 10.1021/acs.nanolett.6b02918.

[157] D. R. Diercks, B. P. Gorman, A. Manerbino, and G. Coors, “Atom Probe Tomography of Yttrium-Doped Barium–Cerium–Zirconium Oxide with NiO Addition,” *J. Am. Ceram. Soc.*, vol. 97, no. 10, pp. 3301–3306, 2014.

[158] D. R. Diercks *et al.*, “Three-dimensional quantification of composition and electrostatic potential at individual grain boundaries in doped ceria,” *J. Mater. Chem. A*, vol. 4, no. 14, pp. 5167–5175, 2016.

[159] K. Babinsky, R. De Kloe, H. Clemens, and S. Primig, “A novel approach for site-specific atom probe specimen preparation by focused ion beam and transmission electron backscatter diffraction,” *Ultramicroscopy*, vol. 144, pp. 9–18, 2014, doi: https://doi.org/10.1016/j.ultramic.2014.04.003.

[160] B. Gault *et al.*, “Behavior of molecules and molecular ions near a field emitter,” *New J. Phys.*, vol. 18, no. 3, p. 33031, 2016.

[161] R. J. H. Morris *et al.*, “Toward accurate composition analysis of GaN and AlGaN using atom probe tomography,” *J. Vac. Sci. Technol. B*, vol. 36, no. 3, p. 03F130, Mar. 2018, doi: 10.1116/1.5019693.

[162] L. Miaja-Avila *et al.*, “Extreme Ultraviolet Radiation Pulsed Atom Probe Tomography of III-Nitride Semiconductor Materials,” *J. Phys. Chem. C*, vol. 125, no. 4, pp. 2626–2635, Feb. 2021, doi: 10.1021/acs.jpcc.0c08753.

[163] M. MUNRO, “Evaluated Material Properties for a Sintered alpha-Alumina,” *J. Am. Ceram. Soc.*, vol. 80, no. 8, pp. 1919–1928, Aug. 1997, doi: 10.1111/j.1151-2916.1997.tb03074.x.

[164] M. YOSHIDA, S. FALCO, and R. I. TODD, “Measurement and modelling of electrical resistivity by four-terminal method during flash sintering of 3YSZ,” *J. Ceram. Soc. Japan*, vol. 126, no. 7, pp. 579–590, 2018, doi: 10.2109/jcersj2.17256.

[165] B. Gault, M. P. Moody, J. M. Cairney, and S. P. Ringer, *Atom probe microscopy*, vol. 160. Springer Science & Business Media, 2012.

[166] A. S. Chang and L. J. Lauhon, “Atom probe tomography of nanoscale architectures in functional materials for electronic and photonic applications,” *Curr. Opin. Solid State Mater. Sci.*, vol. 22, no. 5, pp. 171–187, 2018, doi: https://doi.org/10.1016/j.cossms.2018.09.002.

[167] B. Gault *et al.*, “Atom probe tomography,” *Nat. Rev. Methods Prim.*, vol. 1, no. 1, p.

51, 2021, doi: 10.1038/s43586-021-00047-w.

[168] A. Cerezo, T. J. Godfrey, S. J. Sijbrandij, G. D. W. Smith, and P. J. Warren, "Performance of an energy-compensated three-dimensional atom probe," *Rev. Sci. Instrum.*, vol. 69, no. 1, pp. 49–58, Jan. 1998, doi: 10.1063/1.1148477.

[169] M. Wada, "On the thermally activated field evaporation of surface atoms," *Surf. Sci.*, vol. 145, no. 2–3, pp. 451–465, 1984.

[170] D. R. Kingham, "The post-ionization of field evaporated ions: A theoretical explanation of multiple charge states," *Surf. Sci.*, vol. 116, no. 2, pp. 273–301, 1982, doi: https://doi.org/10.1016/0039-6028(82)90434-4.

[171] D. W. Saxey, "Correlated ion analysis and the interpretation of atom probe mass spectra," *Ultramicroscopy*, vol. 111, no. 6, pp. 473–479, 2011, doi: https://doi.org/10.1016/j.ultramic.2010.11.021.

[172] P. Bas, A. Bostel, B. Deconihout, and D. Blavette, "A general protocol for the reconstruction of 3D atom probe data," *Appl. Surf. Sci.*, vol. 87–88, pp. 298–304, 1995, doi: https://doi.org/10.1016/0169-4332(94)00561-3.

[173] D. J. Larson, B. Gault, B. P. Geiser, F. De Geuser, and F. Vurpillot, "Atom probe tomography spatial reconstruction: Status and directions," *Curr. Opin. Solid State Mater. Sci.*, vol. 17, no. 5, pp. 236–247, 2013, doi: https://doi.org/10.1016/j.cossms.2013.09.002.

[174] D. Haley, P. Choi, and D. Raabe, "Guided mass spectrum labelling in atom probe tomography," *Ultramicroscopy*, vol. 159, pp. 338–345, 2015, doi:

https://doi.org/10.1016/j.ultramic.2015.03.005.

[175] E. Oltman, R. Ulfig, and D. J. Larson, “Background Removal Methods Applied to Atom Probe Data,” *Microsc. Microanal.*, vol. 15, no. S2, pp. 256–257, 2009, doi: DOI: 10.1017/S1431927609095488.

[176] O. C. Hellman, J. B. du Rivage, and D. N. Seidman, “Efficient sampling for three-dimensional atom probe microscopy data,” *Ultramicroscopy*, vol. 95, pp. 199–205, 2003, doi: https://doi.org/10.1016/S0304-3991(02)00317-0.

[177] M. K. Miller, *Atom probe field ion microscopy*. Oxford: Clarendon Press, 1996.

[178] T. J. Godfrey, M. G. Hetherington, J. M. Sassen, and G. D. W. Smith, “The characterization of spinodal structures in duplex CF3 steels,” *Le J. Phys. Colloq.*, vol. 49, no. C6, pp. C6-421, 1988.

[179] M. P. Moody, L. T. Stephenson, A. V Ceguerra, and S. P. Ringer, “Quantitative binomial distribution analyses of nanoscale like-solute atom clustering and segregation in atom probe tomography data,” *Microsc. Res. Tech.*, vol. 71, no. 7, pp. 542–550, Jul. 2008, doi: https://doi.org/10.1002/jemt.20582.

[180] K. Pearson, *On the theory of contingency and its relation to association and normal correlation*. Dulau and Company, 1904.

[181] L. T. Stephenson, M. P. Moody, P. V Liddicoat, and S. P. Ringer, “New Techniques for the Analysis of Fine-Scaled Clustering Phenomena within Atom Probe Tomography (APT) Data,” *Microsc. Microanal.*, vol. 13, no. 6, pp. 448–463, 2007, doi: DOI: 10.1017/S1431927607070900.

[182] T. Philippe *et al.*, “Clustering and nearest neighbour distances in atom-probe tomography,” *Ultramicroscopy*, vol. 109, no. 10, pp. 1304–1309, 2009, doi: https://doi.org/10.1016/j.ultramic.2009.06.007.

[183] D. Vaumousse, A. Cerezo, and P. J. Warren, “A procedure for quantification of precipitate microstructures from three-dimensional atom probe data,” *Ultramicroscopy*, vol. 95, pp. 215–221, 2003, doi: https://doi.org/10.1016/S0304-3991(02)00319-4.

[184] R. P. Kolli and D. N. Seidman, “Comparison of Compositional and Morphological Atom-Probe Tomography Analyses for a Multicomponent Fe-Cu Steel,” *Microsc. Microanal.*, vol. 13, no. 4, pp. 272–284, 2007, doi: DOI: 10.1017/S1431927607070675.

[185] O. C. Hellman and D. N. Seidman, “Measurement of the Gibbsian interfacial excess of solute at an interface of arbitrary geometry using three-dimensional atom probe microscopy,” *Mater. Sci. Eng. A*, vol. 327, no. 1, pp. 24–28, 2002, doi: https://doi.org/10.1016/S0921-5093(01)01885-8.

[186] O. C. Hellman, J. A. Vandenbroucke, J. Rüsing, D. Isheim, and D. N. Seidman, “Analysis of three-dimensional atom-probe data by the proximity histogram,” *Microsc. Microanal.*, vol. 6, no. 5, pp. 437–444, 2000.

[187] B. Jenkins, “Improving the safety and reliability of reactor pressure vessel steels.” University of Oxford, 2019.

[188] B. M. Jenkins *et al.*, “A more holistic characterisation of internal interfaces in a variety of materials via complementary use of transmission Kikuchi diffraction and

Atom probe tomography," *Appl. Surf. Sci.*, vol. 528, p. 147011, 2020, doi: https://doi.org/10.1016/j.apsusc.2020.147011.

[189] K. D. Vernon-Parry, "Scanning electron microscopy: an introduction," *III-Vs Rev.*, vol. 13, no. 4, pp. 40–44, 2000.

[190] M. E. L. I. MENDELSON, "Average Grain Size in Polycrystalline Ceramics," *J. Am. Ceram. Soc.*, vol. 52, no. 8, pp. 443–446, Aug. 1969, doi: 10.1111/j.1151-2916.1969.tb11975.x.

[191] J. C. Russ, M. A. Frs, R. Kiessling, and J. Charles, *Fundamentals of Energy Dispersive X-Ray Analysis : Butterworths Monographs in Materials*. Burlington: Butterworth-Heinemann, 1984.

[192] Oxford Instruments, "EBSD Explained."

[193] G. C. Sneddon, P. W. Trimby, and J. M. Cairney, "Transmission Kikuchi diffraction in a scanning electron microscope: A review," *Mater. Sci. Eng. R Reports*, vol. 110, pp. 1–12, 2016, doi: https://doi.org/10.1016/j.mser.2016.10.001.

[194] R. R. KELLER and R. H. GEISS, "Transmission EBSD from 10 nm domains in a scanning electron microscope," *J. Microsc.*, vol. 245, no. 3, pp. 245–251, Mar. 2012, doi: https://doi.org/10.1111/j.1365-2818.2011.03566.x.

[195] P. D. Nellist, "Scanning transmission electron microscopy," in *Science of microscopy*, Springer, 2007, pp. 65–132.

[196] "Keysight 5500 Scanning Probe Microscope: User's Guide," 2014.

[197] D. Nečas and P. Klapetek, "Gwyddion: an open-source software for SPM data

analysis," *Open Phys.*, vol. 10, no. 1, pp. 181–188, 2012.

[198] M. N. Kelly, W. Rheinheimer, M. J. Hoffmann, and G. S. Rohrer, "Anti-thermal grain growth in SrTiO3: Coupled reduction of the grain boundary energy and grain growth rate constant," *Acta Materialia*, vol. 149. pp. 11–18, 2018, doi: https://doi.org/10.1016/j.actamat.2018.02.030.

[199] J. S. Villarrubia, "JS Villarrubia, J. Res. Natl. Inst. Stand. Technol. 102, 425 (1997).," *J.Res.Natl.Inst.Stand.Technol.*, vol. 102, p. 425, 1997.

[200] N. Ni, Y. Kaufmann, W. D. Kaplan, and E. Saiz, "Interfacial energies and mass transport in the Ni(Al)–Al2O3 system: The implication of very low oxygen activities," *Acta Mater.*, vol. 64, pp. 282–296, 2014, doi: https://doi.org/10.1016/j.actamat.2013.10.041.

[201] Z. Peng, F. Vurpillot, P.-P. Choi, Y. Li, D. Raabe, and B. Gault, "On the detection of multiple events in atom probe tomography," *Ultramicroscopy*, vol. 189, pp. 54–60, 2018, doi: https://doi.org/10.1016/j.ultramic.2018.03.018.

[202] R. Haydock and D. R. Kingham, "Some predictions of a theory of post-ionization of field-evaporated ions," *Surf. Sci. Lett.*, vol. 104, no. 1, pp. L194–L198, 1981, doi: https://doi.org/10.1016/0167-2584(81)90176-6.

[203] Z. Jiang, "GIXSGUI: a MATLAB toolbox for grazing-incidence X-ray scattering data visualization and reduction, and indexing of buried three-dimensional periodic nanostructured films," *J. Appl. Crystallogr.*, vol. 48, no. 3, pp. 917–926, 2015.

[204] Y. Liu, J. Lin, G. Huang, Y. Guo, and C. Duan, "Simple empirical analytical

approximation to the Voigt profile," *J. Opt. Soc. Am. B*, vol. 18, no. 5, pp. 666–672, 2001, doi: 10.1364/JOSAB.18.000666.

[205] A. J. London, D. Haley, and M. P. Moody, "Single-Ion Deconvolution of Mass Peak Overlaps for Atom Probe Microscopy," *Microsc. Microanal.*, vol. 23, no. 2, pp. 300–306, 2017, doi: DOI: 10.1017/S1431927616012782.

[206] A. J. London, "Quantifying Uncertainty from Mass-Peak Overlaps in Atom Probe Microscopy," *Microsc. Microanal.*, vol. 25, no. 2, pp. 378–388, 2019, doi: DOI: 10.1017/S1431927618016276.

[207] J. R. Riley, R. A. Bernal, Q. Li, H. D. Espinosa, G. T. Wang, and L. J. Lauhon, "Atom Probe Tomography of a-Axis GaN Nanowires: Analysis of Nonstoichiometric Evaporation Behavior," *ACS Nano*, vol. 6, no. 5, pp. 3898–3906, May 2012, doi: 10.1021/nn2050517.

[208] J. J. Roa, H. Aboulfadl, J. Barrirero, M. Turon-Vinas, F. Mücklich, and M. Anglada, "Chemical segregation in a 12Ce-ZrO2/3Y-ZrO2 ceramic composite," *Mater. Charact.*, vol. 132, pp. 83–91, 2017, doi: https://doi.org/10.1016/j.matchar.2017.07.045.

[209] R. P. Kolli and F. Meisenkothen, "The Influence of Experimental Parameters and Specimen Geometry on the Mass Spectra of Copper During Pulsed-Laser Atom-Probe Tomography," *Microsc. Microanal.*, vol. 20, no. 6, pp. 1715–1726, 2014, doi: DOI: 10.1017/S1431927614013488.

[210] K. Oh-ishi, C. L. Mendis, T. Ohkubo, and K. Hono, "Effect of laser power and specimen temperature on atom probe analyses of magnesium alloys,"

Ultramicroscopy, vol. 111, no. 6, pp. 715–718, 2011, doi: https://doi.org/10.1016/j.ultramic.2011.01.002.

[211] M. Gilbert, F. Vurpillot, A. Vella, H. Bernas, and B. Deconihout, "Some aspects of the silicon behaviour under femtosecond pulsed laser field evaporation," *Ultramicroscopy*, vol. 107, no. 9, pp. 767–772, 2007, doi: https://doi.org/10.1016/j.ultramic.2007.02.027.

[212] B. Gault *et al.*, "Influence of surface migration on the spatial resolution of pulsed laser atom probe tomography," *J. Appl. Phys.*, vol. 108, no. 4, p. 44904, Aug. 2010, doi: 10.1063/1.3462399.

[213] T. T. Tsong, "Field ion image formation," *Surf. Sci.*, vol. 70, no. 1, pp. 211–233, 1978, doi: https://doi.org/10.1016/0039-6028(78)90410-7.

[214] D.-M. Liu and B.-W. Lin, "Thermal conductivity in hot-pressed silicon carbide," *Ceram. Int.*, vol. 22, no. 5, pp. 407–414, 1996, doi: https://doi.org/10.1016/0272-8842(95)00125-5.

[215] A. M. Limarga and D. R. Clarke, "The grain size and temperature dependence of the thermal conductivity of polycrystalline, tetragonal yttria-stabilized zirconia," *Appl. Phys. Lett.*, vol. 98, no. 21, p. 211906, May 2011, doi: 10.1063/1.3593383.

[216] A. Shariq *et al.*, "Investigations of field-evaporated end forms in voltage- and laser-pulsed atom probe tomography," *Ultramicroscopy*, vol. 109, no. 5, pp. 472–479, 2009, doi: https://doi.org/10.1016/j.ultramic.2008.10.001.

[217] J. M. Hyde *et al.*, "Atom probe tomography of reactor pressure vessel steels: An

analysis of data integrity," *Ultramicroscopy*, vol. 111, no. 6, pp. 676–682, 2011.

[218] F. Meisenkothen, E. B. Steel, T. J. Prosa, K. T. Henry, and R. P. Kolli, "Effects of detector dead-time on quantitative analyses involving boron and multi-hit detection events in atom probe tomography," *Ultramicroscopy*, vol. 159, pp. 101–111, 2015.

[219] A. Cerezo, P. H. Clifton, A. Gomberg, and G. D. W. Smith, "Aspects of the performance of a femtosecond laser-pulsed 3-dimensional atom probe," *Ultramicroscopy*, vol. 107, no. 9, pp. 720–725, 2007, doi: https://doi.org/10.1016/j.ultramic.2007.02.025.

[220] R. Moshe and W. D. Kaplan, "The influence of CaO on alumina grain boundary mobility," *J. Eur. Ceram. Soc.*, vol. 39, no. 4, pp. 1324–1328, 2019.

[221] S. K. Behera, "Kinetics of grain growth in La-doped ultrapure Al2O3," *J. Alloys Compd.*, vol. 683, pp. 444–449, 2016.

[222] R. Akiva, A. Katsman, and W. D. Kaplan, "Anisotropic grain boundary mobility in undoped and doped alumina," *J. Am. Ceram. Soc.*, vol. 97, no. 5, pp. 1610–1618, 2014.

[223] S. J. Dillon and M. P. Harmer, "Demystifying the role of sintering additives with 'complexion,'" *Developments in Ceramic Science and Engineering: the last 50 years. A meeting in celebration of Professor Sir Richard Brook's 70th Birthday*, vol. 28, no. 7. pp. 1485–1493, 2008, doi: https://doi.org/10.1016/j.jeurceramsoc.2007.12.018.

[224] S. J. Dillon, *Relationship between grain boundary complexion and grain growth*

kinetics in alumina. Lehigh University, 2007.

[225] B. MUSSLER, M. V SWAIN, and N. CLAUSSEN, “Dependence of Fracture Toughness of Alumina on Grain Size and Test Technique,” *J. Am. Ceram. Soc.*, vol. 65, no. 11, pp. 566–572, Nov. 1982, doi: https://doi.org/10.1111/j.1151-2916.1982.tb10783.x.

[226] P. Gruffel and C. Carry, “Effect of grain size on yttrium grain boundary segregation in fine-grained alumina,” *J. Eur. Ceram. Soc.*, vol. 11, no. 3, pp. 189–199, 1993, doi: https://doi.org/10.1016/0955-2219(93)90087-8.

[227] A. Ksibi *et al.*, “Experimental and numerical assessment of grain boundary energies in polycrystalline uranium dioxide,” *J. Eur. Ceram. Soc.*, vol. 40, no. 12, pp. 4191–4201, 2020, doi: https://doi.org/10.1016/j.jeurceramsoc.2020.04.041.

[228] M. Marrese, V. Guarino, and L. Ambrosio, “Atomic force microscopy: a powerful tool to address scaffold design in tissue engineering,” *J. Funct. Biomater.*, vol. 8, no. 1, p. 7, 2017.

[229] C. J. Wright, L. C. Powell, D. J. Johnson, and N. Hilal, “MICROSCOPY | Atomic Force Microscopy,” C. A. Batt and M. L. B. T.-E. of F. M. (Second E. Tortorello, Eds. Oxford: Academic Press, 2014, pp. 666–675.

[230] G. S. Rohrer, “The role of grain boundary energy in grain boundary complexion transitions,” *Curr. Opin. Solid State Mater. Sci.*, vol. 20, no. 5, pp. 231–239, 2016, doi: https://doi.org/10.1016/j.cossms.2016.03.001.

[231] J. G. J. Peelen, “Influence of MgO on the Evolution of the Microstructure of

Alumina BT - Sintering and Catalysis," G. C. Kuczynski, Ed. Boston, MA: Springer US, 1975, pp. 443–453.

[232] K. Ando and M. Momoda, "Solubility of MgO in single-crystal Al2O3," *Int. J. High Technol. Ceram.*, vol. 4, no. 1, p. 84, 1988, doi: https://doi.org/10.1016/0267-3762(88)90075-6.

[233] C. J. Marvel, T. Frueh, C. Compson, and M. P. Harmer, "Linking grain boundary structure and composition to microstructure in commercial-grade-doped specialty Aluminas," *J. Am. Ceram. Soc.*, vol. n/a, no. n/a, Jul. 2021, doi: https://doi.org/10.1111/jace.18046.

[234] D. Blavette and X. Sauvage, "Chapter One - Early Developments and Basic Concepts," W. Lefebvre-Ulrikson, F. Vurpillot, and X. B. T.-A. P. T. Sauvage, Eds. Academic Press, 2016, pp. 1–15.

[235] J. Katamura and T. Sakuma, "Computer simulation of the microstructural evolution during the diffusionless cubic-to-tetragonal transition in the system ZrO2–Y2O3," *Acta Mater.*, vol. 46, no. 5, pp. 1569–1575, 1998, doi: https://doi.org/10.1016/S1359-6454(97)00356-X.

[236] S. Shukla and S. Seal, "Mechanisms of room temperature metastable tetragonal phase stabilisation in zirconia," *Int. Mater. Rev.*, vol. 50, no. 1, pp. 45–64, Feb. 2005, doi: 10.1179/174328005X14267.

[237] I. R. Gibson and J. T. S. Irvine, "Qualitative X-ray Diffraction Analysis of Metastable Tetragonal (t′) Zirconia," *J. Am. Ceram. Soc.*, vol. 84, no. 3, pp. 615–618, Mar. 2001, doi: https://doi.org/10.1111/j.1151-2916.2001.tb00708.x.

[238] K. Matsui, H. Horikoshi, N. Ohmichi, M. Ohgai, H. Yoshida, and Y. Ikuhara, "Cubic-Formation and Grain-Growth Mechanisms in Tetragonal Zirconia Polycrystal," *J. Am. Ceram. Soc.*, vol. 86, no. 8, pp. 1401–1408, Aug. 2003, doi: https://doi.org/10.1111/j.1151-2916.2003.tb03483.x.

[239] J. A. Downs, "Mechanisms of flash sintering in cubic zirconia." University of Trento, 2013.

[240] J. Janek and C. Korte, "Electrochemical blackening of yttria-stabilized zirconia – morphological instability of the moving reaction front," *Solid State Ionics*, vol. 116, no. 3, pp. 181–195, 1999, doi: https://doi.org/10.1016/S0167-2738(98)00415-9.

[241] C. A. Grimley, A. L. G. Prette, and E. C. Dickey, "Effect of boundary conditions on reduction during early stage flash sintering of YSZ," *Acta Mater.*, vol. 174, pp. 271–278, 2019, doi: https://doi.org/10.1016/j.actamat.2019.05.001.

[242] C. Bonola, P. Camagni, P. Chiodelli, and G. Samoggia, "Study of defects introduced by electroreduction in YSZ," *Radiat. Eff. Defects Solids*, vol. 119, no. 1, pp. 457–462, 1991.

[243] V. M. Orera, R. I. Merino, Y. Chen, R. Cases, and P. J. Alonso, "Electron and hole trapped defects produced by thermoreduction or irradiation in Stabilized Zirconia," *Radiat. Eff. Defects Solids*, vol. 119–121, no. 2, pp. 907–912, Nov. 1991, doi: 10.1080/10420159108220841.

[244] R. Ben-Michael, D. S. Tannhauser, and J. Genossar, "ESR centers in reduced stabilized zirconia," *Phys. Rev. B*, vol. 43, no. 10, pp. 7395–7404, Apr. 1991, doi: 10.1103/PhysRevB.43.7395.

[245] W. Ma, F. W. Herbert, S. D. Senanayake, and B. Yildiz, “Non-equilibrium oxidation states of zirconium during early stages of metal oxidation,” *Appl. Phys. Lett.*, vol. 106, no. 10, p. 101603, Mar. 2015, doi: 10.1063/1.4914180.

[246] H. B. Lee, F. B. Prinz, and W. Cai, “Atomistic simulations of grain boundary segregation in nanocrystalline yttria-stabilized zirconia and gadolinia-doped ceria solid oxide electrolytes,” *Acta Mater.*, vol. 61, no. 10, pp. 3872–3887, 2013, doi: https://doi.org/10.1016/j.actamat.2013.03.027.

[247] R. L. González-Romero, J. J. Meléndez, D. Gómez-García, F. L. Cumbrera, and A. Domínguez-Rodríguez, “Segregation to the grain boundaries in YSZ bicrystals: A Molecular Dynamics study,” *Solid State Ionics*, vol. 237, pp. 8–15, 2013, doi: https://doi.org/10.1016/j.ssi.2013.02.002.

[248] S. A. Artemov *et al.*, “Effect of the ionic radius of stabilizing oxide cation on the local structure and transport properties of zirconia based solid solutions,” *J. Alloys Compd.*, vol. 870, p. 159396, 2021, doi: https://doi.org/10.1016/j.jallcom.2021.159396.

[249] J. D. t McCullough and K. N. Trueblood, “The crystal structure of baddeleyite (monoclinic ZrO2),” *Acta Crystallogr.*, vol. 12, no. 7, pp. 507–511, 1959.

[250] G.-Q. Qu, W. Fang, and W.-C. Zhenga, “Studies of the Spin Hamiltonian Parameters and the Local Structure of Tetragonal Zr3+ Centers in Orthophosphate MPO4 (M = Sc, Lu, Y) Crystals: ,” *Zeitschrift für Naturforsch. A*, vol. 61, no. 12, pp. 688–690, 2006, doi: doi:10.1515/zna-2006-1212.

[251] M. Gendre, A. Maitre, and G. Trolliard, “A study of the densification mechanisms

during spark plasma sintering of zirconium (oxy-) carbide powders," *Acta Mater.*, vol. 58, no. 7, pp. 2598–2609, 2010.

[252] M. Gendre, A. Maître, and G. Trolliard, "Synthesis of zirconium oxycarbide (ZrCxOy) powders: Influence of stoichiometry on densification kinetics during spark plasma sintering and on mechanical properties," *J. Eur. Ceram. Soc.*, vol. 31, no. 13, pp. 2377–2385, 2011.

[253] N. Shakibi Nia *et al.*, "Zirconium Oxycarbide: A Highly Stable Catalyst Material for Electrochemical Energy Conversion," *ChemPhysChem*, vol. 20, no. 22, pp. 3067–3073, Nov. 2019, doi: https://doi.org/10.1002/cphc.201900539.

[254] D. Hauser, A. Auer, J. Kunze-Liebhäuser, S. Schwarz, J. Bernardi, and S. Penner, "Hybrid synthesis of zirconium oxycarbide nanopowders with defined and controlled composition," *RSC Adv.*, vol. 9, no. 6, pp. 3151–3156, 2019, doi: 10.1039/C8RA09584A.

[255] M. Herbig, D. Raabe, Y. J. Li, P. Choi, S. Zaefferer, and S. Goto, "Atomic-Scale Quantification of Grain Boundary Segregation in Nanocrystalline Material," *Phys. Rev. Lett.*, vol. 112, no. 12, p. 126103, Mar. 2014, doi: 10.1103/PhysRevLett.112.126103.

[256] S. Azuma, N. Shibata, T. Mizoguchi, S. D. Findlay, K. Nakamura, and Y. Ikuhara, "Atomic structure, energetics, and chemical bonding of Y doped Σ13 grain boundaries in α-Al2O3," *Philos. Mag.*, vol. 93, no. 10–12, pp. 1158–1171, Apr. 2013, doi: 10.1080/14786435.2012.733827.

[257] A. E. Hughes and S. P. S. Badwal, "Impurity and yttrium segregation in yttria-

tetragonal zirconia," *Solid State Ionics*, vol. 46, no. 3–4, pp. 265–274, 1991.

[258] M. J. Verkerk, B. J. Middelhuis, and A. J. Burggraaf, "Effect of grain boundaries on the conductivity of high-purity ZrO2□Y2O3 ceramics," *Solid State Ionics*, vol. 6, no. 2, pp. 159–170, 1982, doi: https://doi.org/10.1016/0167-2738(82)90083-2.

[259] J. Bernardini, P. Gas, E. D. Hondros, M. P. Seah, and R. B. Nicholson, "The role of solute segregation in grain boundary diffusion," *Proc. R. Soc. London. A. Math. Phys. Sci.*, vol. 379, no. 1776, pp. 159–178, Jan. 1982, doi: 10.1098/rspa.1982.0011.

[260] S. M. Reddy *et al.*, "Atom Probe Tomography: Development and Application to the Geosciences," *Geostand. Geoanalytical Res.*, vol. 44, no. 1, pp. 5–50, Mar. 2020, doi: https://doi.org/10.1111/ggr.12313.

[261] C. L. Kirkland, D. Fougerouse, S. M. Reddy, J. Hollis, and D. W. Saxey, "Assessing the mechanisms of common Pb incorporation into titanite," *Chem. Geol.*, vol. 483, pp. 558–566, 2018, doi: https://doi.org/10.1016/j.chemgeo.2018.03.026.

[262] C. Hatzoglou, B. Radiguet, and P. Pareige, "Experimental artefacts occurring during atom probe tomography analysis of oxide nanoparticles in metallic matrix: Quantification and correction," *J. Nucl. Mater.*, vol. 492, pp. 279–291, 2017, doi: https://doi.org/10.1016/j.jnucmat.2017.05.008.

[263] E. R. Maddrell, "Pressureless sintering of silicon carbide," *J. Mater. Sci. Lett.*, vol. 6, no. 4, pp. 486–488, 1987.

[264] A. Morley, G. Sha, S. Hirosawa, A. Cerezo, and G. D. W. Smith, "Determining the composition of small features in atom probe: bcc Cu-rich precipitates in an Fe-rich

matrix," *Ultramicroscopy*, vol. 109, no. 5, pp. 535–540, 2009, doi: https://doi.org/10.1016/j.ultramic.2008.09.010.

[265] F. Vurpillot, A. Bostel, and D. Blavette, "Trajectory overlaps and local magnification in three-dimensional atom probe," *Appl. Phys. Lett.*, vol. 76, no. 21, pp. 3127–3129, 2000, doi: 10.1063/1.126545.

[266] A. H. Heuer and G. K. Bansal, "Precipitation Hardening in Ceramics," in *Defects and Transport in Oxides*, Springer, 1974, pp. 415–423.

[267] A. G. Evans and T. G. Langdon, "Structural ceramics," *Prog. Mater. Sci.*, vol. 21, no. 1, pp. 171–425, 1976, doi: https://doi.org/10.1016/0079-6425(76)90006-2.

[268] R. E. SHANNON, D. L. JOHNSON, and M. E. FINE, "Precipitation Hardening of Spinel with Excess MgO," *J. Am. Ceram. Soc.*, vol. 57, no. 6, p. 269, Jun. 1974, doi: https://doi.org/10.1111/j.1151-2916.1974.tb10887.x.

[269] R. A. Langensiepen, R. E. Tressler, and P. R. Howell, "A preliminary study of precipitation in Ti 4+-doped polycrystalline alumina," *J. Mater. Sci.*, vol. 18, no. 9, pp. 2771–2776, 1983.

[270] M. Schnabel *et al.*, "Boron diffusion in nanocrystalline 3C-SiC," *Appl. Phys. Lett.*, vol. 104, no. 21, p. 213108, May 2014, doi: 10.1063/1.4880722.

[271] J. E. Proctor *et al.*, "Stabilization of boron carbide via silicon doping," *J. Phys. Condens. Matter*, vol. 27, no. 1, p. 15401, 2014.

[272] K. Ishida, "Effect of grain size on grain boundary segregation," *J. Alloys Compd.*, vol. 235, no. 2, pp. 244–249, 1996, doi: https://doi.org/10.1016/0925-

8388(95)02094-2.

[273] G. Okuma, D. Kadowaki, T. Hondo, S. Tanaka, and F. Wakai, “Interface topology for distinguishing stages of sintering,” *Sci. Rep.*, vol. 7, no. 1, p. 11106, 2017, doi: 10.1038/s41598-017-11667-2.

[274] T. Ito, T. Kondo, T. Akiyama, and K. Nakamura, “Theoretical investigations of the polytypism in silicon carbide: Contribution of the vacancy formation,” *Phys. status solidi c*, vol. 8, no. 2, pp. 583–585, Feb. 2011, doi: https://doi.org/10.1002/pssc.201000401.

[275] C. Fletcher, M. P. Moody, and D. Haley, “Towards model-driven reconstruction in atom probe tomography,” *J. Phys. D. Appl. Phys.*, vol. 53, no. 47, p. 475303, 2020.